MODULATING THE ELECTRONIC STRUCTURE OF METAL—ORGANIC FRAMEWORKS THROUGH NUCLEAR REARRANGEMENT

by

KEVIN FABRIZIO

A DISSERTATION

Presented to the Department of Chemistry and Biochemistry
and the Division of Graduate Studies of the University of Oregon
in partial fulfillment of the requirements
for the degree of
Doctorate of Philosophy

March 2023

DISSERTATION APPROVAL PAGE

Student: Kevin Fabrizio

Title: Modulating the Electronic Structure of Metal—Organic Frameworks through Nuclear Rearrangement

This dissertation has been accepted and approved in partial fulfillment of the requirements for the Doctorate of Philosophy degree in the Department of Chemistry and Biochemistry by:

Christopher H. Hendon	Chair
Carl K. Brozek	Core Member
James S. Prell	Core Member
Alan W. Rempel	Outside Member

and

Krista Chronister	Vice Provost for Graduate Studies

Original approval signatures are on file with the University of Oregon Division of Graduate Studies.

Degree awarded March 2023

DISSERTATION ABSTRACT

Kevin Fabrizio

Doctorate of Philosophy

Department of Chemistry and Biochemistry

March 2023

Title: Modulating the Electronic Structure of Metal—Organic Frameworks through Nuclear Rearrangement

The emergence of metal-organic frameworks (MOFs) as a class of versatile and renewable materials has instigated a paradigm shift in the field of chemistry. Their exceptional properties, such as high surface area, tunable porosity, and chemical and thermal stability, have garnered intense research interest for a wide range of applications, including gas storage, separation, sensing, and catalysis. Among the expansive library of MOFs, photoredox-active MOFs have gained particular attention due to their ability to reversibly store charges and photocatalytically degrade contaminants – a task necessary in the fight against climate change. However, poor orbital overlap and charge delocalization in most MOFs limit their efficiency in visible-light catalysis. In this dissertation, we explore the idea of improving MOF photocatalyst performance through reversible external stimuli. Each chapter delves into a distinct external stimulus and its effect on the electronic structure of MOFs. We investigate how cations, crystal size, and temperature affect nuclear rearrangements in MOFs, leading to a deepened understanding of how to improve photocatalytic performance. Taken together, this dissertation provides an analysis of the effect of nuclear rearrangement on defining

the electronic structure in MOFs, and it lays a foundation for the development of new, highly efficient MOF photocatalysts.

This dissertation contains both published and unpublished co-authored material.

CURRICULUM VITAE

NAME OF AUTHOR: Kevin Fabrizio

GRADUATE AND UNDERGRADUATE SCHOOLS ATTENDED:

University of Oregon, Eugene, OR, USA
Suffolk University, Boston, MA, USA

DEGREES AWARDED:

Doctor of Philosophy, Organic & Inorganic Chemistry, 2023, University of Oregon
Master of Science, Organic & Inorganic Chemistry, 2020, University of Oregon
Bachelor of Science, Chemistry, 2018, Suffolk University

AREAS OF SPECIAL INTEREST:

Sustainable Energy
Metal-Organic Frameworks
Photocatalysis
Materials Science

PROFESSIONAL EXPERIENCE:

Graduate Teaching Fellow, University of Oregon, 2019-2023

GRANTS, AWARDS AND HONORS:

Renewable Energy Scholarship Foundation, 2022
Migliorini Memorial Award in Chemistry, Suffolk University, 2018
ACS Undergraduate Physical Chemistry Award, Suffolk University, 2018
High Dean's Scholarship, Suffolk University, 2014-2018

PUBLICATIONS:

11.) Huang, J.; Marshall, C.R.; Shen, M.; Kadota, K.; McKenzie, J.; **Fabrizio, K.**; Mitchell, J.B.; Brozek, C.K. "Giant Redox Entropy in the Intercalation Chemistry of Nanoconfined MOF Nanocrystals," *J. Am. Chem. Soc.*, **2023**. Under Review.

10.) **Fabrizio, K.**; Davenport, A.M.; Brozek, C.K. "In situ Evidence of MOF Nanoparticle Photoredox Activity with Solution-State Techniques," *J. Am. Chem. Soc.*, **2023**. Under Review.

9.) **Fabrizio, K.**; Brozek, C.K. "Size-dependent Thermal Shifts to MOF Nanocrystal Optical Gaps Induced by Dynamic Bonding," *Nano Letters*, **2023**. https://doi.org/10.1021/acs.nanolett.2c04286.

8.) **Fabrizio, K.**; Andreeva, A.B.; Kadota, K.; Morris, A.J.; Brozek, C.K. "Guest-Dependent Flexibility in UiO-66, a "Stable" MOF," *Chem. Commun.*, **2023**. https://doi.org/10.1039/D2CC05895B.

7.) Mitchell, J.B.; Chen, L.; Langworthy, K.; **Fabrizio, K.**; Boettcher, S.W. "Catalytic Proton-Hydroxide Recombination for Forward-Bias Bipolar Membranes," *ACS Energy Letters*, **2022**, *7* (11), 3967–3973. https://doi.org/10.1021/acsenergylett.2c02043.

6.) Krivina, R.A.; Lindquist, G.A.; Beaudoin, S.R.; Stovall, T.N.; Thompson, W.L.; Twight, L.P.; Marsh, D.; Grzyb, J.; **Fabrizio, K.**; Hutchison, J.E.; Boettcher, S. W. "Anode Catalysts in Anion Exchange-Membrane Electrolysis without Supporting Electrolyte: Conductivity, Dynamics, and Ionomer Degradation," *Advanced Materials*, **2022**, *34* (35), 2203033. https://doi.org/10.1002/adma.202203033.

5.) Chen, L.; Xu, Q.; Oener, S.Z.; **Fabrizio, K.**; Boettcher, S.W. "Design Principles for Water Dissociation Catalysts in High-Performance Bipolar Membranes," *Nature Comm.*, **2022**, *13* (1), 3846. https://doi.org/10.1038/s41467-022-31429-7.

4.) McNeill, J.N.; Karas, L.J.; Bard, J.P.; **Fabrizio, K.**; Zakharov, L.N.; MacMillan, S. N.; Brozek, C.K.; Wu, J.I.; Johnson, D.W.; Haley, M.M. "Controlling Tautomerization in Pyridine-Fused Phosphorus-Nitrogen Heterocycles," *Chemistry-A European Journal*, **2022**, *28* (22), e202200472. https://doi.org/10.1002/chem.202200472.

3.) **Fabrizio, K.**; Le, K.N.; Andreeva, A.B.; Hendon, C.H.; Brozek, C.K. "Determining Optical Band Gaps of MOFs," *ACS Materials Letters*, **2022**, *4* (3), 457–463. https://doi.org/10.1021/acsmaterialslett.1c00836.

2.) **Fabrizio, K.**; Lazarou, K.A.; Payne, L.I.; Twight, L.P.; Golledge, S.; Hendon, C.H.; Brozek, C.K. "Tunable Band Gaps in MUV-10(M): A Family of Photoredox-Active MOFs with Earth-Abundant Open Metal Sites," *J. Am. Chem. Soc.*, **2021**, *143* (32), 12609–12621. https://doi.org/10.1021/jacs.1c04808.

1.) Mancuso, J.L.; **Fabrizio, K.**; Brozek, C.K.; Hendon, C.H.; "On the Limit of Proton-Coupled Electronic Doping in a Ti(IV)-Containing MOF," *Chemical Science*, **2021**, *12* (35), 11779–11785. https://doi.org/10.1039/D1SC03019A.

ACKNOWLEDGEMENTS

I would like to extend my heartfelt thanks to all the incredible individuals who have played a part in the successful completion of this dissertation, which has not been an easy feat. Their support and guidance have been invaluable and have played a crucial role in shaping my understanding and passion for the subject, as well as my growth as an individual.

Firstly, I would like to acknowledge my advisor Professor Carl K. Brozek, for noticing my unwavering desire to dissect complex questions in chemistry and fostering a true passion and love for the subject. If not for him, this dissertation would be incomplete, and I'd be eating pork roll on a sidewalk somewhere in Philadelphia (still doesn't sound half bad). Professor Christopher H. Hendon for bringing me out here to Oregon and realizing I was more than just a barista applying for grad school. My entire doctoral committee: Carl K. Brozek, Christopher H. Hendon, James S. Prell, and Alan W. Rempel for asking the hard questions that made this dissertation all the better. I would also like to extend my thanks to all the collaborators, included and omitted in this dissertation, whose hard work and contributions have been invaluable in bolstering the research presented here.

To my family: Monica Fabrizio, Thomas Fabrizio, Marlene Muscella, Gabriel Muscella, Emily Fabrizio, Tommy Fabrizio, and Vito Fabrizio, for being thousands of miles away, but still holding me up in incredible ways that I will never forget. My second family: Igor Kutateli, Lolita Kutateli, and Elita Kutateli for sustaining me with вкусная Uzbek, Georgian, and Russian food, and all the vodka toasts that undoubtedly contributed to my success (and late mornings). My labmates:

Checkers Marshall, LeRoy, Jacob McKenzie, Ashley Mapile, Audrey Davenport, Faiqa Khaliq, Jiawei Huang, Kentaro Kadota, Augie Witkowski, Stacey Andreeva, Jeffrey Gombart, Kelsie Heffernan, Jeremy Love, and others, for providing a space for me to ask the dumb questions, posit the crazy ideas, and make the occasional off-kilter joke. To the team at Transaera, for allowing me to be a part of their excellent team working on one of the most pressing issues of our time. To the state of Oregon, for its beauty that helped keep me semi-sane during all of this. Broadway Metro, for its nutritional yeast popcorn and cocktail slushies that I will deeply miss.

Lastly, to my partner Kristina Kutateli, who inspires and motivates me daily, and who truly made this experience an unbelievable one. I would not have been able to complete this without her - literally, I did not know how to use LaTeX – but also who has supported me and loved me in countless ways that I thought I would never get to experience in life, let alone during such a complicated and demanding part of life.

This dissertation is dedicated to my dog Olive, whose white fur has been on my clothes for every part.

TABLE OF CONTENTS

LIST OF FIGURES

Figure Page

Figure Page

Figure Page

LIST OF TABLES

Table Page

Table Page

CHAPTER I

INTRODUCTION

1.1 The Future is Photocatalysis

The future of humanity and the planet we call home is at stake. Over the past century, human activities such as the burning of fossil fuels for energy and transportation have led to a steady increase in global greenhouse gas emissions, particularly carbon dioxide. As a result, the global mean temperatures over the last eight years have been the highest ever observed.[1] Since the beginning of the Industrial Revolution in 1850, the global average temperature has increased 1.21 ^{o}C, resulting in the phenomenon generally known as climate change (Figure 1.1). These drastic temperature changes have led to a wide range of negative impacts such as sea level rise, more intense and frequent heat waves, droughts, storms, as well as the acidification of oceans and the destruction of habitats that support a diverse array of plant and animal species.[2] Researchers estimate that exceeding a difference of +1.5 ^{o}C could trigger global climate tipping points that would irreversible change our world.[3] The effects of these changes all over the world are already apparent, from the melting of the Arctic ice cap to devastating wildfires, hurricanes, and floods that have ravaged communities.[4,5] Climate change is not just a future concern, but a present threat to our economies, security, and way of life. Additionally, the adverse impact is felt the most by the most susceptible communities such as low-income households, people of color, and those in underdeveloped nations.[6]

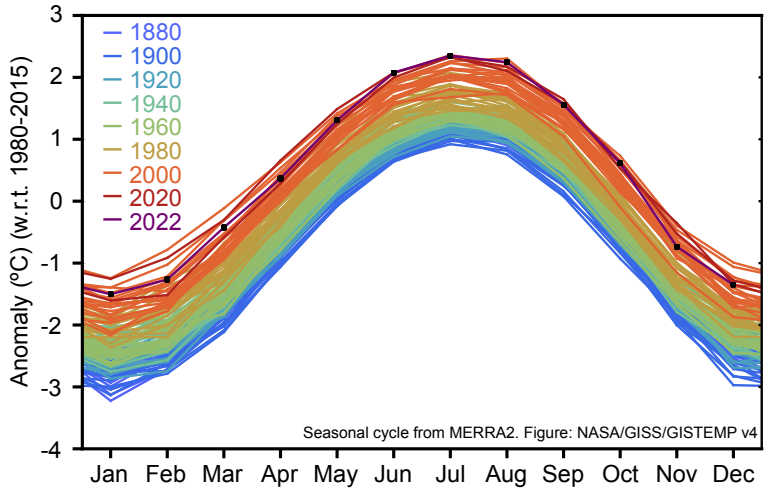

Figure 1.1. NASA Goddard Institute for Space Studies Surface Temperature Analysis *(GISTEMP)* monthly global mean temperature relative to the annual global mean temperature. Each vicennial is comprised of twenty overlaid line, representative of individual years.

Reducing global emissions of greenhouse gases is crucial to address the issue of climate change. Solar energy, while ironically responsible for the planet's warming, has the potential to be harnessed for driving industrial processes without producing greenhouse gases. The sun's power flux density is approximately 1 kilowatt per square meter (kW/m^2) on the surface of Earth. Over the entire Earth's surface, this translates to approximately 173,000 terawatts of power per hour. To put this value into perspective, this is over 10,000 times the total energy consumption of the entire human civilization.[7] Based on this incredible excess of energy, photocatalysis could offer a sustainable route to generate fuels, commodity chemicals, and other vital materials from these massive quantities of solar energy. From a light source, photocatalysts absorb photons greater than or equal to their band gap energies to create an excited state with photogenerated electron-hole pairs. As shown in Figure 1.2, when the photocatalyst is combined with the use of a hole scavenger (e.g., amines, alcohols, oxides), which quench the unoccupied

hole, the photogenerated charges become "trapped" on the catalyst and can be used for conventionally challenging reactions without the aid of high temperature or pressure (e.g., photocatalytic CO_2 reduction,[8] H_2 evolution from water splitting,[9] photochemical nitrogen fixation,[10] and dehalogenation of halogenated organic compounds[11]).

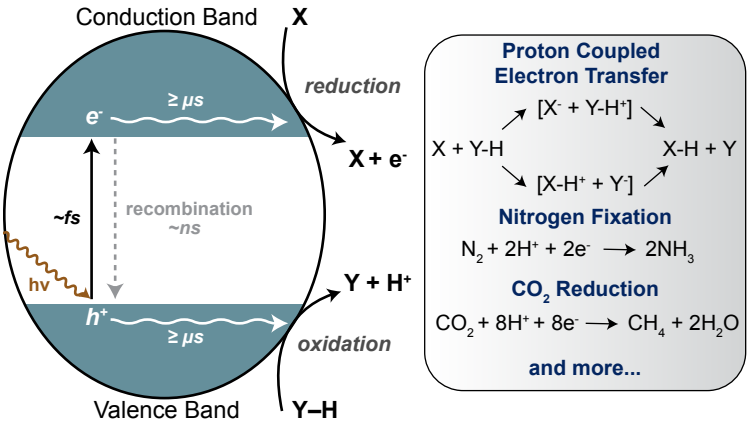

Figure 1.2. General representation of photoredox in a catalyst with relative timescales for competing processes. The active catalyst can produce photoinduced charges which can consequently be used for the oxidation or reduction of a species.

Despite the potential advantages of photocatalysis, significant obstacles must be surmounted to realize its full potential. One of the most pressing challenges is the creation of photocatalysts that are both efficient and stable. Commonly, solar energy conversion technologies use transition metal oxides for their diverse redox reactivity with molecular substrates, narrow band gap energies, and conduction- and valence-band energies that vary greatly between materials, allowing specific reactions to be driven by selecting materials with the appropriate electronic structure.[12,13] To illustrate, titanium dioxide (TiO_2) is a widely studied photocatalyst due to its ability to photocatalytically split water to produce H_2 and O_2.[9,12] On the other hand, conventional semiconductors, such as binary and

ternary metal oxides, lack chemical tunability and are prone to defects that are difficult to identify and control.[14,15] For example, the identity of the oxidizing species generated from photoexciting TiO_2 remains disputed.[15] Furthermore, the defects at the surface and in the lattice of conventional semiconductors result in rapid electron-hole (e^--h^+) recombination, a process that hinders the transfer of the electron to acceptor molecules (X in Figure 1.2) and holes to donor molecules (Y in Figure 1.2) For these reasons, single junction solar cells made with ZnO nanocrystals have yet to surpass photoconversion efficiencies (PCEs) of 5.1% – well below the industry standard of silicon, at 20%.[16,17] Additionally, because of their lack of chemical functionality, many metal oxides possess band gap energies that are confined to the ultraviolet (UV) light range (>3.26 eV).[18–20] However, UV light radiation makes up less than 5% of incident solar light, making visible light use (43%) more promising for improving solar energy usage and large-scale industrial applications. Undoubtedly, to meet the demands of climate change, there is an urgent need to develop materials that can perform as tunable, visible light-responsive photocatalysts with high activity and stability.

1.2 MOFs and MOF Photocatalysts Provide a Solution

MOFs, or porous coordination polymers, are well-ordered, permanently porous materials constructed from inorganic clusters containing metal ions that are bonded to organic ligands, known as linkers, that bridge the inorganic clusters together. For instance, the first MOF, ZIF-8 (Zn(2-methylimidazolate)$_2$), is a mononuclear MOF comprised of Zn^{2+} ions tetrahedrally-coordinated to nitrogens in four imidazolate rings, and was synthesized in the laboratory of Professor Omar Yaghi at the University of Michigan in 1995.[21] Since then, researchers

have developed and synthesized over 90,000 unique MOFs with different chemical compositions and functionalities, and predict that there could be at least 500,000.[22]

Unlike transition metal oxides, the surface area, topology, and pore structure of MOFs can be tailored by careful choice of organic and inorganic precursor, which has led to a surge of applications in renewable energy and sustainability.[23–27] Among these potential applications, photocatalysis has been an area of particular interest.[28–32] MOFs have shown potential as photocatalysts due to their versatility in structural design that enable light absorption across a wide range of wavelengths. Additionally, the highly-ordered crystalline structures of MOFs suppress rapid e^--h^+ recombination. The high porosity of MOFs also proves to be a major asset, allowing for efficient movement of charge carriers, leading to improved e^--h^+ separation and ultimately, enhanced photocatalytic activity. Like TiO_2, most photo-active or photocatalytic MOFs contain Ti^{4+}, due to its low toxicity, natural abundance, and ligand field orbitals (typically oxides) that dominate the frontier orbitals of the MOF.[18,33–36] Under UV irradiation, an excited electron localizes on the Ti center to generate reactive Ti^{3+} sites, while an excited hole localizes on oxide-based orbitals with strong oxidizing potential. Both charges, either the reducing electrons or oxidizing holes, can be harnessed to drive photocatalytic reactions.

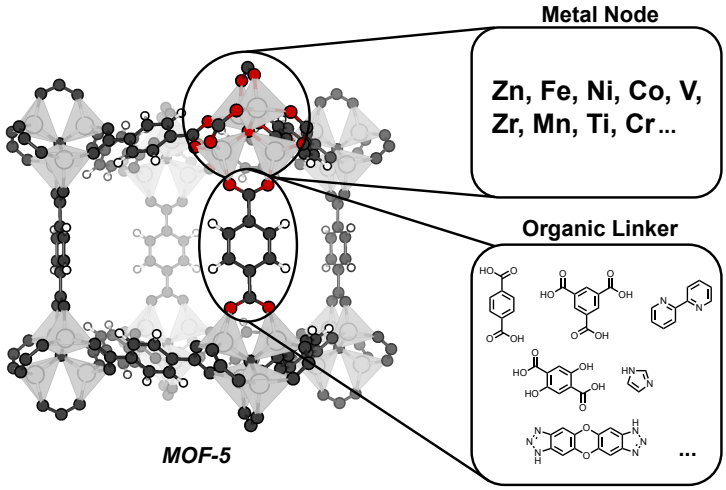

Figure 1.3. General example of a MOF and MOF tunability. Researchers are able to customize a MOF for specific applications by selecting "building blocks": the metal node or organic linker.

In 1999, MOF-5 (Zn_4O(1,4-benzenedicarboxylate)$_3$) (Figure 1.3) was also synthesized in Omar Yaghi's lab,[37] followed by an exploration of its optical and vibrational properties using photoluminescence and diffuse-reflectance spectroscopy in 2004 by the Zecchina group.[38] The intense ligand to metal charge transfer transition (LMCT) observed for MOF-5 suggested that the Zn_4O_{13} clusters and organic linkers within the framework function independently, with the clusters behaving as ZnO quantum dots and the linkers serving as light-absorbing antennae. Because of this investigation, in 2007, researchers first explored using MOF-5 for photocatalytic phenol degradation in aqueous solutions and noted activity comparable to P-25 TiO_2.[39] Despite these advances, the researchers observed decomposition of MOF-5 under exposure to moisture from air or water.

Since this initial foray into the photocatalytic activity of MOF-5, researchers have made great strides in improving MOF photocatalyst performance by a variety of techniques, such as ligand functionalization. For example, when researchers discovered that by merely adding an amino group to the native

benzenedicarboxylate linker in MIL-125 ($Ti_8O_8(OH)_4$(1,4-benzenedicarboxylate)$_6$) shifted the crystal color from white to yellow,[40] it launched a series of investigations into the electronic structure of Ti-containing MOFs. In 2013, Hendon *et al.* indeed confirmed that the band gap energy of NH_2-MIL-125 shifts into the visible spectrum (3.6 to 2.6 eV).[41] They proposed that donating electrons from the functional group, such as N 2p in amino (–NH_2) groups, red-shifted the valence band edge, vastly decreasing the optical band gap. Accordingly, the amino-functionalized MIL-125 (NH_2-MIL-125) has shown great promise for visible-light catalyzed CO_2 reduction and H_2 generation - rivaling the performances of conventional semiconductors.[28,42,43] Alternatively, a mixed-metal/linker strategy can be used to tune MOF photocatalyst performance.[44–46] In 2015, the Cohen group reported a post-synthetic exchange of Ti^{4+} into a Zr^{4+}-based MOF, whereby the introduction of Ti^{4+} as an electron mediator improves the turnover frequency (TOF) by nearly 400% compared to TiO_2 in visible-light CO_2 reduction.[47]

Although MOFs have shown great promise as photocatalysts, there is still much work to be done to fully comprehend and optimize their behavior. For example, while ligand functionalization and mixed-metal/linker strategies serve as useful tools for understanding MOF photocatalyst performance, many linkers and post-synthetic exchanges are costly or unfeasible in purposes of a large-scale application. At the time of writing, one kilogram of the amino-BDC linker in NH_2-MIL-125 is on the order of $5,000, while the unfunctionalized linker is only $80 per kilogram. Therefore, further research is required to investigate the optimal synthesis and functionalization strategies, impact of structural distortions and/or defects, their mechanisms of reactivity, and their performance under various conditions.

1.3 Nuclear Motion as a Strategy to Understand MOF Photocatalyst Performance

While great strides have taken place in terms of MOF TOF and stability in photocatalytic reactions since the advent of MOFs,[48–54] many of these techniques require chemical modification or functionality to drive these reactions forward under ideal conditions. Hence, a non-permanent and/or reversible technique to improve catalyst performance is highly sought after for these purposes. Moreover, at a fundamental level, MOF structures can possess symmetry-lowering defects and exhibit reversible structural flexibility, the extent of which is yet to be fully known. The impact of these structural perturbations on optical behavior remains an open area of research, thereby necessitating further investigation.

Dynamic distortions to solid lattices, such as those in MOFs, contribute a significant role in determining their optical behavior.[55–60] The presence of lattice vibrations, or phonon modes, can result in a range of geometric distortions that alter the equilibrium structure of the MOF. Classically, this effect can be captured with a single well potential, such as those in standard bond vibrations. Still, these vibrations can cause such extreme distortions to the equilibrium geometry, triggering a multitude of physical,[61] magnetic,[62] optical,[63] and electronic properties.[64–66] For example, the dynamic coordination of a carboxylate species improves water oxidation on ruthenium-based single-site catalysts fifty-fold.[67] When these phonon modes couple with electronic phenomena, they give rise to vibronic interactions that can cause significant spectral broadening when studying optical behavior. This broadening is due to the presence of different geometric configurations in the MOF (Figure 1.4a), which are a result of the dynamic motion of the nuclear positions of atoms in the solid lattice.[59,68] Furthermore, thermally-

assisted nuclear motion is a factor that contributes to the optical behavior of MOFs. As temperature increases, the range of geometries that a MOF can exist in also increases, leading to a greater likelihood of vibronic interactions and changes in its optical properties. As a result, investigating these vibrations, and what triggers them, can provide insight into predicting and controlling such properties.

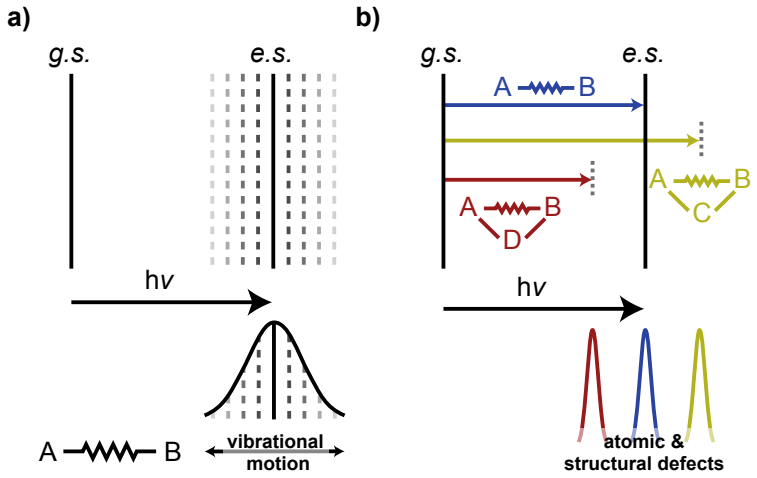

Figure 1.4. Depiction of two scenarios that give rise to optical transitions through symmetry-lowering behavior. **a)** vibrational motion in a crystal lattice result in many states in which an electron can occupy **b)** defects (vacancies/ interstitial atoms (Frenkel defects), or structural/atomic displacement) induce mid-gap states that are accessible by electrons.

Vibrations are not the only cause of structural distortions in solid lattices. In reality, an arrangement of "crystals" deviates from the ideal, perfect periodic repetition of identical groups of atoms and contains numerous structural defects.[69,70] These irregularities can be caused by compositional inhomogeneities, also known as "defects."(Figure 1.4b) The definition of these inhomogeneities is diverse, from simple lattice and interstitial vacancies to substitutional defects (*i.e.*, impurities and dopants).[71] In the context of this dissertation, the term "defect" generally refers to sites that disrupt the regular atomic arrangement of the static

parent crystalline structure. These structural disorders and flaws have a significant impact on the physical and chemical properties of solid-state materials.[72–76] In some instances, such as in transistor fabrication and thermoelectrics,[77] perfect crystals are desired; however, defects do not always have negative effects. In fact, many material properties are contingent on the lattice's unique imperfections. For example, the electrical conductivity of materials such as silicon are entirely attributable to minor quantities of chemical impurities and defects.[78] Additionally, because defects disrupt crystallographic symmetry that give rise to optical properties, shifted or new transitions, coined "mid-gap states" can be observed by optical spectroscopy.[50](Figure 1.4b)

In recent years, researchers have observed intriguing phenomena in MOFs that stray from the conventional view of them being static structures. The concept of dynamic metal-linker bonding, or simply dynamic bonding, has been invoked as a potential explanation for the unique properties of MOFs such as phase changes,[79–85] post-synthetic exchanges,[45,86,87] negative thermal expansions,[88–90] and notably, electronic structure shifts.[91–93] This line of research was sparked by the work of Andreeva *et al.*,[94] who used Variable-Temperature Diffuse Reflectance Infrared Fourier-Transform Spectroscopy (VT-DRIFTS) to study "soft" modes in MOFs. By analyzing the carboxylate stretches of common MOFs, the researchers noticed a reversible red-shift upon heating that could be attributed to an equilibrium mixture of "loose" and "tight" metal-linker configurations (Figure 1.5). The classical definition of bond vibrations, as described in previous paragraphs, assumes that a material can be at equilibrium and exist in a range of geometries, which can be captured with a single well potential. However, the authors of this study propose a different theory, where they suggest the existence of a double

well potential in materials. In this scenario, the material exists in equilibrium between two different states, each with its own unique set of atomic positions triggered by external stimuli. This deviation from the classical theory leads to a new understanding of how lattice vibrations can impact a material's properties. The dynamic motion of the nuclear positions of atoms in the solid lattice, hereafter referred to as "dynamic bonding," can cause the material to transition between the two equilibrium states. This transition is facilitated by the presence of phonons, which act as a soft mode. This study provided a simple and effective method for tracking dynamic bonding in MOFs. Crucially, these results helped explain why a series of ZIF MOFs could be 'melted' into the first examples of 'MOF liquids' wherein the chemical configuration, bonding, and importantly, porosity, remained intact in the disordered liquid phase.[95–97] The phenomenon of melting MOFs is posited to be a balance of T_m (melting temperature) and T_d (decomposition temperature). However, the melting mechanism specifically is proposed to be driven by high-temperature imidazole dissociation/Zn^{2+} undercoordination.

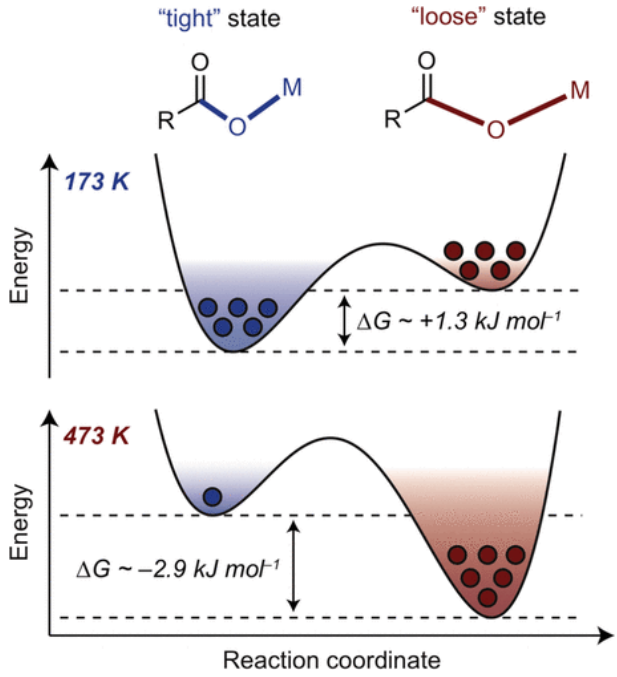

Figure 1.5. Equilibrium between "tight" and "loose" ensembles of MOF metal-carboxylate populations existing near thermoneutral equilibrium. **Top:** Conversion of MOF metal-linker bonds between two ensemble-averaged states. **Bottom:** Temperature-dependent free energies (ΔG) and relative population according to equilibrium constants derived from experimental data. Reproduced with permission from ref.[94]. *Copyright 2020 American Chemical Society.*

Another manifestation of dynamic bonding is in MOF-5, which is usually assumed to contain static tetrahedral Zn^{2+} sites – even in the presence of guest molecules. However, a tetrahedral Zn^{2+} ion within the MOF-5 cluster can bind to two DMF molecules upon solvent soaking, initiating an octahedral geometry change.[98] *Ab initio* molecular dynamics (MD) simulations and solid-state nuclear magnetic resonance spectroscopy (SS-NMR) suggest that the MOF-5 secondary-building units (SBUs) dynamically bind and release DMF molecules without compromising the structural integrity of the framework, but thereby quickly changing the coordination number of the Zn sites. In a similar study, MOF-5 can be soaked in cationic solutions of other metallic ions (Ti^{3+}, V^{2+}, V^{3+}, Cr^{2+},

Cr^{3+}, Mn^{2+}) and post-synthetically replace Zn sites to generate novel MOFs inaccessible by conventional synthetic techniques.[86] Hence, these results indicate that carboxylate linkers must reversibly dissociate and associate at the SBU of MOF-5 to allow for metal ion insertion.

While dynamic bonding has been shown to play a crucial role in explaining various phenomena observed in MOFs, the relationship between these unique stimuli and the electronic structure remains unclear. While some researchers have begun to investigate the effects of dynamic bonding on catalytic performance in MOFs,[99–102] the specific mechanisms and responses of MOFs to nuclear motion have yet to be fully explored.

This dissertation aims to shed light on how the electronic structure and correspondingly, the optical behavior, of MOFs change in response to stimuli-induced atomic motion and rearrangements. In Chapter 2, the electrostatic effect of cations (alkali earth ions and protons) on the redox potentials of photoredox-active MOFs are explored. We discovered that the presence of redox-inactive cations nearby the SBUs of the MOFs greatly impact their redox potentials, and consequently, the selectivity and performance of the MOF in specific reactions. Furthermore, we elucidated a general technique to extract optical band gap energies from solid-state diffuse reflectance data. In Chapter 3, the modulation of crystal sizes of a photoredox-active MOF and the investigation of its electronic structure using solution-state techniques is performed to unveil its unique reactivity patterns and vibronic distortions for the first time. In Chapter 4, temperature is utilized as a tool to reversibly control the band gap energies of common MOFs and vibronic parameters are established to explain the size-dependent optical behavior of MOF nanocrystals. Next, "flexibility constants" are proposed to help broadly define the

population of “loose” and “tight” states across the field of dynamic bonding. These findings will provide valuable insights for the wider photocatalytic community to develop reversible techniques for improving the performance and selectivity of MOF photocatalysts, as well uncover the source of optical behavior caused by structural distortions in MOFs.

CHAPTER II

CATION-INDUCED NUCLEAR MOTION AND OPTICAL BAND GAP ASSIGNMENT

2.1 Tunable Band Gaps in MUV-10(M): A Family of Photoredox-Active MOFs with Earth-Abundant Open Metal Sites

This section includes an excerpt from previously published and co-authored material from Fabrizio, K.; Lazarou, K. A.; Payne, L. I.; Twight, L. P.; Golledge, S.; Hendon, C. H.; Brozek, C. K. Tunable Band Gaps in MUV-10(M): A Family of Photoredox-Active MOFs with Earth-Abundant Open Metal Sites. *J. Am. Chem. Soc.* **2021,** *143* (32), 12609–12621.

The article was co-written by Kevin Fabrizio, Konstantinos A. Lazarou, Christopher H. Hendon, and Carl K. Brozek. The idea was conceptualized by Kevin Fabrizio, Konstantinos A. Lazarou, Christopher H. Hendon, and Carl K. Brozek. Experiments were performed by Kevin Fabrizio and Konstantinos A. Lazarou. Lilian I. Payne performed the computational simulations. Liam P. Twight and Stephen Golledge assisted in characterization.

Introduction. The frontier orbital energies of photocatalysts and molecular substrates dictate key aspects of photoredox reactions, ranging from the thermodynamic driving forces of charge transfer to the wavelengths necessary for photoexcitation.[103–106] Although solid-state materials benefit from greater stability compared to homogeneous systems, defining the energetic positions of relevant orbitals, such as the band-edge potentials, is often complicated by compositional defects that dominate the electronic structures.[15,107]

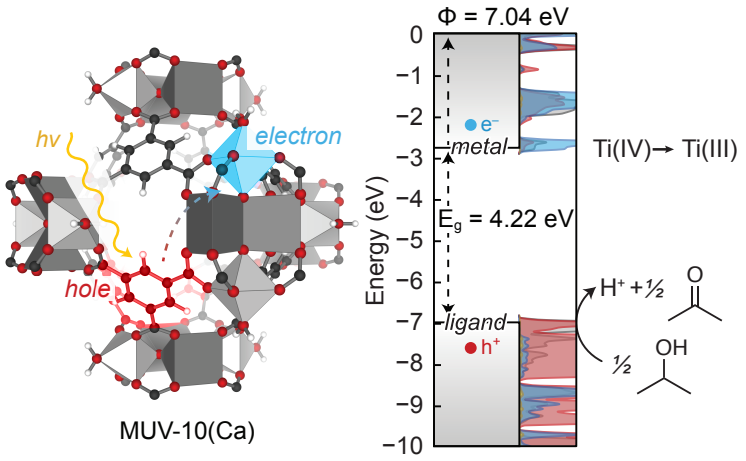

Figure 2.1.1. Molecular and band-diagram representation of the photodoping process in MUV-10(Ca). Partial density-of-states contributions from Ti, O, and C are denoted in blue, red, and black, respectively.

Studying site-isolated metal centers in crystalline solids has therefore become an important strategy for investigating interfacial reactivity with molecular control. Whereas the active sites of conventional heterogeneous catalysts can be ill-defined, crystallographic metal centers in metal-organic frameworks (MOFs) combine the atomic precision of molecules with the convenience of solids. In place of typical organic linkers that bridge metal cluster "nodes" in MOFs, such as 1,4-benzenedicarboxylate, "metalloligands" offer an effective approach for installing precise catalytic species. Metalloligands are constructed by functionalizing well-studied homogeneous catalysts with carboxylates or other binding groups to repurpose them as MOF linkers.[108–110] Although they boast improved stabilities, metalloligands exhibit reactivity patterns that still resemble the chemistry of the homogeneous analogs. When viewed as discrete coordination complexes, the metal nodes of MOFs, on the other hand, often exist without molecular precedent,[111] thereby enabling unusual small molecule reactivity,[112] the stabilization of reactive intermediates,[113] and impressive catalytic performance.[114,115] For example,

the family of M-MFU-4l (M = Ti, V, Cr, Ni, Zn) materials achieve ethylene oligomerization and polymerization activities superior to other homogeneous or heterogeneous catalysts.[114,116–119], MOF metal nodes therefore offer a unique platform for studying interfacial heterogeneous reactivity, whether for uncovering fundamental parameters difficult to pinpoint in less precise heterogeneous systems, *e.g.*, TiO_2, or to discover entirely new chemical transformations. Whereas most reports of catalysis at MOF metal nodes have focused on thermochemical and electrochemical reactions,[120–122] investigations into their photochemical reactivity typically involve co-catalysts. In these systems, photoexcited charges migrate from the MOF clusters to metalloligands, or to impregnated nanoparticles and molecular catalysts, for subsequent reactivity.[123–129 130–132] By comparison, the intrinsic photoredox chemistry of MOF nodes remains underexplored.[133–139]

Titanium-based MOFs (Ti-MOFs) offer a useful platform for studying heterogeneous photoredox chemistry. Because the low-lying empty d-orbitals of titanium dominate the conduction bands, the lowest-energy optical absorption features can be understood as linker-to-titanium charge transfer bands.[140] Synthetic manipulation of either metal or linker consequently leads to predictable changes to the band gap. For example, the amino-functionalized version of the material known as MIL-125-NH_2 ($Ti_8O_8(OH)_4$(2-aminoterephthalate)$_6$) displays a bandgap of 2.6 eV compared to the unfunctionalized variant, with a gap of 3.6 eV, resulting from the destabilization of the valence band, composed of linker-based orbitals upon amino functionalization.[28,141] Interestingly, many titanium MOFs are capable of storing charges upon photoexcitation in the presence of sacrificial reductants. For example, irradiating (MUV-10(M) ($Ti_3M_3(\mu_3\text{-}O)_2$(1,3,5-benzenetricarboxylate)$_4(H_2O)_6$, M = Ca or Mn) with UV-visible light and excess

ethanol leads to promotion of carboxylate-based electrons to empty titanium orbitals, with the resulting orbital holes quenched by oxidation of ethanol to furnish acetaldehyde and protons (Figure 2.1.1). In the absence of air, such photochemical electronic doping (photodoping) leads to generation of indefinitely stable Ti^{3+} centers that are charge-balanced by H+.[140] In other words, the H^+ – e^- pairs become stabilized at the MOF clusters, rather than combine to form H_2. Similar attempts to photodope titanium MOFs featuring single Ti ions rather than multinuclear clusters does not lead to isolation of Ti^{3+}, however. To explain the unique ability of cluster-based Ti-MOFs to generate Ti^{3+} through photodoping, the Martí-Gastaldo group has proposed that clusters tend to produce photoexcited states where the electron localizes on the Ti atoms and the holes center on the linkers.[53] The spatial separation of excited-state charges therefore disfavors rapid electron-hole recombination, allowing ethanol to quench the linker-based hole and trap the Ti^{3+} state. The clusters in these materials typically contain inorganic oxos that bridge titanium centers. In support of the Martí-Gastaldo hypothesis, we propose that bridging oxos prevent H_2 generation by serving as proton acceptors, thereby lowering the electrochemical potential of the H^+ – e^- pair. In a similar vein, the Mayer group, has justified the charge storage capacity of titanium cluster MOFs in terms of cation-oxo electrostatic pairing stabilization.[142,143] Although MIL-125 nodes contain eight titanium centers, steady-state photoirradiation does not lead to quantitative reduction of all metal ions to Ti^{3+}, as evidenced by electron paramagnetic spectroscopy (EPR). Treatment of MIL-125 particles with sodium-based reductants, however, increases the average number of reduced metal ions per MIL-125 cluster, suggesting a strong cation-dependence and ion-pairing effect of charge storage in titanium MOFs.[142] The photoredox chemistry of MOFs,

therefore, depends strongly on the chemical factors that control the electrochemical potentials of the resulting photoexcited charges. We therefore seek Ti-MOFs with open metal sites (OMSs) and synthetic tunability for investigating the chemical factors that control photoredox activity.

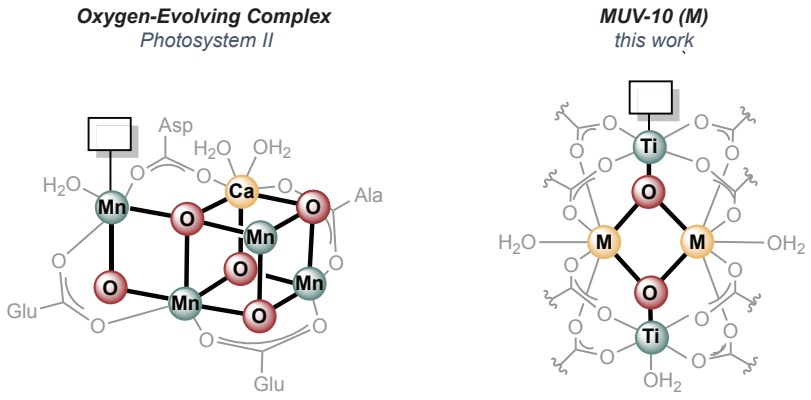

Figure 2.1.2. Comparison of the oxygen-evolving complex of Photosystem II and the heterometallic cluster of MUV-10(M). Redox-active metal sites noted in blue, bridging oxygens in red, redox-inactive metal sites in yellow, and open metal sites as boxes.

In designing a system for studying heterogenous photoredox chemistry, the oxygen evolving complex (OEC) of Photosystem II (Fig. 2.1.2) provides a useful example because the Mn_4O_5Ca cluster accomplishes one of the most important examples of photoredox catalysis by harnessing a carboxylate ligand field akin to typical MOF structures.[144–147] The OEC possesses several design principles for photoactive MOFs: In addition to being comprised of Earth-abundant metal ions, the redox-active Mn^{2+} bears an OMS and a redox-inactive (*i.e.*, redox potential inaccessible under relevant conditions) Ca^{2+} ion influences the energetics of the OEC. Indeed, replacing Ca^{2+} with other alkaline Earth or transition metals leads

to systematic shifts in the redox potentials of the native and biomimetic complexes, and in the redox chemistry of poloxometallates.[148–151] We hypothesize that Ti-MOFs containing redox-inactive metal ions would offer a convenient platform for photoredox chemistry with tunable electrochemical properties.

Here, we report that the Ti-MOF known as MUV-10(M)[152] can be expanded into an isostructural family of materials with clusters that incorporate a range of redox-inactive metal ions and Ti centers that support OMSs. Measurement of band gap (HOMO-LUMO) energies reveals that while the identity of the redox-inactive ions electrostatically shifts the Ti-based orbital energies, their dominant effect is to introduce structural flexibility that strongly impacts optical absorption profiles, especially in the presence of solvent. A similar effect is observed with the introduction of redox-inactive ions to the MOF pores, further illustrating their energetic influence on the orbital energies of photoredox materials. Importantly, the interpretation of these band gap energies required a reevaluation of the applicability of Tauc analysis, which will guide the future analysis of MOFs and other materials in general. Finally, the Fermi levels (electrochemical potentials) of photodoped MUV-10 were approximated using a contactless optical redox indicator method, providing evidence of heterogeneous photoredox reactivity and a thermodynamic justification for the charge-storage properties of Ti-MOFs.

Experimental.

Materials and Equipment. All manipulations were performed under an atmosphere of nitrogen in an LC Technology Glovebox or by using standard Schlenk techniques. All reagents were purchased from commercial sources and used without further purification. Solvents were purified using a LC Technologies SP-1 solvent purification system. Powder X-ray Diffraction (PXRD) patterns were

recorded by dispersing activated dry samples on zero-background Si plates using a Bruker D2 Phaser, in the range of 3 to 35 º 2θ using a copper K-α radiation source. N_2 gas sorption isotherms were collected on a Micromeritics ASAP 2020 Plus. X-ray fluorescence data was collected using a Rigaku ZSX Primus II wavelength dispersive X-ray fluorescence spectrometer with a rhodium X-ray source. IR spectra were collected on a Bruker Alpha II with an ATR attachment in a nitrogen filled glovebox and a Nicolet 6700 FT-IR spectrometer with an ATR attachment in open air. UV-vis measurements were performed using a PerkinElmer Lambda 1050 spectrophotometer with a Peltier-cooled InGaAs and PbS detector. MUV-10(M) samples were diluted with $BaSO_4$ as a reference, loaded into a Harrick high temperature environmental chamber and attached to a Harrick praying mantis accessory to perform DRUV-vis measurements. The chamber was allowed to equilibrate at a set temperature from 25 ºC to 350 ºC for 30 minutes under dynamic vacuum before each measurement was taken at static vacuum.

Preparation of MUV-10(Ca, Mn). MUV-10(Ca) and MUV-10(Mn) were synthesized according to a literature method.[152] Briefly, a solvothermal reaction of calcium chloride dihydrate (0.0176 g, 0.12 mmol) or manganese (II) chloride tetrahyrate (0.0238 g, 0.12 mmol), titanium (IV) isopropoxide (36 μL, 0.12 mmol) and trimesic acid (0.125 g, 0.595 mmol) in DMF (12 mL), using glacial acetic acid (3.5 mL) as a modulator for crystal growth, is conducted at 120 ºC for 48 hours in a 50-mL Pyrex Schott bottle.

Preparation of MUV-10(Ba, Sr, Cd). Following a procedure adapted from Castells-Gil *et al.*,[152] trimesic acid (0.125 g, 0.60 mmol) and either barium chloride dihydrate (0.044 g, 0.18 mmol), strontium chloride hexahydrate (0.048 g, 0.18 mmol), or cadmium chloride hemi(pentahydrate) (0.041 g, 0.18

mmol) were added to a 50-mL Schott bottle dissolved in dry DMF (12 mL). The solution was then transferred to a benchtop N_2 glovebox, where glacial acetic acid (3.5 mL for Cd/Sr, and 5.0 mL for Ba) and titanium (IV) isopropoxide (36 μL, 0.12 mmol) were added, and the bottle was resealed. Then, the solution was heated in a fixed-temperature oven at 120 °C for 48 hours. The resulting white powder was centrifuged and washed three times sequentially with 20 mL clean DMF and methanol, and then dried under dynamic vacuum overnight at room temperature.

Fermi Level Estimation by Optical Redox Indicator. In an N_2 glovebox, decamethylferrocene ($FeCp^*_2$) was weighed into a Schlenk flask and dissolved in ca 5 mL hexanes. In air, benzoquinone was dissolved in ca 5 mL of ethyl ether, and HBF_4 was added. The $FeCp^*_2$ and benzoquinone solutions were combined by cannula transfer, creating a cloudy dark-green mixture. This solution was left to stir for one hour, and let stand for 30 minutes, yielding a green precipitate. The flask was transferred to a benchtop N_2 glovebox, where it was vacuum filtered and washed with dry hexanes (∼40 mL). Once transferred into a standard N_2 glovebox, the powder was dissolved in dry MeCN. The concentration of the solution was tested via UV vis by way of a dilution of 300 μL in 3 mL MeCN in an air-free quartz cuvette with pathlength 1 cm, and the concentration was determined to be 4.06 mM by the 30 minute irradiation absorbance value at 778 nm for an absorptivity coefficient of 488 L mol^{-1} cm^{-1}, according to prior studies of the decamethylferrocene/decamethylferrocenium ($[FeCp^*_2]$/ $[FeCp^*_2]^+$) redox couple.[153] Similar to the previous experiment, 3 mg of MUV-10(Ca) were added to 3 mL of stock $[FeCp^*_2]^+$ in MeCN and 300 μL of dry ethanol. The cuvette was irradiated with a mercury arc lamp, and the UV-vis spectra were recorded after

allowing the powder to settle. After 1290 min of irradiation (21.5 hr) the vibrant green solution had turned yellow, indicating the complex's conversion to $FeCp_2^*$.

Soaking MUV-10(Ca) in Nitrate Salts. The impact of H^+ on MUV-10(M) was tested by soaking 1 mg of MUV-10(Ca) in 2 mL of 10^{-3} M HNO_3 overnight (> 16 h) and then measuring the diffuse reflectance spectrum. Similarly, the impact of different cations was examined by preparing suspensions consisted of 2 mL aqueous solutions of $LiNO_3$, $NaNO_3$, and KNO_3, respectively together with 1 mg of MUV-10(Ca) such that the ratio of cation to Ti in the MOF would be 5:1. After every soaking experiment, a powder diffraction pattern was collected to ensure that the crystal lattice remained intact (Fig. S23).

Computational Methods. Density Functional Theory (DFT) calculations were performed to identify the density of states (DOS) and band gap energy (E_g) of MUV-10 (M) derivatives, in addition to different hydration states and cation localization on the MOF cluster.

All MOF structures were geometrically equilibrated with the GGA functional PBEsol[154] in VASP[155–157] and a 500 eV planewave cutoff basis set. A Γ-only k-grid was converged to ionic and electronic criteria of 0.005 eV and 1×10^{-6} eV, respectively. Then, using the range separated hybrid GGA approach, HSEsol06[158] (PBEsol + 25 percent HF) the electronic band gap was computed using a Γ-only k-grid and the same convergence criteria as above. This approximation was determined to be suitable, as the PBEsol electronic band structure (Figure A.40), revealed that MUV-10(Ca) has extremely flat bands, indicating a direct band gap, and localized electronic states. Thus, Γ-only is suitable to assess the band gap.

In the transmetallated structures, all Ca atoms in the unit cell were exchanged for the respective metal before a full optimization. For the hydrogen functionalized structures, one inorganic oxo in the unit cell was functionalized with a hydrogen atom. The same procedure was followed for the proton functionalized structures, with one electron removed from the unit cell to constitute the addition of a proton. Manganese and cadmium structures were converged with H_2O coordinated solely to titanium at the nodes. The manganese-substituted parent scaffold was found to have lower energy in the antiferromagnetic magnetic orientation, and so the electronic structures of all manganese substituted derivatives were calculated in the antiferromagnetic state after geometric optimization. We present a comparison of the manganese structure in Figure A.33.

Finally, both hydrogen-functionalized and parent bulk structures were aligned to the vacuum level using a previously reported method.[159] In brief, we probe the internal electrostatic potential at the center of the pore, using the method depicted in Figure A.35.

Results and Analysis.

Preparation of the MUV-10(M) Isostructural Series. The Ti-MOF known as MUV-10(M), where M = Ca or Mn, was selected as a molecularly defined platform for studying heterogeneous photoredox chemistry. In an idealized disorder-free model, the heterobimetallic clusters of MUV-10(M) consist of two octahedral Ti(IV) centers bridged to two heterometals by inorganic oxos and trimesate carboxylate linkers (Figure 2.1.2). By combining the carboxylate and aqueous ligand environments, metal-oxo architecture, redox-inactive heterometals, and photoactive Ti ions with OMSs therefore renders MUV-10(M) an ideal candidate for pursuing the design principles of the oxygen-evolving complex (OEC)

of PSII. Just as the redox-inactive heterometal tunes the redox chemistry of OEC and molecular inorganic clusters, we sought to prepare analogs of MUV-10(M) with a range of metal ions, based on the hypothesis that they would influence the $Ti^{4+/3+}$ reduction potential through electrostatic interactions. By building a library of MUV-10(M) variants, we planned to investigate the energetic effect of cations on the electronic structure of photoredox materials.

Three new MUV-10(M) derivatives (M = Ba, Sr, Cd) were prepared by a modified solvothermal synthesis. Figure 2.1.3a plots the powder X-ray diffraction (PXRD) patterns, confirming retention of the original MUV-10(Ca) structures. Attempts to synthesize MUV-10 solely from Sr^{2+}, Ba^{2+}, or Cd^{2+} precursors yielded amorphous materials. We note that an attempt at post-synthetic cation exchange in MUV-10(M) was recently reported not to yield isostructural products.[160] Although relative peak intensities differ from the calculated geometries as-is, simulating preferred growth in the [111] direction shows almost an identical fit, with the [222] and [333] phases growing in intensity as well (Figure A.1). Furthermore, a recent report on the applications of MUV-10(Ca) particles noted that by simulating the equilibrium shape of the crystal, the (111) planes energetically show preferential formation with minor contributions from the (001) planes.[161] Correspondingly, the (110) and (111) Bragg intensities have differed by varying crystal growth modulator equivalents in nanoparticle syntheses of MUV-10(Ca).[162] While attempts to incorporate Mg^{2+} to complete the series of alkaline Earth metals did not yield a crystalline product, a recent study demonstrated that the inclusion of Mg^{2+} results in a separate MOF isostructural to the MIL-100 family.[163] We suspect that ionic radius is a critical determinant of isostructural MOF syntheses, given that the ionic radius for Mg^{2+} in a six-

coordinate geometry is 0.72 compared to Ca^{2+} = 1.0, Mn^{2+} = 0.83, Ba^{2+} = 1.35, Sr^{2+} = 1.18, and Cd^{2+} = 0.95.[164] Interestingly, computational methods in the seminal report on MUV-10(Ca, Mn) predicted that an MUV-10(Cd) variant would be the least thermodynamically favorable, and yet we demonstrate it can be prepared following similar procedures. Cd^{2+} was targeted in order to compare the energetic impact of a d^{10} transition metal ion in comparison to Mn^{2+}, which is d^5, and to expand upon examples of redox-inactive variants beyond alkaline Earth metals. X-ray fluorescence spectra of all powders confirmed that both metal ions incorporate into the structures (Figures A.2-A.7). X-ray photoelectron spectroscopy reveals the anticipated metal ion valences and confirms a 1:1 ratio between Ti^{4+}:M^{2+} in MUV-10(Sr) and MUV-10(Cd). The results for MUV-10(Ba) suggest an excess of titanium, however. Inductively coupled plasma mass spectrometry (ICP-MS) further corroborates these findings that the Cd and Sr analogs possess the anticipated stoichiometry, whereas the Ba material shows excess Ti. The synthesis of synthesis of MUV-10(Ba) qualitatively produced a gel-like byproduct that could be largely removed with washing. Residual gel in the elemental analysis of this material could contribute to the nonstoichiometric ratio of metal ions. Moreover, attempts to synthesize derivatives with nonstoichiometric equivalents of heterometal (Ba, Sr, Cd) were unsuccessful, which demonstrate the necessary presence of heterometal.

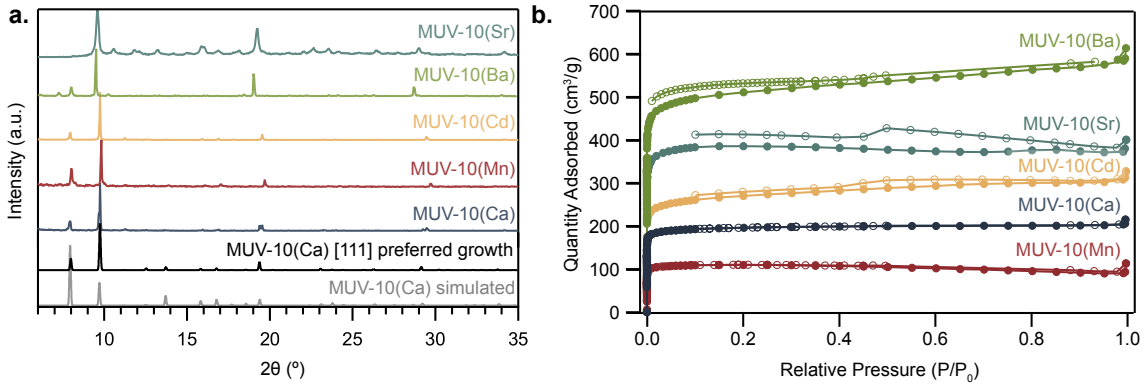

Figure 2.1.3. **a)** Powder X-ray diffraction patterns of MUV-10(M), M = Ca^{2+}, Mn^{2+}, Cd^{2+}, Ba^{2+}, or Sr^{2+}. Simulated patterns are shown based on isotropic and preferred growth in the [111] direction. **b)** N_2 gas adsorption measurements of MUV-10(Sr, Ba, Cd) derivatives collected at 77 K. Adsorption curves are denoted by full circles and desorption by open circles. MUV-10(Ca) and MUV-10(Mn) are shown as a comparison to the new derivatives.

For further evidence of isostructural MUV-10(M) derivatives, N2 gas sorption isotherms were measured at 77 K for MUV 10(Ba, Sr, Cd) following activation under vacuum at 130 ^{o}C. Figure 2.1.3b plots both adsorption and desorption data, revealing the expected Type I isotherms and reversibility for all materials. Multi-point Brunauer-Emmett-Teller (BET) analysis yields specific surface areas of 1902.99, 1227.63, and 871.44 m^2/g (2.89×10^6, 1.68×10^6, 1.27×10^6 m/mol), for Ba, Sr, and Cd respectively. The Ba^{2+} and Sr^{2+} variants showed surprisingly high uptake, in qualitative comparison with that of the Cd^{2+} derivative. We hypothesize that their increased surface areas can be attributed to large ionic radii (1.35 and 1.18 Å, respectively), which may expand pores sizes, but also create linker vacancies through lattice strain.[164] The increased quantity of defects and disorder (interstitial vacancies in the lattice, M^{2+} or linker) present in these two derivatives allows for higher N_2 uptake than that of more pristine derivatives (Ca^{2+}, Cd^{2+}, Mn^{2+}). We further analyzed the powder patterns for

experimental unit cell parameters and noted that the larger ionic radii cause unit cell expansions of almost 0.5 Å compared to MUV-10(Mn) (Table 2.1.1). The correlations between unit cell dimensions and large ionic radii of the heterometal in MUV-10(M) are further represented in the experimental powder patterns, that shift to slightly lower 2θ values, suggesting an increase in unit cell volume. As a final point of comparison, we simulated the solvent accessible pore space in the geometry-optimized structures (Table A.2) and noted that the Ba and Sr analogs have the highest uptake, which complements their higher experimental N_2 gas sorption isotherms.

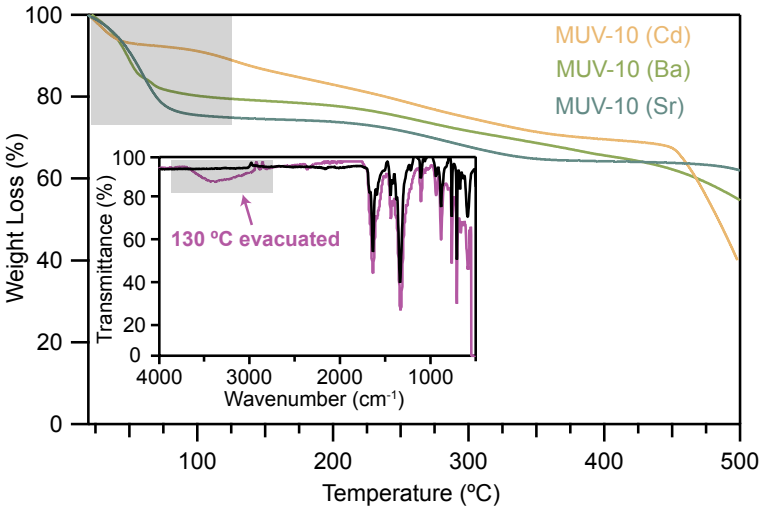

Figure 2.1.4. Thermogravimetric analysis for new MUV-10(M) derivatives (Cd, Ba, Sr) showing a significant weight loss between 0-100 ºC after solvent exchange and activation at elevated temperatures. Inset: IR spectra of as prepared MUV-10(Ca) and activated MUV-10(Ca) suggesting a loss of the –OH stretch in water at 3700-3000 cm^{-1}.

Generation of Photoactive Open Metal Sites. For insight into the structural stability of the new MUV-10(M) derivatives and for initial evidence that they support OMSs via removal of water ligands, we performed thermogravimetric analysis (TGA). All three derivatives (Ba, Sr, Cd) show thermal stability to 475

ºC and significant weight loss below 150 ºC: 21.03% for MUV-10(Ba), 24.48% for MUV-10(Sr), and 13.42% for MUV-10(Cd) (Fig. 4). Based on the assumption that one water molecule coordinates to each metal in an idealized formula unit of MUV-10(M), we would anticipate a weight loss of 6.65% for MUV-10 (Ba), 7.60% for MUV-10 (Sr), and 6.97% for MUV-10 (Cd) for complete removal of terminally bound aqua ligands. Because the actual weight losses for all three derivatives is markedly higher than expected, we attribute these weight changes to loss of pendant water molecules, interactions of the alkali earth metals with excess water (as evidenced by the difference in experimental weight losses between MUV-10(Ba, Sr)) and MUV-10(Cd)), and residual water/methanol mixtures from the pores. For direct evidence of OMS generation, we compared Fourier transform infrared (FT-IR) spectra of all derivatives before and after treatment with vacuum at 130 ºC. Figure 2.1.4 compares IR spectra of the as-prepared and evacuated materials, showing the disappearance of the broad peak associated with the –OH stretch of water. Given prior evidence from CO adsorption studies that water can be removed from the Ti sites of MUV-10(Ca),[165] these data suggest MUV-10(M) comprises an unusual family of photoactive MOF with OMSs. Given the ability of MUV-10(M) to stabilize Ti^{3+} – H^{+} pairs, we envisioned use of these materials for photoredox transfer hydrogenation catalysis, where bond formation to substrates at photoactive OMS will be beneficial.

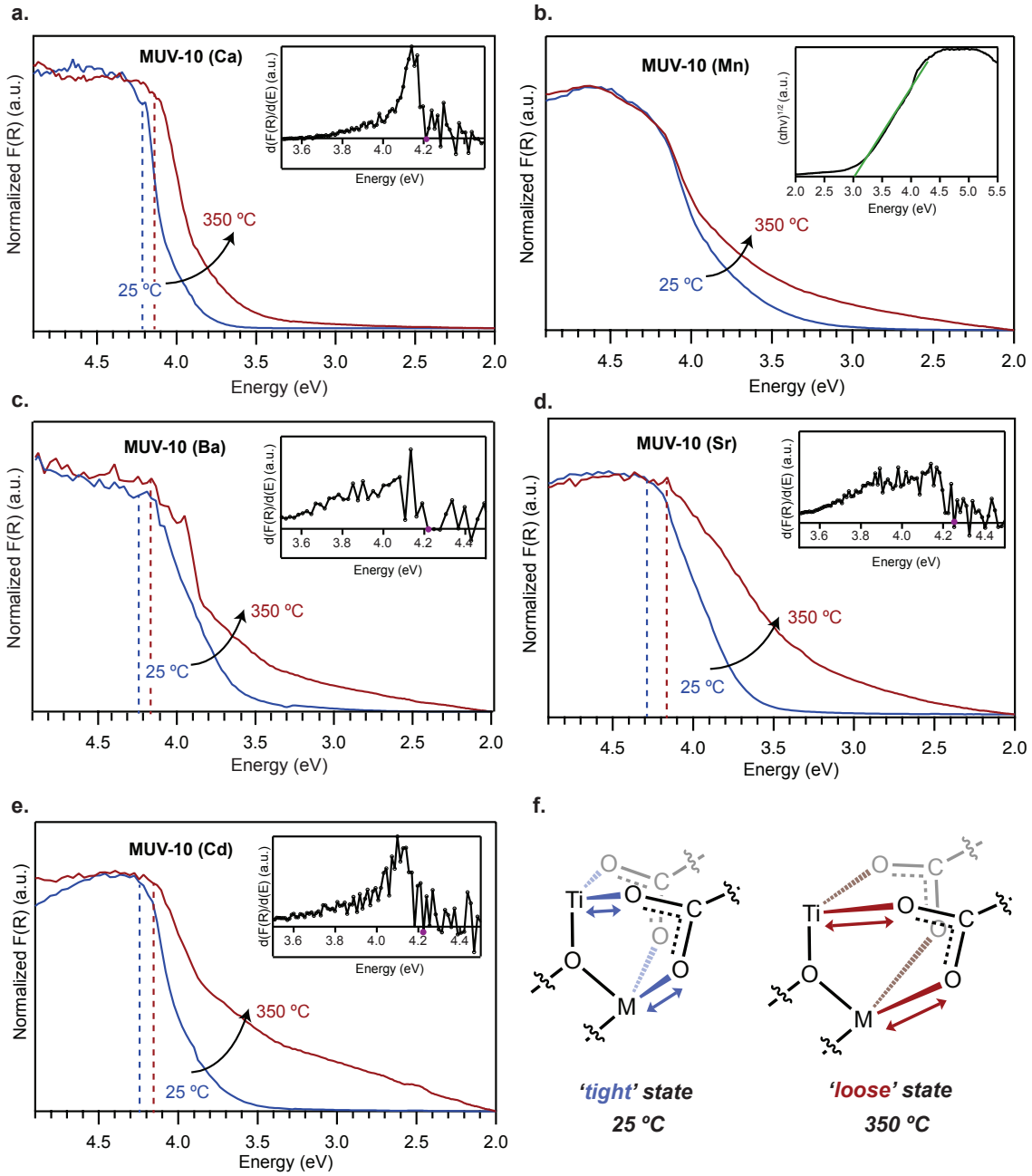

Figure 2.1.5. **a-e)**Variable temperature diffuse reflectance UV-vis-NIR spectra for MUV-10(Ca, Mn, Cd, Ba, Sr) to monitor dehydration. Dashed lines indicate band gap energies determined by derivative analysis (Ca, Ba, Sr, Cd) or Tauc plot analysis (Mn). Insets show derivative or Tauc plots. **f)** Scheme of 'tight' and 'loose' states of dynamic metal-carboxylate bonding in MUV-10 (M) cluster at high temperatures.

Electrostatic control of band gap energies. UV-vis spectra were collected *in situ* of all materials during evacuation and heating to probe changes of the titanium ligand field upon water removal and for evidence that varying the heterometal identities electrostatically tunes titanium redox potentials. Because the Ti 3d orbitals dominate the composition of Ti-MOF conduction bands, we reasoned that changes to the band gap energies can be interpreted in terms of alterations to the $Ti^{4+/3+}$ redox potential. For example, if a chemical modification causes the conduction band edge to lower in energy and narrow the band gap, then the $Ti^{4+/3+}$ redox potential therefore stabilized. Figure 2.1.5 plots UV-vis spectra of MUV-10(Ca, Mn, Cd, Sr, Ba) collected in diffuse-reflectance spectroscopy. The spectra compare the samples analyzed under ambient-pressure N_2 at 25 ^{o}C vs dynamic vacuum while heating between 25 ^{o}C and 350 ^{o}C. By collecting spectra *in situ*, we were therefore able to monitor the dehydration and creation of OMSs in the MUV-10 family. Plotted in Kubelka-Munk units, all 25 ^{o}C spectra exhibit a gradual increase in absorption beginning around 3.0 eV and maximizing near 4.5 eV. When heated under dynamic vacuum to 350 ^{o}C, however, all samples show a significant increase in absorption at lower energies, beginning around 2.0 eV. By assigning the peak maximum to an O(2p)—Ti(3d) ligand-to-metal charge transfer (LMCT) band, dehydration and varying the heterometal identities were expected to shift the $Ti^{4+/3+}$ redox couples and, hence, peak maxima. The pronounced absorption tails at higher temperatures, however, were unexpected. Rather than simple shifts to band gap energies, we suspected that the low-energy absorption features arise from thermally activated distortions to the Ti ligand sphere, thereby creating transitions between midgap defect orbitals. With this in mind, the defects could be irreversibly formed, such as by water removal, or they

could form reversibly, such as by thermally induced dynamic bonding between "tight" and "loose" configurations (Figure 2.1.5), as reported recently.[9] Figure 2.1.6 shows that the absorption tailing across 20 ºC to 250 ºC is reversible, suggesting a thermodynamically controlled equilibrium process rather than an irreversible creation of defects. Consequently, assigning band gap energies and interpreting the electronic structures of MUV-10(M) materials depends on identifying the origin of such low-energy features.

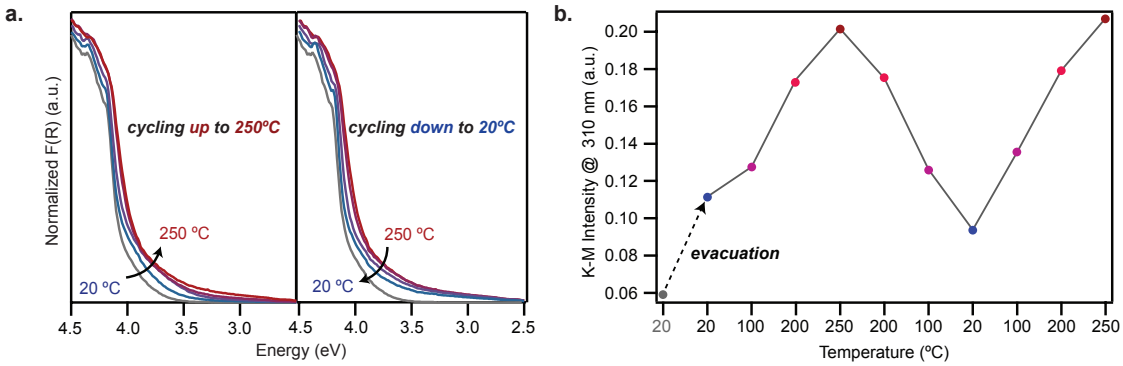

Figure 2.1.6. **a)**Diffuse reflectance UV-vis data of MUV-10(Ca) collected under dynamic vacuum and cycled between 20 – 250 ºC. **b)** Kubelka-Munk intensities at 4.0 eV versus temperature.

Choosing methods for assigning band gap energies depends on whether low-energy absorption tails arise from the band edges or from mid-gap orbitals. On one hand, the peak maxima can be taken as the excitation of a valence-band electron to the conduction band. If many overlapping bands contribute to the absorption onset, however, the band gap energy can be determined from the intersection of the energy axis and a linear fit of the absorption edge, known as Tauc Plot analysis. Superficially, the absorption profiles of all derivatives, except MUV-10(Mn), display increased absorption at lower excitation energies, suggesting dehydration causes a considerable band gap narrowing of nearly 1.0 eV by Tauc analysis in the case

of MUV-10(Cd). Increased absorption involves pronounced tailing of the optical bands rather than significant shifts to the band maxima, however. Understanding the origin of such drastic changes to optical absorption requires precise knowledge of the electronic structures of MUV-10(M) materials.

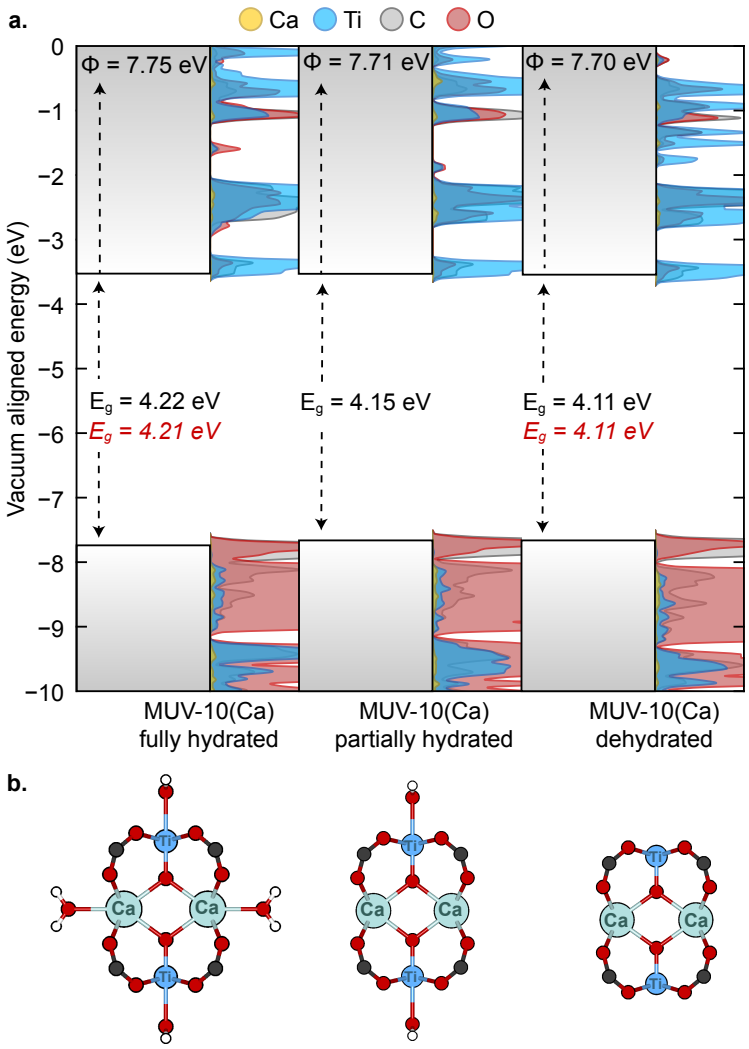

Figure 2.1.7. **a)**Density functional theory (DFT) density of states (DOS) calculations for "fully hydrated" MUV-10(Ca), "partially hydrated" MUV-10(Ca), and "dehydrated" MUV-10(Ca). Experimental and computed band gap energies are shown in red and black, respectively. **b)** Geometry-optimized structures for three forms of MUV-10 (Ca) hydration.

Figure 2.1.7 shows the computed DOS diagrams for MUV-10(Ca) in different states of hydration compared to experimental values. The "fully hydrated" structure was constructed with one H_2O bound to each Ti and Ca metal site. The "partially hydrated" structures feature just a single H_2O bound to each titanium atom and "dehydrated" includes no H_2O ligands. Because, experimentally, the degree of hydration cannot be quantified *in situ*, the empirical band gap value for the "partially hydrated" analog has not been measured. Upon full dehydration, however, the calculated band gaps narrow by ∼100 meV from 4.22 to 4.11 eV. Inspection of the electronic structures suggests that the frontier orbitals remain largely intact and simply shift towards lower-energy potentials as a result of water removal. To compare these computed band gaps to experimental values, we attempted Tauc analysis of MUV-10(Ca) at 25 ^{o}C, which involved fitting the absorption band tails, yielding a gap of 3.83 eV. The difference between this value and the computed gap of 4.22 eV was outside the typical margin of error for this level of theory, however. Derivative analysis, on the other hand, produced a band gap of 4.21 eV, which is nearly identical to the computed value. The prominence of absorption tails at higher temperatures therefore cannot be attributed to a well-ordered structural change. We reasoned that the dynamic metal-linker bonding of MUV-10(Ca), as detailed previously,[9] could give rise to the absorption tail by creating mid-gap orbitals that arise from disorder around the MOF node. A thermally induced shift of the bonding equilibrium from "tight" to "loose" binding is also consistent with the reversibility evidenced in Figure 2.1.6.

To understand the effect of varying heterometals on the electronic structures of MUV-10(M) materials, we computed DOS diagrams of all "fully hydrated" MUV-10(M) derivatives (Figure 2.1.8). Comparison of the MUV-10(Ca, Sr, Ba)

electronic structures shows a clear electrostatic influence of the alkaline Earth metals, with heavier elements exerting greater stabilization on frontier orbital energies. F or example, replacing Ca^{2+} with Ba^{2+} causes the O-based valence band to shift by 50 meV and the Ti-based conduction band to stabilize by 140 meV.

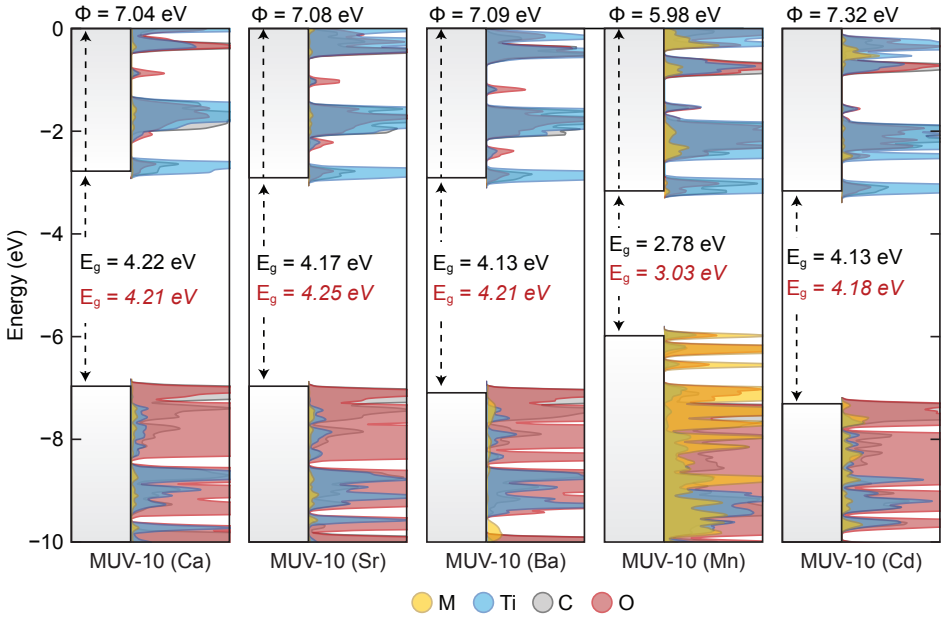

Figure 2.1.8. Density functional theory DOS calculations for all hydrated derivatives. Experimentally determined values shown in red, either by derivative analysis (Ca, Sr, Ba, Cd) or Tauc analysis (Mn).

By Tauc analysis, comparison of computed band gap energies did not match experimental results, except for MUV-10(Mn). Derivative analysis, however, yielded experimental band gap energies in close agreement with theory (Table 2.1.1). These results suggest that the chemical factors contributing to the absorption tail do not arise from simple alterations to the heterometal identities. Instead, the optical band gaps of the MUV-10(Ca, Ba, Sr, and Cd) materials are best described as a valence-to-conduction band edge transitions, regardless of hydration state and presence of mid-gap orbitals.

MOF names	E_g Tauc (eV)	E_g Deriv. (eV)	E_g DFT (eV)
MUV-10(Ca)	3.83	4.21	4.22
MUV-10(Mn)	3.03	4.34	2.78
MUV-10(Sr)	3.29	4.25	4.17
MUV-10(Ba)	3.29	4.21	4.13
MUV-10(Cd)	3.54	4.18	4.13

Table 2.1.1. Comparison of experimentally determined band gap energies for fully hydrated MUV-10 (M) using Tauc analysis and derivative analysis, versus DFT calculated band gap energies.

MOF name	Eg Tauc (eV)
MUV-10(Ca)	3.83
MUV-10(Mn)	3.22
MUV-10(Sr)	3.39
MUV-10(Ba)	3.20
MUV-10(Cd)	3.24

Table 2.1.2. External cation incorporation into MUV- 10(Ca) band gap energy comparisons via Tauc plot analysis.

For example, in the case of MUV-10(Ca) the band gap energy determined by Tauc analysis is 0.40 eV less than expected, whereas derivative analysis is off within a margin of error (0.01 eV) for this technique. We propose that whereas most MUV-10 materials exhibit wide band-gap transitions appropriate for derivative analysis, band gap assignment of MUV-10(Mn) requires Tauc analysis because the multitude of ligand-field transitions overlap with the O(2p)—Ti(3d) absorption band. Because proton-coupled electron transfer and, more broadly, ion-coupled charge transfer of Ti-MOFs has been described in terms of electrostatic interactions between soluble cations and MOF nodes, we investigated the impact of introducing cations to the MUV-10 (Ca) pores. In particular, we were interested in whether the

electrostatic influence of cations could explain the high charge capacitance of Ti-MOFs, with recent evidence for H^+ and Na+ coordination to the oxo-bridges of the Ti8O8 molecular cluster analog of MIL-125.[142] Given the electrostatic impact of redox-inactive cations within the MUV-10 node, introducing soluble cations outside the node offers a means to compare the effect of cation location. After activation at 130 ^{o}C under dynamic vacuum, MUV-10(Ca) was soaked in 0.1-M inorganic nitrate salt solutions ($LiNO_3$, KNO_3, $NaNO_3$) and 10^{-3}-M HNO_3. Stability and phase purity after cation treatment were confirmed by PXRD (Figure A.29). Following cation treatment, the optical absorption of all materials were analyzed at 25 ^{o}C via diffuse reflectance UV-vis spectroscopy (Figure 2.1.9).

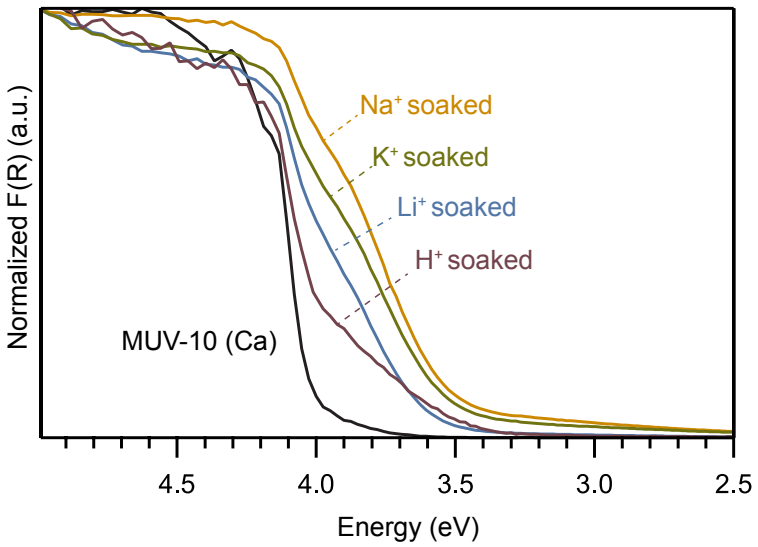

Figure 2.1.9. Diffuse reflectance UV-vis-NIR spectra of MUV-10(Ca) soaked with different nitrate salts.

Rather than simple shifts to the band maxima, all spectra show the emergence of new, lower-energy absorption with the introduction of soluble cations. We hypothesized that the cations bind to the MOF nodes, causing a lowering in symmetry and, hence, the introduction of mid-gap orbitals that cause low-

energy absorption. Due to differences in size, we expect the series Alkali metals to exhibit different binding modes to the MUV-10(Ca) SBU and, hence different UV-vis spectra. Although inappropriate for the wide-gap MUV-10(Ca) without cations, Tauc analysis is suitable for analyzing materials with overlapping bands arising from mid-gap orbitals. Compared to hydrated MUV-10(Ca) (3.83 eV), Tauc analysis of all cation-soaked samples indicates considerable narrowing of band gap energies, with H^+-MUV-10(Ca) showing a gap of just 3.22 eV. To explore the origin of this cation-induced effect, we computed the DOS for H^+-MUV-10(Ca) modeled by placing H^+ near the nodes and allowing the structure to relax (Fig. 10). Compared with the DOS of hydrated MUV-10(Ca), the DOS of H^+-MUV-10(Ca) show the valence band destabilizing by 900 meV but the conduction band stabilizing 740 meV. Additionally, protonation breaks the energetic degeneracy of MUV-10(Ca) orbitals, causing the initially sparse electronic structure to spread into many inequivalent orbitals, indicating a lowering of symmetry. Indeed, the computed structure of H^+-MUV-(10) shows considerable disorder around the node, caused by H^+ binding to the oxo bridges (Figure 2.1.10b).

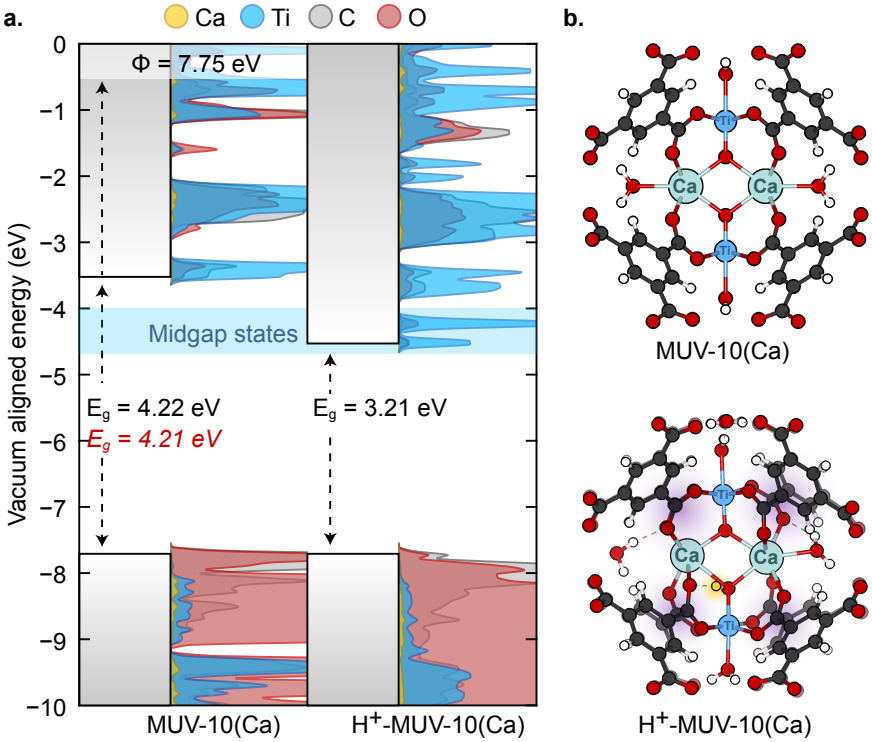

Figure 2.1.10. **a)** Computed DOS diagrams for hydrated MUV-10(Ca) and H^+-MUV-10(Ca) with midgap states highlighted in light blue **b)** Optimized structures for hydrated MUV-10(Ca) versus H^+-MUV-10(Ca).

Measurement of light-induced Fermi levels. Evidence for tunable band gaps and frontier orbital energies of MUV-10(M) provide a basis for understanding the energetics of Ti-MOF photoredox activity. To complement these insights, we therefore sought to measure redox potentials of MUV-10(M) during photoredox conditions. Inspired by prior reports of colloidal semiconductor nanocrystals,[166–168] we sought to use a soluble optical redox indicator as a contactless probe of the Fermi-level energy (E_F) of MUV-10(M) during photoredox chemistry. This method involves suspending MOFs in solution with a molecule having an electrochemically reversible redox couple that gives rise to distinct sets of optical bands. By allowing the MOF and redox indicator to equilibrate,

changes to the UV-vis spectra of the molecule therefore indicate that the MOF has also experienced changes in its redox state, *i.e.*, E_F. The absolute absorbance of the optical redox indicator in a given redox state can be related through the appropriate extinction coefficient to its solution concentration. For example, if the absorbance of the reduced state of a molecule decreases, then the new, decreased concentration of the reduced species can be determined. Through the Nernst equation, the ratio of the oxidized and reduced forms of the optical redox indicator can be used to derive a solution E_F, which is equivalent to the E_F of the MOF after equilibration. As a proof-of-concept photoredox reaction, we sought to measure the E_F of MUV-10(M) under photodoping conditions. In brief, the photoredox chemistry would involve the photoexcited MOF oxidizing ethanol, accumulating conduction-band electrons, and exchanging charges with an optical redox indicator (Figure 2.1b).

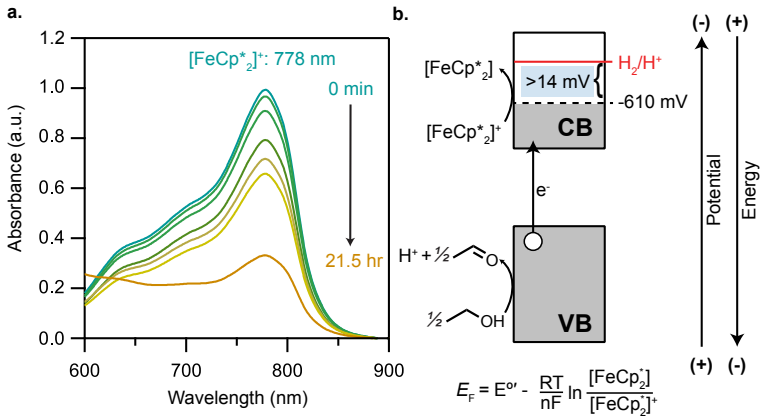

Figure 2.1.11.
+]**a)**Solution – stateUV – visspectraofphotodopingMUV – 10(Ca)powderwithexcessopticalredoxindi
b) Band-diagram representation of photodoping process in MUV-10(Ca).

By monitoring the absorption of the indicator, we would thereby measure the steady-state E_F *in situ*. In an air-free quartz cuvette, MUV-

10(Ca) was suspended in 3 mL of dry acetonitrile with excess ethanol and decamethylferrocenium ($[FeCp^*_2]^+$) (1.5$[FeCp^*_2]^+$:1Ti^{4+}) as the optical redox indicator. The mixture was irradiated with a broadband photolysis lamp and the concentration of $[FeCp^*_2]^+$ and, hence the $[FeCp^*_2]^+/[FeCp^*_2]$ ratio, was determined from the absorbance at 778 nm, attributable to an LMCT transition of $[FeCp^*_2]^+$.[153,169] Figure 2.1a shows a gradual decrease in the absorption bands of $[FeCp^*_2]^+$, indicating photoreduction by MUV-10(Ca). After 21.5 h of irradiation, the system reached steady state, as indicated by no further decrease in absorption bands. Calculating the concentration of $[FeCp^*_2]^+$ suggests MUV-10(M) reduced 67% of the indicator, giving a steady-state redox potential, *i.e.*, E_F, of –610 mV vs Fc^+/Fc.[169] This redox potential sits 14 mV positive of the electrochemical potential for the hydrogen evolution reaction (HER) in acetonitrile, -624 mV vs Fc^+/Fc at pH = 1.71 In a similar experiment using instead the cobaltocenium/cobaltocene redox couple (–1.33 V vs Fc^+/Fc), no photoreduction was observed, which is consistent with the steady-state E_F of photodoped MUV-10(Ca) being assigned to the milder potential of –610 mV vs Fc^+/Fc.

Discussion. These results indicate that the frontier orbital energies (band-edge potentials) and band gaps of MUV-10(M) can be tuned by redox-inactive cations. Similar effects have been widely reported for a range of molecular and material systems, including biomimetic models of the oxygen evolving cluster,[148,149] synthetic Fe-oxo complexes,[170,171] polyoxovanadate anions,[150] and semiconductor nanocrystals.[166,167,172–175] In these systems, Lewis acidic ions, *e.g.*, Na^+, Ca^{2+}, Sc^{3+}, modulate redox potentials by hundreds of mV through electrostatic interactions. Whereas harder Lewis acids, such as Sc^{3+}, typically induce greater stabilization, the computational results presented here indicate

the opposite trend, that MUV-10(Sr) and MUV-10(Ba) exhibited lower Ti-based orbitals than MUV-10(Ca). A key caveat to interpreting this result is that optical absorption energies do not involve nuclear rearrangement in the excited state, while redox potentials are impacted by the nuclear motion associated with ion-pairing.[176] In other words, the stronger influence of harder Lewis acids may be borne out only when they can rearrange to bind more tightly. Instead, we propose that the Ti-based orbitals become stabilized by the larger lattices created by the softer Sr^{2+} and Ba^{2+} ions. The use of framework- vs external-cations also draws interesting comparisons to the electrostatic impact of redox-inactive cations in degenerately doped semiconductor nanocrystals.[173,177,178] Whereas aliovalent dopants, such as Sn^{4+} in In_2O_3,[127] exert greater stabilization on the potentials of delocalized charges compared to surface-bound electrolyte, MOFs lack conventional "bulk" interiors and can be viewed instead entirely as "surface". Consequently, the introduction of soluble cations had a systematic effect on MUV-10(M) band gap energies and electronic structure because every MOF node could be accessed and distorted by the cations. We therefore argue that the electrostatic influence of electrolyte in the pores of MOFs play an important role in determining MOF properties, in general.

Evidence for cation-induced stabilization of Ti-based orbitals helps explain the ability of Ti-MOFs to photodope and trap Ti^{3+}-H^+ pairs. Because photodoping of Ti-MOFs involves trapping an electron as Ti^{3+} and the liberation of H^+, the e^--H^+ pair has the potential to recombine as H_2, but energetic aspects of the process ensures that it does not. These results support several hypotheses put forward by the Mayer[142] and Martí-Gastaldo[53] labs, and own: First, the calculated geometry of H^+-MUV-10(Ca) indicates localization of H^+ on bridging

oxos and, second, concomitant stabilization of Ti-based conduction-band potentials. Importantly, the *in situ* measurement of E_F through an optical redox indicator places the steady-state redox potential of photodoped MUV-10(Ca) below the HER electrochemical potential, providing an energetic justification for the ability of Ti-MOFs to photodope. It is important to note that the low activity of H^+ in this system would shift HER to further negative potentials, meaning that the true difference between E_F of MUV-10 and HER is greater than 14 mV, implying that MUV-10 greatly stabilizes the e^--H^+ pairs against recombination. These experiments involved a rare example of direct reduction of a molecular substrate by a photoexcited MOF node, whereas charges typically transfer from the node to a co-catalyst. To the best of our knowledge, these experiments comprise the only measurements of MOF redox potentials without the use of electrodes, in a contactless, non-invasive technique. Based on these results, we hypothesize that bridging oxo units are generally necessary for Ti-MOFs to stabilize H^+ against HER. We also expect that photodoped Ti-MOFs will serve as photocatalysts for transferring the e^--H^+ pairs to molecular substrates. Previous reports on photocatalysis with Ti-MOFs employed the Ti cluster as a photosensitizer rather than as a site for reactivity, but the availability of OMSs of MUV-10(M), demonstrated here, will allow photoredox chemistry without co-catalysts. The significant optical changes induced by nitrate salts or by heating may arise from structural disorder surrounding the MUV-10(M) nodes. These results suggest that structural disorder near MOF nodes may play an important role in determining MOF optical absorption properties in general. Introduction of nitrate salts caused the emergence of low-energy bands (Figure 2.1.9 and heating gave rise to absorption tails spanning the visible region (Figure 2.1.6). Naively, these

changes could have been attributed to simple shifts in band-edge potentials rather reordering of the electronic structures. Computational results suggest that binding of alkali ions to the MUV-10(Ca) node causes a symmetry lowering that introduces mid-gap orbitals. The reversibility of the temperature-induced absorption tails demonstrated in Figure 2.1.5 suggests geometric distortion as well. In a recent study, variable-temperature IR data provided evidence for dynamic metal-linker bonding in MUV-10(Ca) and other common MOFs.[179] At higher temperatures, the metal-carboxylate linkages thermally populate a "loose" configuration that may involve an array of disordered geometries. The energetic degeneracy of the loose geometries could create a high density of mid-gap orbitals that would produce low-energy absorption, akin to Urbach tailing.[180,181] Although typically assumed to be crystalline, defects in MOFs, along with amorphous, liquid, and phase-change MOFs have attracted intense attention recently,[71,182–184] and we propose that disorder near MOF nodes must be considered as well, especially to understand optical behavior.

Finally, these results demonstrate that Tauc analysis is not always appropriate for assigning band gaps to MOFs. In systems with a low DOS, such as molecules and quantum dots, the energy of discrete transitions can be assigned from the peak maxima, often aided by finding the zero-crossing-point of the absorption derivative.[185] Although the majority of MOFs also exhibit low DOS, Tauc analysis is used in nearly all cases. Tauc analysis assumes such a high DOS that the transitions between frontier orbitals cannot be identified, which is typical for amorphous and semiconducting materials.[186,187] Here, we found agreement between experimental and calculated band gap energies for MUV-10(Mn) through Tauc analysis because the charge-transfer bands involving Mn overlapped with

those involving the linker and Ti. Tauc analysis was also appropriate for analyzing band gap energies for H^+-MUV-10(Ca) and other salt-treated variants because disorder at the MOF node introduced a spectrum of overlapping transitions between mid-gap orbitals. For all other MUV-10(M) materials, their wide band gaps and low DOS required derivative analysis. These results suggest that interpreting the optical behavior of MOFs will require reevaluation of Tauc analysis and the band gap energies it has derived.

Conclusion. A combined experimental and computational effort indicates that the optical absorption of MUV-10(M) can be tuned by introduction of redox-inactive ions and by structural disorder. On one hand, expanding the MUV-10(M) to include a family of Lewis acid ions (Sr^{2+}, Ba^{2+}, and Cd^{2+}) caused stabilization of the frontier orbital energies, compared to the original MUV-10(Ca). On the other hand, the binding of soluble electrolyte cations (H^+, Li^+, Na^+, K^+) to the metal-oxo cluster lowered the symmetry of the material, giving rise to mid-gap orbitals and absorption at longer wavelengths. Previous observations of photodoping (Ti^{3+} trapping) of Ti-MOFs can be explained by the stabilization of the Ti-based orbitals by either form of cations. *In situ* optical redox indicators provide direct evidence that the Ti^{3+}-H^+ pair remains indefinitely stable because its redox potential sits below that of the hydrogen-evolving reaction. With evidence MUV-10(M) can support open metal sites at the photoactive Ti centers, this family of materials combines key design principles of the oxygen evolving cluster, poising it as a well-defined platform for heterogeneous photoredox chemistry.

2.1.1 Determining Optical Band Gaps of MOFs.

This section includes an excerpt from previously published and co-authored material from Fabrizio, K.; Le, K. N.; Andreeva, A. B.; Hendon, C. H.; Brozek, C. K. Determining Optical Band Gaps of MOFs. *ACS Materials Lett.* **2022**, *4* (3), 457–463.

The article was co-written by Kevin Fabrizio, Khoa N. Le, Christopher H. Hendon, and Carl K. Brozek. The idea was conceptualized by Kevin Fabrizio, Christopher H. Hendon, and Carl K. Brozek. Experiments were performed by Kevin Fabrizio. Khoa N. Le performed the computational simulations.

Electronic fundamental gaps (or electronic band gaps in solids, HOCO-LUCO gaps in molecular crystals, and HOMO-LUMO gaps in molecules, E_{g}) define the difference in energy between the highest filled orbital (valence band) and lowest empty orbital (conduction band) of a material. Measuring the electronic band gap of a material is important for understanding its redox, optical, and electronic properties.[188–191] Optical band gaps (E_{opt}), hereafter termed optical gaps, on the other hand, refer to the photon energy required to access the lowest-energy optically excited state.[192] In comparison to the electronic band gap, the energy of the optical gap is reduced due to the stabilizing interaction between the photogenerated hole and electron, termed the exciton binding energy (E_{b}). When exciton binding energies are small in comparison to the band gap, E_{opt} serve as a useful approximation for the E_{g}, for example as in bulk CdSe $E_{\mathrm{b}} = 15$ meV, with $E_{\mathrm{g}} = 1.66$ eV.[193–195] However, E_{opt} becomes comparable to E_{b} in chemical systems with more localized binding, such as organic polymers and molecules. For

example, polythiophene has an E_{b} of 0.6 eV, anthracene exhibits an E_{b} of 1.0 eV, and MOF-5 was recently estimated to have $E_{\mathrm{b}} = 3.5$ eV.[196–198] In such molecular-type systems, the E_{opt} substantially underestimates the band gap, but E_{g} may be obtained by photoelectron spectroscopy, or estimated using a DFT-based quasiparticle perturbation theory (*e.g.* G_0W_0),[199,200] instead. Knowing the optical gaps of materials, on the other hand, is critical for harnessing the photophysical properties of materials to design devices for photocatalysis, solar energy conversion, optical sensors, and display technologies, where excitonic interactions become relevant. Assigning optical gaps poses significant challenges, however, especially for materials with localized, molecular-type bonding.

In general, optical gaps of materials are determined from optical absorption spectroscopy, but data analysis depends on the electronic structures and, hence, the bonding characteristics of the material. Methods generally fall into two categories: 1) peak fitting or 2) Tauc analysis. In the former, the peak position of the lowest-energy optical transition is determined by fitting a spectrum to Gaussian band-shapes or by locating the zero-crossing-point of the derivative of the spectrum. These methods find widespread use across spectroscopy involving well-resolved band-shapes, such as electron paramagnetic resonance or photoluminescence spectroscopies.[201–203] Accordingly, optical absorption spectra of materials with molecular-type electronic structures are amenable to these methods because the discrete transitions between a sparse density of states (DOS) produce spectra with well-resolved peak positions. For example, analysis of quantum dot and perovskite spectra relies on Gaussian fittings due to the quantum-confined electronics of quantum dots and the highly ionic bonding of perovskites.[204–206] On the other hand, in typical semiconductors and amorphous materials, numerous overlapping

transitions complicate Gaussian fitting.[187] In such cases, spectra are interpreted by Tauc analysis, with the spectra replotted as $(\alpha h\nu)^{1/n}$ versus photon energy, where α refers to the absorption coefficient of the material, $h\nu$ is the photon energy, and the exponent 1/n denotes the nature of the optical transition, with n = 1/2 for direct allowed transitions, n = 3/2 for direct forbidden transitions, n = 2 for indirect allowed transitions, and n = 3 for indirect forbidden transitions.[187] Typically, the region with the highest slope is fitted to a line and the intersection of the line with the abscissa (*i.e.*, photon energy) is taken as the optical gap. Conventional semiconductors, such as Si and Ge, and defective materials with a high concentration of mid-gap states, require Tauc analysis.[207,208] Unlike in molecular-type systems where a well-resolved band clearly defines the optical gap, the onset of absorption defines the optical gap because defects and covalent bonding (dispersive bands) give rise to numerous transitions with comparable intensities. Figure 2.1.1.1 compares hypothetical sets of data where, on one hand, flat band curvature permits facile Gaussian fitting, while the other example involves numerous overlapping Gaussian peaks due to dispersive electronic bands, necessitating Tauc analysis.

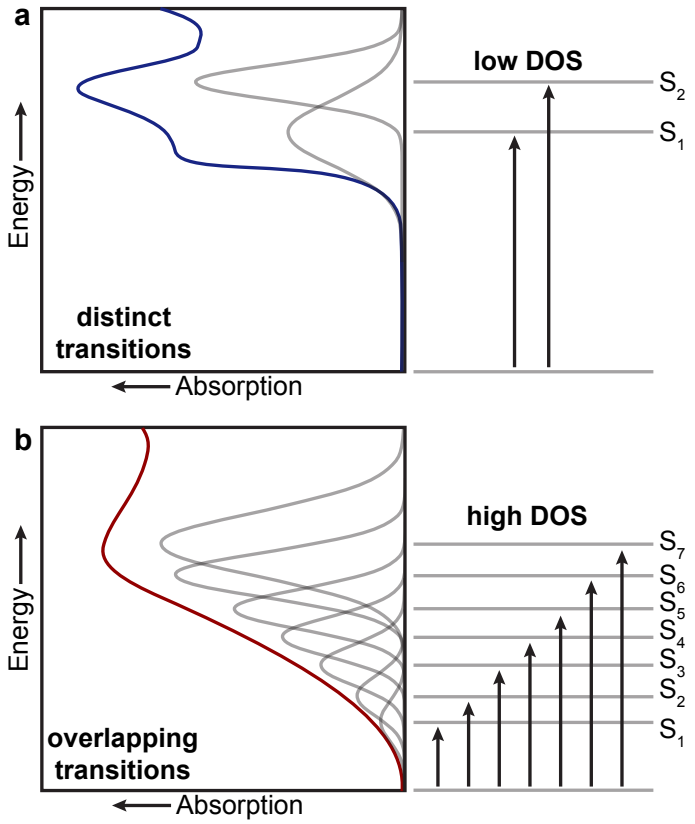

Figure 2.1.1.1. Hypothetical absorption spectra with Gaussian fits and state diagrams for **(a)** a material with flat band curvature and **(b)** a material with high band curvature requiring Tauc analysis.

Metal-organic frameworks (MOFs) pose a fundamental challenge to assigning optical gaps because, despite being extended solids, the vast majority of examples comprise of molecular-building blocks with highly localized bonding interactions. To our knowledge few, if any, photoelectron experiments have been reported for common MOFs as direct experimental measurement of MOF electronic band gaps. In other words, estimating E_b remains elusive. Yet, computational studies of common MOFs, such as MOF-5, suggest the optical gap to be nearly half of the electronic band gap,[197] implying that optical gaps obtained from spectroscopy vastly underestimate electronic band gaps. While knowing E_g

facilitates the understanding of MOF reactivity and electrochemical properties, harnessing their photophysical properties and gaining insight into their excitonic interactions requires proper assignment of MOF optical gaps.

Yet even for common MOFs, optical gaps remain disputed in the literature. In general, literature reports employ Tauc analysis to analyze the optical absorption spectra of MOFs, giving rise to optical gaps that vary by more than 1 eV, likely due to discrepancies between linear fits. For example, reported "band gaps" (used interchangeably with optical gap) of ZIF-8 (Zn-(imidazolate)$_2$) vary between 3.87 eV and 5.45 eV,[209–211] UiO-66 ($Zr_6O_4(OH)_4$(terephthalate)$_{12}$) vary between 2.50 eV and 4.07 eV,[212–214] and MIL-125 ($Ti_8O_8(OH)_4$(terephthalate)$_6$) range from 3.1 eV to 4.62 eV.[141,215–217] Furthermore, calculated electronic band structures indicate most MOFs possess localized bonding, with discrete, non-overlapping states.[33] Given their molecular, rather than band-type, nature as well as the empirical observation that experimental spectra bear well-resolved peaks, suggests that MOFs should be well suited to Gaussian peak-fitting, not Tauc analysis, to obtain optical gaps.

Here, we report experimental optical spectra of common MOF materials and propose a standard procedure for assigning MOF optical gaps, using experiment and/or computation. Specifically, we propose that Gaussian fittings serve as the appropriate method to assign optical gaps to the vast majority of MOFs unless the MOF possesses numerous overlapping transitions bands, *i.e.* as in systems with open-shell transition metals and dispersive bands, such as materials with strongly covalent metal-ligand bonds. Furthermore, we present a reliable ground-state DFT approach to examine the DOS at the band edges and predict the optical gaps of common MOFs. Comparison of experiment and theory suggests that assigning

gaps with Gaussians serves as a simple approach that requires the least insight into the electronic structure and consistently shows agreement with DFT-computed gaps within 30 meV, on average. These guidelines radically alter the conventional approach to understanding MOF electronic structures and serve as quick methods for ascertaining optical, not electronic band gaps.

To determine the appropriate method for assigning MOF optical gaps, UV-Vis-NIR diffuse reflectance spectra were collected on a representative collection of common MOFs. These include materials with open d-shell transition metal ions, such as Cu_3(benzenetricarboxylate)$_2$ (Cu-HKUST-1) and Cu(1,2,3-triazolate)$_2$ (Cu(ta)$_2$), materials with closed d-shell transition metal ions, such as Zn(imidazolate)$_2$ (ZIF-8), and materials with non-transition metals, such as Mg_2(2,5-dioxido-1,4-benzenedicarboxylate) (Mg-MOF-74). The spectra of all MOFs were transformed as the Kubelka-Munk function and are shown in Figures B.13-B.25. To assign the optical gaps, all spectra were analyzed by three methods: Gaussian fitting, derivative analysis, and from Tauc **Appendix B**. In short, Gaussian analysis involved an initial guess of the absorption maximum prior to algorithmic fitting and Gaussians were allowed to shift in location, height, and width. The final number of Gaussians was chosen to minimize residuals and the optical gap was determined as the peak position of the lowest-energy Gaussian. In derivative analysis, a derivative was taken of the spectra and the optical gap was chosen as the lowest-energy photon energy where the derivative crosses zero. In Tauc analysis, the reflectance values plotted as the Kulbeka-Munk function (F(R)) were treated as the absorption coefficient and all spectra were plotted with both $n = 2$ and $n = \frac{1}{2}$ to evaluate them as either indirect- or direct-gap materials. The Tauc analysis of several MOF materials, such as in MIL-53(Fe) and Cu-HKUST-

1, required multiple linear fits to distinct linear regions. In such cases, the optical gaps derived from all linear fits were considered in comparison to theory.

To determine the nature of the optical transitions, *i.e.*, direct or indirect, we employed hybrid density functional theory (DFT) calculations because many hybrid functions (*e.g.* HSE06, B3LYP, M06, etc.) tend to underestimate the true electronic band gap and instead match experimental optical gaps by design. Specifically, unlike Hartree-Fock methods, DFT computes the energies of LUMOs (conduction bands) in the presence of n–1 electrons and, when combined with a portion of exact exchange, the functionals approximate the electron-hole attraction, *i.e.*, the exciton binding energy.[218] Because the vast majority of MOFs are thought to possess localized electronic states,[219] hybrid DFT serves as an accurate estimate of MOF optical gaps, and should fail to recover the true electronic band gap if E_{b} is large. Indeed, Poloni and colleagues calculated a gap of ∼4.5 eV for MOF-5 from hybrid DFT, which matched the experimentally determined optical gap, but estimated the exciton binding energy to be ∼3.5 eV from GW perturbation theory, suggesting the true electronic band gap of MOF-5 to be ∼8 eV.[197] Due to the great expense of GW-methods and due to the practical utility of estimating E_{opt} for understanding MOF photophysical properties, we employed relatively inexpensive hybrid-GGA approaches, in particular the tightly converged HSE06/HSEsol06 functional (See **Appendix B** for computational methods) because of its broad implementation in standard quantum chemical software packages. Furthermore, this level of DFT theory has been shown to yield remarkable agreement with experimental optical gaps,[220] especially in MOFs.[219,221]

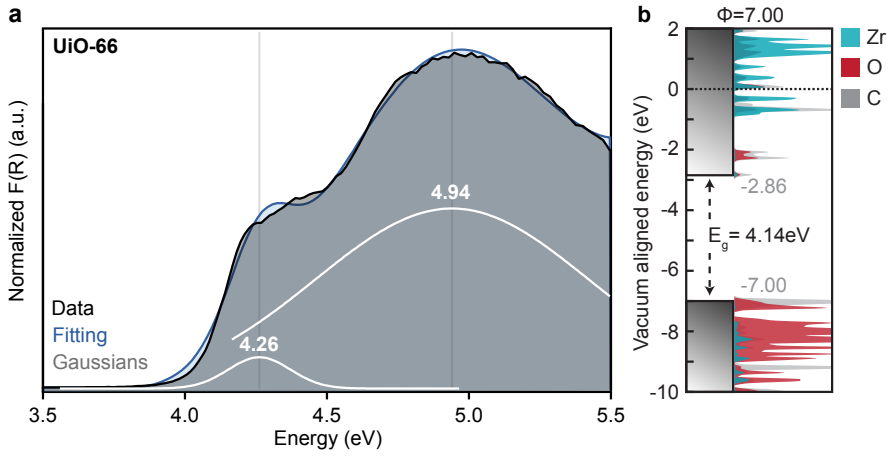

Figure 2.1.1.2. Analysis of UiO-66 optical spectra. **a)** Diffuse reflectance UV-vis data with Gaussian fits and **b)** computed DOS aligned to the vacuum level using the method detailed in Ref.[217]

Table 2.1.1.1 summarizes optical gaps and the nature of the optical transitions determined by DFT, and experimental optical gaps determined from Tauc, Gaussian, and derivative analysis for a set of common MOFs. Although the vast majority of MOFs involve closed-shell metal ions, such as Mg^{2+} or Zn^{2+},[222–224] this collection overrepresents the share of open-shell systems because we deliberately sought MOFs that would test the limits of Gaussian analysis. Table 2.1.1.2 shows the absolute difference between the experimental and DFT-computed values (E_{diff}), and as the percentage difference ($E_{\%}$), defined as [1 – (experimental gap / DFT gap)]. For most MOFs, Gaussian fitting shows good agreement with DFT, with E_{diff} of 150 meV or less and $E_{\%}$ of 5% or less for most systems. In general, the MOFs most suited to analysis by Gaussian fittings contained alkali Earth metals, such as Mg^{2+}, as in Mg-MOF-74, closed-shell metal ions, such as Zn^{2+}, as in ZIF-8, or d^0 metal ions, such as Zr^{4+} in UiO-66. Derivative analysis, overall showed worse agreement with DFT than Gaussian fits, suggesting it is less accurate at determining the position of individual transitions. Figure 2.1.1.2a shows

the experimental spectrum for UiO-66 analyzed by Gaussian fits that provide a clear peak maxima in good agreement with DFT (both the fundamental gap E_{g} 4.14 eV matches the $E_{\mathrm{opt}} = 4.26$ eV, and the second absorption feature measured at 4.^{225} eV corresponds to the DOS at $\sim$2.25 eV below the vacuum level), despite prior literature reporting a range of UiO-66 band gaps extracted from Tauc plots.[212–214,226–228]

MOF Name	Organic Ligand	Metal(s)	Direct/Indirect	DFT E_{opt}	Gaussian E_{opt}	Tauc – Direct E_{opt}	Tauc – Indirect E_{opt}
MOF-5	terephthalate	Zn	indirect	4.64	4.71	5.26	3.71
MIL-125	terephthalate	Ti	direct	3.87	3.88	4.02	3.68
UiO-66	terephthalate	Zr	direct	4.14	4.26	4.01	3.91
Mg-MOF-74	terephthalate	Mg	indirect	2.89	2.86	2.75	2.60
MIL-53(Fe)	terephthalate	Fe	indirect	2.28	2.35	2.93	2.01
PCN-415	terephthalate	Ti, Zr	direct	3.15	3.76	3.51	3.25
Cu-HKUST-1	trimesate	Cu	direct - AFM	3.82	3.17	3.38	2.24
MUV-10(Ca)	trimesate	Ca	direct	4.22	4.23	4.06	3.70
MUV-10(Mn)	trimesate	Mn	indirect	2.98	4.52	3.91	3.04
Cu(ta)2	1,2,3-triazolate	Cu	indirect - AFM	3.20	4.06	3.69	3.35
ZIF-8	1-methylimidazolate	Zn	direct	5.32	5.35	5.36	5.17
MFM-300(Sc)	biphenyl-3,3´,5,5´-tetracarboxylate	Sc	indirect	3.95	4.00	3.83	3.69
SU-101(Bi)	ellagate	Bi	indirect	2.34	2.45	2.76	2.39

Table 2.1.1.1. Summary of MOFs with optical gaps determined by experiment and DFT simulations.

MOF Name	E_{opt} Tauc - Direct	E_{opt} Tauc - Indirect	E_{opt} Gaussian	% Difference Tauc - Direct	% Difference Tauc - Indirect	% Difference Gaussian
MOF-5	0.62	0.93	0.07	13.4	20.0	1.51
MIL-125	0.15	0.19	0.005	3.88	4.91	0.13
UiO-66	0.13	0.230	0.12	3.14	5.56	2.90
Mg-MOF-74	0.20	0.29	0.03	4.84	10.0	1.04
MIL-53(Fe)	0.65	0.27	0.07	28.5	11.8	3.07
PCN-415	0.36	0.10	0.61	11.4	3.17	19.4
Cu-HKUST-1	0.44	1.58	0.65	11.5	41.3	17.0
MUV-10(Ca)	0.16	0.52	0.01	3.79	12.3	0.24
MUV-10(Mn)	0.93	0.06	1.54	31.2	2.01	51.7
Cu(ta)2	0.49	0.15	0.86	13.3	4.48	21.1
ZIF-8	0.04	0.15	0.02	0.75	2.82	0.36
MFM-300(Sc)	0.12	0.26	0.05	3.04	6.58	1.27
SU-101(Bi)	0.42	0.05	0.11	17.9	2.14	4.70

Table 2.1.1.2. Comparison of optical gaps determined from experiment and DFT.

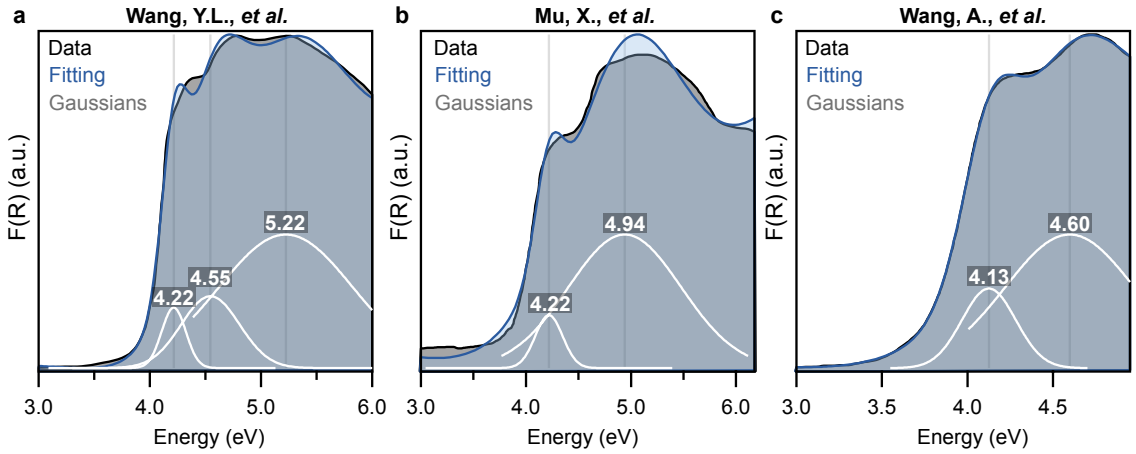

Figure 2.1.1.3. Gaussian-fitted diffuse-reflectance UV-vis data for UiO-66 digitized from **a)** Wang, Y.L., *et al.*,[214] **b)** Mu, X. *et al.*,[229] and, c) Wang, A. *et al.*.[230]

As reflected in the conduction band DOS of UiO-66, Figure 2.1.1.2b, most MOFs exhibit discretely spaced frontier orbitals, making them better suited to Gaussian peak fitting. To examine the applicability of Gaussian analysis to experimental spectra reported elsewhere and to compare our E_{opt} values to literature reports, we applied Gaussian band-shapes to several previously reported spectra of UiO-66, MOF-5, and MIL-125.[214,229–233] Figure 2.1.1.3 shows data digitized from three distinct reports of UiO-66 with our fits. Gaussian fits in panels a, b, and c give E_{opt} of 4.22, 4.22, and 4.13 eV, all in excellent agreement with the DFT-predicted value of 4.14 eV, and our measured value of 4.26 eV shown in Figure 2.1.1.2. In comparison, the reported Tauc analysis gave values of 3.82, 3.91, and 3.45 eV, respectively.[214,229,230] These results suggest that even for MOFs, such as UiO-66, prone to mid-gap states (attributed to surface-bound or missing-linker defects) that lead to significant Urbach tailing, Gaussian fitting provides a facile technique for identifying absorption maxima in MOFs that can be attributed to the optical gap. Similar analysis of data digitized for MOF-5 and MIL-125 (Figures B.26-B.27) gave E_{opt} values agree with our DFT-computed values, suggesting this

technique is generally applicable to MOFs with distinct absorption features.

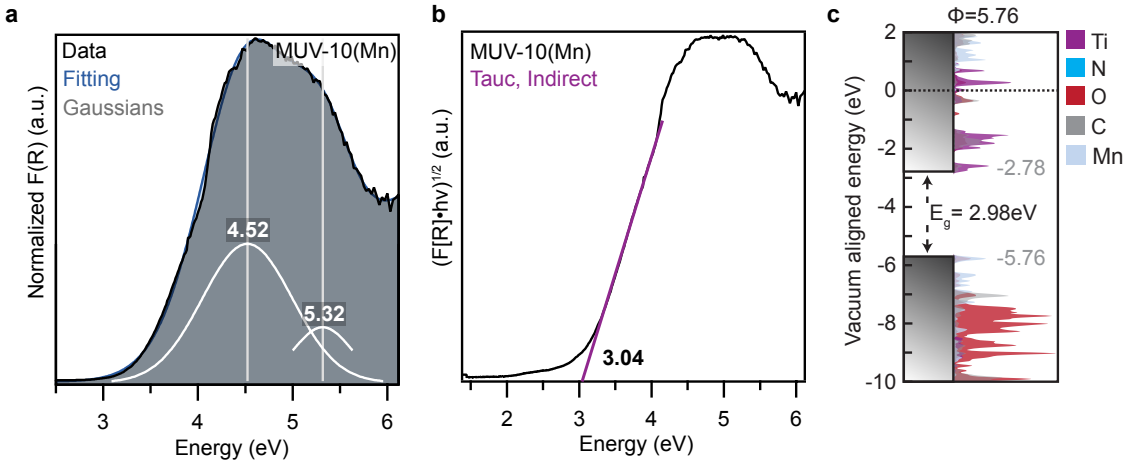

Figure 2.1.1.4. Analysis of MUV-10(Mn) optical spectra. **a)** Diffuse reflectance UV-vis data and corresponding Gaussian fits, **b)** Tauc plot and linear fit, and **c)**computed DOS and band alignment

This analysis indicates that a subset of MOFs shows better agreement with Tauc analysis if they possess closely spaced excited states due to dispersive band curvatures, partially filled d-orbitals giving rise to multiple d-d transitions, as in $Cu(ta)_2$, covalent metal-ligand bonding, as in SU-101(Bi), or overlapping ligand-field transitions, as in MUV-10(Mn). For example, Figure 2.1.1.4a shows the experimental spectrum of MUV-10(Mn) and the attempted Gaussian fitting. Due to the numerous overlapping transitions, as corroborated by the DOS diagram shown in Figure 2.1.1.4c, Tauc analysis is more appropriate, as shown in Figure 2.1.1.4b. Similarly, Tauc should be considered for conductive MOFs due to the curvature of their band structures, which produce numerous overlapping optical transitions.[234] Although PCN-415 is computed to be a direct-gap material, its spectra showed better agreement with an indirect-gap ($E_{\%}$ of 3.14% vs 11.4%, respectively, Figure B.23). Because calculations predict a valence band dispersion

of only ∼2 meV for PCN-415, we suspect this discrepancy arises from numerous indirect-gap transitions becoming thermally activated at room temperature. Therefore, while Gaussian fitting is appropriate for typical MOF materials, the onset of absorption determined by Tauc analysis might still prove useful for investigations into the presence of mid-gap states that give rise to absorption "tails" and to the limited set of MOFs with dispersive band-type electronic structures. For example, Gaussian analysis of UiO-66 materials with varying defect concentrations still permits identification of the optical band gap, whereas the onset of absorption can be independently determined by Tauc fitting and additional Gaussian bands can be used to identify the position of discrete midgap states (Figure B.28).

Based on these comparisons, we offer the following recommendations for assigning optical gaps to MOFs:

1. From the computed electronic band structure and corresponding DOS, determine the nature of the transition, use the appropriate Tauc fitting, and compare the results to values from Gaussian fits, as demonstrated here.

2. If full band diagram calculations of a MOF are not available, fit experimental data to Gaussians.

3. If working with MOFs that contain highly covalent metal-linker bonds, as in MOFs with nitrogen, sulfur, carbon-containing atoms bound to the metal, consider Tauc, but compare to Gaussian fits. If a peak maximum is clearly seen at the lowest-energy portion of the spectrum, likely use Gaussian fits.

4. If working with MOFs that contain transition metal ions with partially filled d-blocks, consider Tauc. If a peak maximum is clearly seen at the lowest-energy portion of the spectrum, likely use Gaussian fittings.

5. If working with MOFs that contain a high concentration of missing metal/linker defects, structural disorder, and/or midgap states, consider Tauc to identify the onset of absorption. Gaussian fitting, however, can still prove useful in independently determining the position of discrete midgap states and the position of E_{opt} of the pristine material.

In conclusion, this combined experimental-computational study reports the optical gaps of common MOFs through several experimental methods and by DFT calculations. In general, Gaussian fits to experimental reflectance spectra show greatest agreement with DFT-derived optical gaps, owing to the localized bonding found in most MOFs. For a subset of MOFs, such as systems with partially filled d-orbitals, Tauc analysis produced greater agreement, which we attribute to the greater number of overlapping optical transitions that impede Gaussian fitting. Overall, these results justify a set of recommendations for using simple methods to report the optical band gaps of MOFs.

2.2 On the Limit of Proton-Coupled Electronic Doping in a $Ti^{(IV)}$-Containing MOF

This chapter includes an excerpt from previously published and co-authored material from Mancuso, J. L.; Fabrizio, K.; Brozek, C. K.; Hendon, C. H. On the Limit of Proton-Coupled Electronic Doping in a Ti(IV)-Containing MOF. *Chem. Sci.* **2021**, *12* (35), 11779-1785.

The article was co-written by Jenna L. Mancuso, Kevin Fabrizio, Carl K. Brozek, and Christopher H. Hendon. The idea was conceptualized by all authors, the theoretical chemistry was performed by Jenna L. Mancuso and the experimental chemistry was performed by Kevin Fabrizio.

Introduction. By coupling to the motion of protons, electrons can enter reactivity patterns, charge storage, and electron transport pathways that would be difficult to achieve otherwise, through a mechanism known as proton-coupled electron transfer (PCET).[235] In net, the reaction can be thought of as a hydrogen atom transfer, and is consequently invoked in various chemical processes found in enzymes[236,237] chloroplasts[154,238] hydrogen fuel cells[155,235] and reductive catalysts[156,157,239] However, achieving selective PCET depends on knowledge of the relative redox potentials of the reagents. With the appropriate frontier energy level alignments, PCET can be either thermally or photochemically promoted in both molecular and solid-state manifolds,[159–163] but mismatched energetics creates pitfalls ranging from sluggish kinetics to undesirable H_2 formation or back-hydrogenation to reform reactants.[165] There is hence a desire to leverage the PCET manifold to, for example, suppress the hydrogen evolution reaction (HER)

by stabilizing the e^-–H^+ pair (H^*) below that of the NHE (-4.4 eV relative to vacuum)[240].

In conventional solid-state scaffolds, the ill-defined nature of surface-active sites hinders catalyst design for selective PCET reactivity. For instance, the surface of TiO_2 — a semiconductor known to perform HER[9] — features a broader array of active sites, beyond the idealized (101)-Anatase surface presented in Figure 2.2.1,[235,241,242] limiting efforts to identify and tune specific localities for selective reactivity other than H_2 formation. Conversely, molecular catalysts offer well-defined single-atom active sites with wide synthetic tunability, but suffer from poor recyclability[243]. Combining the best of both approaches, metal-organic frameworks (MOFs) combine the benefits of heterogeneous catalysis and synthetic modularity.[170,171,244,245] Previous studies in MOF catalysis have primarily focused on thermally driven reactions at either the linker or node using intrinsic[33,246,247] and extrinsic[131,248,249] catalytically active metals. Conversely, MOF photoredox chemistry[36,250,251] typically focuses on electron transfer between the inorganic and organic MOF components[252], shuttling electrons to interstitial molecular catalysts[253–255] or guests.[256–259]

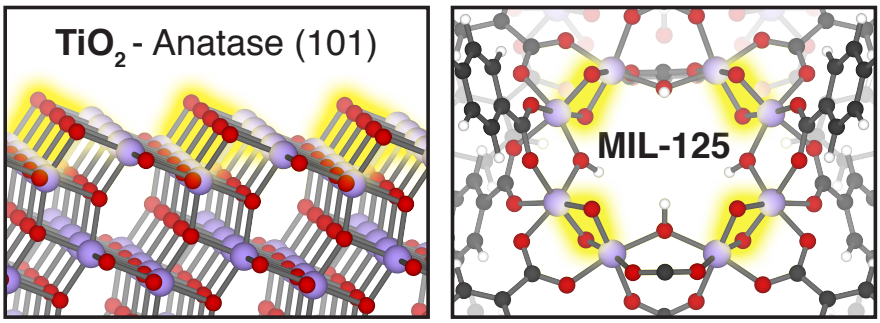

Figure 2.2.1. TiO_2-based materials can be reduced via PCET, with a corresponding $Ti^{IV/III}$ reduction, and O-H formation. Depicted are Lewis basic μ^2-oxo sites on TiO_2 (shown is the (101)-Anatase surface). In a MOF analogue, octameric $Ti_8(\mu^2-O)_8(\mu^2-OH)_4$ clusters offer four isolated pairs of bridging O per node (highlighted in yellow). These sites are thought to host extrinsic cations (*e.g.* H^+, Na^+, etc.), affecting the reduction potential of vicinal Ti^{IV} centers.

However, one burgoening area of MOF research has been the exploration of the chemistry afforded by the compositional similarity between inorganic clusters in MOFs, and their conventional dense-phase semiconducting counterparts, Figure 2.2.1.[260] In particular, a central theme of our research is the study of chemical opportunities enabled by the Lewis basic inorganic ligands in the inorganic clusters. Such anions are prevelent in Ti-MOFs, and it is these scaffolds that have been shown to stabilize H^*, while also enabling a designed, well-defined, PCET active site.[225,261–264]

In the seminal report, UV irradiation in the presence of alcohols caused MIL-125 to turn from colorless to black.[140]The color was shown to persist indefinitely, returning to colorless upon exposure to air. The authors attributed the apparent bandgap reduction to the formation of Ti^{III} centers stabilized by protons liberated from the oxidation of alcohol by the photogenerated holes, *i.e.*, PCET from the solvent to the framework, Figure 2.2.2. EPR later validated the presence of Ti^{III} centers and,[265] paired with electronic structure calculations, rationalized

their formation by identifying the conduction band minimum (CBM) origin as Ti d-states in the pristine MOF — a general property extending to all reported Ti^{IV}-containing MOFs.[33]

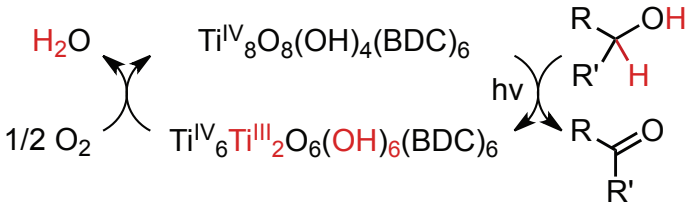

Figure 2.2.2. As posited by Dan-Hardi *et al.* (ref[140]), MIL-125 forms Ti^{III} upon photo-promoted reaction with primary and secondary alcohols ($R^{'}$ = H or alkyl, respectively).

The reversible colorless-to-black transformation, spectroscopic evidence of Ti^{III}, and aldehyde formation observed in irradiated MIL-125[140] demonstrates that the MOF is undergoing photochemical electronic doping, *i.e.*, photodoping. Kinetically, this process requires that rate of exciton recombination be slower than hole quenching, wherein a sacrificial reductant (alcohol) diffused to the photogenerated hole. Although subsequent reports have detected small quantities of H_2 evolved from this process,[266,267] these data suggest that a significant portion of the Ti^{III}–OH^+ pairs generated through photodoping remain indefinitely stable,[140,142,143] suppressing H_2 formation. This is further supported by the requirement for MIL-125 and other Ti-containing MOFs to use a co-catalyst to promote H_2 formation.[257,268]

The maximum charge capacity, *i.e.*, relative stability of Ti^{III} centers, of MIL-125 shows a strong cation dependence. Recent studies by the Mayer group demonstrated that Na^+–based chemical reductants enable stoichiometric reduction of all eight Ti centers per node,[142] while the PCET-based photodoping strategy

only two H^* per Ti octamer.[143] Since Na^+ is undoubtedly less stabilizing than H^+ (which forms a covalent bond with bridging oxos), we hypothesize that H_2 formation sets the thermodynamic limit to PCET-based charge storage in MIL-125: in the low-charging regime, the energies of electron-proton pairs are more stable relative to HER, but exceed the redox potential of HER in the high-charging regime. Further, stoichiometric reduction of the Ti centers can only be achieved with Na^+ because the Na^+/Na redox couple lays far more negative (closer to the vacuum level) than the new conduction band of the all-Ti^{III}-MOF. Consequently, we surmise that the charge storage capacity of MOF nodes depends on both the redox potentials of the metal ions and the node nuclearity or, more specifically, the presence of inorganic anions to accept protons.

Here, we sought to understand the limits to PCET-based charge storage in MIL-125. To do so, we have combined electronic structure calculations and experiments to identify the microscopic origin of 1) the stability of Ti^{III}–OH^+ pairs towards H_2 evolution in the low-charging regime, and 2) the thermodynamic limit to the number of Ti^{III}–OH^+ that can accumulate. We find the inorganic oxo units in the MIL-125 clusters accept the protons liberated after PCET photodoping, thereby stabilizing the e^-/H^+ pairs against H_2 formation by spatially separating them as Ti^{III}–OH^+ units. From this study, we offer a more general design principle for forming MOFs with the potential to act as transfer hydrogenation catalysts, but not dehydrogenation catalysts: the incorporation of Brønsted-basic inorganic inner sphere ligands paired with redox-active metals may achieve controllable PCET reactions in MOFs. In other words, we offer a general observation of accessing non-equilibrium reactivity in MOFs featuring metal oxide clusters.

Results and Discussion. While the CBM of a semiconductor provides an estimate for the reduction potential of that material (*i.e.*, the electron affinity),[269,270] it alone is insufficient to assess the thermodynamic tendency to host additional electrons because the ground state structure does not account for local reorganization (for example, distortions due to ion pairing, or reduction in bond order) upon conduction band population. Computational chemistry is well-suited to study both instantaneous reduction of the MOF, as well as the emergent structural deviations. Using plane-wave DFT we are able to compute the ground state electronic structure for MIL-125 and subsequent PCET products. Using a vacuum level alignment,[217] the conduction band minimum of MIL-125 sits at -3.7 eV, closer to the vacuum level than H_2 formation from H^+ (-4.4 eV, Figure 2.2.3a). We note that functionalization of the linkers does not dramatically affect the CBM position, as it is composed of inorganic metal-oxo orbitals. Together, one might anticipate that electrons that occupy the conduction band would be sufficiently high in potential to reduce protons.

Upon irradiation, in the presence of a primary or secondary alcohol, the MOF becomes black, Figure 2.2.3b. Due to the persistent color change, these experiments indicate that there is at least one doped configuration that suppressed H_2 formation, otherwise MIL-125 would fade back to colorless over time without exposure to air. We hence surmise that MIL-125-H* is a thermodynamic minimum on the potential energy surface of hydrogen transfer. In the simplest case, where a single H* is added to a bridging oxo, our calculation reveals that the newly formed "mid-gap" state, a half-occupied Ti-centered orbitals (Figure 2.2.3c) that has an electronic potential of -4.5 eV, ∼100 meV more positive of H^+/H_2 reduction

potential (shown in purple, Figure 2.2.3a). Hence, we offer that the PCET product should be thought of as a stable Ti^{III}–OH moiety rather than an ill-defined H^*.

However, the recent experimentation by Saouma *et al.* revealed an apparent thermodynamic limit of two protons and two electrons per Ti_8 node.[143] It remains unclear whether the two protons would preferentially adhere to vicinal μ^2-oxos or in some other configuration. It is further unclear why only two reductive events can occur in excess alcohol. Lastly, we wanted to understand the thermodynamic origin of that two-electron limit. To assess this energetic landscape, we developed an assortment of models containing two hydrogen atoms at various positions around the nodes, Figures 2.2.4.

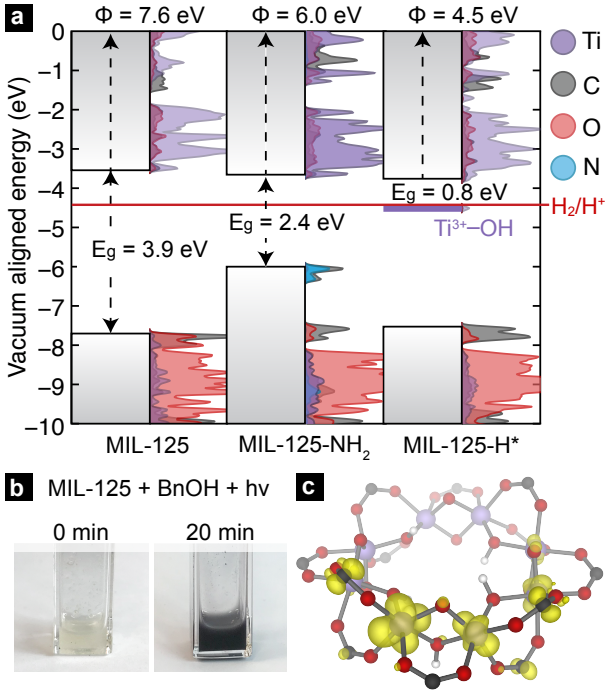

Figure 2.2.3. **a)** Vacuum-aligned DOS plots show that both the bulk and organo-functionalized derivatives of MIL-125 have CBMs above H^+/H_2 (-4.44 eV, shown in red). A new mid-gap state emerges upon H^* addition, with a potential 100 mV below that of H^+/H_2. **b)** The addition of a proton and electron via photoillumination can be evidenced by a change in colour, which persists as long as the MOF is kept free from oxidants. **c)** Electronic structure calculations of the H^* adduct reveals that the additional electron localizes on a Ti-center near the adatomic proton, bound to one of the μ^2-oxo ligands.

From these calculations, we find that the addition of two hydrogen atoms to MIL-125 yields consistently HER-positive mid-gap Ti^{III} states. The most stable configuration arises from the addition of two additional H^* on geminal μ^2-oxos (Figure 2.2.4c, second column). When the H^* are added to μ^2-oxos on different nodes (Figure 2.2.4c, fifth column), connected by benzene dicarboxylate (BDC), is disfavored by up to 11.3 kcal/mol, Figure 2.2.4d. In that case, the Ti^{III} radicals delocalize through the π^*-system of the linker (see Figure C.1). We find, however, that if the two hydrogen atoms are added to different nodes and not connected by

a common linker, the reduction potential is stabilized to the same level as a single addition (approximately 60 mV positive of HER).

We also examined the 2H∗-per-node limit presented by Saouma, Figure 2.2.5. Practically, this amounts to four hydrogen atoms per computational cell, and several observations may be made from these calculations. First, we note that isolated vicinal pairs of protons/electrons result in additive density of the mid-gap states. Second, same-node-separated protons result in splitting of the mid-gap DOS, and this process is energetically disfavored both in terms of formation energy (2.2.5, lower panel) and potential to reduce protons. Third, we note that the four separated protons on a single node is more than twice the energy of two protons on a single node (from 2.2.5, column four, ∼21 kcal/mol, and 2.2.4, column three, ∼8 kcal/mol). We can hence make the general conclusion that the adatomic hydrogenic atoms thermodynamically prefer to add across pairs of bridging oxos. Kinetically, we also expect that alcohol radicals would react with pairs of bridging oxos before diffusing unreacted to distant oxo units.

As yet, these calculations have not identified the chemical origin of the MIL-125 doping limit of two H^* per node. Thus, we further explored higher H^* loadings, up to the stoichiometric hydrogenation of the μ^2-oxo units, and we determined a thermodynamic doping limit of four e^-/H^+ pairs per node within certain configurational parameters. In order for HER to remain suppressed with more than four PCET events at the same node, neighbouring nodes must be in the fully oxidized Ti^{IV}-state (Figures C.3 and C.4). HER remains suppressed when six H^* are added to a single node, but the presence of a hydrogenated μ^2-oxo pair on the adjacent node facilitates H_2 formation.

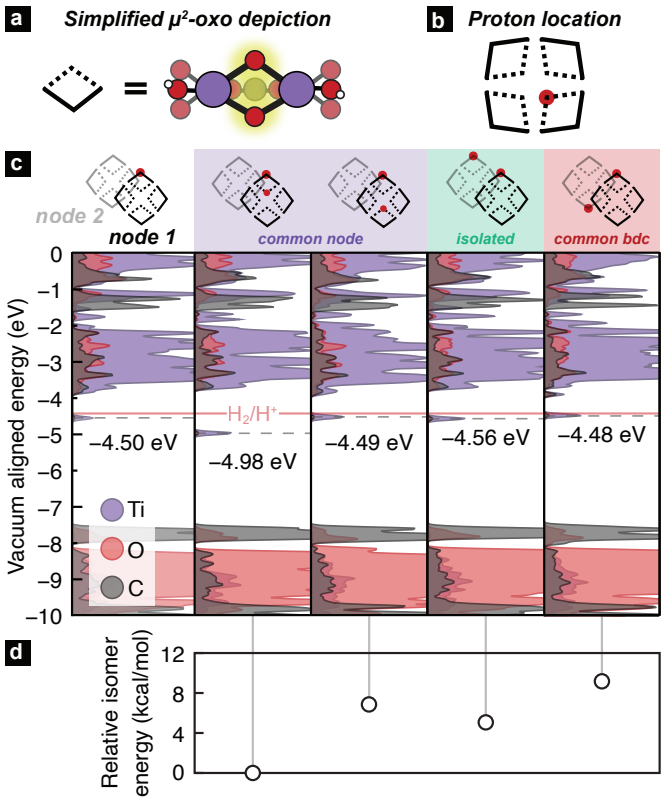

Figure 2.2.4. **a)** A schematic of a portion of the Ti_8 node, highlighting the μ^2-oxos, and simplifying them to diamonds, whose central apexes represent the bridging oxos. **b)** A node represented by our simplified notation. The unit cell of MIL-125 contains two nodes, thus **c)** the vacuum-aligned atom-projected DOS plots contain two nodes per DOS plot, with the depicted PCET product shown above. The Fermi level (*i.e.* the gas phase reduction potential) is denoted by the dotted gray lines.

Meanwhile, four H^* per node are stable with respect to HER as long as two pairs coexist on each node, or all four localize on one, Figures C.3 and C.4. Higher loadings become progressively less stable (**??**), and beyond 4 electrons per the node (*i.e.*, 50% doping), the occupied states are split such that many configurations exceed the reduction potential of H^+, an extreme example is presented in Figure C.3. Importantly, these calculations suggest as many as six Ti^{III}–OH pairs can be accumulated in each MIL-125 despite the previously observed limit of two. Finally, we also note that examined stabilizing the Ti^{III} with adatomic Na^+,

Figure C.5. A similar effect is observed (a metastable mid-gap Ti^{III}–ONa^{+} state is half populated). In this case, the electron sits negative to HER, but should not form protons since there is no H^{+} available to reduce and, calculations would hence agree with the previous observation that stoichiometric reduction of Ti^{III} is achieved in the presence of Na^{+}.

In summary, computations have uncovered two possible thermodynamic explanations for the observed limit to PCET-based charge storage in MIL-125; i) e^{-}/H^{+} pairs accumulate until protons are reduced, generating H_2 or ii) e^{-}/H^{+} pairs accumulate until saturating the available cluster orbitals, at which point alcohol oxidation would cease. To test these possibilities, we sought to experimentally quantify MOF cluster photo-charging and associated H_2 evolution by irradiating MIL-125 for varying durations in the presence of a) excess of benzyl alcohol and b) stoichiometric quantities (four alcohol molecules per cluster), respectively. Scenario 1 serves to test whether MIL-125 can continuously consume alcohol, while scenario 2 serves to test whether the clusters cease charging after complete reduction of the clusters. The reaction was monitored by comparing benzylaldehyde 1H NMR signals with those of an internal standard (see **Appendix C** for further experimental detail).

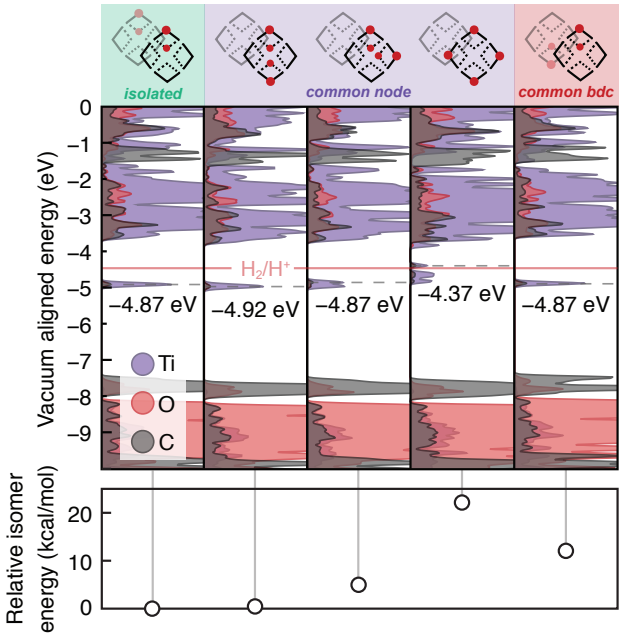

Figure 2.2.5. At the experimental limit presented by Saouma *et al.*, two hydrogen atoms per node, the MOF appears electronically indistinguishable from one another, unless a single hydrogen atom is added to each one μ^2-oxo per pair in a single node. While this structure may still be accessible, it is only kinetically stable compared to H_2 formation.

Quantification by ^{1}H NMR of unreacted alcohol at each time point relative to the amount of aldehyde generated provides indirect measure of H_2 evolution and other side-reactions, *i.e.*, any deviation from 1:1 would imply an e^-/H^+ "leak". After 20 minutes of irradiation in the presence of stoichiometric quantities of benzylic alcohol, an average of 2% of the clusters in MIL-125 accumulated one-electron, one-proton. Importantly, stoichiometric conversion of each alcohol to the corresponding aldehydes was observed. In a separate experiment, excess alcohol and a 2-h irradiation led to just 6% of the clusters storing an average of one electron, whereas irradiation for 18 h led to reduction of 20% of the clusters, with Ti^{III} per cluster, on average. All materials retained the white-to-black color charge after irradiation, supporting the computational insights that e^-/H^+ pairs

remain stable towards HER in the low-charge regime. Because photocharging ceases prior to complete cluster reduction, we surmise that HER must serve as the thermodynamic limit, and yet scarce H_2 can be tracked by us and other groups, and most of the ethanol remains unreacted. Kinetic factors therefore likely prevent further reduction and subsequent H_2 generation. Specifically, depletion of ethanol near Ti-oxo clusters during photodoping would prevent continued accumulation of charges because exciton recombination would outcompete hole quenching due to the slow diffusion of new ethanol molecules. This kinetic-based explanation remains the focus of current studies in our labs.

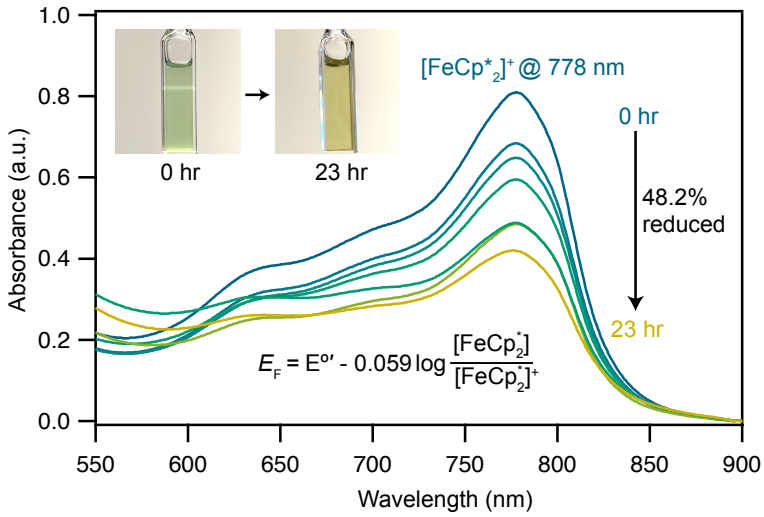

Figure 2.2.6. Electronic absorption spectra collected at various illumination times between 0 and 23 h during photochemical reduction of MIL-125 powder nanocrystals in the presence of 25 mM $[FeCp^*_2][BF_4]$ in a MeCN/EtOH mixture

To further test the hypothesis that e^-/H^+ pairs are stabilized against H_2 evolution in MIL-125 during photodoping, we sought to measure their redox potentials during the photodoping process. Considering that previous reports of photodoped MIL-125 shares similar redox potentials to decamethylferrocenium

$[FeCp_2^{*+}]$[142], we sought to use the latter as an optical redox indicator of the photodoped MOF suspension. By measuring the concentration of $[FeCp_2^{*+}]$ *in situ* through monitoring the absorption feature at 778 nm, attributable to a LMCT transition,[153] the ratio of $[FeCp_2^{*+}]$ to $[FeCp_2^{*}]$ can be determined and related through the Nernst equation to calculate the solution Fermi level, Figure 2.2.6.[166,167] Assuming redox equilibration between all species in the suspension, this value also reports the redox potential of the photodoped MOF at that time point. Hence, we can compare this value to the known redox potential of HER in acetonitrile (-624 mV vs Fc^+/Fc)[271] as further proof that the electron-proton pair is stabilized against recombination. Toward this aim, the mixture was dispersed in an air-free quartz cuvette, irradiated with a broadband photolysis lamp, and stopped intermittently to measure UV-vis spectra.

Figure 2.2.6 shows that irradiation of the MOF-ethanol mixture induces a decrease in the $[FeCp_2^{*+}]$ absorption bands, signaling reduction by photodoped MIL-125. As a control, $[FeCp_2^{*+}]$ does not undergo photoreduction in the absence of MIL-125 (Figure C.9). After 23 h of irradiation, the absorption bands of $[FeCp_2^{*+}]$ stopped decreasing, indicating a steady-state concentration of all redox-active species in the mixture. Analysis of these spectra indicate MIL-125 photoreduced 48.2% of the original $[FeCp_2^{*+}]$, yielding a steady-state redox potential of –588 mV vs Fc^+/Fc, just +36 mV milder than that of the electrochemical potential of HER. The comparatively positive potential of photodoped MIL-125 helps explain the lack of detectable H_2 generation and supports our computational results that estimate the Ti^{III}–OH^+ mid-gap state to sit ∼100 meV more stable than HER. The slight difference between experimental and computational results can be easily attributed to accounting for the true H^+

activity of the suspension, which is considerably lower than the pH = 0 conditions defined for NHE. In other words, the true redox potentials of photodoped MIL-125 sit energetically even farther from vacuum than HER and closer to the calculated results. Remarkably, given that 1.25 equivalents of Fc^{*+} per Ti atom were introduced for this experiment, 48.2% reduction would imply that each MIL-125 cluster supports approximately five Ti^{III}–OH pairs, on average, in excellent agreement with our computational predictions of the thermodynamic limit to MIL-125 charge storage.

Cation-induced electrostatic stabilization of the MIL-125 clusters can account for the considerable increase in charge storage when performed with Fc^{*+} compared to normal photodoping conditions. During the optical redox indicator experiment, each electron that transfers from MIL-125 to Fc^{*+} must be associated with a H^+ liberated from alcohol oxidation. When the MOF-Fc^{*+} reaches steady-state conditions, therefore, the H^+ activity is higher than during normal photodoping conditions. We expect that these additional cations impart strong electrostatic stabilization of the $Ti^{IV/III}$ redox couples. Additionally, we expect that the increased concentration of H^+ increase the likelihood of achieving the specific arrangement, as outlined above by our calculations, that permit up to size Ti^{III}–OH pairs per cluster. The impact of cations on the redox potentials of Ti-MOFs has been recently investigated by us and will be a fruitful strategy for photoredox reactivity.

Conclusion. In sum, a combined computational and experimental study has been used to explain the microscopic origin of PCET-based charge storage MIL-125 as arising from the inorganic oxos of the clusters. These motifs accept

the H^+ liberated during the photodoping reaction, thereby providing Coulombic stabilization and separation from the otherwise highly reducing photogenerated Ti^{III} center. Computational and experimental results place the redox potential of these Ti^{III}–OH+ pairs at reduction potentials more stable than HER in the low-charging regime. The lack of gaseous byproduct from the oxidation of alcohol molecules within MIL-125 pores is seen to result from electron delocalization across $Ti^{III/IV}$ redox couples and the covalent association of a functional counter-ion. Single PCET events, or those that occur at remote active sites, yield conduction band electrons too low in energy to afford molecular hydrogen formation from the associated protons. Paired events at geminal μ^2-oxo ligands further suppress HER. We identified routes for hydrogen loading exceeding 4 H^* per node, and certain spatial configurations allowed for up to 50% reduction of Ti-sites. With this in mind, the spatial distribution of PCET sites formed under kinetic conditions is likely to inhibit access to this configuration, as evidenced by experiment. Irradiation of MIL-125 in the presence of benzylic alcohol showed negligible hydrogen formation, consistent with HER suppression. Quantitative ^{1}H NMR suggests, nevertheless, that photodopant concentrations of only 20% were obtained with excess reductant over 18 h, but as many as five Ti^{III} could be stabilized in each cluster when performed with an optical redox indicator.

The extent of e^-/H^+ accumulation is therefore likely due to a thermodynamic limit set by HER and electrostatic interactions of the electrolyte medium. Kinetically, they may be inaccessible due to depletion of sacrificial reductant. While these results suggest H_2 must evolve during steady-state charge accumulation, this work and previous studies imply minimal H_2 generation. We therefore expect kinetics to be slow for accessing the states that are unstable

towards HER. It is also notable that a few photodoped states in the low-charge regime were computed to be unstable towards HER, while the vast majority are stable. Therefore, the accumulation of e^-/H^+ pairs and minimal H_2 generation may stem from the greater probability of e^-/H^+ finding stable arrangements. In all, this study indicates MOFs featuring inorganic clusters with redox-active early transition metals and inorganic basic sites could offer a platform to stabilize excited electrons in the conduction band, broadening the gamut of photochargeable materials.

CHAPTER III

PROBING VIBRONIC INTERACTIONS USING CRYSTAL SIZE

This chapter includes an excerpt from a recently submitted article to *Journal of the American Chemical Society* by Kevin Fabrizio, Audrey M. Davenport, and Carl K. Brozek.

The article was co-written by Kevin Fabrizio and Carl K. Brozek. Kevin Fabrizio and Carl K. Brozek conceptualized the idea. Experiments were performed by Kevin Fabrizio. Audrey M. Davenport synthesized and characterized NH_2-MIL-125.

Introduction

Tuning photocatalyst performance requires direct and molecular-level insight into the underlying photoredox mechanisms. For example, the optimization of homogeneous photoredox catalysts in recent years relies on knowing the effect of small atomistic changes to catalyst sterics and redox potentials.[272,273] Such structure-function relationships are typically established with a range of solution-state techniques that afford *in situ* insight. Whereas probing molecular aspects of solid-state photocatalysts remains an outstanding challenge, the design of colloidal semiconductor nanocrystals into sophisticated photocatalysts has relied on studying them with solution-state methods, enabled by sub-30 nm sizes that reduce light scatter during spectroscopic measurements.[274] Metal-organic frameworks (MOFs) bridge these two classes by combining vast molecular diversity with the architecture of a solid-state lattice. In the context of catalysis, the well-defined and synthetically tunable nanopores offer a platform for controlling substrate diffusion,[275,276] while the lattice provides matrix stabilization of reactive species

otherwise unusable as small molecules.[113,277] Although MOFs have become widely studied as heterogeneous photocatalysts, clear structure-function relationships remain elusive without *in situ* solution-state analysis. Preparing MOFs as nanoparticles smaller than 30 nm would minimize their light scatter and improve colloidal stability during solution-state spectroscopy, electrochemistry, and other *in situ* methods critical to building a molecular understanding of this distinct class of photocatalysts.

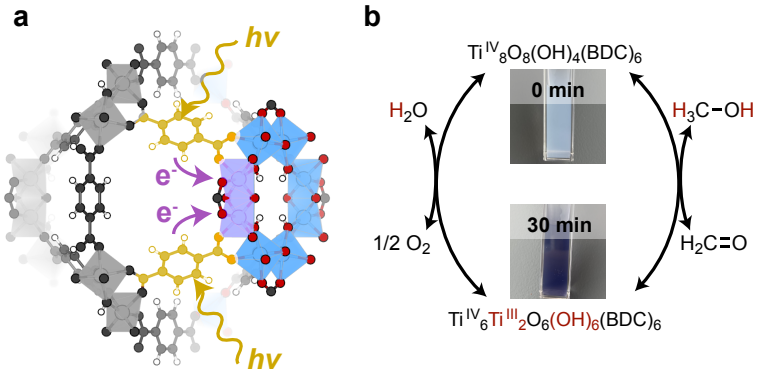

Figure 3.1. **a** Structural representation of the photodoping process in MIL-125. Photoexcited electrons transfer from benzenedicarboxylate to the Ti centers. **b** Chemical representation of the "photodoping" process in MIL-125 as proposed by Dan-Hardi *et al.*[140]. Photoexcitation in the presence of sacrificial reductants (methanol) leads to trapping of Ti^{3+} centers balanced by H^+ by quenching HOMO (linker)-centered holes through methanol oxidation. This reaction manifests qualitatively as a white-to-black color transformation of the MOF.

Among photoactive MOFs, those containing Ti centers are particularly attractive as molecularly tunable materials because the Ti and surrounding ligand orbitals dominate the frontier orbitals of the MOF. As a result, optical gaps may be controlled by altering the energetics and composition of the Ti ligand sphere.[41,221] For example, modifying $Ti_8O_8(OH)_4$(terephthalate)$_6$ (MIL-125) to $Ti_8O_8(OH)_4$(4-amino-terephthalate)$_6$ (NH_2-MIL-125) decreases the optical gap from 4.0 eV to 2.6 eV.[42] Light absorption by these materials can be leveraged

to achieve photoredox transformations, either by oxidation from photogenerated holes in the HOMO (valence band) or by reduction from photogenerated electrons promoted to the LUMO (conduction band), acting either as photosensitizers for shuttling charges to co-catalysts11 or as photocatalysts themselves.[182] Dan-Hardi *et al.*[140] demonstrated that MIL-125 irradiated across its optical gap in the presence alcohols induces a photochromic change of the MOF from white to black.

Corroborated by EPR measurements,[140] the authors proposed a mechanism shown in Scheme 3.1 involving accumulation of charges in the form of Ti^{3+} centers in the Ti-oxo clusters and hole quenching achieved by alcohol oxidation. Since this seminal report, photochemical electronic doping, termed "photodoping", has been demonstrated for a variety of MOFs containing Ti-oxo clusters,[53,152,182,278] and mechanistic aspects have been analyzed in terms of proton-coupled electron transfer theory.[142,143] Despite these advancements, direct evidence of Ti^{3+} formation remained unobserved and *in situ* measurement of any MOF during photoredox conditions still poses an outstanding challenge.

Here, we report a rapid reflux-based synthesis of MIL-125 nanoparticles to access sizes below 30 nm with indefinite colloidal stability and BET surface areas exceeding that of the bulk. Afforded by this stability and minimal light scattering, we employ solution-state spectroscopy to probe the photodoping process in situ. These measurements provide definitive evidence of photogenerated Ti^{3+} and accumulation of numerous charges at the MOF metal nodes. Electrochemical potentiometry collected during photodoping conditions and voltammetry of free-standing colloids allow determination of the nanoMOF redox potentials underlying this photochemistry. By harnessing the solution processability of the sub-50 nm colloids, MOF-polymer membranes can be fabricated that retain the original

photochromic behavior. These results demonstrate the utility of preparing MOFs as nanoparticles for addressing outstanding fundamental questions and progressing MOFs toward industrial implementation.

Methods

Material Characterization. Sample purity was verified by powder X-Ray diffraction (PXRD) with a Bruker D2 Phaser benchtop diffractometer and infrared spectroscopy (IR) using a Bruker Alpha II compact IR with an ATR attachment in a N_2 glovebox. UV-vis-NIR spectra were collected on an Agilent Cary 5000 UV-Vis-NIR spectrophotometer in the range of 190-2200 nm or a Shimadzu Biospec-1601 and all samples were collected with a baseline solvent mixture matching the sample medium. Photoluminescence data was collected on a Horiba Jobin Yvon Fluoromax-4 Fluorimeter with an excitation wavelength of 280 nm. No fluorescence was observed in pure solvent. Gaussian fittings were performed in Igor Pro Version 6.37 using the Multipeak Fitting 2 package. For N_2 sorption experiments, samples were washed twice with DMF, MeOH, acetone, and hexanes as recommended from Howarth *et al.*[279] Samples were suspended in analysis tubes before being dried on a Schlenk line at ambient temperature. Then, samples were degassed under high vacuum at 140 ^{o}C on a Micromeritics ASAP 2020, and degassing was considered complete when the outgas rate fell below 2.5 μtorr/min. All solution-state electrochemical data was collected using a Biologic SP200 in a N_2-filled glovebox. For acid digestion ^{1}H-NMR, samples were washed with methanol (3×, 10 mL) before being dried under vacuum and digested in a 20% DCl/D_2O in DMSO-d_6 mixture in air. Undissolved solids were separated by centrifugation, and the supernatant was analyzed using a Bruker Advance III-

HD 600 NMR spectrometer. Scanning electron microscopy (SEM) was performed using a FEI Helios 600i instrument with 5.0 kV energy and 0.69 nA current. SEM samples were prepared by drop-casting MIL-125 suspensions onto clean silicon substrates and drying under N_2 flow. Particle sizing was performed in ImageJ using the line tool to determine crystal diameter, and histograms created in Igor Pro 6.37. The polydispersity index (PDI) was calculated by dividing the standard deviation of the Gaussian fit by the mean particle size. Dynamic light scattering (DLS) experiments were performed with a Malvern Zetasizer Nano.

Modulated Synthesis of MIL-125 NPs. A two-neck round-bottom flask fitted with a reflux condenser was charged with H_2BDC (0.352 g, 2.12 mmol) and dry DMF (5 mL). The reaction was then allowed to stir at 110 ^{o}C for 30 min. After complete dissolution of the linker, methanol (1.5 mL) and modulator were added, and the solution continued to stir under reflux for an additional 30 min. Next, the Ti(IV) source (1.23 mmol) was added by syringe and the reaction was vigorously stirred at 110 ^{o}C under reflux. Once a precipitate was observed, aliquots ($\sim$500 μL) were taken from the reaction mixture and centrifuged at 13200 rpm for 3 min, then washed sequentially with 3 mL of cold DMF and MeOH before crystallinity was confirmed by PXRD. Once the reaction was deemed complete by PXRD, an excess ($\sim$20 mL) of cold DMF was added to the reaction mixture to halt the reaction. The final nanoparticles were collected by centrifugation and subsequently washed with 15 mL of cold DMF twice and then MeOH twice, and finally suspended and sonicated in fresh MeOH. For the scaled reaction, all reactants are simply increased by 3- or 10-fold.

Controlled Water Addition to MIL-125 NP Syntheses. All manipulations were performed under an N_2-atmosphere with Schlenk techniques. Otherwise, the procedure was analogous to the modulated synthesis of MIL-125 NPs described above. All glassware was heated and dried at 120 ^{o}C and cycled 3× between vacuum and N_2 before use. MilliQ H_2O was added to DMF before modulator addition in concentrations 0.1, 0.25, 0.50, 1.0, or 2.0% v/v to DMF.

Synthesis of 38 nm NH_2-MIL-125 NPs. Analogous to the unfunctionalized procedure, dry DMF (5 mL) was combined in a small glass vial with H_2O (5 µL). H_2BDC-NH_2 (0.364 g, 2.12 mmol) along with the prepared DMF was added into a multi-neck round-bottom flask fitted with a reflux condenser. The reaction stirred at 110 ^{o}C in an oil bath under N_2 for 30 minutes, until the linker dissolved. Next, benzoic acid (1.18 g, 9.7 mmol) was added to the flask followed by methanol (1.5 mL) and stirred for 30 minutes. The Ti(IV) source (1.23 mmol) was added, and the reaction was left to stir. Aliquots (∼500 µL) were taken periodically and centrifuged at 13200 rpm for 3 minutes. After, they were washed with DMF and MeOH and PXRD was taken to confirm crystallinity. Once crystallinity was confirmed, the rest of the reaction mixture was collected, and the same washing procedure was performed before drying the particles on a Schlenk line under vacuum and storing them in a scintillation vial until use.

Synthesis of 105 nm NH_2-MIL-125 NPs. In a modified procedure from Romero-Angel et al.,[280] a multi-neck RBF was fitted with a condenser and heated to 110 °C with an oil bath under N_2. The flask was charged with H_2BDC-NH_2 (0.3802 g, 2.12 mmol) and DMF (5 mL) and left to stir for 30 minutes.

Dodecanoic acid (2.12 g, 10.6 mmol) was then added followed by methanol (1.5 mL) and left to stir for 30 minutes. The Ti(IV) source (1.23 mmol) was then added with a syringe through a septa while stirring. Aliquots (∼500 μL) were taken periodically to check for crystallinity by PXRD. Aliquots were centrifuged for 3 minutes at 13200 rpm and washed with DMF and MeOH. After the product was confirmed to be crystalline by PXRD, the reaction mixture was collected and washed by the same procedure used for the aliquots. The particles were then dried on a Schlenk line under vacuum and stored in a scintillation vial until use.

***In situ* UV-Vis-NIR Solution Spectroscopy during Photodoping.** Concentrations of MIL-125 nanoparticle dispersions in methanol were determined by sonicating a "stock" solution and drying a 1 mL aliquot to determine the mass of an ensemble of activated nanoparticles. The concentrations of the "stock" solutions were thereby determined to be ∼20-30 mg/mL. A concentration of 0.025 mg/mL was deemed sufficient for achieving optical densities below 1.0 by UV-vis spectroscopy. Correspondingly, an amount of "stock" MIL-125 solution was washed with methanol (6×, 10 mL) and dried under vacuum at 110 ^{o}C to reach the final concentration of 0.025 mg/mL. The activated nanoparticles were redispersed in dry MeOH (10 mL) in an N_2 glovebox and sonicated for 30 min. to avoid particle aggregation. To a clean custom-made air-free quartz cuvette, 3.0 mL of the MIL-125 dispersion was transferred. Finally, the cuvette was irradiated for intermittent time intervals to record optical absorption spectra until no further changes are noted in the UV-vis traces. For observation of Ti(III) d-d transitions, the procedure was identical, except that the concentration of MIL-125 NPs was increased to 0.10

mg/mL.

Cyclic Voltammetry and Open Circuit Voltage Measurements. Prior to electrochemical experiments, DMF was freeze-pump-thawed 6× and brought into an N_2 glovebox. The MIL-125 NPs were suspended in a 0.1-M $TBAPF_6$/DMF solution and transferred to a quartz cuvette fitted with a standard three-electrode cell with a platinum working electrode, a silver wire pseudo-reference electrode, and a platinum wire counter electrode. All electrodes were cleaned with dilute HNO_3 before use. Data was collected in the range of -1.50 V to +1.50 V, and no Faradaic features were observed in background scans. At the end of all electrochemistry experiments, 10 mg of ferrocene was added to the solution to provide a quantitative measurement of $E_{1/2}$ versus Ag. For *in situ* photodoping while measuring OCV, the silver wire was shielded from the 308 nm LED to avoid photochemical degradation.

Computational Methods. A MIL-125 crystal structure was acquired from Walsh[281] and truncated according to the "full linker sterics/electronics" procedure outlined by Mancuso *et al.* using Avogadro 1.2.0.[219,282] Structural relaxation calculations were performed to obtain the lowest energy geometry with density functional theory (DFT) as implemented in the ORCA program system v5.0.3.[283] The unconstrained geometry optimizations and orbital density calculations were performed using the RIJCOSX integral and B3LYP hybrid functional for an accurate depiction of Hartree-Fock exchange, with def2-SVP basis sets for organics (C, H, O) and def2-TZVP for titanium.

Results and Discussion

Although nanoMOFs containing Ti-oxo and related Zr-oxo motifs have been previously prepared,[280,284] the smallest reported sizes typically range from 60 to 100 nm. To prepare MIL-125 particles suitable for solution-state techniques (sub-30 nm diameters), we adopted synthetic strategies that would allow efficient optimization of reaction conditions. Whereas most MOF and nanoMOF synthesis involve solvothermal conditions lasting 8-24 h,[280] that preclude reaction monitoring, reagents were refluxed and products were analyzed as aliquots *ex situ* by PXRD. This approach was inspired by a previous report of using reflux to prepare bulk NH_2-MIL-125, but not nanoparticles.[285] Because nanoMOF syntheses typically rely on organic acids as "crystal growth modulators", we explored the ability of four monocarboxylic acids to control particle sizes. Previously, we reported a "seesaw model" of MOF growth that relates the ligation strength and acidity of modulators to their ability to generate nanoMOFs of different sizes.[286,287] Therefore, we compared "pseudo-linkers" benzoic acid (pKa = 4.19) and p-toluic acid (pKa = 4.36) versus the small molecular acetic (pKa = 4.74) and formic (pKa = 3.75) acids.[284] As a starting point, terephthalic acid and tetrabutyl orthotitanate were refluxed under flowing N_2 for 6 h in DMF/MeOH with five equivalents of a modulator. Scherrer analysis indicated that under these fixed conditions, benzoic acid yields the smallest nanocrystal sizes (Figure D.2). Although formic acid bears the lowest pKa, benzoic acid generally has comparable or larger metal-ligand stability constants to formic acid, suggesting that once deprotonated it produces smaller nanoparticles by serving as a better competitor with terephthalate. We surmise that the steric similarity between benzoic and terephthalic acids also enhances its mechanistic role. To test the applicability of the

"seesaw model" to this system, we explored whether particle sizes would exhibit the predicted U-shaped relationship versus modulator equivalents. Therefore, we repeated this synthesis with between 0–10 equivalents of benzoic acid as a modulator. Indeed, this synthetic variation yielded the characteristic U-shaped dependence (Figure 3.2a) by both PXRD (Figure D.1) and SEM (Figures D.9-D.13) sizing, with five equivalents generating the smallest nanocrystals. For quantitative insight into the role of modulator serving as a capping ligand, ^{1}H acid digestion NMR spectroscopy was collected on the smallest nanocrystals. Surprisingly, we observed no modulator incorporated as internal defects or surface capping ligands (Figure D.21), suggesting that modulators function by influencing the competing acid-based and metal-ligand coordination chemistry equilibria, as outlined by the "seesaw model".

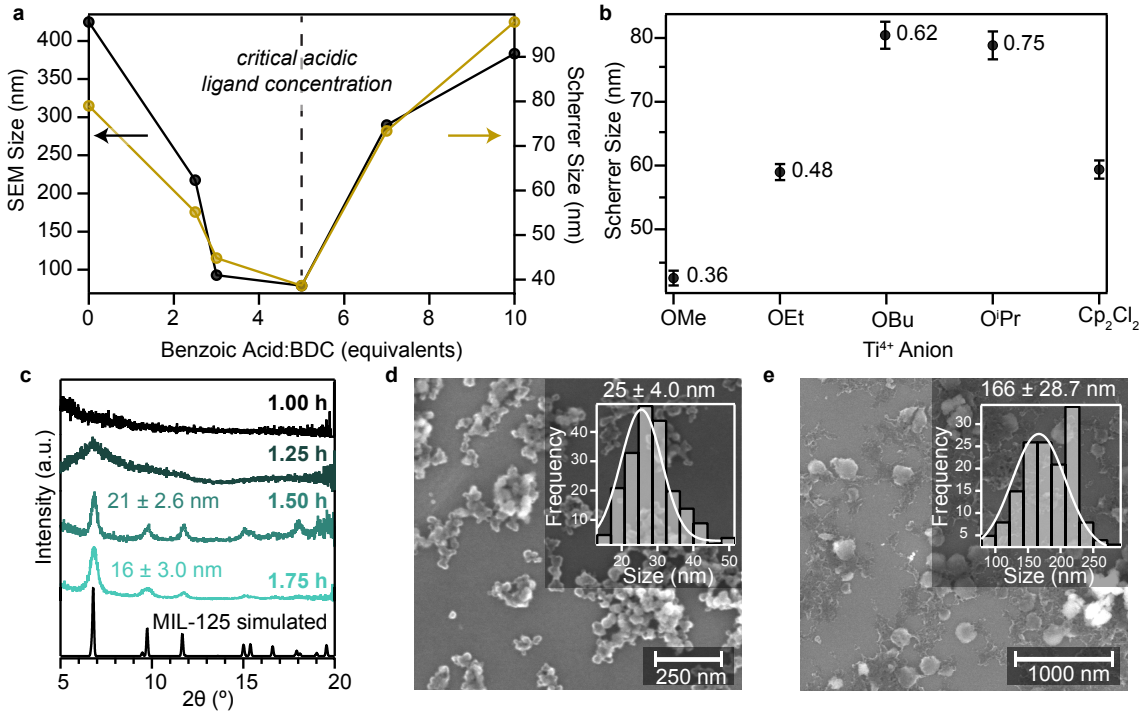

Figure 3.2. **a** MIL-125 nanocrystal sizes versus benzoic acid equivalents under constant reflux conditions (110 ºC, 3.33 DMF:1MeOH, 1.2 mmol $Ti(OBu)_4$). Sizes reported by both SEM (left) and Scherrer analysis (right). **b** MIL-125 nanocrystal Scherrer sizes versus ligand identity of Ti^{4+} precursors. Charton steric parameters (**ν**) for each ligand are included next to each corresponding size. **c** *Ex situ* PXRD patterns and corresponding Scherrer sizes for particles aliquoted during the reaction process. The synthesis involved 5 eq. of BA per BDC and $Ti(OMe)_4$. **d** Representative SEM images and particle sizes for 0.25 % H_2O rel. to DMF and **e** 2.0 % H_2O rel. to DMF.

Because the synthesis of Ti-containing MOFs commonly relies on moisture-sensitive Ti^{4+} alkoxide salts, both the impact of Ti precursor and moisture content were explored as parameters to control particle size. With five equivalents of benzoic acid and by holding constant all other parameters used to study modulator equivalents, as described above, we varied the anion identities of the Ti precursors. To control for moisture exposure, the reactions were carried out in parallel under the same relative humidity. Given that rigorously anaerobic conditions inhibit the formation of MIL-125, we expect that hydrolysis of Ti salts

induces the formation of Ti-oxo clusters required for the structural assembly. Performing the standard set of synthetic conditions with titanium(IV) methoxide, titanium(IV) ethoxide, titanium(IV) isopropoxide, titanium(IV) butoxide, or di(cyclopentadienyl)titanium(IV) dichloride produced crystalline MIL-125 nanoparticles of varying sizes, with the methoxide and ethoxide salts consistently producing the smallest nanocrystals (42 and 55 nm by SEM, respectively), as summarized in Figure 3.2b. By comparing Charton steric parameters of the alkoxide anions, a direct relationship emerges between Charton parameters and nanocrystal sizes.[288] These results suggest that smaller ligands facilitate the trapping of solubilized Ti^{4+} and thereby arresting nanoMOF growth.

To explore the impact of water content on the formation of nano-MIL-125, varying quantities of water were added to the reaction mixture prior to reflux. Interestingly, while hydrolysis is necessary (air- and water-free syntheses yielded amorphous products), uncontrolled amounts of water yield TiO_2 byproducts. These results suggest that hydrolysis facilitates the formation of the Ti-oxo clusters. We hypothesized that by controlling the hydrolysis of Ti precursors, free Ti^{4+} would be liberated slowly to form Ti-oxo clusters prior to ligand assembly. Therefore, aside from small quantities of water (0.25, 0.50, 1.0, and 2.0 vol%), reactions were kept free from ambient humidity under an N_2 atmosphere. Screening these conditions indicated that 0.25% water relative to DMF yielded the smallest nanocrystals of MIL-125 reported at 25 ± 4.0 nm (Figure 3.3d), while a higher amount of water, such as 2.0% relative to DMF yielded non-uniform larger crystals (166 ± 28.7 nm) with amorphous TiO_2 also in solution (Figure 3.3e).

Taken together, this search through synthetic parameters implies that using titanium(IV) methoxide, 0.25% H_2O relative to DMF, and 5 equivalents of benzoic

acid yields the smallest nanoparticle sizes. In comparison to the bulk synthesis of MIL-125, which produces particles with a polydispersity index (PI) of 0.59, this route creates a narrow size distribution with a PDI of just 0.17. In addition, the particles remain colloidally stable for at least 6 months, as corroborated by hydrodynamic diameters and polydispersity indexes consistent with SEM images and large zeta potentials of ca. –30 mV (Table D.4). Furthermore, the reflux-based reaction can be easily scaled to produce gram-scale quantities in a single batch. Lastly, the reaction progress could be monitored to minimize reaction times. By using these conditions as a standard set of reaction parameters, we removed aliquots that were quenched and washed with cold DMF and MeOH and analyzed by PXRD. As shown in Figure 3.2c, crystalline MIL-125 nanoparticles form in less than 2 h, whereas typical routes towards bulk and nanoparticle MOFs require half-day or multi-day periods.

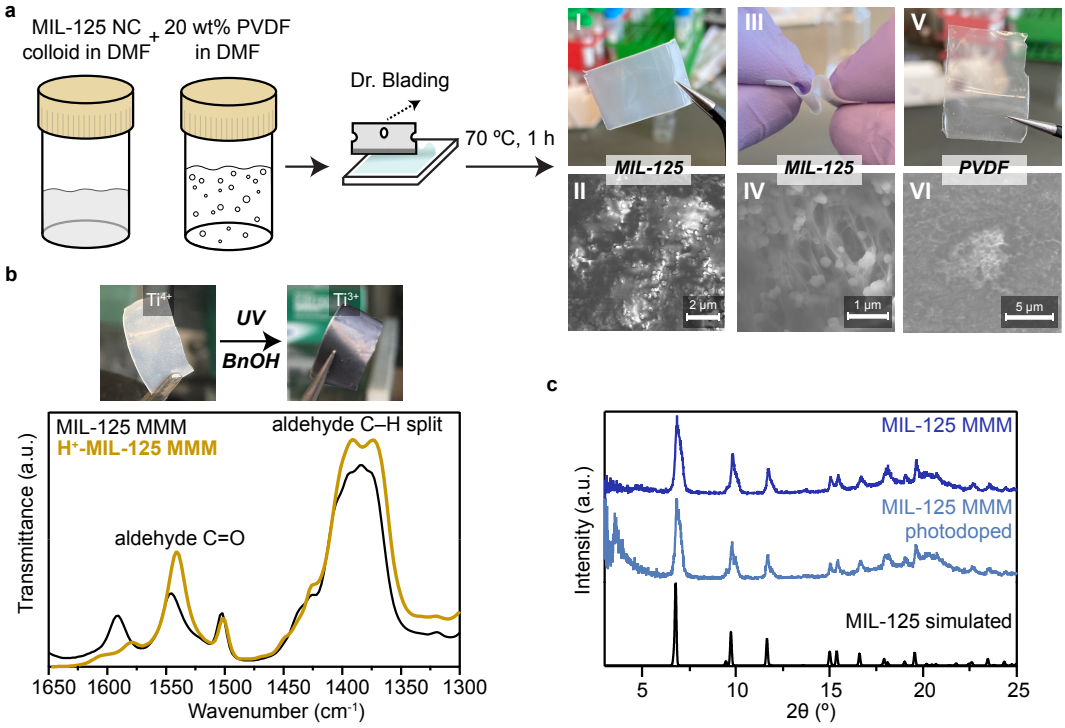

Figure 3.3. a**a** Generic reaction scheme for synthesizing MIL-125 MMMs, optical images of a MMM (I, III), top-down SEMs of a MMM, (II, IV), and optical (V) and SEM (VI) images of a standalone polymer membrane. **b** Optical images of a MIL-125 MMM and FT-IR before and after photodoping. **c** PXRD of MIL-125 MMM before and after photodoping highlighting retained crystallinity.

Given such small particle sizes, and the scalable reaction conditions, we expected improved solution processability to form photoactive MOF-polymer composites at industrially relevant scales. Membranes and films of metal-organic frameworks have long been targeted for water purification, gas separation, liquid-phase separations, electronics, and electrochemical applications,[289,290] but bulk MOF crystals yield inhomogeneous and brittle films incapable of withstanding practically relevant conditions.[291] Thus far, flexible bulk MOF composites (*i.e.*, mixed-matrix membranes, MMMs) have been realized with the inclusion of polymeric binder.[292,293] Despite the potential utility of photoredox-active MMMs, MIL-125 and related MOFs have only been incorporated as bulk crystals

and failed to show photochromic activity.[294–296] To demonstrate the improved processability of MIL-125 nanoparticles, we employed an approach originally reported by Cohen *et al.* to create MMM with high (∼50 wt%) MOF loadings.[293] Briefly, a polyvinylidene fluoride (PVDF) solution in DMF was mixed with a DMF suspension of the MIL- 125 nanocrystals and then the resulting viscous solution was coated onto a glass substrate and allowed to dry in the oven at 70 ^{o}C. It should be emphasized that a substrate of any arbitrarily large size could be used given the gram-scale quantities afforded by the reflux route. Finally, the nanoMOF MMM could be released from the substrate by a short soaking procedure in methanol (Figure 3.3a). The MIL-125 nanocrystals remain intact (Figure 3.3c) and homogeneously integrated with the polymer binder. Interestingly, while the MOF nanocrystals possess high BET surface areas, the membranes exhibit decreased BET surface areas at 50 m^2/g. We ascribe this diminishment to polymer entrapment and/or polymer freezing within the large pore matrix of MIL-125. Figure 3.3a(IV) shows a small tear within the membrane, highlighting the even distribution of nanoMOF within the PVDF matrix, not just at the surface. To quantitatively measure the MOF content within the polymer, SEM-EDX provided insight into the Ti-to-F concentration. We hypothesized that since titanium should only be found in the MOF, and fluorine in the polymer, that a relative weight percent of titanium should be equal to the amount of MOF loading in the MMM. Experimentally, we synthesized 25 wt% MMM, and by SEM-EDX, the MOF loading was almost identical at 25.85 wt% (Figure D.28 and Table D.3). These results highlight the facile solution-processability of the MOF into a simple, but widely used polymer.

To explore the reactivity and consequent utility of these membranes, we tested whether the MOF retained photoactivity. A 50 wt% MMM was dispersed in a solution of dry benzyl alcohol and placed into an air-free quartz cuvette. Under steady-state UV irradiation, the MOF performed the characteristic white-to-black transformation (Figure 3.3b). We posited that although Ti^{3+} cannot be seen via standard FT-IR techniques, the hole quenching oxidation of an alcohol to an aldehyde could be observed. Accordingly, IR bands consistent with aldehyde carbonyl and alkane stretches became evident in the photodoped thin films, demonstrating that the polymer matrix does not interfere with the MOF photoreactivity. These findings suggest that nano-MIL-125 MMMs may be applied to degrade emerging pollutants, many of which contain alcohol groups (atenolol, bisphenol A, nonyl phenol, etc.).

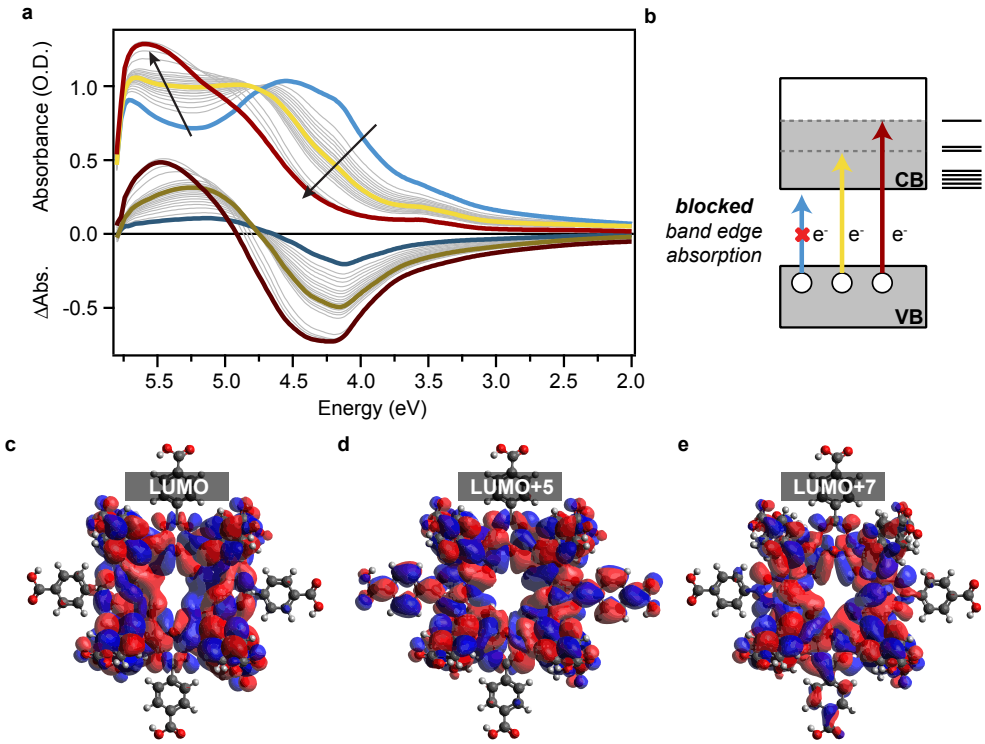

Figure 3.4. **a** Solution-state optical absorption spectra of a 25 μg/mL solution of 25 nm MIL-125 nanoparticles collected *in situ* during the photodoping process in neat methanol. Differential absorption represents the absorption difference at a time point and the initial spectrum (blue). **b** Schematic representation of MIL-125 optical absorption during photodoping process. **c-e** DFT-computed electron densities of a model cluster for the LUMO, LUMO+5, and LUMO+7.

With colloidally stable MIL-125 nanoparticles amenable to solution-state spectroscopy due to their sub-30 nm sizes, we sought *in situ* evidence of Ti^{3+} formation during photodoping conditions. A 25 μg/mL mixture of 25-nm MIL-125 particles in methanol was monitored by optical absorption spectroscopy following increments of UV irradiation. Figure 3.4a shows the initial spectrum (blue) and subsequent spectra. Immediately after initial light exposure, the first excitonic absorption feature at 4.1 eV begins to bleach. Interestingly, after irradiating for 270 s, the initial excitonic bands give rise to distinct spectral features. The clear

isosbestic point seen ∼4.5 eV suggests the disappearance of an electronic state and the rise of another, highlighted in yellow. With additional irradiation, this state also decayed, giving rise to a final electronic state at 5.5 eV. Photodoping was considered complete at 60 min when spectra ceased to change and this 5.5 eV feature saturated. To highlight this spectral evolution, Figure 3.4a includes differential absorption spectra. The final trace in black indicates that overall photodoping bleaches the features centered between 4.0 – 4.5 eV and generates a new transition at 5.5 eV. These data strongly resemble the spectral evolution of ZnO, CdSe, PbSe, ITO, AZO, and other semiconductor nanocrystals during photodoping conditions.[173,174,297–300] In these materials, band-edge bleaching and the concomitant rise of higher-energy bands arise from the blocking of band-gap absorption due to charge accumulation in the conduction band, which also turns on excitation from the valence band into higher-energy unfilled orbitals. Hence, we propose a similar scenario, as illustrated in Figure 3.4b. We assign the bleaching of the blue spectrum to blocking of the HOMO-LUMO gap, whereas the yellow and red spectra originate from the promotion of HOMO electrons to higher-lying unoccupied orbitals. To simulate the photodoping process and investigate this proposal, we employed density-functional theory calculations with ORCA v5.0.3 on a truncated MIL-125 Ti-oxo cluster.[283] In particular, we examined the frontier orbital energies and found that Ti 3d orbitals of the Ti-oxo cluster dominate the LUMO through LUMO+7 orbitals. In other words, the eight Ti^{4+} sites combine to create at least eight empty 3d cluster orbitals. Interestingly, the calculated density of these models suggests a significant charge delocalization across the octameric cluster. Figures 3.4c-3.4d depict selected cluster orbitals. Additionally, the eight unoccupied cluster orbital energies split in a 5/2/1 pattern, suggesting that the

blue spectrum bleaches completely only upon accumulation of five Ti^{3+} centers. Furthermore, the appearance of the final red spectrum suggesting accumulation of at least seven electrons, surpassing previous estimates of charge accumulation in MIL-125.[142,143,301] Under these dilute concentrations, however, the predicted formation of Ti^{3+} could not be evidenced by the weakly absorbing d-d transitions.

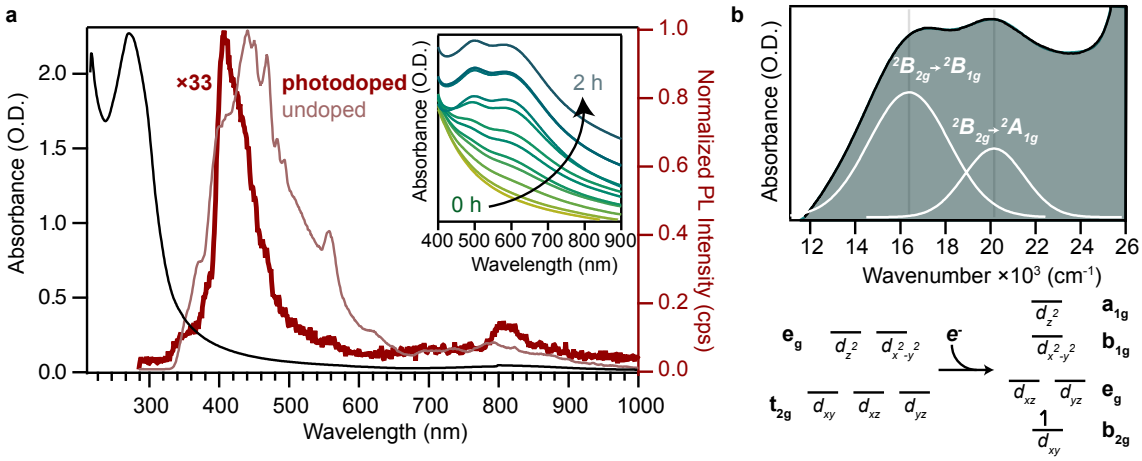

Figure 3.5. **a** Solution-state optical absorption and photoluminescence spectra of a 25 μg/mL colloid of 25 nm MIL-125 nanoparticles Inset: Growth of d-d transitions in a 0.25 mg/mL suspension during 2-h photodoping reaction with methanol. **b** Ligand-field analysis of photodoped MIL-125 indicates that two d-d bands arise from Jahn-Teller distorted Ti^{3+}.

Figure 3.5a plots the undoped absorption spectrum of 25-nm nanoparticles in neat methanol. Shown in the inset is the solution at ten-fold greater concentration, indicating that UV light induces the formation of two absorption features centered at 610 nm and 495 nm, corresponding to 16,400 and 20,200 cm^{-1}. These bands are hallmark features of a d^1 transition-metal ion subject to Jahn-Teller distortions, as exemplified by $Ti(H_2O)_6{}^{3+}$ complexes.[302,303] Figure 3.5b summarizes this assignment and fits the spectra to Gaussian line shapes. Accordingly, we assign the band centered at 20,200 cm^{-1} to a $^2B_{2g} \rightarrow$

$^2B_{1g}$ transition and the shoulder at 16,400 cm^{-1} to a $^2B_{2g} \rightarrow {}^2A_{1g}$ transition consistent with the electronic configuration of a d^1 ion in a pseudo-octahedral ligand field subject to a Jahn-Teller distortion (Figure 3.5b).[304] When reduced to D_{4h} symmetry, three electronic transitions (two visible, one infrared) previously forbidden become possible through dynamic vibronic coupling. Interestingly, in molecular Ti-oxo clusters, Jahn-Teller distortions are not observed upon photodoping.[305] We hypothesize that the unique extended metal-carboxylate coordination environment in MOFs allows for dynamic expansion and contraction, directly impacting electronic and orbital degeneracy. To further harness the solution-processability of these nanoMOFs and provide additional insight into the electronic effects of photodoping, solution-state photoluminescence spectra were collected of colloidal particles before and after photodoping. Figure 3.5a includes the spectra of colloidal 25-nm MIL-125. An excitation wavelength was selected near the band edge absorption at 280 nm. In undoped conditions, the emission data display a feature centered at 420 nm. To probe the origin of this luminescence, the particles were excited with sub-gap energies as low as 375 nm. Because the feature persisted, we tentatively assign it to radiative relaxation from mid-gap orbitals (Figure D.29). Interesting, upon photodoping for 2 hours, the higher energy transition decreases in intensity by 33-fold and blueshifts slightly, suggesting the charges relax from a higher energy orbital due to accumulation of charges in the LUMO, as expected for a photodoped material.

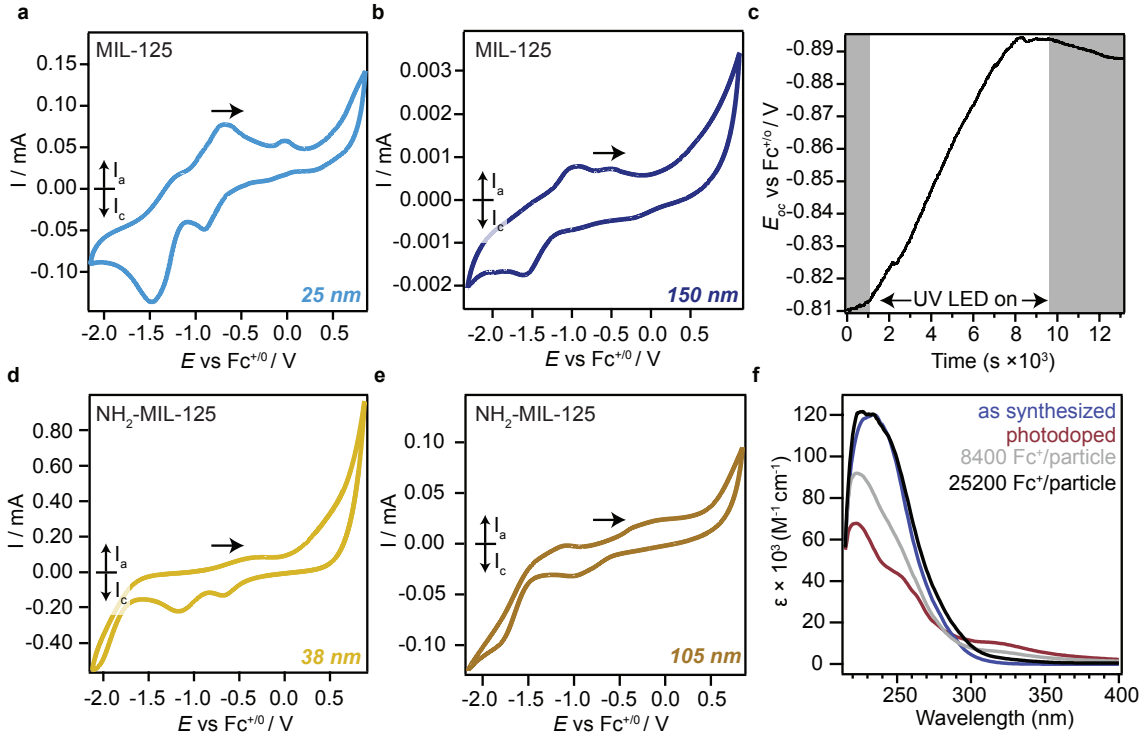

Figure 3.6. Cyclic voltammetry of undoped **a** 25-nm and **b** 150-nm MIL-125 NCs in 0.1-M $TBAPF_6$. Arrow denotes the initial scan direction. **c** *In situ* open-circuit voltage measurements collected during the photodoping process. **d** Cyclic voltammetry of undoped 38-nm and **e** 105-nm NH_2-MIL-125 nanocrystals in 0.1-M $TBAPF_6$. Arrow denotes initial scan direction. **f** Solution-state absorption spectra of photodoped 25 nm MIL-125 nanocrystals in MeOH titrated with $FcBF_4$ equivalents.

To probe the redox properties of bulk MOFs, decades of research has relied on polymeric binders, such as Nafion, and/or deposition techniques that provide indirect insight into the bare MOFs.[305–308] Recently, our lab demonstrated the first voltametric analysis of MOF colloids.[309] Here, we harnessed the indefinite stability of MIL-125 nanoparticles to probe their ability to store numerous charges by electrochemical methods.Figures 3.6a and b show cyclic voltammogram traces of 25-nm and 150-nm MIL-125 nanocrystal colloids in a 0.1-M $TBAPF_6$/DMF electrolyte mixture using a three-electrode cell (W: Pt, C: Pt, Ref: Ag) under

open-circuit voltage (OCV) conditions. Both nanocrystal sizes show two clear reduction features located at ca. –0.90 V and –1.50 V *vs* $Fc^{+/0}$. Based on the spectroscopic analysis shown in Figure 3.4, we expected either sequential orbital filling of the 5/2/1 splitting pattern of states or a single, broad redox feature. Based on previous analysis of Fe(1,2,3-triazolate)$_2$ nanocrystals, we propose that the less negative feature arises from the reduction of Ti at the external particle surface and the more negative feature arises from reduction of internal Ti sites. In other words, the electrolyte desolvation and reorganization creates an additional electrochemical potential coupled to Ti reduction. Interestingly, the larger particles show diminished current at the feature ascribed to external Ti reduction, highlighting the impact of surface-to-volume ratio in MOF nanocrystals. In other words, the nanoscopic origin of external Ti reduction are only observed in the smaller nanocrystals, likely due to the increased ratio of surface Ti versus internal Ti. For insight into the energetics of photodoping, the Fermi-level energy of the 25-nm reaction mixture, E_F, was monitored *in situ* by measuring the open-circuit voltage, E_{oc}. This approach has been demonstrated to great effect for semiconductor nanocrystals.[173] Figure 3.6c plots E_{oc} over a period of 2.5 h of exposure using a 308 nm, 600 mA LED for a mixture of 25-nm MIL-125 in neat methanol. Upon irradiation, E_{oc} raises steeply to negative potentials, as expected for photoreduction of Ti. Remarkably, the E_{oc} stabilized at -0.89 V *vs* $Fc^{+/0}$, coinciding with the more positive redox potential observed by voltammetry. According to our interpretation, these data suggest that the surface chemistry of the nanoMOFs dominates the E_F of the reaction mixture. Interestingly, all redox potentials reported here appear more negative than the 0.6 mV *vs* $Fc^{+/0}$ estimated previously for photodoped MIL-125.41 We note, however, that the

technique in the prior report generated huge excess of H^+, which shifts E_F to more positive potentials. To determine whether the observed redox features arise from the MOF particles, specifically the $Ti^{4+/3+}$ couple, we prepared colloids of 19-nm and 80-nm NH_2-MIL-125 nanocrystals and performed cyclic voltammetry under identical conditions (Figures 3.6d and e). The preparation of these particles also demonstrates the generality of the reflux technique in preparing sub-30 nm nanoMOFs. By studying a close analog to MIL-125, we hypothesized that similar CV traces would be observed with redox features shifted due to electronic differences. In the 19-nm particles, both reduction features are observed but shifted anodically ca. +200 mV *vs* $Fc^{+/0}$. Although surprising given the electron donating nature of -NH_2, we propose that the ability of the amino moiety to accept protons and other charge-balancing cations coupled to Ti reduction could account for the anodic shifts. Interestingly, the larger NH_2-MIL-125 particles also exhibit diminished current at the more positive "external Ti" feature. We hypothesize this "external Ti reduction" is only clearly observed in smaller nanocrystals due to the increased local population of surface titania versus internal titania. To our knowledge, these results represent the first redox potentials of photo-active MOFs measured by colloidal electrochemistry, enabled by preparing colloidally stable nanoparticles. Furthermore, these results underscore the importance of characterization in the nano-regime, as larger crystals shadow the distinct potential difference required for equal ("internal" and "external") reduction of Ti. Inspired by the photochemical redox titrations demonstrated for degenerately doped semiconductor nanocrystals,[297,299,300,310] we performed spectroscopic titrations with outer-sphere one-electron oxidant $FcBF_4$. By comparing spectral changes to the number of titrated oxidant, we aimed to assign spectra changes in Figure 3.4

to electron count configurations. These results would reveal the extent of charge storage on each nanocrystal given that for each Fc^+ added, one electron would be removed until the spectrum returned to its undoped profile. Interestingly, when performing these experiments in stoichiometric conditions ($1Fc^+$:$1Ti^{3+}$), no change was observed in the spectra (Figure D.30). However, as shown in Figure 3.6f, when excess amounts of oxidant were added to solution ($163Fc^+$:$1Ti^{3+}$) we observe complete recovery of the original absorption spectrum. We hypothesize that these data point to a large chemical potential driving force required to diffuse Fc^+ into the nanocrystal. More broadly, these results underscore an important observation that one should not assume uniform and facile diffusion of redox reagents, especially in the context of molecular reactivity, with MOFs in general.

Conclusion

In summary, we demonstrate a reproducible and rapid synthesis towards sub-30 nm MIL-125 nanoparticles at gram scale with excellent solution-processability as membranes. The colloidal stability of these nanocrystals enables rare access to solution-state spectroscopy and electrochemistry as tools for probing the heterogeneous photoredox chemistry of MOFs. These insights offer the first direct evidence of Ti^{3+} trapping, accumulation of numerous charges per cluster, and the redox potentials associated with these processes.

CHAPTER IV

THERMALLY-ASSISTED AND GUEST-INDUCED NUCLEAR MOTION

4.1 Size-Dependent Thermal Shifts to MOF Nanocrystal Optical Gaps Induced by Dynamic Bonding

This section includes an excerpt from Fabrizio, K.; Brozek, C. K. Size-Dependent Thermal Shifts to MOF Nanocrystal Optical Gaps Induced by Dynamic Bonding. *Nano Lett.* **2023.** https://doi.org/10.1021/acs.nanolett.2c04286.

The article was co-written by Kevin Fabrizio and Carl K. Brozek. Kevin Fabrizio and Carl K. Brozek conceptualized the idea. Experiments were performed by Kevin Fabrizio.

Introduction

Optical gaps define the light needed to drive photocatalysis, photovoltaics, photoconductivity, and other optical properties by dictating the minimum energy required to photogenerate an electron-hole pair. Controlling these energies therefore permits thermodynamic optimization of wide-ranging optical processes, from charge transport across semiconductor junctions,[311–313] to product selectivity in photoredox catalysis.[314] Manipulating optical absorption is often achieved through doping, core-shell structures, cation exchange, or simply synthesizing new compositions of commonly studied materials. For example, bulk CdSe exhibits an optical gap of 1.7 eV compared to bulk HgSe, which possesses no optical gap and rather, semimetal-like behavior.[315,316] Over 100,000 distinct structure types of metal-organic frameworks (MOFs) have been reported with a wide range of topologies, metal ions, and organic linkers, offering an extensive platform for studying the relationship between structure and optical absorption.[49,152,317–323]

Rather than prepare entirely new materials, we demonstrated previously that adsorption of redox-inactive metal ions to MOF clusters causes optical gaps to shift by modulating orbital energies.[221] Whereas these techniques still require chemical modification, albeit through post-synthetic methods, external stimuli, such as heat or pressure, could offer contactless methods for controlling MOF optical behavior.

Prior work from our lab has shown that the metal-linker bonds of MOFs exist in a dynamic equilibrium between tightly and loosely bound states.[94,221,324] These flexible bonds can trigger phase changes in MOFs by serving as "soft modes," and help to explain important MOF behavior, ranging from MOF crystal growth mechanisms and post-synthetic exchange to catalysis and MOF melting. As equilibrium species, we expect these bonds to respond to external stimuli because metal ions and linkers dominate frontier orbitals, and because the strength of metal-linker interactions dictate orbital energies. We therefore anticipate MOF optical behavior that can be tuned by altering the equilibrium of metal-linker tight and loose bond configurations.

Particle size offers another important parameter for controlling optical properties without altering the atomic composition of a material. By preparing a semiconductor smaller than its excitonic Bohr radius, the electronic structure undergoes quantum confinement: the electronic bands become discretized into orbitals separated by tens-to-hundreds of millielectronvolts, and the optical absorption and photoluminescence bands narrow and blueshift with smaller particle sizes.[325] Due to the insulating nature of most MOFs, however, quantum confinement is unlikely to occur in MOF nanoparticles (nanoMOFs). By and large, MOF nanoparticles remain unexplored due to synthetic difficulty. Recently, we demonstrated that the semiconductor MOF Fe(1,2,3-triazolate)$_2$ can be prepared

as sizes ranging from hundreds of nanometers to six nanometers—the smallest nanoMOF prepared to-date.[309] These synthetic methods leveraged previous insights into a "seesaw model" of MOF growth that relies on the presence of a molecular additive termed a "modulator".[286,287] Surprisingly, the optical absorption profiles of these nanoMOFs blueshift relative to the bulk spectrum of Fe(1,2,3-triazolate)$_2$ by as much as ∼200 meV, even for particles as large as ∼120 nm. For quantum confinement to cause these size-dependent optical shifts, the excitonic Bohr radius would need to be similarly large, *i.e.*, at least ∼120 nm. This explanation is unlikely given that conventional semiconductors exhibit Bohr radii smaller than 10 nm. While this phenomenon remains actively studied, we surmise that the higher surface-to-volume ratios of smaller particles play an important role in controlling the nanoMOF electronic structure. Despite these promising investigations, the impact of particle size on MOF optical properties remains an open research frontier.

Here, we demonstrate that the optical gaps of common MOFs decrease by hundreds of millielectronvolts at temperatures far below MOF decomposition, in stark contrast to the behavior of conventional semiconductors. Additionally, this temperature response depends strongly on MOF particle sizes, suggesting MOF metal-linker bonds become more flexible with smaller crystallites. These results illustrate the utility of harnessing labile metal-ligand bonds—the basic building block of inorganic structure-function relations—in achieving unprecedent size- and stimuli-dependent properties.

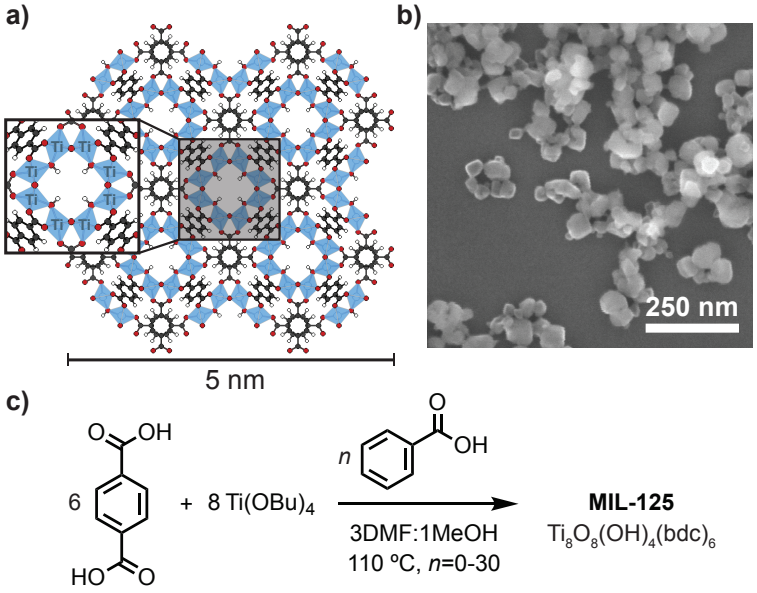

Figure 4.1.1. Synthesis and representations of MIL-125 nanoparticles. **a)** A 5-nm portion of MIL-125, **b)** SEM images of MIL-125 particles with average diameter 79 nm, and c) general synthesis scheme of MIL-125 nanoparticles.

Results and Discussion

To understand the impact of particle size and dynamic bonding on the optical properties of MOFs, we targeted $Ti_8O_8(OH)_4$(terephthalate)$_6$ (MIL-125) due to its frequent use as a sensitizer for photoredox reactivity and because seminal reports of MOF optical properties were first demonstrated with it and related derivatives, such as $Ti_8O_8(OH)_4$(2-amino-terephthalate)$_6$ (MIL-125-NH_2). Following our recently reported reflux-based synthesis,[326] three batches of MIL-125 nanoparticles were prepared with particle sizes controlled by varying the equivalents of benzoic acid, as a modulator, relative to the amount of $Ti(OBu)_4$ precursor (see **Appendix E**). Figure 4.1.1 provides a general synthesis route with representative SEM images and an approximate depiction of a 5-nm MIL-125 particle. After synthesis, the samples were washed thoroughly with fresh *N,N*-dimethylformamide, methanol, and then dried. Detailed synthetic procedures

can be found in **Appendix E**. Phase purity was verified by PXRD analysis (Fig.E.1-E.3 and sizes were determined by SEM (Fig.E.4-E.13. Based on statistical analysis of the SEM images, the resulting batches exhibited averages sizes of 79±18 nm, 215±19 nm, 424±249 nm with dispersity indices of 0.23, 0.32, and 0.59, respectively.

To probe the impact of thermal energy on the optical absorption of MIL-125 nanoMOFs, variable-temperature diffuse-reflectance UV-vis spectra were collected on powder samples of each of the three sizes. Figure 4.1.2 shows the resulting spectra of the materials kept under dynamic vacuum and analyzed between 163 and 523 K. Qualitatively, all three samples exhibit dramatic changes to their absorption profiles with several distinct features: 1) higher temperatures induce the formation of low-energy absorption tails; 2) higher temperatures causes the low-energy peak maxima to redshift; and 3) higher temperatures cause an inversion of the relative intensities of high-energy charge-transfer bands. By contrast, the optical gaps of conventional semiconductors, such as Si and InP, also redshift, but to a much lesser degree.[327] For example, the optical gap of InAs redshifts by ∼80 meV over a 300 K range, whereas the onset absorption of 79-nm MIL-125 particles at 573 K appears nearly ∼2.0 eV below the onset at 163 K. Variable temperature absorption spectra of TiO_2 were collected to investigate the accuracy of these shifts. Consistent with previous reports, a shift of just 60 meV was found between low and high temperatures (Figure E.22). These temperature-induced absorption tails were observed previously for bulk crystals of the family of MOFs known as $Ti_3M_3(\mu^3\text{-}O)_2$(1,3,5-benzenetricarboxylate)$_4$ (M = Ca, Sr, Ba, Cd) (MUV-10). This effect was ascribed to the loose-tight bonding equilibrium of MOFs causing reversible changes to the frontier orbitals.[221] While

drastic changes in absorption tailing often indicate defect creation, these features are reversible across a wide temperature range (Figure E.23). This microscopic explanation of dynamic bonding in MOFs is analogous to the cause of thermal shifts in conventional semiconductors, where higher temperatures weaken the orbital overlap between adjacent atoms, causing orbital splittings to diminish.[328] But whereas the absorption redshifts in semiconductors arise from expansions of lattice constants, the thermal shifts observed for MUV-10 were attributed to thermally induced, albeit reversible, geometric rearrangements. In other words, thermal shifts in conventional semiconductors retain the electronic symmetry of the material, whereas thermal shifts in MOFs involve more severe geometric distortions. This microscopic picture would explain the features in Fig. 4.1.2 because such distortions generate 1) "midgap" orbitals, producing the absorption tails, 2) the rigid shifts to absorption maximum through lattice expansion, and 3) changes to high-energy absorption bands through symmetry-lowered electronic structures.

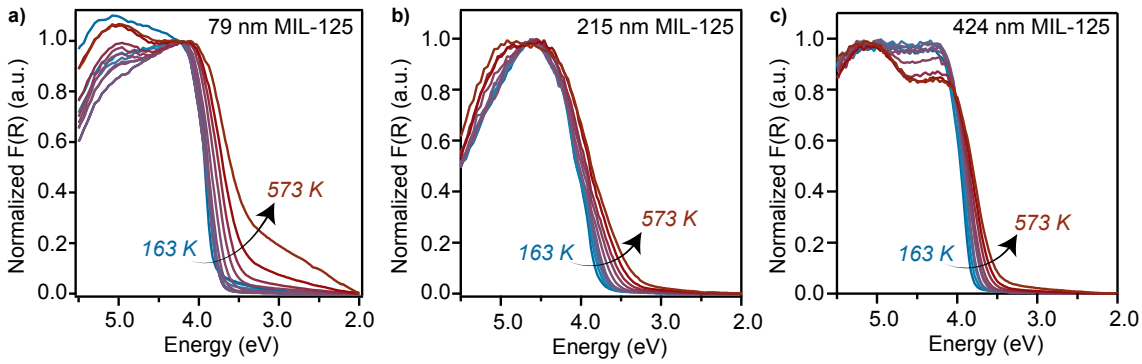

Figure 4.1.2. Variable-temperature diffuse reflectance UV-vis spectra of MIL-125 nanoparticles with diameters a) 79 nm b) 215 nm, and c) 424 nm. All samples were evacuated at room temperature and cooled to 163 K. Spectra correspond to 25 K increments between 163 – 298 K, and 50 K increments between 298 and 573 K.

While all sizes show temperature-dependent absorption profiles, smaller particles exhibit far greater sensitivity to temperature. To understand these size- and temperature-dependent spectral shifts, we sought a model that would provide a microscopic explanation. Seminal studies of temperature-dependent optical gaps were pioneered by Varshni and the phenomenon has since been termed the "Varshni effect" in semiconductors.[327] Although the model developed by Varshni remains in use for quantifying aspects of the temperature dependence, the fitted parameters lack a clear physical meaning. Therefore, we employed an alternative model pioneered by O'Donnell and Chen that employs parameters related to bonding and vibronic interactions (Eq. 4.1).[329]

$$E_{\mathrm{opt}}(\mathrm{T}) = E_0 - S\langle\hbar\omega\rangle\left[\coth\left(\langle\hbar\omega\rangle/2\mathrm{kT}\right) - 1\right] \tag{4.1}$$

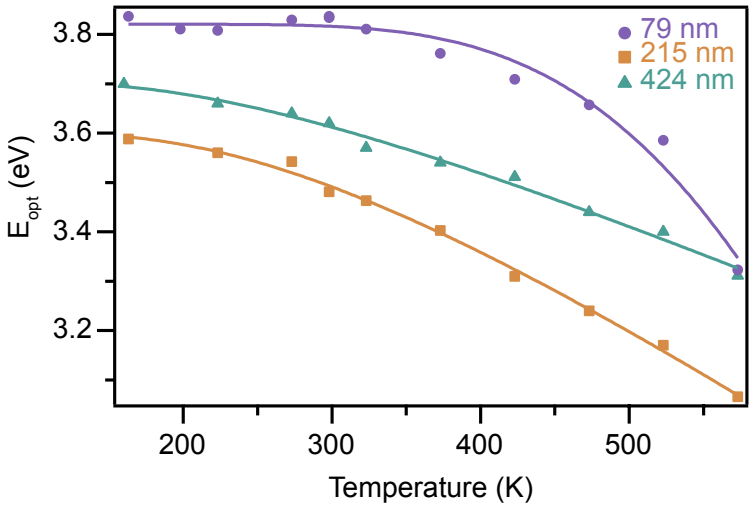

Figure 4.1.3. Optical gaps of MIL-125 nanoparticles plotted versus temperature. Solid lines represent fits based on the O'Donnell and Chen model described in Ref.[329]

To determine the optical gaps (E_{opt}), the spectra in Fig.4.1.2 were fitted through Tauc analysis. Recently, we evaluated different methods of determining

MOF optical gaps and endorsed the Tauc analysis only for MOFs with overlapping optical bands, typically resulting from ligand field transitions or midgap states.[330] Although Gaussian fitting is appropriate for analyzing the MIL-125 spectra at low temperatures where optical bands are clearly distinguishable, Tauc analysis is best suited for the pronounced absorption tails at higher temperatures. Figure 4.1.3 plots the resulting E_{opt} for the 79 nm, 215 nm, and 424 nm particles across all temperatures. Due to the uncertainty inherent in determining E_{opt} by Tauc analysis, we place greater emphasis on temperature-dependence of the values rather than the absolute energies. Fitting these data to the O'Donnell and Chen model produced excellent fits displayed as solid lines in Fig. 4.1.3. As seen in the curvature of the fits, and as reflected qualitatively in Fig. 4.1.2, the smaller particles exhibit the greatest sensitivity to temperature. In this model, E_0 denotes the 0-K E_{opt}, S represents the Huang-Rhys parameter, and $\hbar\boldsymbol{\omega}$ gives the average phonon energy. Chemically, S is a unit-less measure of vibronic coupling and is proportional to the offset in the equilibrium nuclear positions (ΔQ_{i}) between ground and excited state geometries.[331] For typical molecules and semiconductors S < 10, while for ionic solids S > 50.[332,333] Therefore, both $\hbar\boldsymbol{\omega}$ and S indicate the structural flexibility of material because large $\hbar\boldsymbol{\omega}$ implies many vibrational states can be activated at a given temperature, while a large S implies strong vibronic distortions. Table 4.1.1 summarizes the fitting results. Because S dominates the slope of the fit, according to the O'Donnell and Chen model, an inverse relationship between nanoMOF size and S is evident from the data in Fig. 4.1.3. Clearly, the unusually large S values for 79-nm MIL-125 nanoparticles suggest MOF bonding becomes more dynamic with smaller crystallites.

To explore the generality of these size-dependent thermal shifts and their relation to metal-linker bonding, variable-temperature diffuse-reflectance UV-vis spectra were collected on nanoparticles of two distinct classes of MOF materials. Considered among the most stable MOFs, $Zr_6O_4(OH)_4$(terephthalate)$_6$ (UiO-66) and Zn(2-methylimidazolate)$_2$ (ZIF-8) should display less dynamic metal-linker bonding than MIL-125. Additionally, they offer a useful comparison because MIL-125 and UiO-66 have similar metal bonding environments and because ZIF-8 is comprised of metal-azolate, rather than carboxylate, linkages. Following previous reports, 26±3.2 nm, 105±19 nm, and 4.05±0.27 μm (bulk) particles were prepared for UiO-66 and 49±9.7 nm, 205±9.8 nm, and 2.35±0.45 μm (bulk) particles were prepared for ZIF-8 (see **Appendix E**).[334–337] Figures E.17 and E.18 show that the resulting spectra of UiO-66 and ZIF-8 collected under similar conditions to MIL-125. Qualitatively, UiO-66 exhibits greater size- and temperature-dependence than ZIF-8, but less than MIL-125. Table 4.1.1 summarizes fits of the E_{opt} values to the O'Donnell and Chen model. Like MIL-125, smaller particles of UiO-66 show larger S and $\hbar\omega$.

	MIL-125			UiO-66			ZIF-8		
Size (nm)	79	215	424	26	105	4050	49	205	2350
E_0 (eV)	3.82	3.60	3.70	4.12	4.47	4.11	5.30	5.32	5.28
S	89.5	12.7	7.82	11.9	3.45	2.53	0.83	0.59	2.83
$\hbar\omega$ (eV)	0.221	0.075	0.064	0.089	0.078	0.033	0.048	-0.002	0.055
χ^2	7.9e-3	1.0e-3	1.4e-3	9.2e-3	7.5e-3	2.0e-4	2.2e-3	7.9e-5	3.0e-4

Table 4.1.1. Fit parameters derived from fitting temperature-dependent optical gaps for MIL-125, UiO-66, and ZIF-8 nanoparticles to the O'Donnell and Chen Model. E_0, S, and $\hbar\omega$ denote the zero-temperature optical gap, Huang-Rhys parameter, and average phonon energy, respectively.

The smaller absolute values of these parameters corroborates UiO-66 being considered among the most water- and pH-stable MOFs.[338] By comparison, the E_{opt} of bulk and nanosized ZIF-8 show little sensitivity to temperature or size, suggesting greater rigidity of the Zn-imidazolate bonds. To compare the temperature- and size-dependent thermal shifts of all three MOFs, Figure 4.1.4 plots difference spectra defined as the difference between F(R) collected at 473 K and 163 K for each of the bulk and smallest nanoMOF samples. Therefore, positive intensity corresponds to increased absorption at higher temperatures. Inspection of Fig. 4.1.1, E.17, and E.18 suggest that the well-defined bands in Fig. 4.1.4 between 3.0 – 4.0 eV correspond to redshifts to the original HOMO-LUMO absorption profiles, whereas the positive intensity observed between 2.0 – 3.5 eV correspond to the formation of midgap states. Between all samples, MIL-125 showed the largest increase in redshifted band-edge (HOMO-LUMO) absorption. The inset of Fig. 4.1.4 compares the normalized differential absorption onsets between UiO-66 and MIL-125. Interestingly, the nanoparticles of UiO-66 displayed a greater redshift relative to the bulk spectra in comparison to the redshifts of MIL-125. These results suggest that size reduction causes a greater thermal redshift in the band-edge absorption for UiO-66 compared to MIL-125. On the other hand, the main effect of size reduction of MIL-125 is the thermally induced creation of midgap states. For ZIF-8, nanoparticles showed a greater temperature dependence than the bulk material, overall, with a minor increase in absorption intensity near the band-edge around ∼4.0 eV, but differences were less pronounced in comparison to MIL-125 and UiO-66.

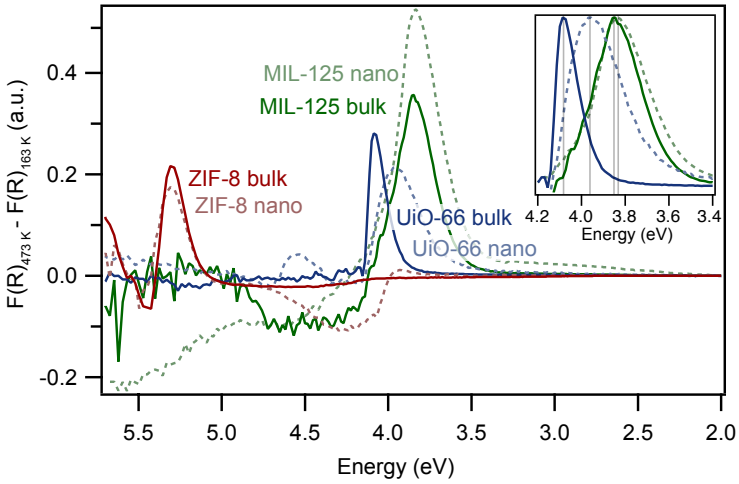

Figure 4.1.4. Temperature-differential UV-vis spectra for bulk and nano-sized MOFs defined as the difference in the Kubelka-Munk functions F(R) recorded at 473 K and 163 K for each material. Data for ZIF-8, MIL-125, and UiO-66 are shown in red, green, and blue, respectively. 50 and 2350 nm ZIF-8, 79 and 424 nm MIL-125, and 26 and 4050 nm UiO-66 were used. Inset: Normalized differential absorption for UiO-66 and MIL-125.

These results for MOF nanocrystals represent an extreme example of temperature- and size-dependent optical behavior observed previously for quantum-confined semiconductor nanocrystals (quantum dots). For example, fitting E_{opt} data for CdTe quantum dots to the O'Donnell and Chen model showed that decreasing particle sizes from 3.6 nm to 2.6 nm caused an increase in S from 1.9 to 2.4 and an increase in $\hbar\omega$ from 12.3 meV to 12.7 meV.[339] This phenomenon has been widely observed for quantum dots and has been attributed to enhanced exciton-phonon interactions in smaller crystallite sizes.[340] Furthermore, theoretical analysis predicts S to be proportional to α^3/V, where a represents the Bohr radius and V the particle volume. Although quantum confinement is unlikely for MOF particles of these sizes, we explored whether the size-dependence of electron-phonon interactions in MIL-125 nanoparticles, S, relates to changes in nanoMOF volumes. Indeed, Fig. 4.1.5a and E.21 show a remarkable correlation between S for MIL-125

and UiO-66 nanoparticles versus inverse particle volumes. We propose that this linear relationship arises from changes to the nature of metal-linker bonding with decreased crystallite sizes, as has been observed in other classes of nanocrystals lacking quantum confinement effects. For example, lattice parameters of metal oxide nanocrystals generally increase in smaller particles. This effect has been ascribed to weaker Madelung fields that create a "negative pressure". In other words, large surface-to-volume ratios decrease the electrostatic stabilization that holds the particles intact and thereby bonding weakens.[341] Similarly, smaller alumina nanoparticles become more compressible,[342] and Si nanocrystals exhibit lower melting point temperatures and smaller bulk moduli.[343] The smaller slope for UiO-66 would therefore imply less flexible bonding compared to MIL-125, further support that UiO-66 is among the most stable MOFs. In conjunction with Huang-Rhys parameter, Figure 4.1.5b highlights the significant increase in average phonon energy as particle diameter decreases in MIL-125. These results highlight an increase in overall lattice vibration frequency, as previously observed in semiconductor nanoparticles.[344] Taken together, these results suggest that the optical absorption of smaller MOF particles display greater temperature dependence due to enhanced bond flexibility.

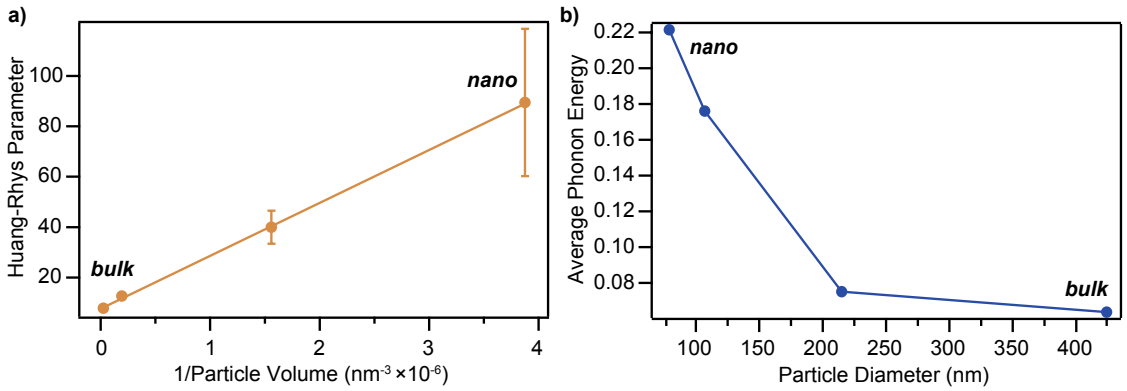

Figure 4.1.5. (a) Huang-Rhys parameters and average phonon energies derived for different MIL-125 sizes plotted against inverse particle volumes and (b) particle diameters, respectively.

Conclusion

This experimental study shows that the optical gaps of the common MOFs MIL-125, UiO-66, and ZIF-8 decrease at elevated temperatures to a far greater degree than conventional semiconductors and that this effect becomes magnified for smaller nanoparticle sizes. Whereas MIL-125 exhibits the greatest sensitivity, ZIF-8 shows the least. Given that UiO-66 and ZIF-8 are considered the among the most stable MOFs, these results suggest a relationship between optical gap thermal shifts to bonding strength. Based on fitting the temperature-dependent optical gaps to a model based on vibronic coupling, these results suggest that MOF metal-linker bonding becomes more dynamic and flexible with smaller particle sizes, allowing control over optical behavior difficult to achieve with other classes of molecules and materials.

4.2 Guest-Dependent Bond Flexibility in UiO-66, a "Stable" MOF

This chapter includes an excerpt from Fabrizio, K.; Andreeva, A. B.; Kadota, K.; Morris, A. J.; Brozek, C. K. Guest-Dependent Bond Flexibility in UiO-66, a "Stable" MOF. *Chem. Commun.* **2023.** https://doi.org/10.1039/D2CC05895B.

The article was co-written by Kevin Fabrizio, Carl K. Brozek, Kentaro Kadota, and Amanda J. Morris. Anastasia B. Andreeva, Kevin Fabrizio, and Carl K. Brozek conceptualized the idea. Experiments were performed by Kevin Fabrizio and Anastasia B. Andreeva, and analysis was performed by Kevin Fabrizio.

Labile metal-ligand bonds drive important phenomena of both molecules and materials. In molecules, labile bonding gives rise to ligand exchange and the creation of open metal sites that enable catalysis,[345] whereas in materials, they cause vibronic interactions that strongly influence myriad magnetic, optical, and electronic properties.[346] Polaronic charge transport, Stokes shifts caused by self-trapped excitons, and structural phase changes induced by Peierls distortions exemplify the important role of structural dynamics. Soft modes comprise a special family of dynamic interactions, whereby particular vibrations trigger phase transitions by displacing atomic positions from one phase into the positions of the other phase.[347]

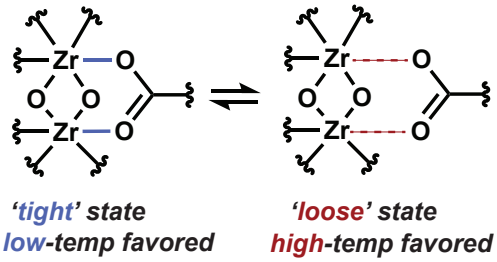

Figure 4.2.1. A portion of the UiO-66 metal node, illustrating the dynamic equilibrium between ensembles of Zr-linker species existing as either tightly or loosely bound states.

The melting mechanism of many materials, for instance, involves vibrations that exceed the Lindemann ratio between the atomic displacement of a vibration and the nearest-neighbor distances that otherwise remains constant at around 0.1 for many stable phases.[348] While soft modes, and vibronic interactions in general, have been intensely studied for conventional solid-state materials, such as binary lattice semiconductors, their role in materials with more complex compositions remains an open frontier. For example, recent studies reveal that vibronic interactions explain important emergent properties of hybrid perovskites.[349,350]

Despite crystal structures that suggest rigid and static bonding, recent evidence has shown that metal-linker bonds in metal-organic frameworks (MOFs) are dynamic. We demonstrated through variable-temperature diffuse reflectance Fourier transform spectroscopy (VT-DRIFTS) that metal carboxylate and metal-azolate bonds in many common MOFs exist in an equilibrium between tightly and weakly bound configurations, as shown in Figure 4.2.1.[94,324] As a result, the MOF bonding environment straddles two shallow potential-energy surfaces that shifts towards bond dissociation at high temperatures. The vibrations associated with these dynamic bonds exhibit the hallmark characteristics of soft modes, *i.e.*, frequencies that redshift close to T_c of a phase transition, due to the vibration

dissipating its energy to the lattice through anharmonic coupling. Dynamic metal linker bonds help explain many curious MOF properties.[351,352] For example, we demonstrated that the metal-triazolate bonds in the isostructural family of MOFs termed M(1,2,3-triazolate)$_2$ (M = Mn, Fe, Co, Cu, Zn, Cd) are labile and consequently serve as soft modes that trigger the unusually cooperative spin crossover transition in the Fe variant and the structural phase change in the Cu analog.[324] Dynamic bonding would also explain the ability of MOFs to undergo post-synthetic linker and cation exchange.[86,87,353] Labile metal-linker bonding could also explain how MOFs with metal sites that seem coordinatively saturated catalyze chemical transformations that require open metal sites.[354–356] The equilibrium constants of the reversible binding and unbinding of metal-linker bonds, termed stability constants, offer a quantitative measure of the microscopic aspects of bond dynamics. Previously, we reported a thermodynamic parameter akin to stability constants, defined as the ratio of "tight" and "loose" states. This quantity, which we term "flexibility constants", X, represent a thermodynamic equilibrium bonding mixture, X =([tight]/[loose]), as opposed to an equilibrium constant for the formation/dissociation of bonds, as for stability constants. Previous analysis of VT-DRIFTS data revealed that Cu$_3$(1,3,5-benzene tricarboxylate)$_2$, (CuBTC), the prototypical carboxylate MOF, and M(1,2,3-triazolate)$_2$ exhibit surprisingly small flexibility constants given the absence of solvent, and compared favorably to stability constants of molecular analogs.[357]

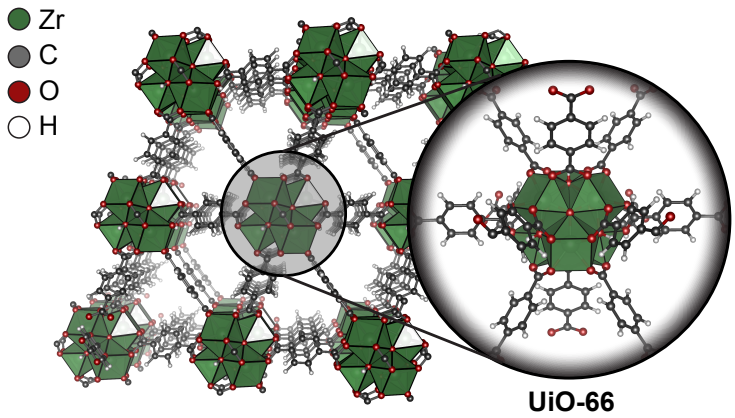

Figure 4.2.2. Representation of the crystallographic structure of UiO-66 prior to dehydration. The Zr-oxo node is highlighted.

Here, we report the flexibility constants of UiO-66 ($Zr_6O_4OH_4$(1,4-benzenedicarboxylate)$_6$), a particularly "stable" MOF, extract thermodynamic parameters of the dynamic bonding equilibrium through a modified van't Hoff analysis designed for phase change systems, and show that the material is surprisingly dynamic.[358] These values provide a framework for understanding the chemical stability of MOFs, and for predicting and rationalizing behavior that involves dynamic bonding. Furthermore, these results reveal the sensitivity of the metal-linker dynamics to guest molecules, providing microscopic insight into the bonding equilibrium, and reveal an unexpected but important guest-host interaction relevant to the use of MOFs in gas capture and separation technologies.

The unusual pH- and water-stability of UiO-66 and related MOFs with zirconium oxo clusters has been attributed to robust Zr-O bonds, and yet our previous analysis hinted at metal-linker bond dynamics comparable to MOF-5 and other less stable MOFs. In a prior report, redshifting carboxylate stretches were evidenced by VT-DRIFTs for these and other common MOFs and were interpreted as thermal population of an ensemble of "loose" states that could

be reversibly cycled, suggesting an equilibrium process akin to phase changes.[94] The red-shift slopes, χ, provided a quantitative measure of the "softness" of the carboxylate stretches, with steeper slopes indicating weaker bonding. Whereas MOF-5 displayed an asymmetric χ of –0.02 cm^{-1}/K, UiO-66 showed a comparable slope of –0.015 cm^{-1}/K, also consistent with the other surveyed carboxylate MOFs. Given the apparent discrepancy between the chemical stability of UiO-66 and evidence for dynamic Zr-O bonding, we reinvestigated the thermodynamic details of metal-linker lability in UiO-66 in comparison to less stable carboxylate MOFs.

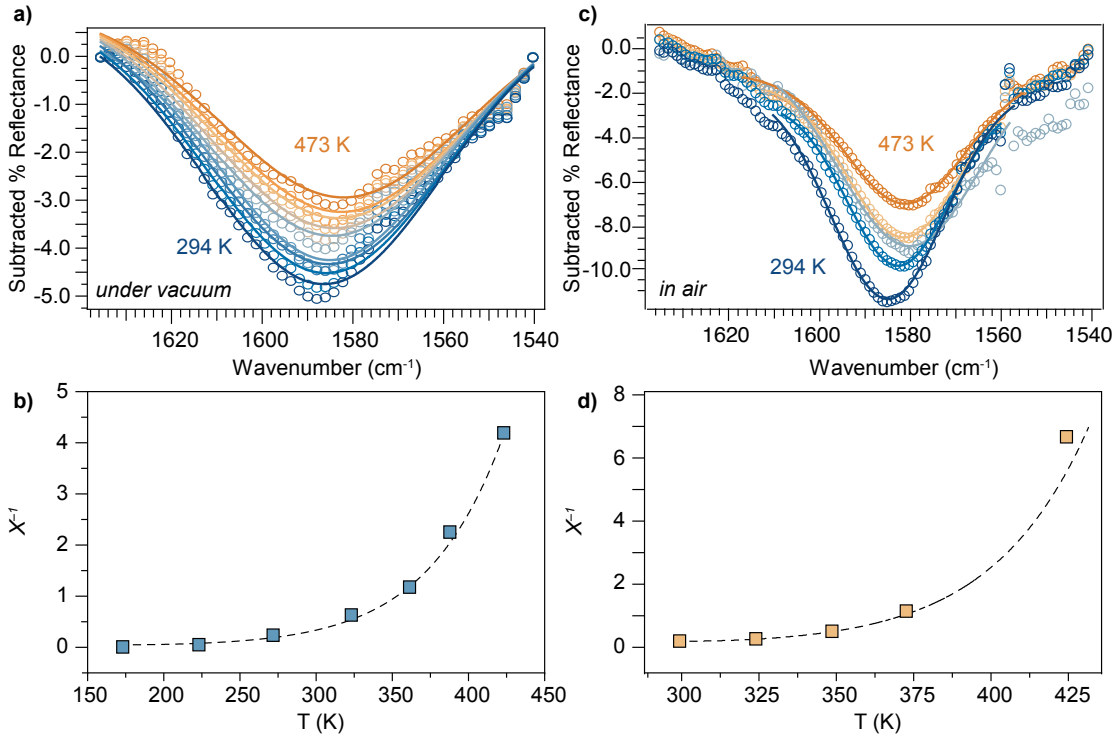

Figure 4.2.3. (a) Subtracted reflectance VT-DRIFTS of the UiO-66 asymmetric stretch under dynamic vacuum. (b) Modified van't Hoff plot of the asymmetric stretch of UiO-66 under dynamic vacuum. (c) Subtracted reflectance VT-DRIFTS of the asymmetric stretch of UiO-66 in air. (d) Modified van't Hoff plot of the asymmetric stretch of UiO-66 in air. X^{-1} denotes inverse flexibility constants [loose]/[tight]. Data were fitted to $X^{-1} = \exp[-(\Delta H + \Delta C_P(T - 298.15\ K) - T(\Delta S + \Delta C_P \ln(T/298.15\ K)))/RT]$.

Following a modified procedure,[335] bulk powder of UiO-66 was prepared, washed, and activated prior to analysis. Figure 4.2.2 depicts the octahedral Zr-oxo clusters held together by Zr- carboxylate moieties at the focus of this report. To interrogate the lability and thermodynamics aspects of the Zr-linker bonding in UiO-66, we employed VT-DRIFTS. Figure 4.2.3 summarizes the temperature dependence of the asymmetric carboxylate stretch of UiO-66 under dynamic vacuum and in air. Figure 4.2.3a shows the baseline-subtracted VT-DRIFTS spectra of UiO-66 collected between 294 K and 473 K under dynamic vacuum. The peak maxima redshift from 1589 cm^{-1} to 1586 cm^{-1} over this temperature range, consistent with a previous report that the Zr-carboxylate bonds weaken at higher temperatures by favoring the "loose" state conformation in a dynamic bond equilibrium.[94] Interestingly, the full-width-at-half-maximum (FWHM) values of the asymmetric stretch decreases across the measured temperature range (294 – 473 K, Figure F.7). Based on our earlier work, the observation of an increase and decrease in FWHM across low (< 294 K) and high (> 294 K) temperatures strongly implies the co-exist of two species in equilibrium and in nearly 1:1 mixtures at intermediate temperatures. Peak asymmetry across temperature ranges has been described in detail for other MOF systems by Andreeva and coworkers.[94,324] Rather than consider the exact metal-carboxylate configuration in the system, the equilibrium model estimates the population of two shallow potential energy surfaces that are more "tight" or "loose." Thus, fitting these spectra to a two-Gaussian model produces relative ratios of the "tight" and "loose" species, *i.e.*, the flexibility constant, at each temperature. Global fitting examples are provided in **Appendix F**. Any Gaussian fit that was below an R^2 value of 0.990 was considered unsuitable and not used in the calculation of X. Flexibility

constants (X) reflect the equilibrium ratio of the population of bound and unbound ([bound]/[unbound]) species for a given metal-ligand bond, in an analogous fashion to the definition of stability constants. We derive the inverse flexibility constant, X^{-1}, from the ratio [loose]/[tight] extracted from the relative population ratios through Gaussian fitting. Figure 4.2.3b plots X^{-1} versus temperature for UiO-66 under dynamic vacuum derived from the asymmetric carboxylate stretch. The room temperature value of X corresponds to $\ln X = 1.84$ which compares well to stability constants reported for molecular metal carboxylate species.[357] Consistent with our previous analysis of CuBTC, we interpreted these data using a modified van't Hoff plot intended for phase change systems,[358] due to the soft mode nature of these vibrations. This fitting produces an excellent agreement, with $\Delta H = 17$ kJ mol^{-1}, $\Delta S = 48$ J mol^{-1}, and $\Delta C_p = 80$ J mol^{-1} K^{-1}. Consistent with UiO-66 being chemically robust, it possesses larger flexibility constants and larger endothermic enthalpy barriers than reported previously for CuBTC or M(1,2,3-triazolate)$_2$ MOFs.[94,324] And yet, a $\ln X$ of 1.84 is lower than stability constants reported for coordination polymers, including metal-carbene and metal-pyridyl materials known to exhibit self-healing behavior.[359,360] As reference, a table of stability constants for these materials is provided in **Appendix F** (Table F.4). In comparison to the $\Delta S = 22.0$ J mol^{-1} K^{-1} of CuBTC the larger entropy term of UiO-66 suggests a bigger difference in the number of microstate metal-linker bond configurations between the "tight" and "loose" states, while the comparatively large ΔC_p implies that the conversion into the "loose" state involves more degrees of freedom than the corresponding process for CuBTC. Because MOF applications, ranging from gas separations to catalysis, involve the presence of guest molecules, we explored the metal-linker equilibrium in air. Figure 4.2.3c plots the

baseline-subtracted asymmetric carboxylate stretch in air between 294 K – 473 K. Remarkably, the peak maxima redshift increases in slope from –0.015 to –0.051 cm^{-1} K^{-1}. This slope, the largest yet observed for a MOF, suggests the presence of guest molecules favor the "loose" state bond conformations. Evidence abounds that guest molecules, as innocuous as N_2, interact with MOF metal nodes.[361,362] Given the composition of air, we assume that the interaction involves water molecules and, to a lesser extent, CO_2 and N_2, which both possess large quadrupole moments,[363,364] and, hence, high polarizability. Figure 4.2.3c plots the shifting asymmetric stretch in the presence of air. To avoid moisture condensation, 300 K was the lowest temperature employed. Global fitting analysis of these data indicate that the presence of air favors the "loose" state more than in vacuum, with larger $\ln X^{-1}$ values observed at each temperature. The corresponding van't Hoff analysis produces ΔH = 15 kJ mol^{-1}, ΔS = 32 J $mol^{-}1$, and ΔC_p = 220 J mol^{-1} K^{-1}. While the enthalpic barrier and entropic driving force are similar in magnitude, albeit smaller, than in vacuum, the change in specific heat is significantly larger. We propose that the bond equilibrium process involves greater degrees of freedom when in air, suggesting the participation of N_2, CO_2, and H_2O.

Solvent	Asymmetric peak (cm^{-1})	ln$X$ [asymmetric]
Vacuum	1589	1.8(4)
Air	1589	1.7(3)
N_2	1589	1.6(6)
THF	1587	1.3(9)
DMF	1585	0.85(8)
EtOH	1581	0.50(5)
H_2O	1579	0.04(0)
Et_3N	1577	-0.61(7)

Table 4.2.1. Environment-dependent flexibility constants at room temperature (lnX when X = [tight]/[loose] of the asymmetric carboxylate stretch in UiO-66.

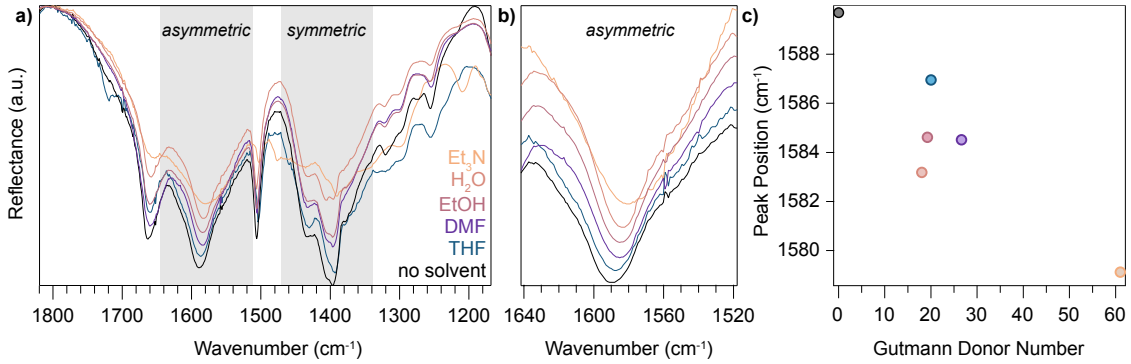

Figure 4.2.4. (a) Solvent-dependent VT-DRIFTS of UiO-66 displaying asymmetric and symmetric carboxylate stretch. (b) Highlighted portion of the spectra demonstrating the shift in the asymmetric stretch with each solvent. (c) Correlation plot between asymmetric stretch peak position versus Gutmann donor number for each solvent.

Given this evidence that UiO-66 metal-linker bonds destabilize in the presence of air, we explored the effect of solvent. Specifically, guest molecules were targeted for their Lewis and Brønsted basicity, given that the interaction with air likely involves water molecules associating to metal sites, promoting metal-linker bond weakening. Figure 4.2.4 shows DRIFTS spectra of UiO-66 soaked

with different solvents and collected at 298 K, with the evacuated material plotted for comparison. The addition of all solvents, Et_3N, H_2O (pH 7), EtOH, DMF, and THF, induced significant redshifts to both the asymmetric and symmetric peak maxima. Despite studies of UiO-66 structurally degrading under extremely basic/acidic conditions,[365] we observe the MOF retains crystallinity over a 3-hour time period exposed to Et_3N, which exceeds the duration of VT-DRIFTS data collection (Figure F.6). Solvent-dependent stability constants have been reported previously, notably for multi-dentate ligands, with water being highly effective at promoting metal-ligand bond cleavage.[366] Gutmann donor numbers also provide a convenient metric for understanding the redshifting trends by quantifying Lewis basicity.[367] With the largest donor number, at 61, Et_3N likely promotes the "loose" state by attacking the Zr centers. This microscopic picture is further demonstrated by the negative flexibility constant, $\ln X$, for Et_3N, -0.61. The remaining solvents have donor numbers between ∼20-30 whose flexibility constants scale with increasing donor number. Figure 4.2.4c illustrates the apparent correlation between the peak position of the asymmetric stretch and the donor number of the guest solvent. Table 4.2.1 summarizes the solvent-dependence of UiO-66 metal-linker dynamics. The solvents that induce the greatest redshifts also cause the smallest flexibility constants, $\ln X$. Remarkably, these data suggest strongly binding solvents, such as H_2O and Et_3N, destabilize MOF metal-linker bonding to such a degree that the loose states begin to dominate the coordination environments even at room temperature. We attribute the strong effect of water to its high molar volumetric density and its strong ability to engage in hydrogen bonding, to which the metal-oxide clusters of a MOF are highly susceptible.

In conclusion, through analysis of VT-DRIFTS and by fitting the spectra to a two-state equilibrium model of "tight" and "loose" bond conformations, flexibility constants, comparable with metal-linker stability constants of metal complexes, could be determined for UiO-66, the prototypical "stable" MOF. Employing a modified van't Hoff analysis of these data suggests the chemical stability of UiO-66 and its higher stability constants arise from the "loose" state bearing similar bond enthalpies and entropies to the "tight" state favored at lower temperatures. These values are comparable to metal-carboxylate stability constants reported for molecular and polymeric materials and become more labile in the presence of gas-phase and liquid guest molecules. These results provide quantitative tools for rationalizing previous phenomena of MOFs and for harnessing their labile bonding.

CHAPTER V

CONCLUDING REMARKS

This dissertation presents three approaches to induce nuclear motion in metal–organic frameworks (MOFs), the effects on electronic structure, and namely, the potential for photocatalytic applications.

In Chapter II, we investigated the effect of redox-inactive cations installed on the interior and the exterior of the MOF MUV-10(M), and determined that through structural frustration of the heterometallic nuclear cluster, the catalytic redox potentials were significantly affected. Through this study, we identified a critical barrier in the field of MOF photocatalyst design and solved this by developing a method to determine optical band gap energies using simple spectroscopic and analytical techniques. Furthermore, through a synergistic computational-experimental study, we studied the loading of protons and electrons on an archetypal MOF photocatalyst, MIL-125, to assess the thermodynamic limit of photoelectrochemical 'doping' in this material. Similar to the first study, we discovered that this limit is not only defined by redox-active metal sites within the MOF, but by inorganic inner-sphere Lewis basic ligands within the MOF nodes. In Chapter III, synthetic parameters are meticulously defined to produce nano-scale MOF photocatalysts, and for the first time, solution-state spectroscopic techniques can be used to study the mechanism of charge storage. We further showed that the MOF photocatalysts can be easily fabricated into mixed-matrix membranes (MMMs) and that their catalytic activity remained intact. In Chapter IV, temperature is employed to study optical band gap shifts to MOF nanocrystals, and it is found that MOF electronic structures are deeply coupled to crystal size through reversible metal-linker bond flexibility. We apply a general model to

describe the electron-phonon coupling in a series of MOFs and MOF crystal sizes, paving the way for industrial photocatalyst application. Lastly, we established "flexibility constants," akin to classical stability constants, to describe the extent of reversible metal-linker bond flexibility in MOFs, and studied the impact of guest molecules on these constants. We found that strongly binding guest molecules destabilize the "tight" and "loose" bond equilibrium, which ultimately defines the ambient environment necessary for harnessing nuclear motion in photocatalytic applications.

Taken together, these findings demonstrate the potential for using nuclear motion in MOFs for photocatalytic applications. To summarize, through the various studies presented in this dissertation, we have identified key factors that affect the electronic structure of MOFs and have developed methods for inducing nuclear motion in these materials. We have also shown that by controlling the size and structure of MOFs, it is possible to tune their electronic properties and optimize their photocatalytic activity. Additionally, our work has highlighted the importance of considering the role of guest molecules in the design and optimization of MOF-based photocatalysts.

The use of nuclear rearrangement in MOFs for photocatalytic applications represents a promising avenue of research, with the possibility to revolutionize photocatalyst design. However, several challenges must be overcome to fully realize this potential. Firstly, the precise control and optimization of nuclear motion in MOFs is crucial for achieving high photocatalytic activity and improved charge separation capabilities. While in most cases metal-linker flexibility is reversible, studies on maintaining bond elongation and contraction for extended periods of time must be conducted. Moreover, further studies are required to understand the

underlying mechanisms of nuclear motion in MOFs and to develop strategies for its precise control. Secondly, the mechanism of charge storage and transfer across a locally distorted MOF is not fully understood. Further research is needed to understand if charge carrier recombination is affected by this phenomenon. Lastly, the stability and durability of MOFs that utilize nuclear motion must be improved to make them suitable for practical applications. While we have explored the effects of nuclear motion under relatively mild conditions (temperature, pH, pressure), experiments must be conducted at extreme temperatures or UV-light exposure. Consequently, developing methods for stabilizing these materials against self-degradation and reactants is crucial for their long-term stability. With continued research and development, MOFs that utilize reversible nuclear motion have the potential to be a transformative technology in the field of photocatalysis.

APPENDIX A: SUPPLEMENTARY INFORMATION FOR CHAPTER 2.1

Experimental Methods

Materials. All commercial chemicals were used as received unless stated otherwise. Calcium chloride dihydrate (Malinnckrodt), barium chloride dihydrate (Baker), strontium chloride hexahydrate (Baker), cadmium chloride hemi(pentahydrate) (Mallinckrodt), manganese(II) chloride tetrahydrate (ACS grade, Baker), glacial acetic acid (ACS grade, Fisher Scientific), N,N-dimethylformamide (DMF, ACS grade, Fisher Scientific), 1,3,5-benzenetricarboxylic acid (trimesic acid, 98%, TCI America), titanium (IV) isopropoxide (97%, Sigma Aldrich), bis(pentamethylcyclopentadienyl) iron (decamethylferrocene, Me_10Fc, 99%, Strem), acetonitrile (MeCN, ACS grade, Fisher Scientific), hexanes (ACS grade, Fisher Scientific), fluoroboric acid (HBF_4, 48% w/w aq soln, Oakwood), and nitric acid (67-70% ARISTAR® PLUS for trace metal analysis, VWR).

Characterization. Sample purity was verified by powder X-Ray diffraction (PXRD) with a Bruker D2 Phaser benchtop diffractometer. Variable-temperature diffuse reflectance UV-vis spectroscopy (VT-DRUV-vis) was performed on a Perkin Elmber Lambda 1050 UV/Vis/NIR spectrometer, with a 150 mm InGaAs integrating sphere in the range of 2000-200 nm paired with a Harrick Scientific Praying Mantis Diffuse Reflection (DRP) accessory. A Harrick Scientific Low Temperature Reaction Chamber (CHC) that enabled introducing vacuum and heat to the sample was equipped with UV quartz. To ensure adequate absorbance, all samples were diluted with ground $BaSO_4$. IR spectra were collected on a Bruker Alpha II with an ATR attachment in a nitrogen filled glovebox and a Nicolet 6700 FT-IR spectrometer with an ATR attachment in open air. Nitrogen (N_2)

adsorption/desorption isotherms were obtained at 77 K using a Micromeritics ASAP 2020 surface area analyzer. Specific surface areas (SBET) of the samples were calculated using Brunauer-Emmett-Teller (BET) theory, unless otherwise stated. Prior to gas sorption measurements, samples were soaked twice with 20 mL DMF, acetone, methanol, and then hexanes for 12 hours each, and the washed sample was collected by centrifugation. Finally, the samples were dispersed in ca. 3 mL hexanes and dried at room temperature under vacuum for 18 hr. Prior to analysis, the samples were activated at 403 K for at least 24 hours to remove solvent and trapped gas. Activation was considered complete when the outgassing rate fell below 2.5 μtorr min^{-1}. Sample masses were then determined as the difference in mass between the empty sample tube and the loaded sample tube post-activation. ICP-MS was performed on a Thermo iCAP ICP-MS on samples dispersed in 2% HNO_3 using yttrium as an internal standard. XPS was performed on a ThermoScientific ESCALAB 250 X-ray Photoelectron Spectrometer.

Computational Methods

Density Functional Theory (DFT) calculations were performed to identify the density of states (DOS) and band gap energy (E_g) of MUV-10 (M) derivatives, in addition to different hydration states and cation localization on the MOF cluster.

All MOF structures were geometrically optimized with PBEsol[368] in VASP[369–371] and a 500 eV planewave cutoff basis set. A Γ-only k-grid was converged to ionic and electronic criteria of 0.005 eV and 1×10^{-6} eV, respectively. The HSEsol06 (PBEsol + 25% HF) level of theory, with a Γ-only k-grid and the same convergence criteria as above, was used to recover more accurate band gap energies. Parent structures and hydrogen-functionalized structures were fully optimized and aligned to the vacuum level using a previously reported method.[217]

Proton-functionalized structures were fully optimized and aligned to the vacuum level of the parent scaffold. In the transmetallated structures, all Ca atoms in the unit cell were exchanged for the respective metal before a full optimization. For the hydrogen functionalized structures, one inorganic oxo in the unit cell was functionalized with a hydrogen atom. The same procedure was followed for the proton functionalized structures, with one electron removed from the unit cell to constitute the addition of a proton. Manganese and cadmium structures were converged with H_2O coordinated solely to titanium at the nodes. The manganese-substituted parent scaffold was found to have lower energy in the antiferromagnetic state, and so the electronic structures of all manganese substituted derivatives were calculated in the antiferromagnetic state after geometric optimization.

Creation of open metal sites and DMF binding experiments

Removal of terminal H_2O ligands was performed by charging a Schlenk flask with ca. 20 mg of each of the MUV-10(M) derivatives and heating it at 180 ^{o}C under reduced pressure overnight. The flask was then transferred in the glovebox, where dry DMF was added and the solid was left to soak in dry DMF overnight. The next day, the off-white solid was recovered with vacuum filtration in the glovebox, quickly washed twice with methylene chloride and left to dry. The IR spectra of the vacuum/heat dried solid and the DMF-soaked one were collected in a N_2 filled glovebox.

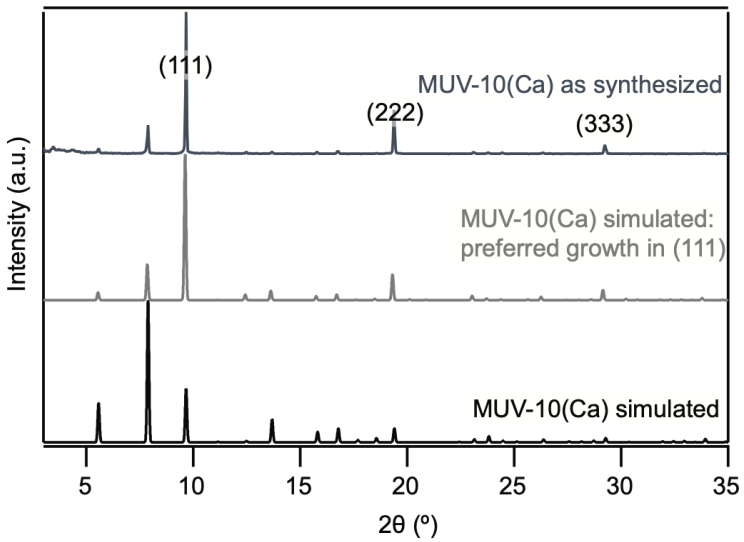

Figure A.1. PXRD of MUV-10(Ca) simulated based off an unaltered crystal structure, preferred growth of the (111) facet, and MUV-10(Ca) as synthesized.

X-ray Fluorescence Spectrometry

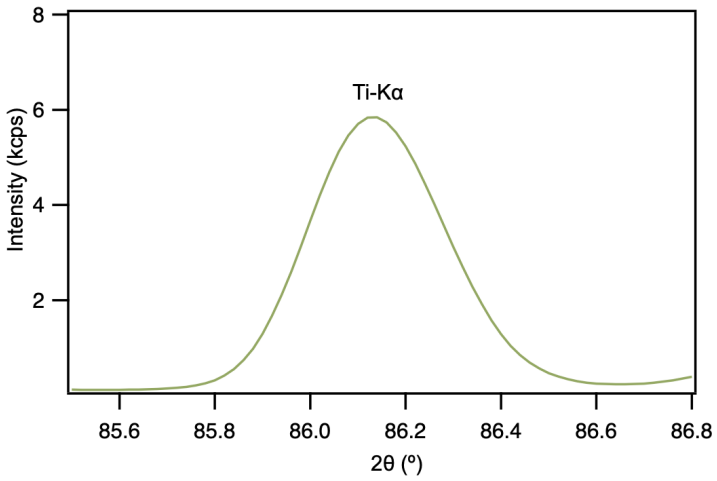

Figure A.2. XRF Ti scan MUV-10 (Ba) after solvent exchange and activation at elevated temperatures.

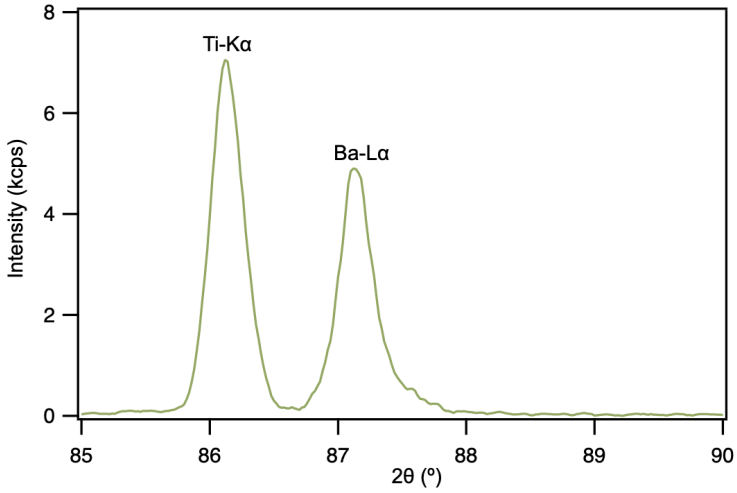

Figure A.3. XRF Ba scan for MUV-10 (Ba) after solvent exchange and activation at elevated temperatures.

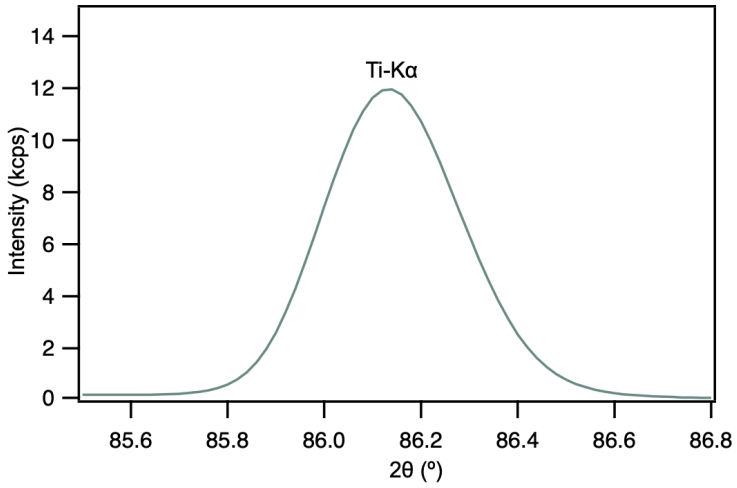

Figure A.4. XRF Ti scan for MUV-10 (Sr) after solvent exchange and activation at elevated temperatures.

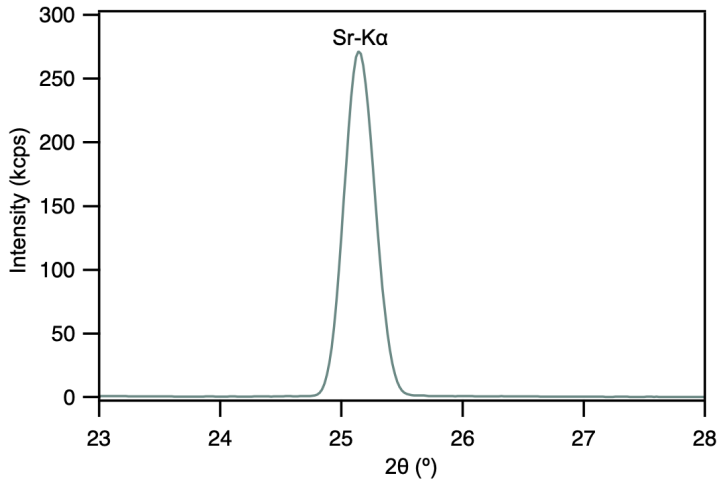

Figure A.5. XRF Sr scan for MUV-10 (Sr) after solvent exchange and activation at elevated temperatures.

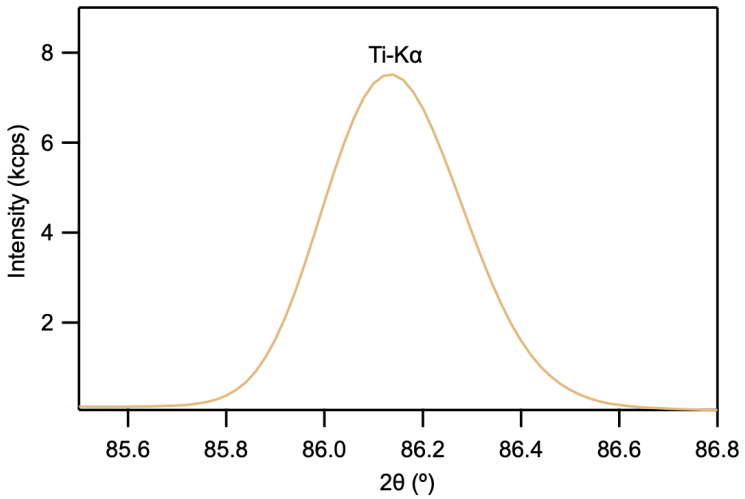

Figure A.6. XRF Ti scan for MUV-10 (Cd) after solvent exchange and activation at elevated temperatures.

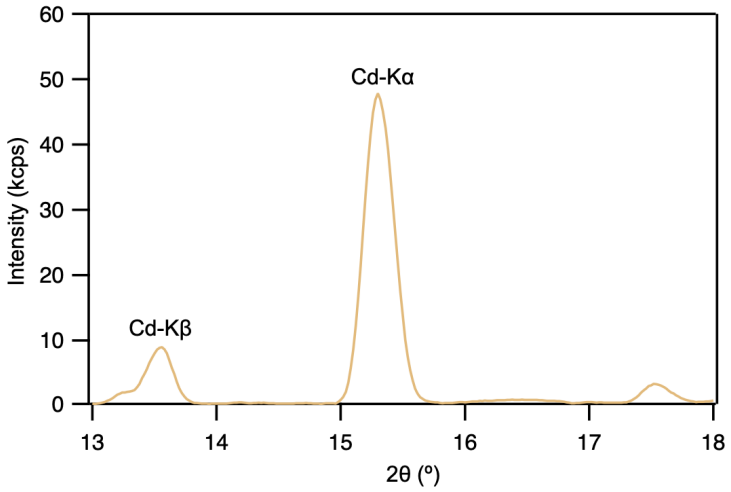

Figure A.7. XRF Cd scan for MUV-10 (Cd) after solvent exchange and activation at elevated temperatures.

Compound	a=b=c (Å)	V (Å^3)	DFT a=b=c (Å)	DFT V (A3)	Castells-Gils et. al. a=b=c (Å)	Castells-Gils et. al. V (Å^3)
MUV-10(Ca)	15.8403	3974.55	15.9060	4024.22	15.8172	3957
MUV-10(Mn)	15.6208	3811.62	15.6370	3823.46	15.6330	3820
MUV-10(Ba)	16.0583	4140.91	16.2615	4300.13	-	-
MUV-10(Sr)	15.9618	4066.76	16.1115	4182.20	-	-
MUV-10(Cd)	15.7229	3886.68	15.8313	3967.84	-	-

Table A.1. LeBail refinement unit cell parameters of all MUV-10(M) derivatives, compared with computationally optimized geometries and originally reported unit cell parameters derived from single crystal crystallographic information. LeBail refinements were carried out on powder XRD samples using the EXPO2014 software package.

Compound	Cell V (Å^3)	Structure V (Å^3/%)	Solvent Accessible V (Å^3/%)
MUV-10(Ca)	4024.2	1829.4/45.5	2194.8/54.5
MUV-10(Mn)	3823.5	1796.7/46.9	2031.8/53.1
MUV-10(Ba)	4300.1	2123.1/49.4	2177.0/50.6
MUV-10(Sr)	4182.2	2093.3/50.1	2088.9/49.9
MUV-10(Cd)	3967.8	1824.2/46.0	2143.6/54.0

Table A.2. Porosity of all MUV-10(M) derivatives as estimated from PLATON v 260421, build date Apr. 26 2021, using the SOLV subroutine to approximate solvent accessible pore volume.

X-ray photoelectron spectroscopy

Sample	Average Binding Energy (eV)	Ratio Ti^{4+}:M^{2+}
MUV-10(Ba)	Ba 780 ± 0.4, Ti 458.5 ± 0.3	2.2 ± 0.2
MUV-10(Sr)	Sr 133.1 ± 0.3, Ti 458.6 ± 0.1	3.0 ± 0.2
MUV-10(Cd)	Cd 405.4 ± 0.1, Ti 458.8 ± 0.1	1.4 ± 0.0

Table A.3. X-ray photoelectron spectroscopy (XPS) for MUV-10(M) derivatives

Inductively coupled plasma mass spectrometry

Sample	Ti (ppm)	Sr (ppm)	Cd (ppm)	Ba (ppm)	Ratio Ti:M (mol)
MUV-10(Ba)	0.829	0.000	0.002	0.794	2.98
MUV-10(Sr)	0.273	0.592	0.000	0.000	0.85
MUV-10(Cd)	0.226	0.000	0.469	0.001	1.12

Table A.4. Inductively coupled plasma mass spectrometry (ICP-MS) for MUV-10(M) derivatives

Diffuse Reflectance UV-vis Spectroscopy

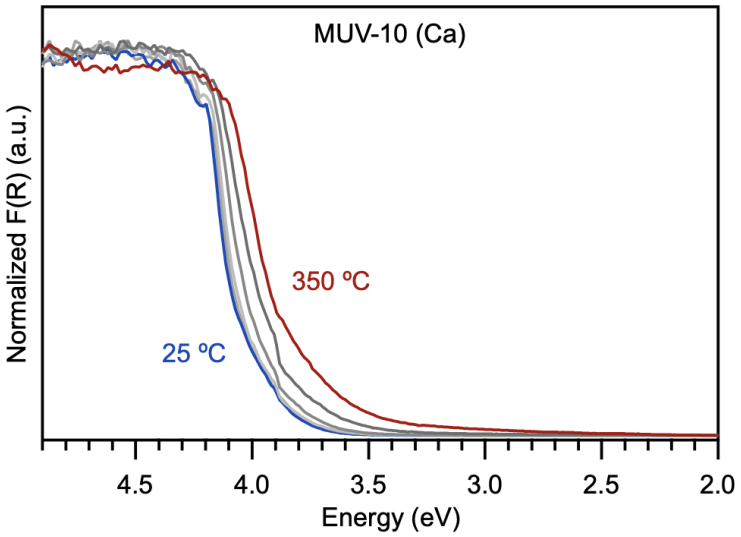

Figure A.8. In situ UV-vis spectra of MUV-10 (Ca) heated to 25 ºC, 100 ºC, 200 ºC, 300 ºC, and 350 ºC under dynamic vacuum.

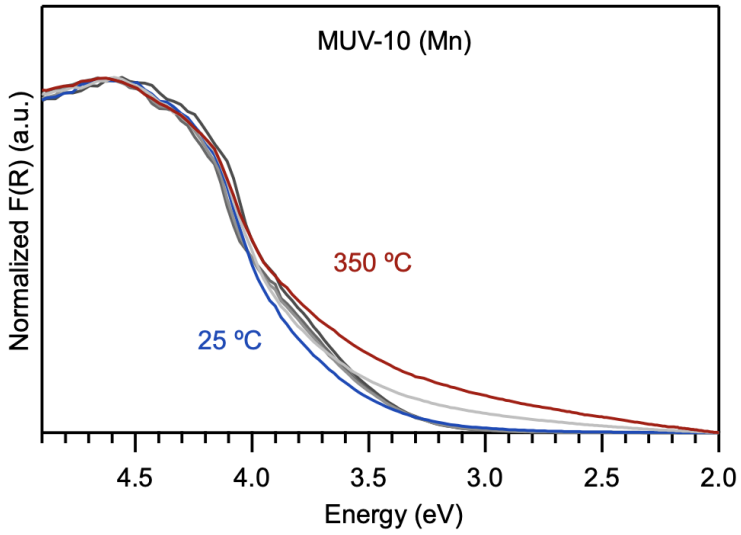

Figure A.9. In situ UV-vis spectra of MUV-10 (Mn) heated to 25 ºC, 100 ºC, 200 ºC, 300 ºC, and 350 ºC under dynamic vacuum.

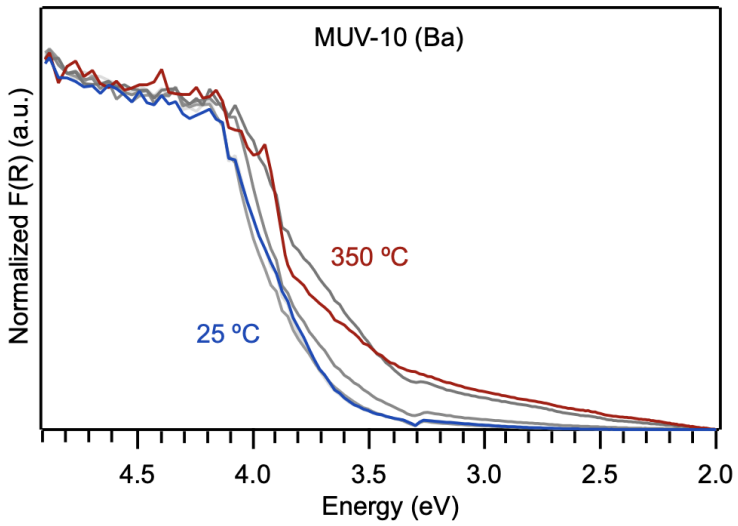

Figure A.10. In situ UV-vis spectra of MUV-10 (Ba) heated to 25 ºC, 100 ºC, 200 ºC, 300 ºC, and 350 ºC under dynamic vacuum.

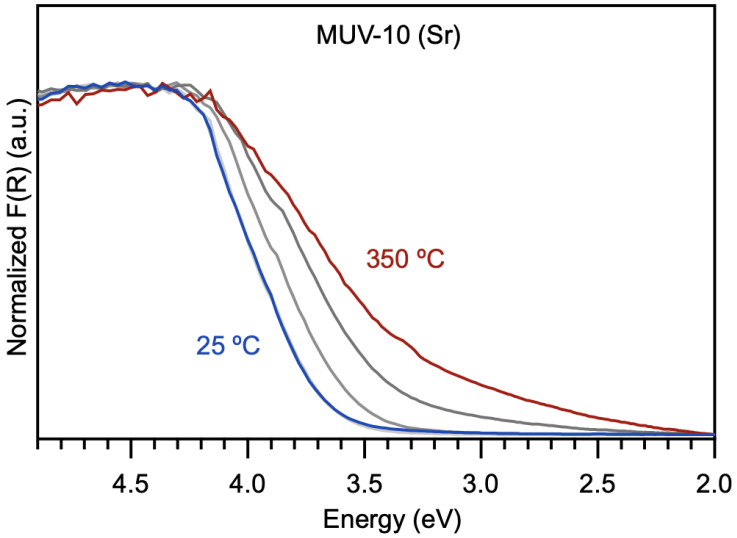

Figure A.11. In situ UV-vis spectra of MUV-10 (Sr) heated to 25 ºC, 100 ºC, 200 ºC, 300 ºC, and 350 ºC under dynamic vacuum.

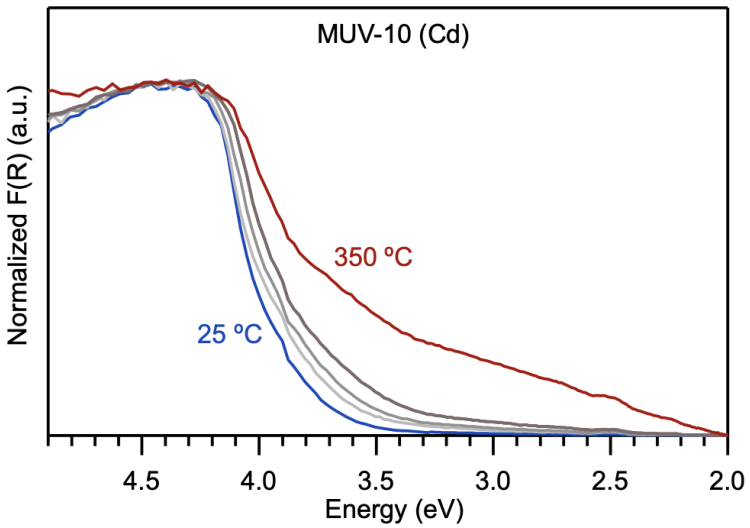

Figure A.12. In situ UV-vis spectra of MUV-10 (Cd) heated to 25 ºC, 100 ºC, 200 ºC, 300 ºC, and 350 ºC under dynamic vacuum.

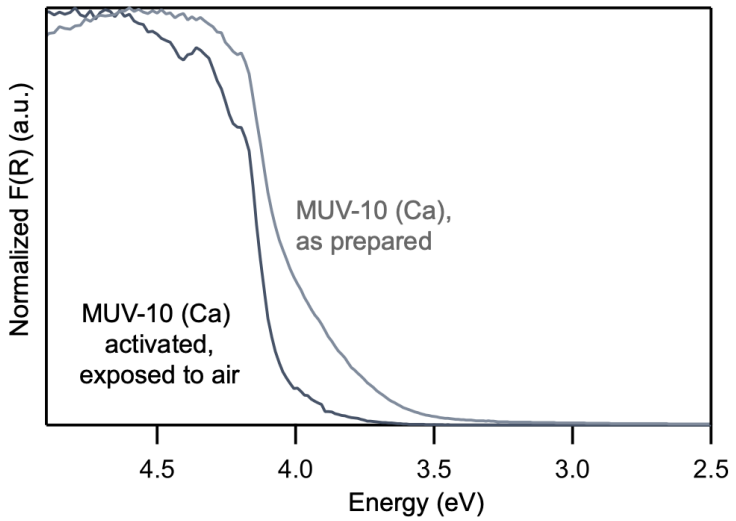

Figure A.13. UV-vis spectra of MUV-10 (Ca) exposed to air by two different methods.

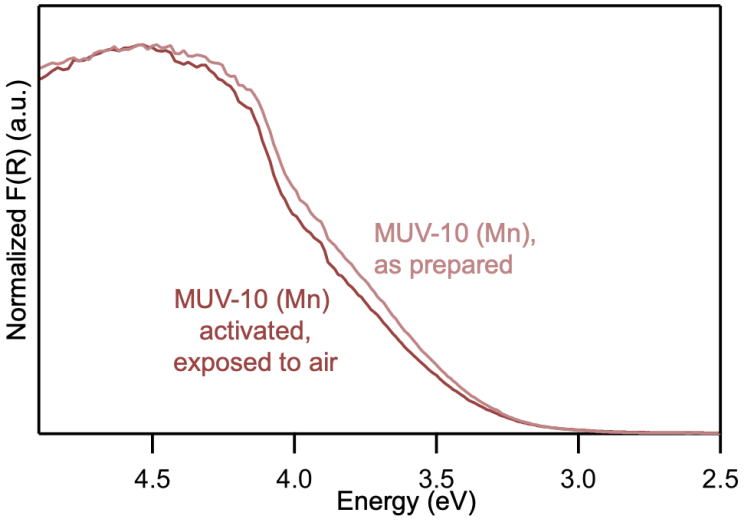

Figure A.14. UV-vis spectra of MUV-10 (Mn) exposed to air by two different methods.

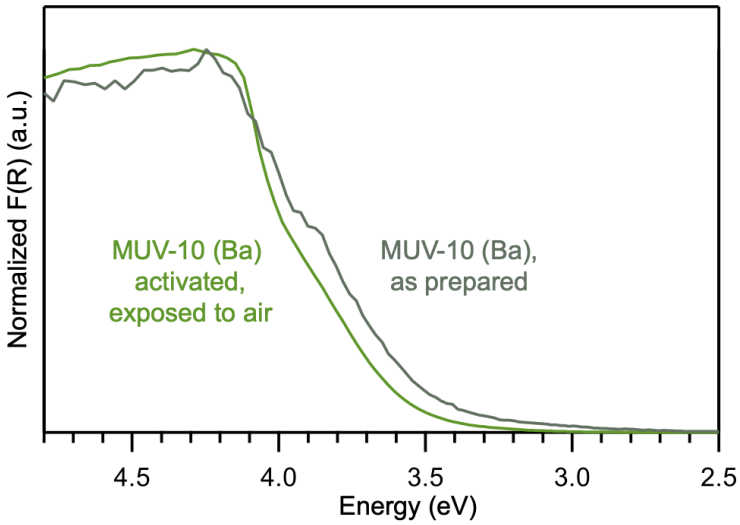

Figure A.15. UV-vis spectra of MUV-10 (Ba) exposed to air by two different methods.

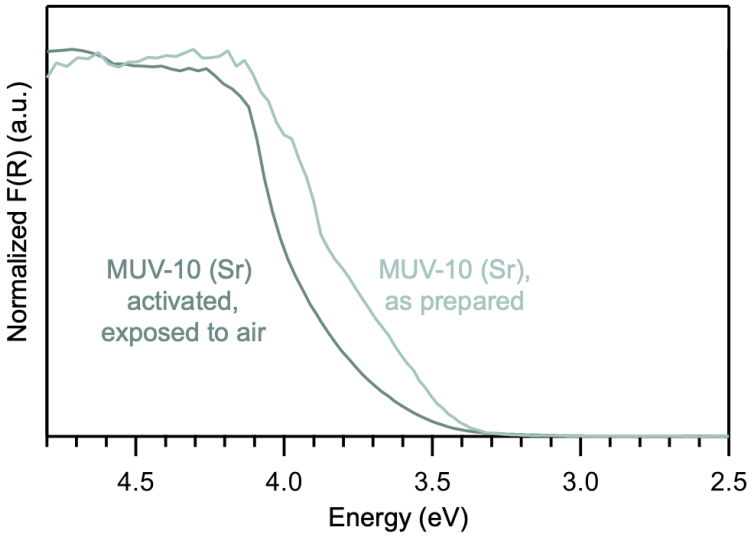

Figure A.16. XUV-vis spectra of MUV-10 (Sr) exposed to air by two different methods.

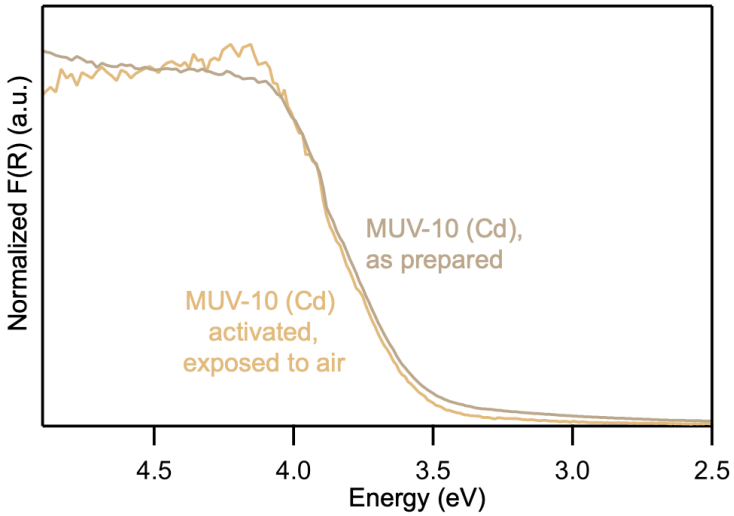

Figure A.17. UV-vis spectra of MUV-10 (Cd) exposed to air by two different methods.

Tauc Analysis

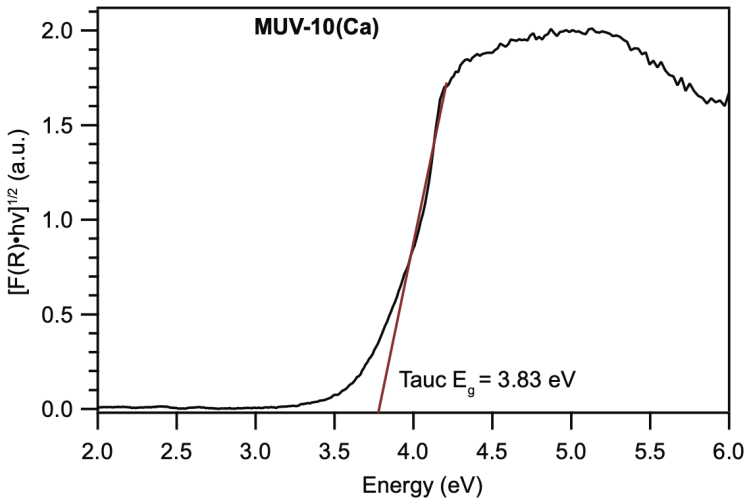

Figure A.18. Tauc analysis of fully hydrated MUV-10(Ca) at RT.

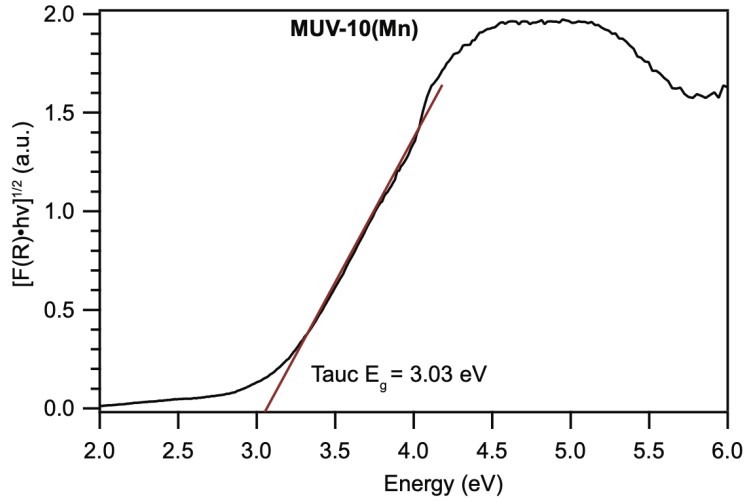

Figure A.19. Tauc analysis of fully hydrated MUV-10(Mn) at RT.

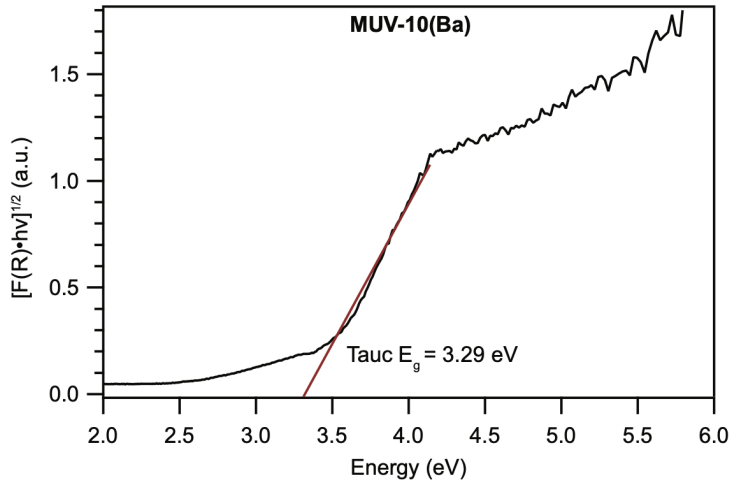

Figure A.20. Tauc analysis of fully hydrated MUV-10(Ba) at RT.

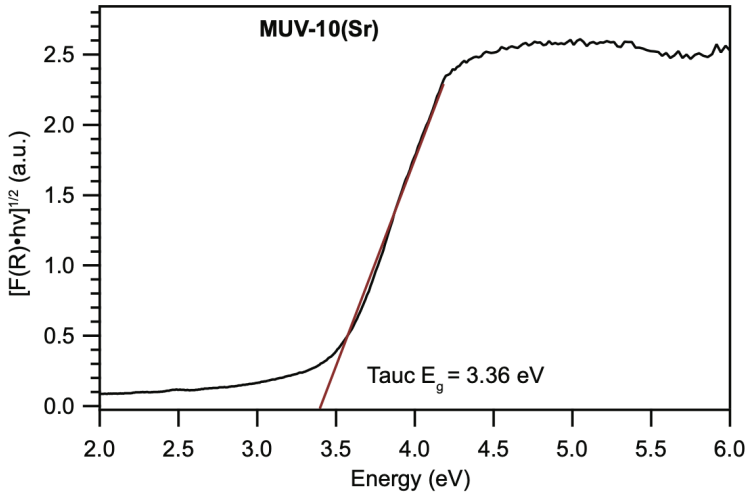

Figure A.21. Tauc analysis of fully hydrated MUV-10(Sr) at RT.

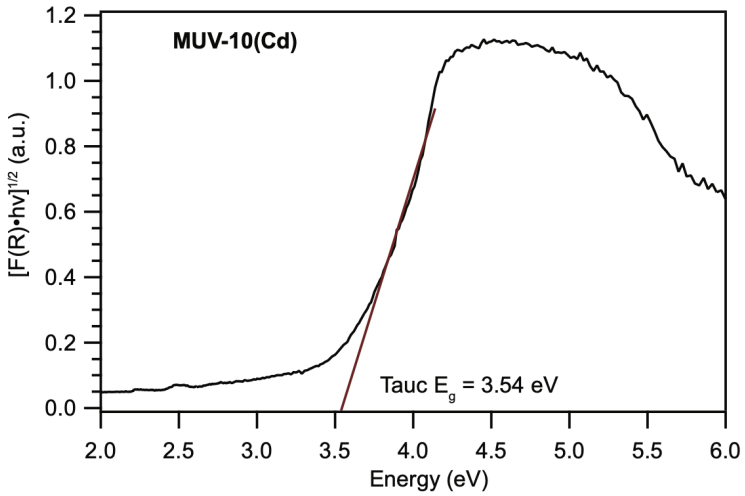

Figure A.22. Tauc analysis of fully hydrated MUV-10(Cd) at RT.

Thermogravimetric Analysis (TGA)

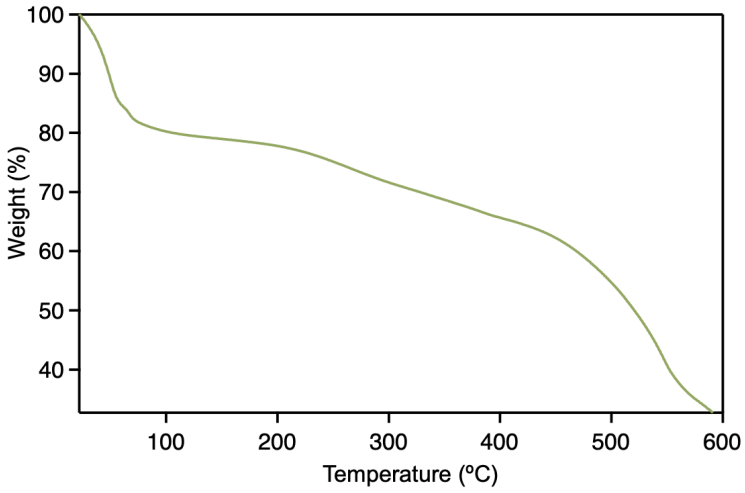

Figure A.23. Thermogravimetric analysis (TGA) trace of MUV-10 (Ba) after treatment with MeOH.

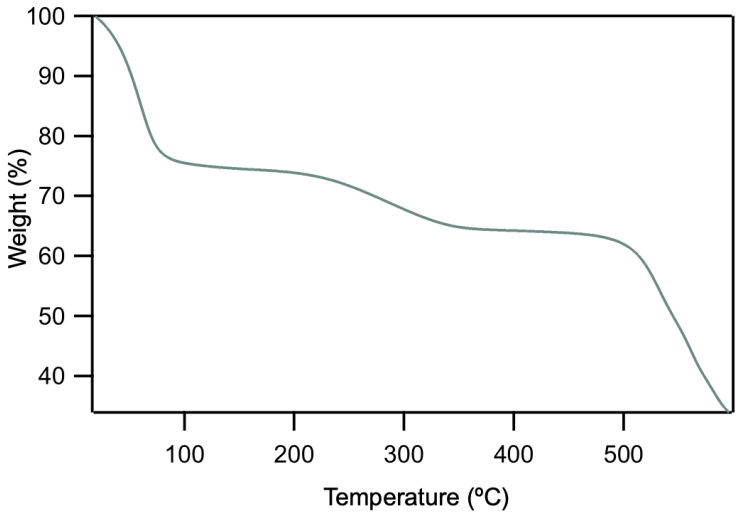

Figure A.24. Thermogravimetric analysis (TGA) trace of MUV-10 (Sr) after treatment with MeOH.

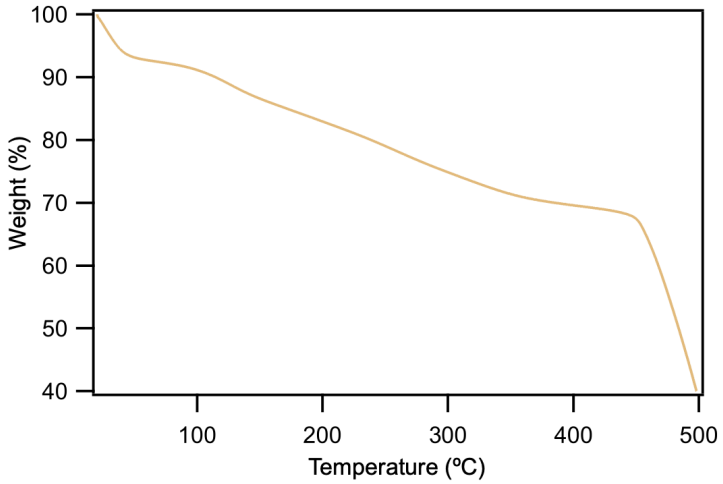

Figure A.25. Thermogravimetric analysis (TGA) trace of MUV-10 (Cd) after treatment with MeOH.

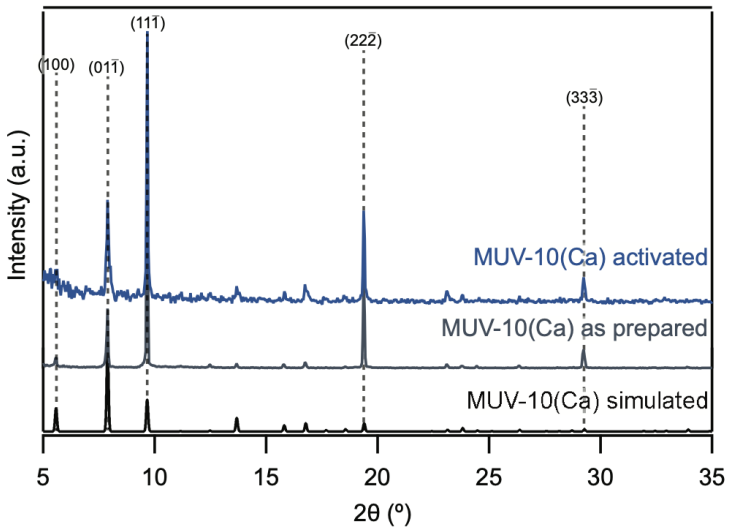

Figure A.26. PXRD of MUV-10 (Ca) after being heated at 150 ºC and evacuated under dynamic vacuum until the outgassing rate fell below 2.5 µtorr · min^{-1}.

IR Spectroscopy

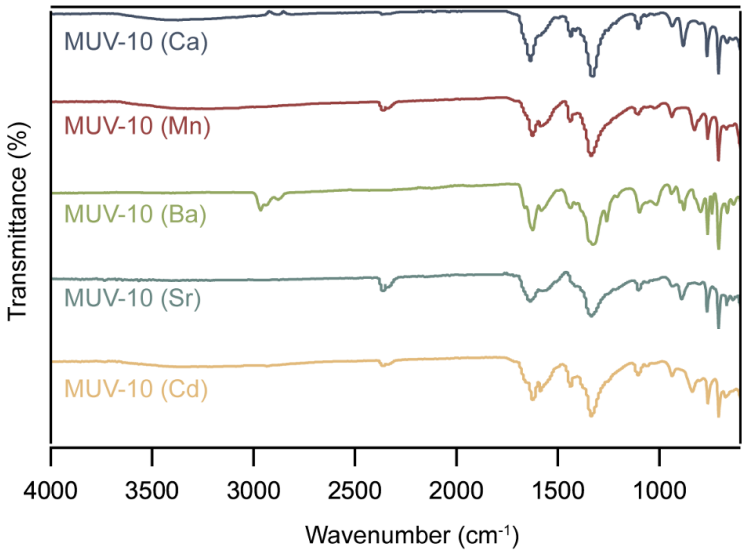

Figure A.27. XIR spectra of all derivatives in air, except for MUV-10 (Ba), which was evacuated at elevated temperatures and transferred to an N_2-atmosphere prior to data collection.

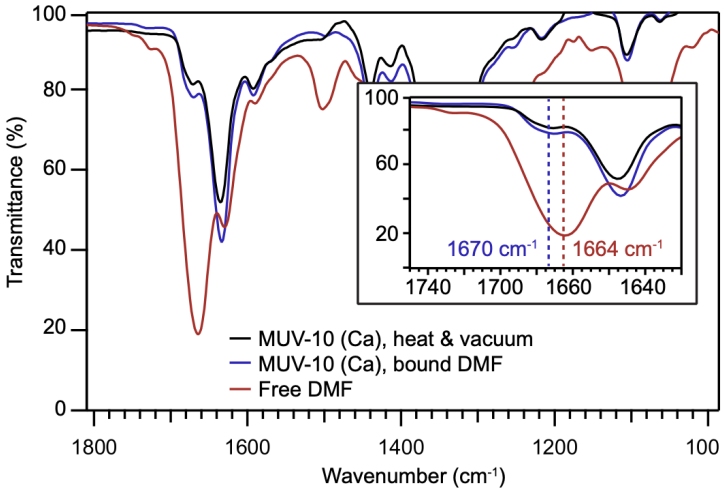

Figure A.28. IR spectra of MUV-10 (Ca) after being heated and evacuated and then soaked in dry DMF, and compared to neat dry DMF. Inset: A shift in the local minima of Free DMF and MUV-10 (Ca) treated with DMF are indicated by dashed lines.

Cation incorporation into MUV-10 (Ca) and effect on electronic structure

First, the impact of H^+ was tested by soaking ∼1 mg of MUV-10(Ca) in 2 mL of 10^{-3} M HNO_3 overnight (>16 h) and then measuring the diffuse reflectance spectrum. Similarly, the impact of different cations was examined by preparing suspensions consisted of 2 mL aqueous solutions of $LiNO_3$, $NaNO_3$, and KNO_3, respectively together with ∼1 mg of MUV-10(Ca) such that the ratio of cation to Ti in the MOF would be 5:1.

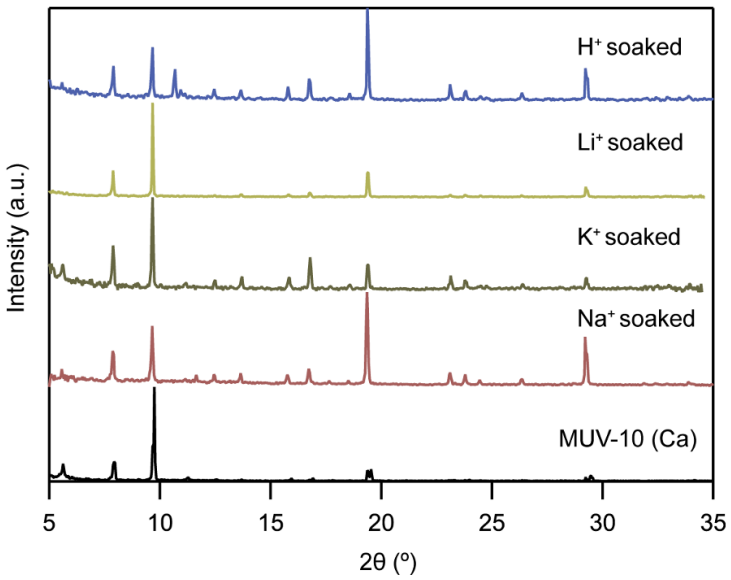

Figure A.29. PXRD patterns MUV-10 (Ca) after soaking in solutions of NO3 salts of different inorganic cations.

Fermi Level Estimation by Optical Redox Indicator

Preparation and Reduction of $[CoCp_2][PF_6]$. A 6.0-mM solution of cobaltocenium hexafluorophospate in DMF was prepared by dissolving 10 mg of the former in 5 mL DMF under an inert atmosphere. The resulting clear yellow solution was irradiated in an air-free quartz cuvette for several minutes without any effect. Then, 1 mL of dry isopropanol (excess) was added to the above solution under N_2 and a UV-Vis spectrum of the resulting solution was collected before and after irradiation for several minutes. No changes were observed (max remained unchanged). The cuvette was transferred to a N_2-filled glovebox, where 3 mg of MUV-10 (Ca) was added (1:6 ratio MOF:cobaltocenium). The suspension was then irradiated for a total of 2 h without any differences to the corresponding UV-Vis spectra. The above procedure was repeated again without the presence of IPA, effecting no changes to the UV-vis spectra.

Preparation and Reduction of $[FeCp^*_2][BF_4]$**.** In an N_2 glovebox, $[FeCp^*_2]$ was weighed into a Schlenk flask and dissolved in ca 5 mL hexanes. In air, benzoquinone was dissolved in ca 5 mL of ethyl ether, and HBF_4 was added. The $[FeCp^*_2]$ and benzoquinone solutions were combined by cannula transfer, creating a cloudy dark-green mixture. This solution was left to stir for one hour, and let stand for 30 minutes, yielding a green precipitate. The flask was transferred to a benchtop N_2 glovebox, where it was vacuum filtered and washed with dry hexanes ($\sim$40 mL). Once transferred into an N_2 glovebox, the powder was dissolved in dry MeCN. The concentration of the solution was tested via UV vis by way of a dilution of 300 µL in 3 mL MeCN in an air-free quartz cuvette with pathlength 1 cm, and the concentration was determined to be 4.06 mM by the 30 min irr. abs value at 778 nm for an absorptivity coefficient of 488 $L \cdot mol^{-1}$ cm^{-1}. Similar to the previous experiment, 3 mg of MUV-10 (Ca) were added to 3 mL of stock $[FeCp^*_2]^+$ in MeCN and 300 µL dry ethanol. The cuvette was irradiated with a mercury arc lamp, and the UV-vis spectra were recorded after allowing the powder to settle. After 1290 min of irradiation (21.5 hr) the vibrant green solution had turned the characteristic yellow color of $[FeCp^*_2]$.

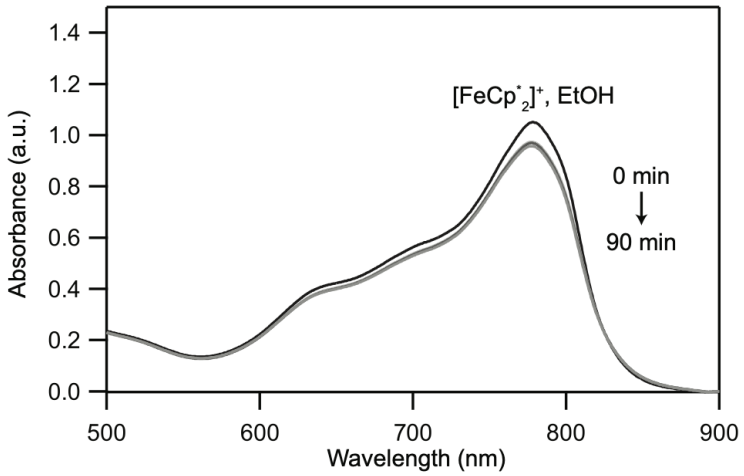

Figure A.30. Solution-phase UV-vis spectra of the acetonitrile mixture containing a $[FeCp^*_2]/[FeCp^*_2]^+$ – ethanol mixture collected at 30 min intervals during a 90-minute irradiation with UV light by Mercury arc lamp.

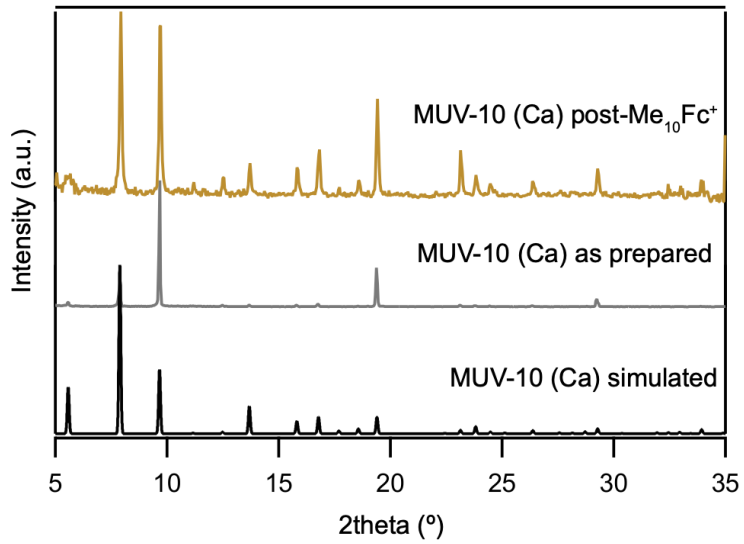

Figure A.31. PXRD patterns of MUV-10 (Ca) before and after exposure to a 4.06 mM $[FeCp^*_2]/[FeCp^*_2]^+$– ethanol mixture for 21.5 h.

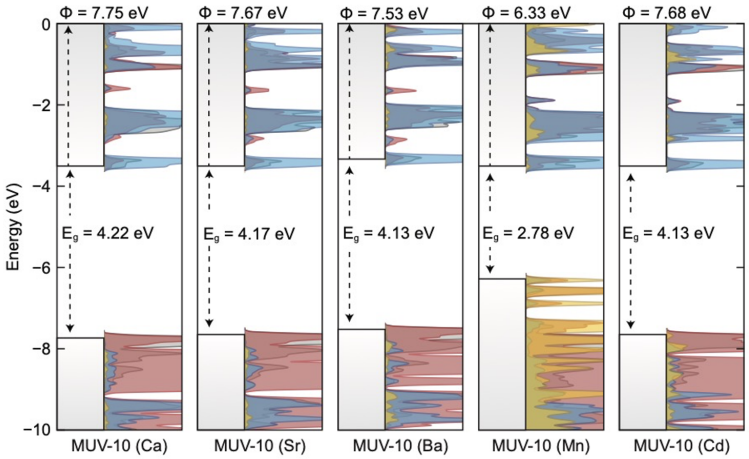

Figure A.32. Band alignment of equilibrium hydrated MUV-10(M) series, where M = Ca, Sr, Ba, Cd, Mn. The metal contribution to the DOS is shown in yellow.

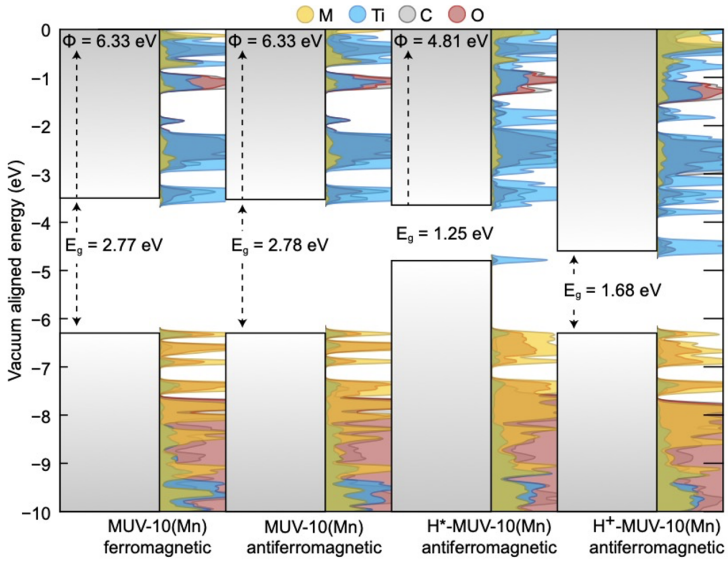

Figure A.33. Band alignment diagrams and accompanying density of states for both magnetic configurations of MUV-10(Mn), as well as the protonated, and hydrogen adatomic material.

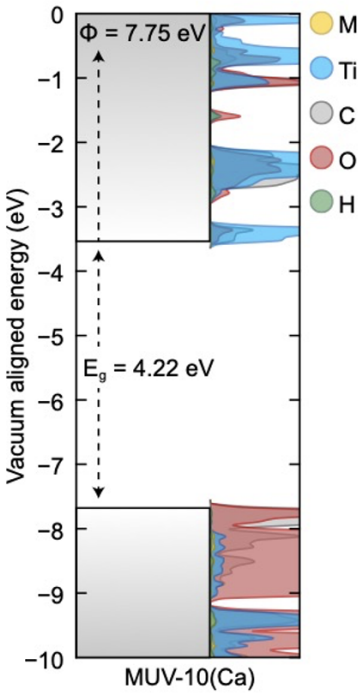

Figure A.34. Band alignment and density of states of MUV-10(Ca) include hydrogen. Here, M = Ca, and hydrogen contribution to the valence and conduction band extrema is minimal.

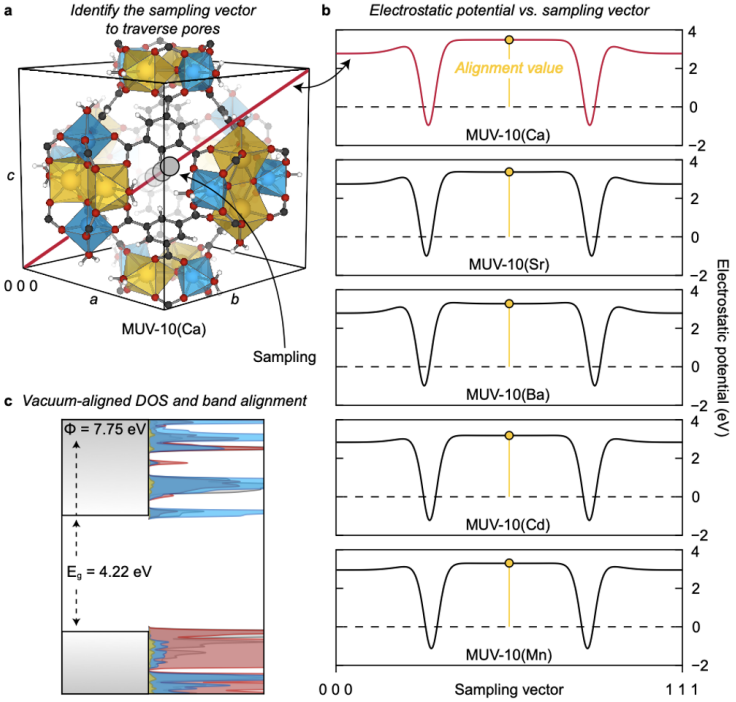

Figure A.35. An overview of the band alignment procedure. **a)** A vector is selected that bisects the pores in the MOF. In this case, MUV-10 contains two dissimilar pores, centered at 0, 0, 0 and 0.5, 0.5, 0.5. The potential is then probed by sampling along the vector shown in red. **b)** the plot of potential vs. position in unit cell reveals two vacuous spaces, evidenced by regions of flat/unchanging potential. The most positive potential is used to vacuum align the valence band. **c)** As a result, we recover an internally referenced vacuum level and associated workfunction ($\mathbf{\Phi}$), and the band gap is unperturbed.

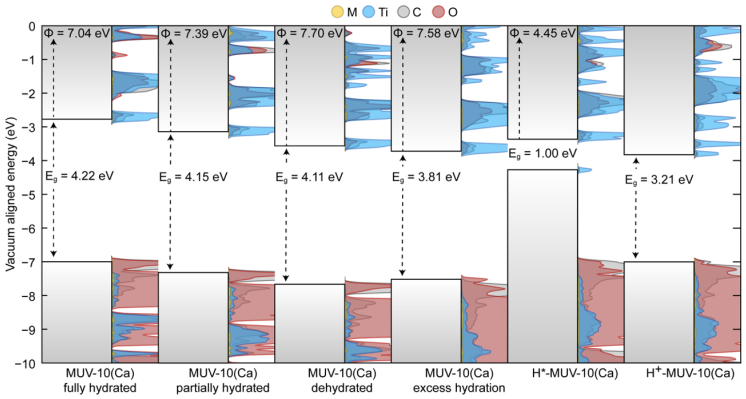

Figure A.36. Computed DOS calculations for "fully hydrated" MUV-10 (Ca), "partially hydrated" MUV-10 (Ca), "dehydrated" MUV-10 (Ca), "excess hydration" MUV-10(Ca), H*–MUV-10(Ca), and H^+–MUV-10(Ca) (carbon represented in grey, oxygen in red, titanium in blue, and calcium in yellow). "Excess hydration" MUV-10(Ca) features an additional H_2O placed near each Ca and Ti metal site (in addition to the single H_2O bound to each in the "fully hydrated" structure). The H*–MUV-10(Ca) and H^+–MUV-10(Ca) structures were constructed from the "fully hydrated" MUV-10 (Ca) parent structure.

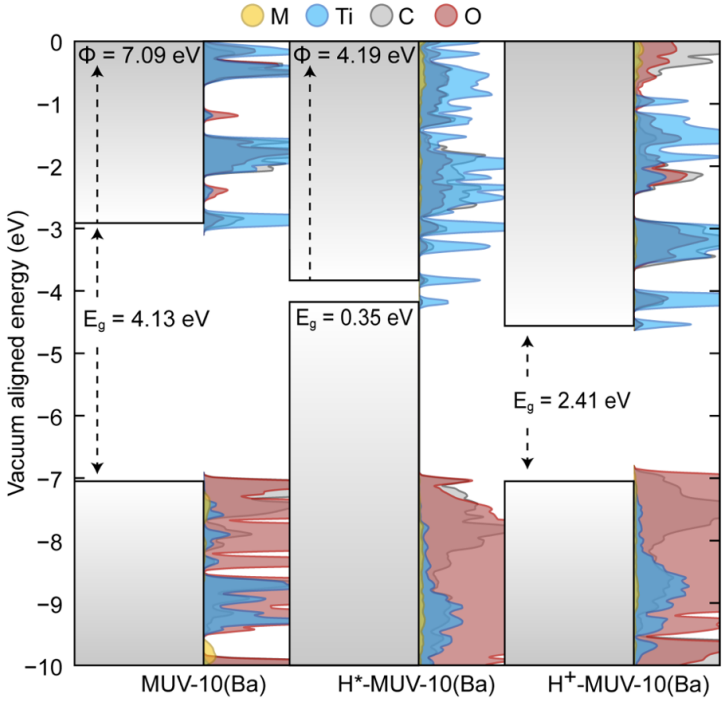

Figure A.37. Computed DOS calculations for MUV-10(Ba), H*–MUV-10(Ba), and H$^+$–MUV-10(Ba) (carbon represented in grey, oxygen in red, titanium in blue, and barium in yellow). All structures are in their "fully hydrated" forms, with one H_2O bound to each Ti and Ba metal site.

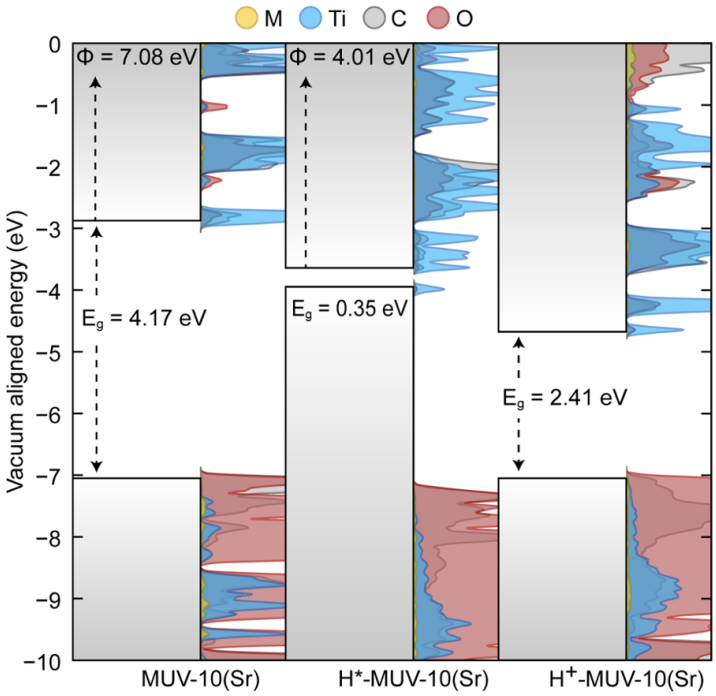

Figure A.38. Computed DOS calculations for MUV-10(Sr), H*–MUV-10(Sr), and H^+–MUV-10(Sr) (carbon represented in grey, oxygen in red, titanium in blue, and strontium in yellow). All structures are in their "fully hydrated" forms, with one H_2O bound to each Ti and Sr metal site.

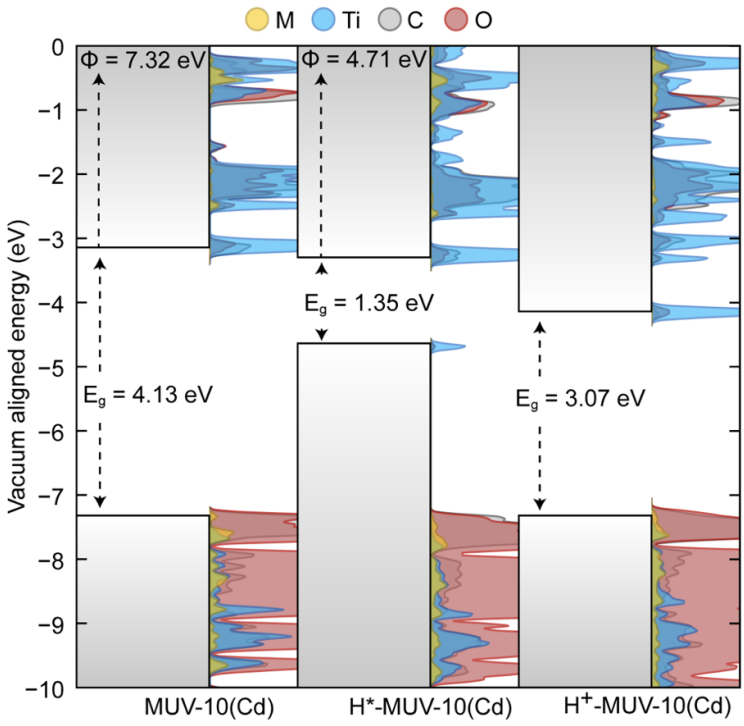

Figure A.39. Computed DOS calculations for MUV-10(Cd), H*–MUV-10(Cd), and H^+–MUV-10(Cd) (carbon represented in grey, oxygen in red, titanium in blue, and cadmium in yellow). All structures are in their "fully hydrated" forms, in this case meaning one H_2O bound to each Ti (as Cd is hexacoordinate).

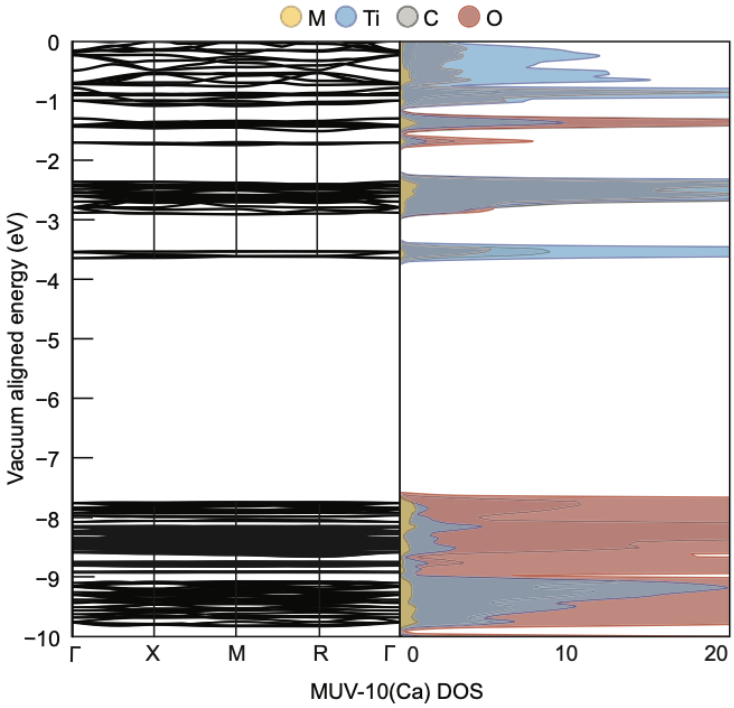

Figure A.40. Band diagram and DOS diagram of MUV-10(Ca) computed at multiple k-points. The band structure was computed using spin-unrestricted GGA, and the band gap was adjusted to reflect the value obtained using the hybrid DFT approach (HSEsol06).

Example Input

INCAR FOR PBESOL BAND STRUCTURE

```
SYSTEM = Name

!Start Parameters

 ISTART     = 1     (Read existing wavefunction, if present)

 INIWAV     = 1     (Random initial wavefunction)

 ICORELEVEL = 1     (Print core levels in OUTCAR)

 !!NGX        = 500   (FFT grid mesh density)

 !!NGY        = 500   (FFT grid mesh density)

 !!NGZ        = 500   (FFT grid mesh density)
```

```
 ICHARG   =  11   (Non-selfconsistent: band structures)
 !!NELECT   = 352   (Number of electrons: charged cells)
 !!NBANDS   = 468   (Increase number of bands)

!Parallel Options
 !!LPLANE = .TRUE.   (Real space distribution)
 NPAR   = 14        (Max is no. nodes)

!Decomposed Charge Density:}
 !!LPARD   = .TRUE. (Generate PARCHG)
 !!LSEPB   = .TRUE. (Separate Bands into PARCHG.band)
 !!IBAND   =  774    (Average over bands)
 !!EINT    = -10 0  (Energy range)
 !!NBMOD   =  -3    (With reference to E_F)
 !!KPUSE   =  1     (Average over k-points)

!Electronic Relaxation
 PREC     = Accurate    (Precision level for FFT grid)
 LREAL    = Auto        (Projection operators: automatic)
 !!ALGO     = Fast      (Electronic minimisation algorithm: 38/48)
 ENMAX    = 500.00 eV   (Plane-wave cutoff)
 NELM     = 200         (Max number of SCF steps)
 NELMAX   = 5           (Min number of SCF steps)
 EDIFF    = 1E-06       (SCF convergence criteria)
 GGA      =  PS         (PBEsol exchange-correlation)
```

```
!Ionic Relaxation
 EDIFFG   =      -0.005 (Ionic convergence criteria, eV/AA)
 NSW      =      0      (Max ionic steps)
 IBRION   =      1      (Ions: 0-MD, 1-Quasi-New, 2-CG)
 ISIF     =      3      (Stress/Relaxation: 2-Ions, 3-Shape/Ions/Vol, 7-Vol)
 ISYM     =      0      (Symmetry: Use all, 0: none)
 ISMEAR   =      0      (Gaussian smearing, Metals:1, MP)
 SIGMA    =      0.05   (Smearing value in eV, Metals:0.2)

!Hybrid-DFT Calculations
 !!LHFCALC     = .TRUE.   (Activate Hartree Fock)
 !!PRECFOCK    = FAST     (HF FFT grid)
 !!ALGO        = DAMPED   (Dampen: IALGO=53)
 !!TIME        = 0.30     (Timestep for IALGO5X)
 !!HFSCREEN    = 0.207    (Switch to screened exchange:HSE06)
 !!AEXX        = 0.25     (25% HF exchange - PBE0)
 !!LDIAG       = .True.   (Diagnolise Eigenvalues)
 !!NKRED     = 2        (Reduce k-grid: even only)
 !!LMAXFOCK  = 6        (Maximum quantum number: 4d,6f)
 !!HFLMAX    = 4        (Max quantum number: 4d,6f)

!Miscellaneous
 LORBIT      =   10     (PAW radii for projected DOS)\\
 NEDOS       =  1000    (Increase DOSCAR points)
```

```
 LVHAR       = .TRUE.    (Output electrostatic potential)
 !!LOPTICS   = .TRUE.    (Output OPTIC file)
 !!LELF      = .TRUE.    (Output electron localization function)
 !!LVDW      = .TRUE. (DFT-D van der Waals interactions)

!Magnetic Calculations
 ISPIN       =  2        (Closed shell: 1, Spin Polarised: 2)
 !!MAGMOM    = 10*-1 2*0 16*0     (Initial magnetic mom each ion)
 !!NUPDOWN   = -1        (Enforce spin multiplet)
 !!LSORBIT   = .TRUE.    (Spin-orbit coupling)

!DFT+U Calculations
 !!LDAU      = .TRUE.    (Activate DFT+U)
 !!LDATYPE   = 2         (Dudarev, only U-J matters)
 !!LDAUL     = 2 -1      (Orbital for each species)
 !!LDAUU     = 2  0      (U for each species)
 !!LDAUJ     = 0  0      (J for each species)
 !!LMAXMIX   =  4        (Mixing cutoff: 4-d,6-f)

!Molecular Dynamics
 POTIM     =  0.5      (Timestep fs)
 !!TEBEG     =  100     (Start temperature K)
 !!TEEND     =  100     (End temperature K)
 !!SMASS     =  0       (Canonical ensemble)
```

```
KPOINTS FOR PBESOL BANDSTRUCTURE

K-Path
   50
Line-Mode
Reciprocal
   0.0000000000   0.0000000000   0.0000000000     GAMMA
   0.0000000000   0.5000000000   0.0000000000     X

   0.0000000000   0.5000000000   0.0000000000     X
   0.5000000000   0.5000000000   0.0000000000     M

   0.5000000000   0.5000000000   0.0000000000     M
   0.5000000000   0.5000000000   0.5000000000     R

   0.5000000000   0.5000000000   0.5000000000     R
   0.0000000000   0.0000000000   0.0000000000     GAMMA
```

APPENDIX B: SUPPLEMENTARY INFORMATION FOR CHAPTER 2.1.1

Experimental Methods

Materials. All commercial chemicals were used as received unless stated otherwise. 1,3,5-benzenetricarboxylic acid (trimesic acid, 98%, TCI America), *N,N*-dimethylformamide (DMF, ACS grade, Fisher Scientific), calcium chloride dihydrate (Malinnckrodt), manganese(II) chloride tetrahydrate (ACS grade, Baker), titanium(IV) isopropoxide (97%, Sigma-Aldrich), glacial acetic acid (ACS grade, Fisher Scientific), ethanol (ACS grade, Fisher Chemical), methanol (ACS grade, Fisher Chemical), 2,5-dihydroxyterephthalic acid (Alfa Aesar), magnesium(II) nitrate hexahydrate (99%, ACS reagent, Sigma-Aldrich), zinc(II) nitrate hexahydrate (Sigma-Aldrich), terephthalic acid (98%, Sigma-Aldrich), tetrabutyl titanate (TCI Chemicals), iron(III) chloride hexahydrate (Strem), zirconium (IV) chloride (99.5% trace metals basis, Beantown Chemical), copper(II) hydroxide (Sigma-Aldrich), ammonia (28-30%, Sigma-Aldrich), 2-methylimidazole (Acros 99%, Fisher Scientific), trifluoroacetic acid (99%, Fisher Scientific).

Characterization. Sample purity was verified by powder X-Ray diffraction (PXRD) with a Bruker D2 Phaser benchtop diffractometer. Variable-temperature diffuse reflectance UV-vis spectroscopy (VT-DRUV-vis) was performed on a Perkin Elmer Lambda 1050 UV/Vis/NIR spectrometer, with a 150 mm InGaAs integrating sphere in the range of 2000-200 nm paired with a Harrick Scientific Praying Mantis Diffuse Reflection (DRP) accessory. A Harrick Scientific Low Temperature Reaction Chamber (CHC) that enabled introducing vacuum and heat to the sample was equipped with UV quartz. To ensure adequate absorbance, all samples were diluted with ground $BaSO_4$. All Gaussian fittings were performed

in Igor Pro Version 6.37 using the Multipeak Fitting 2 package and a LogPoly5 or LogCubic baseline, with the choice reliant on minimizing residuals. In fitting, all peaks were first estimated based on experimental absorption features, but allowed to move location, width, and height in order to minimize residual contribution and obtain the highest quality fittings.

MOF Synthesis

Cu_3BTC_2/Cu-HKUST-1. In a typical solvothermal synthesis, trimesic acid (0.72 g, 3.43 mmol) and DMF (8 mL) were combined in a Pyrex Schott bottle and sonicated for 5 minutes. Copper nitrate trihydrate (4.02 g, 16.64 mmol) was dissolved in water (8 mL) and ethanol (8 mL) and transferred to the Schott jar. This mixture was sealed and heated in a fixed-temperature oven at 80 °C for 24 h. After cooling to room temperature, the product was centrifuged, mother liquor decanted and replaced with clean *N,N*-dimethylformamide (DMF), the solid was dispersed in solvent and left soaking overnight. The next day, DMF was decanted after centrifuging and replaced with clean ethanol, and the solid was again dispersed in solvent and left soaking for a day. On the third day, the ethanol was decanted, and the product was dried under reduced pressure and ambient temperatures for 18 h.

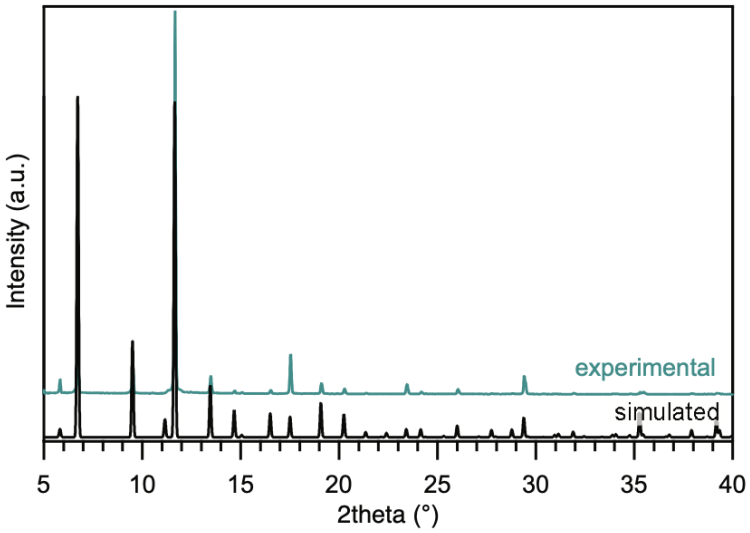

Figure B.1. Experimental and simulated powder X-ray diffraction patterns for Cu-HKUST-1.

MUV-10(Ca, Mn). Following an adapted literature procedure,1,2 calcium chloride dihydrate (0.0176 g, 0.12 mmol) or manganese(II) chloride dihydrate (0.0238 g, 0.12 mmol), titanium(IV) isopropoxide (36 L, 0.12 mmol) and trimesic acid (0.125 g, 0.595 mmol) were mixed with DMF (12 mL) and glacial acetic acid (3.5 mL) in a Pyrex Schott bottle and heated at 120 ^{o}C for 48 hr. The solids were recovered by sequential centrifugation and washing with DMF (2×, 25 mL) and methanol (MeOH, 2×, 25 mL) to remove any unreacted precursor.

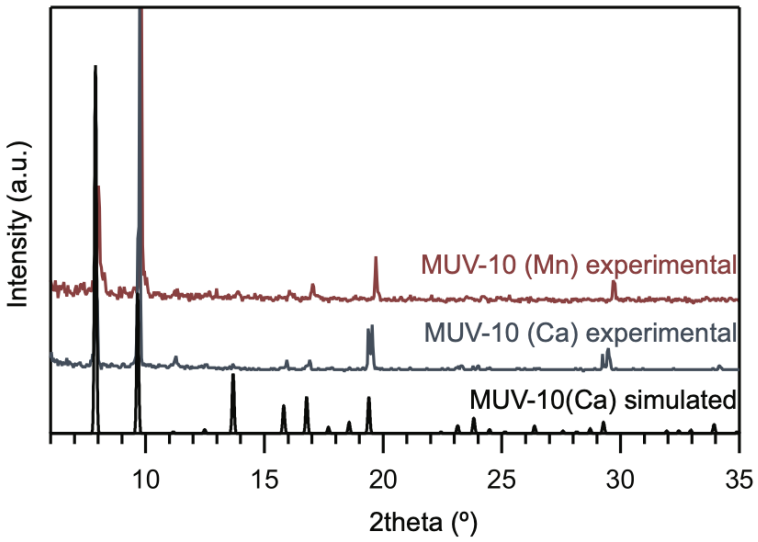

Figure B.2. Experimental and simulated powder X-ray diffraction patterns for MUV-10(Ca) and MUV-10(Mn).

Mg-MOF-74. Following a literature procedure,3 2,5-dihydroxyterephthalic acid (0.114 g, 0.565 mmol) and magnesium(II) nitrate hexahydrate (0.474 g, 1.848 mmol) were dissolved in a mixture of DMF (45 mL), ethanol (3 mL) and water (3 mL). The solution was capped tightly in a Pyrex Schott bottle and placed into a fixed-temperature oven at 125 ^{o}C for 21.5 hr. After cooling, the yellow solid was recovered by sequential centrifugation and washing with DMF (2×, 25 mL) and MeOH (2×, 25 mL).

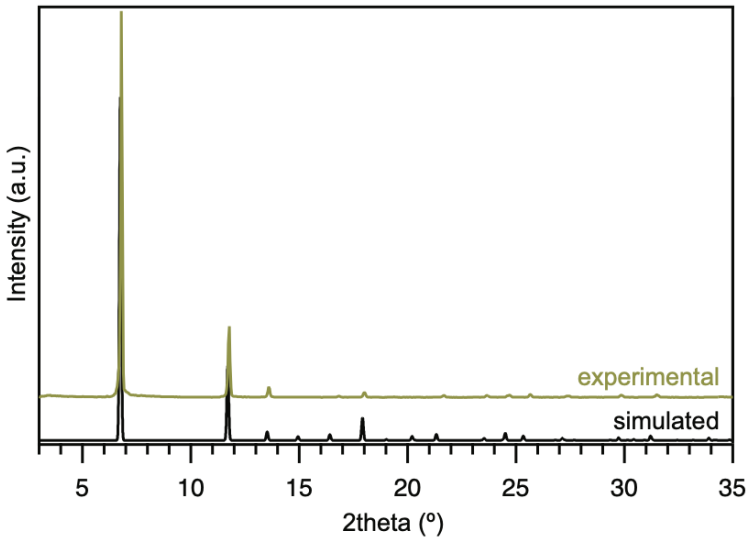

Figure B.3. Experimental and simulated powder X-ray diffraction patterns for Mg-MOF-74.

MOF-5. Following a procedure adapted from Kaye et. al,4 zinc(II) nitrate hexahydrate (0.453 g, 1.5 mmol), terephthalic acid (0.083 g, 0.50 mmol), *N,N*-dimethylformamide (DMF, 49 mL), and water (1 mL) were mixed in a Pyrex Schott bottle, sealed under N_2, and heated to 100 ^{o}C for 7 h. After cooling to room temperature, the resulting precipitate was isolated by gravity filtration under an N_2 atmosphere in a benchtop glovebox, and washed with dry DMF (20 mL). The slurry was transferred to a N_2-filled glovebox and washed with fresh DMF over the course of 1 day (3×, 20 mL) and with dichloromethane (DCM, 3×, 20 mL) over the course of 3 days. After 3 days, the DCM was decanted, and the product was stored under inert atmosphere.

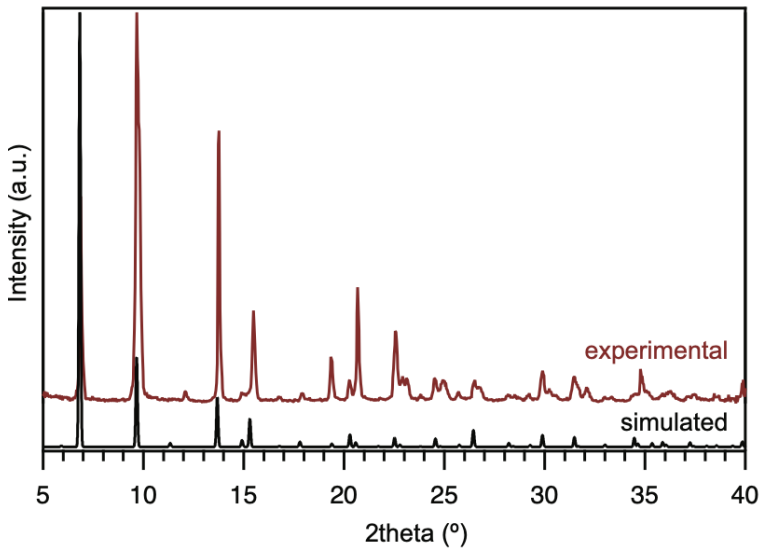

Figure B.4. Experimental and simulated powder X-ray diffraction patterns for MOF-5.

MIL-125. MIL-125 was synthesized via a reflux method, in which a water condenser was connected to a two-neck round bottom flask heated at 110 ^{o}C. While stirring, terephthalic acid (0.325 g, 2.12 mmol) and DMF (5 mL) were mixed, followed by MeOH (5 mL) and tetrabutyl titanate (0.42 mL, 0.12 mmol). The mixture was allowed to stir under reflux for 18 h, and the crystals were isolated by sequential centrifugation and washing with DMF (2×, 25 mL) and MeOH (2×, 25 mL).

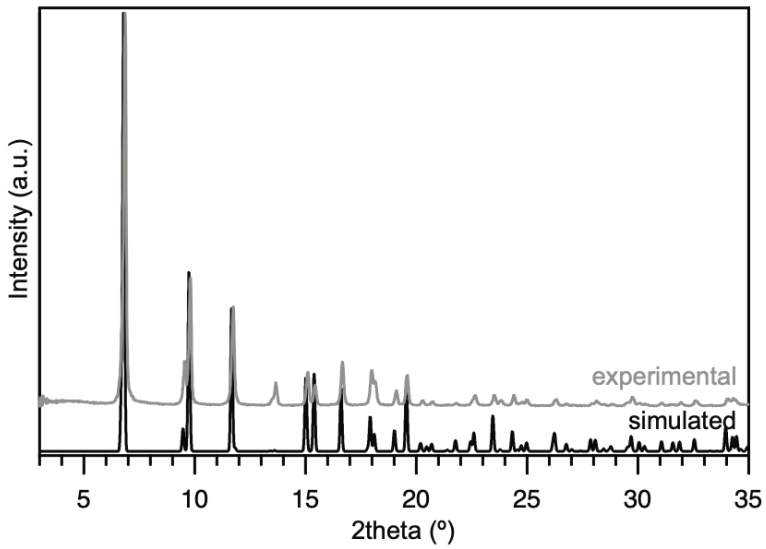

Figure B.5. Experimental and simulated powder X-ray diffraction patterns for MIL-125.

MIL-53(Fe). Following literature procedure,5 in a Schott bottle, iron(III) chloride hexahydrate (0.540 g, 2.00 mmol) and terephthalic acid (0.332 g, 2.00 mmol) were combined with 10 mL DMF and heated at 150 ^{o}C for 6 hr. The reddish-brown powder was recovered by washing with DMF (2×, 25 mL) and acetone (2×, 25 mL).

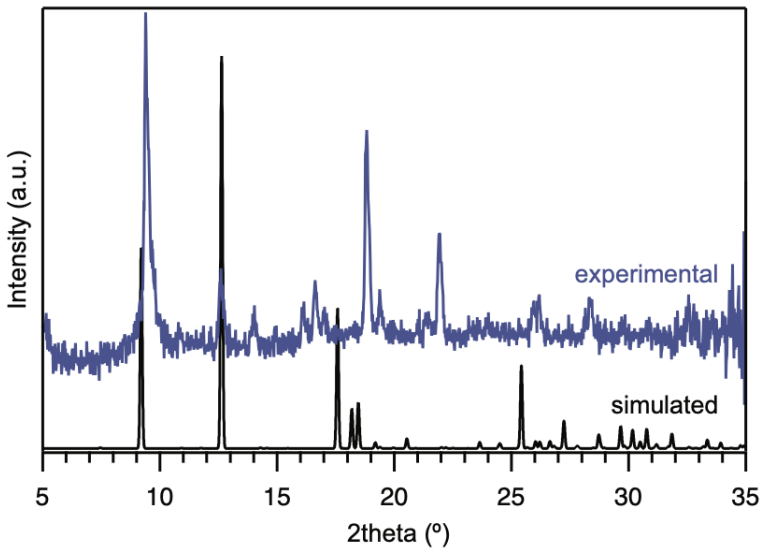

Figure B.6. Experimental and simulated powder X-ray diffraction patterns for MIL-53(Fe).

UiO-66. Using standard Schlenk technique and under a N_2 atmosphere, a solution of zirconium(IV) chloride (0.27 mmol in 5 mL of DMF) was added to a solution of terephthalic acid (0.38 mmol in 5 mL of DMF) via cannula transfer. Thereafter, 330 μL of DI water was added at once. The mixture was heated at 100 ^{o}C to reflux for 4 h under constant stirring and nitrogen atmosphere to yield a white dispersion of UiO-66 crystals. After 4 h, an excess of MeOH was added to the reaction mixture to halt the reaction, and transferred to two centrifuge tubes that were placed on ice. After this, the particles were collected by centrifugation and repetitively washed with 10 mL of DMF for three times. Thereafter, the solid product was extensively washed with MeOH (×3, 50 mL) to completely remove residual DMF, and finally dried at ambient conditions.

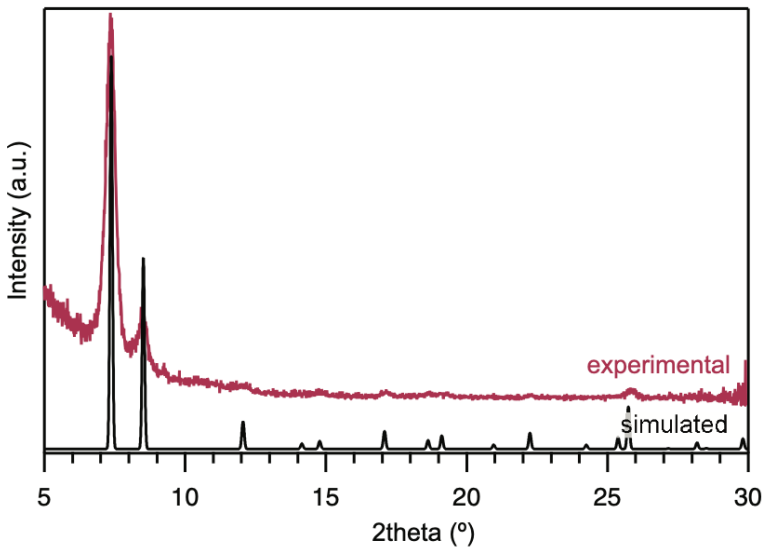

Figure B.7. Experimental and simulated powder X-ray diffraction patterns for UiO-66.

Cu(triazolate)$_2$. Adapted from Grzywa et. al,6 copper(II) hydroxide (0.072 g, 0.73 mmol) was dissolved in 30% ammonia (4.5 mL). Separately, 1,2,3-triazole (0.15 g, 2.22 mmol) was dissolved in ethanol (1.5 mL), and upon dissolution of copper(II) hydroxide, the mixture was added to linker solution, with resulting mixture containing 1:3 metal-to-linker ratio. The reaction was stirred for 18 h at 120 °C. The product was soaked in ethanol, changing the solvent daily for 3 days. The resulting powder was dried and heated under reduced pressure before use.

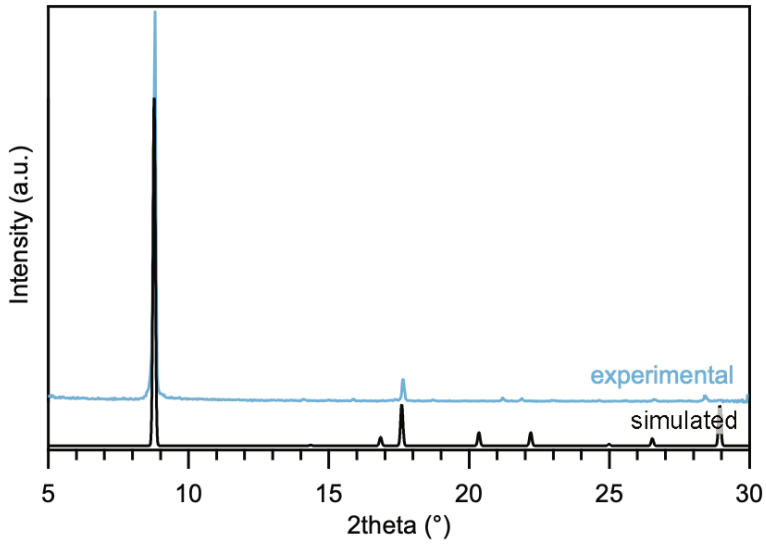

Figure B.8. Experimental and simulated powder X-ray diffraction patterns for Cu(triazolate)$_2$.

ZIF-8. Following a literature procedure7, zinc(II) nitrate hexahydrate (0.673 g, 2.00 mmol) and 2-methylimidazole (0.167 g, 2.00 mmol) were stirred to combine with DMF (50 mL) in a Pyrex Schott bottle. The bottle was sealed and heated at 140 ^{o}C for 24 hr. The solids were collected by filtration and washed with DMF (2×, 25 mL) and MeOH (2×, 25 mL).

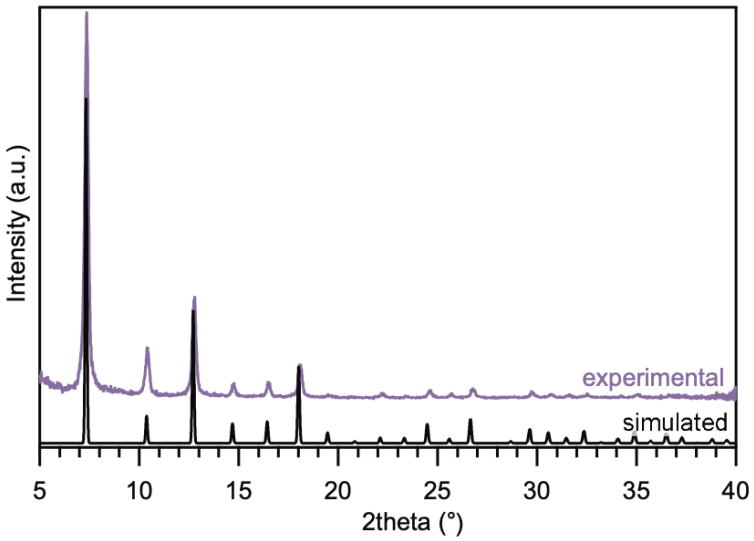

Figure B.9. Experimental and simulated powder X-ray diffraction patterns for ZIF-8.

PCN-415. PCN-415 was synthesized in a one-pot solvothermal method, described in the original report of the MOF and corresponding Ti/Zr cluster.8 Briefly, zirconium(IV) chloride (0.05 g, 0.215 mmol), titanium(IV) isopropoxide (0.1 mL, 0.353 mmol), glacial acetic acid (0.5 mL) and DMF (5 mL), were added to a Schott bottle. The solution was sonicated for 15 minutes before being placed into an oven at 150 ^{o}C for 24 hr. After the solution had cooled, terephthalic acid (0.8 g, 4.82 mmol), trifluoroacetic acid (1.0 mL), and DMF (10 mL) were added. Again, the mixture was sonicated for 15 min before being placed into an oven at 140 ^{o}C for another 24 hr. The white solid was collected by sequential centrifugation and washing with DMF (2×, 25 mL) and MeOH (2×, 25 mL).

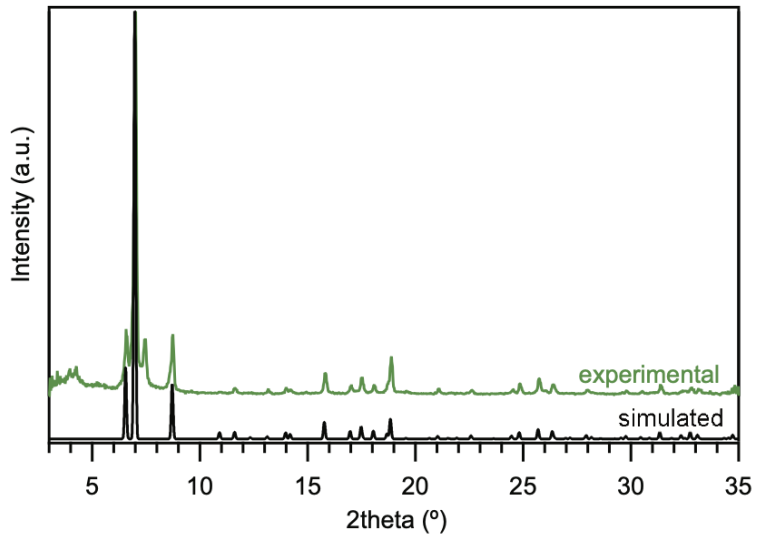

Figure B.10. Experimental and simulated powder X-ray diffraction patterns for PCN-415.

MFM-300(Sc). The MOF was synthesized according to a literature procedure reported by Ibarra and co-workers.[372]

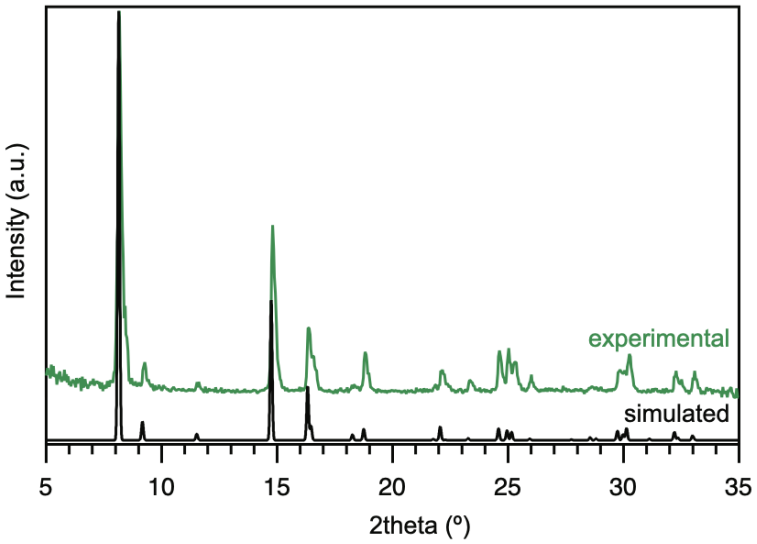

Figure B.11. Experimental and simulated powder X-ray diffraction patterns for MFM-300(Sc).

SU-101(Bi). The MOF was synthesized according to a literature procedure reported by Grape and co-workers.[373]

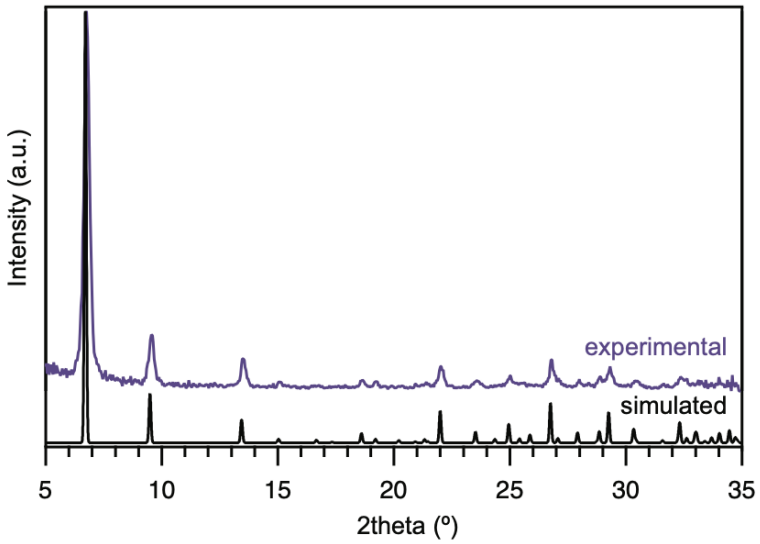

Figure B.12. Experimental and simulated powder X-ray diffraction patterns for SU-101(Bi)

Diffuse Reflectance UV-vis Spectroscopy and Respective Fits

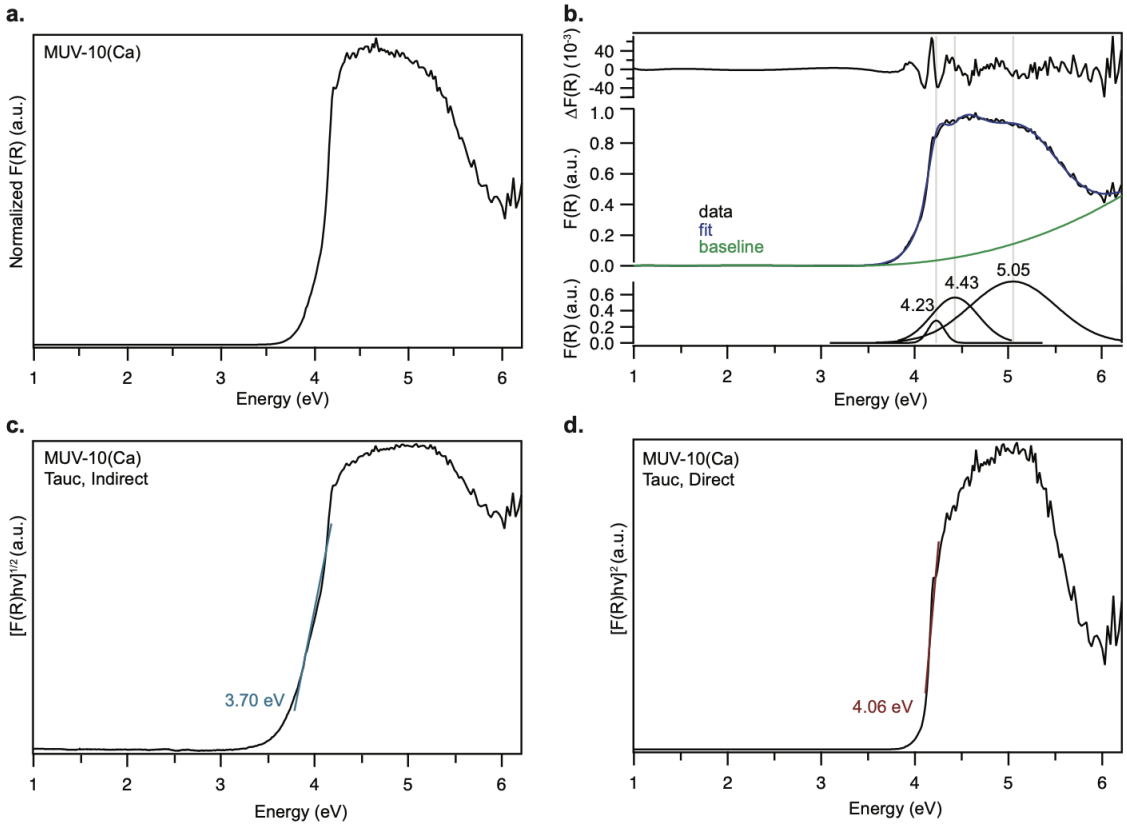

Figure B.13. Diffuse reflectance UV-vis data for MUV-10(Mn) **a)** Normalized data in Kubelka-Munk units. **b)** Gaussian fitting of normalized DRUV-vis data **c)** Tauc transformation and estimated band gap energy for an indirect assumption. **d)** Tauc transformation and estimated band gap for a direct assumption.

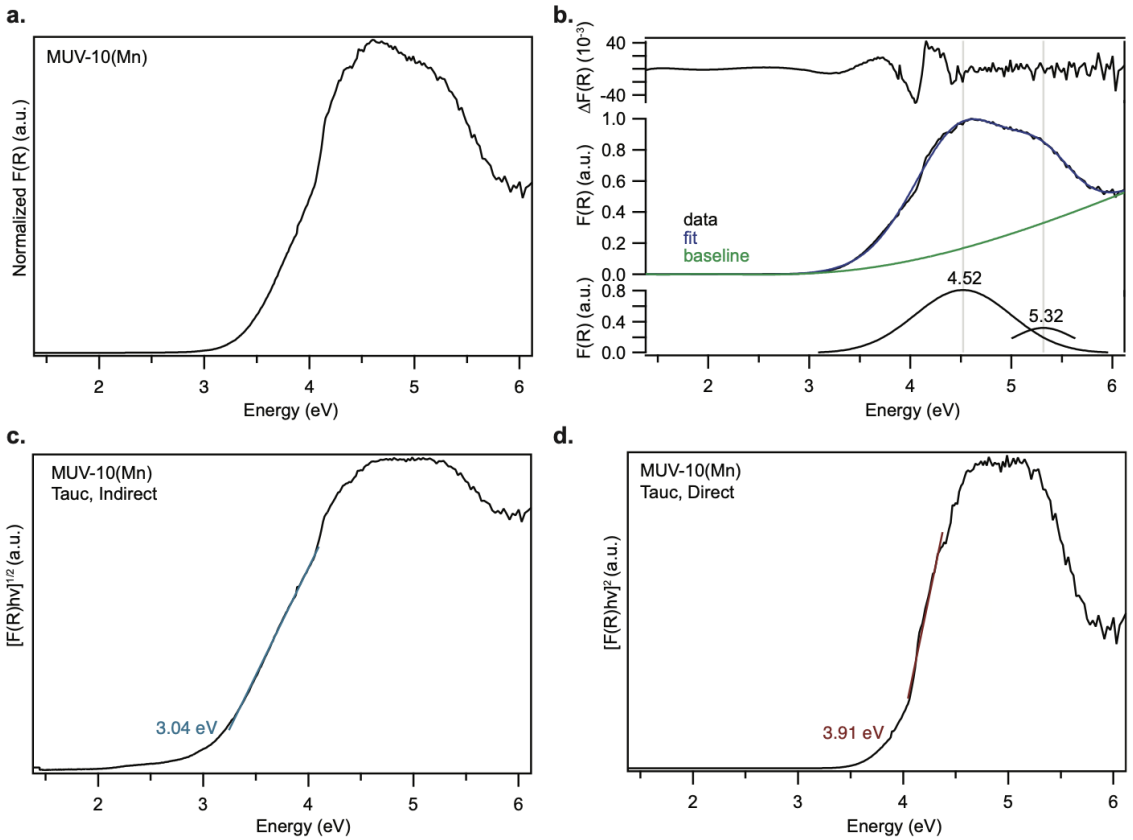

Figure B.14. Diffuse reflectance UV-vis data for MUV-10(Ca) **a)** Normalized data in Kubelka-Munk units. **b)** Gaussian fitting of normalized DRUV-vis data **c)** Tauc transformation and estimated band gap energy for an indirect assumption. **d)** Tauc transformation and estimated band gap for a direct assumption.

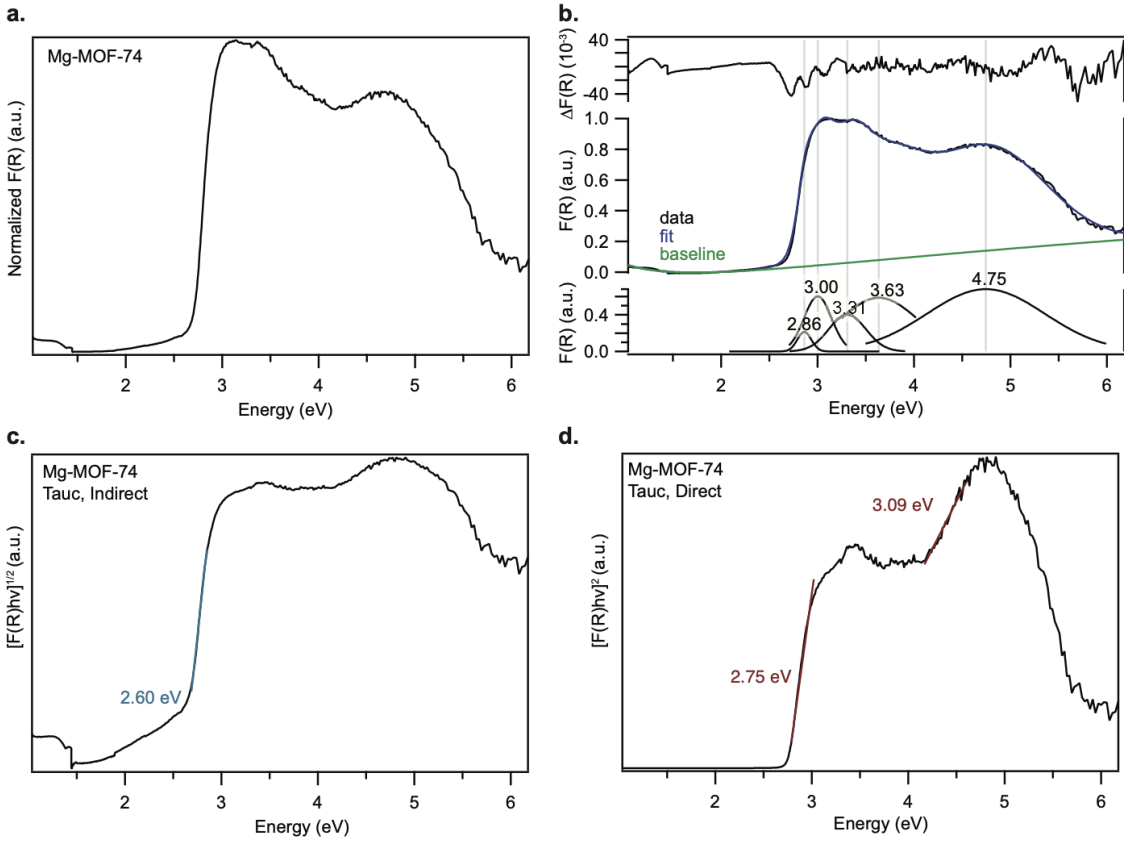

Figure B.15. Diffuse reflectance UV-vis data for Mg-MOF-74 **a)** Normalized data in Kubelka-Munk units. **b)** Gaussian fitting of normalized DRUV-vis data **c)** Tauc transformation and estimated band gap energy for an indirect assumption. **d)** Tauc transformation and estimated band gap for a direct assumption.

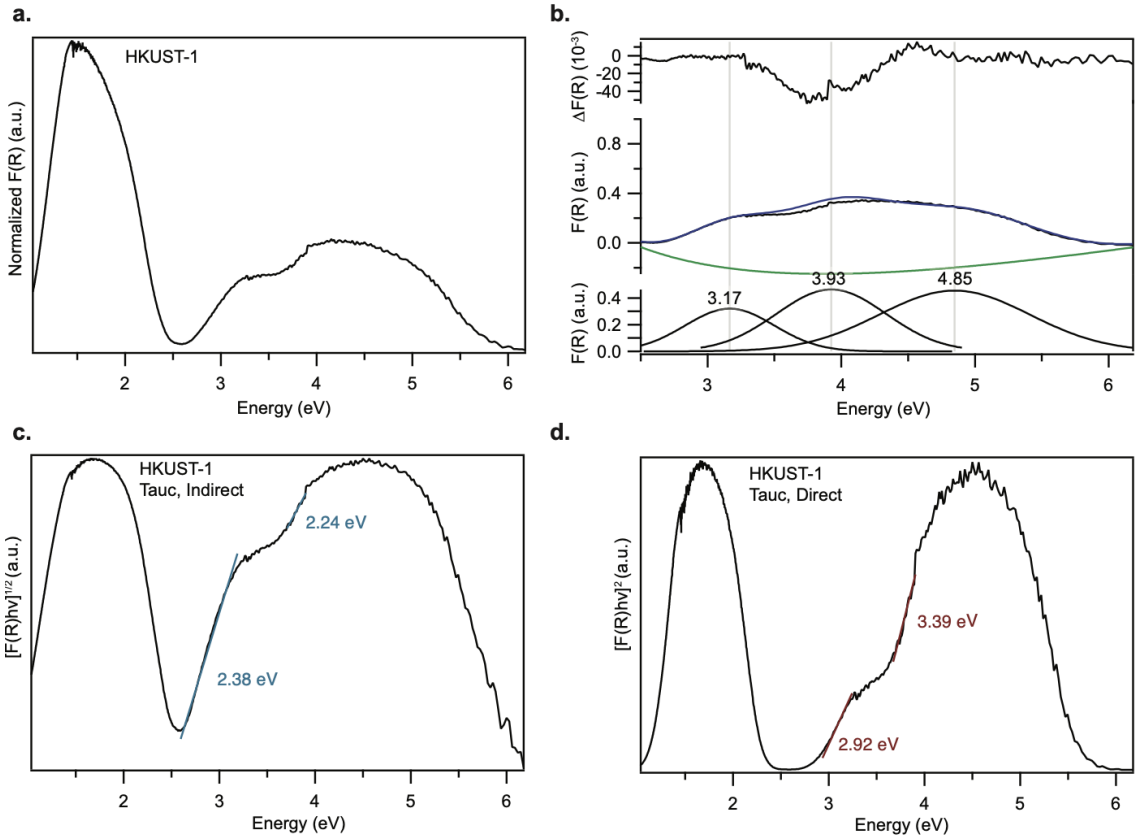

Figure B.16. Diffuse reflectance UV-vis data for HKUST-1/Cu3(BTC)2 **a)** Normalized data in Kubelka-Munk units. **b)** Gaussian fitting of normalized DRUV-vis data **c)** Tauc transformation and estimated band gap energy for an indirect assumption. **d)** Tauc transformation and estimated band gap for a direct assumption.

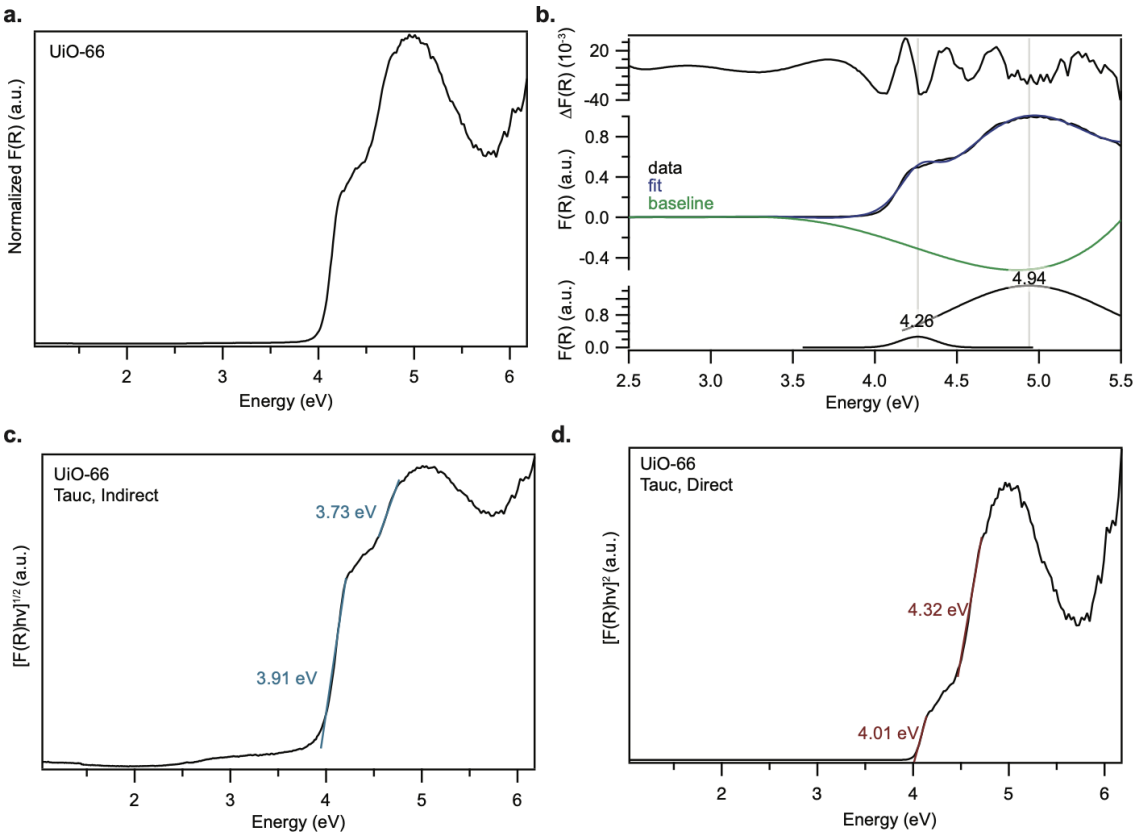

Figure B.17. Diffuse reflectance UV-vis data for UiO-66 **a)** Normalized data in Kubelka-Munk units. **b)** Gaussian fitting of normalized DRUV-vis data **c)** Tauc transformation and estimated band gap energy for an indirect assumption. **d)** Tauc transformation and estimated band gap for a direct assumption.

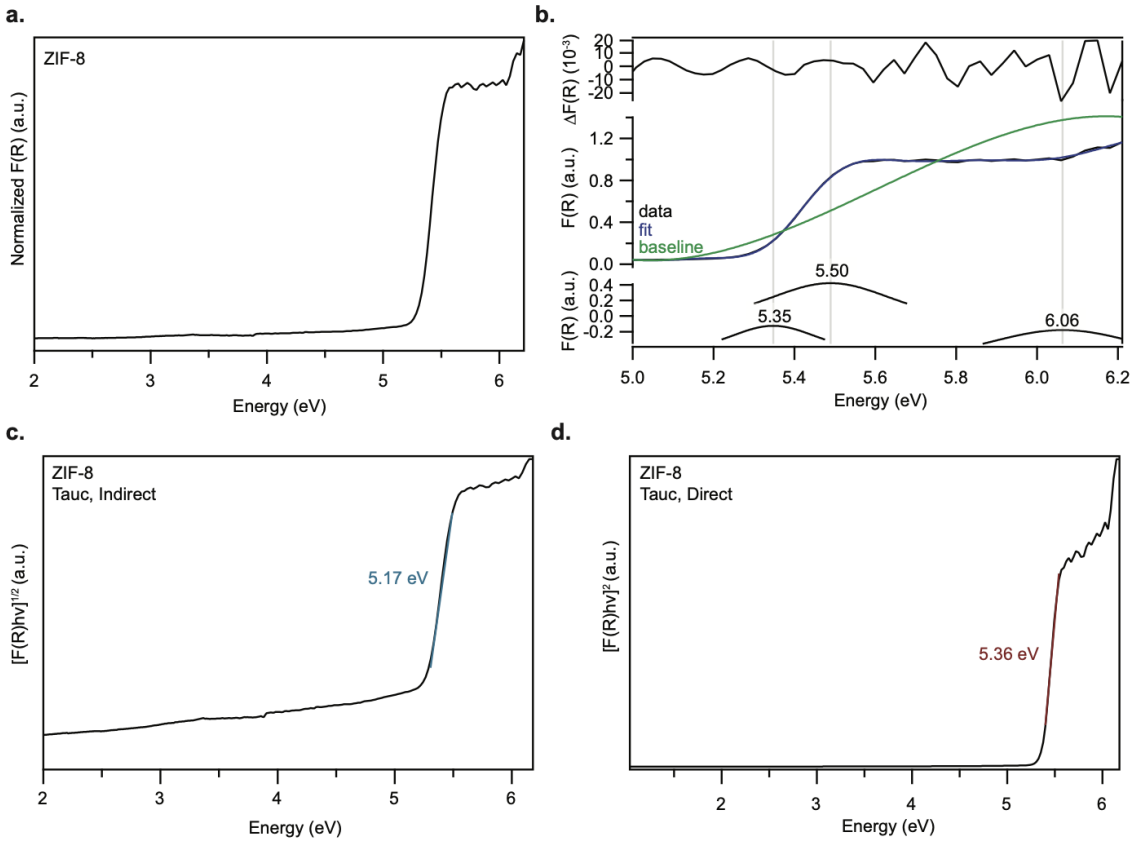

Figure B.18. Diffuse reflectance UV-vis data for ZIF-8 **a)** Normalized data in Kubelka-Munk units. **b)** Gaussian fitting of normalized DRUV-vis data **c)** Tauc transformation and estimated band gap energy for an indirect assumption. **d)** Tauc transformation and estimated band gap for a direct assumption.

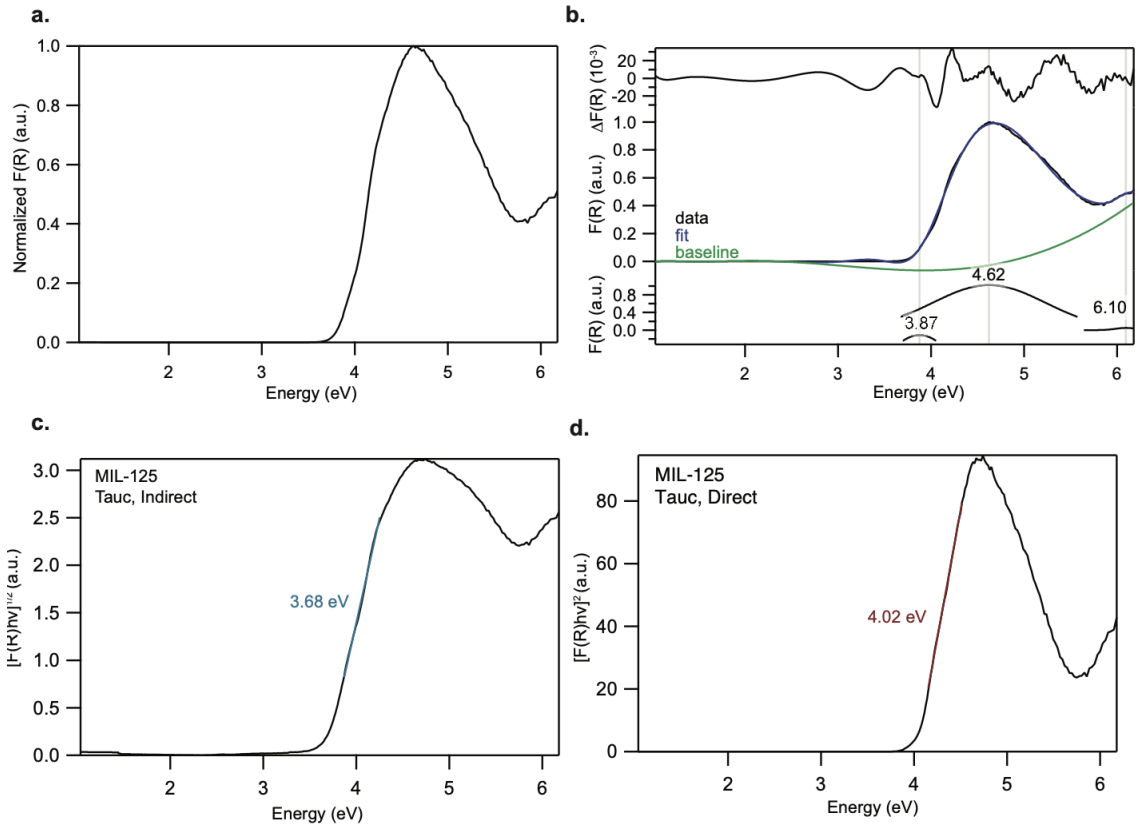

Figure B.19. Diffuse reflectance UV-vis data for MIL-125 **a)** Normalized data in Kubelka-Munk units. **b)** Gaussian fitting of normalized DRUV-vis data **c)** Tauc transformation and estimated band gap energy for an indirect assumption. **d)** Tauc transformation and estimated band gap for a direct assumption.

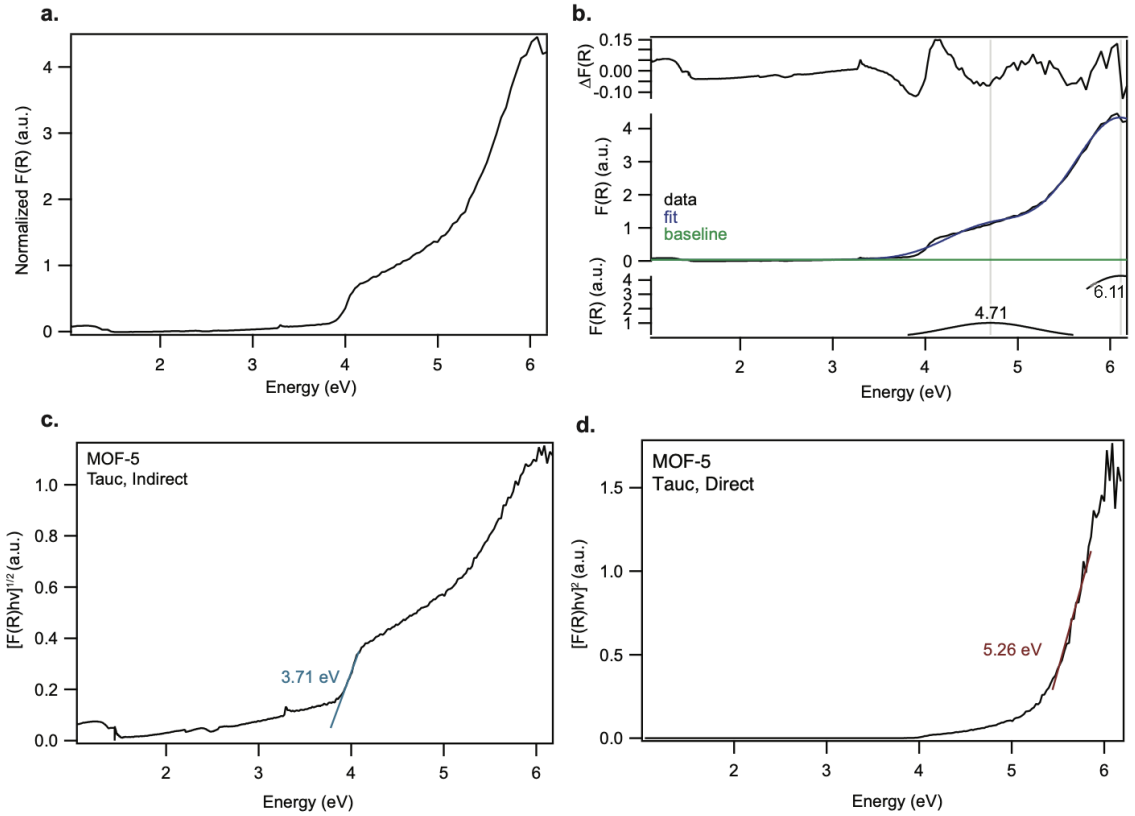

Figure B.20. Diffuse reflectance UV-vis data for MOF-5 **a)** Normalized data in Kubelka-Munk units. **b)** Gaussian fitting of normalized DRUV-vis data **c)** Tauc transformation and estimated band gap energy for an indirect assumption. **d)** Tauc transformation and estimated band gap for a direct assumption.

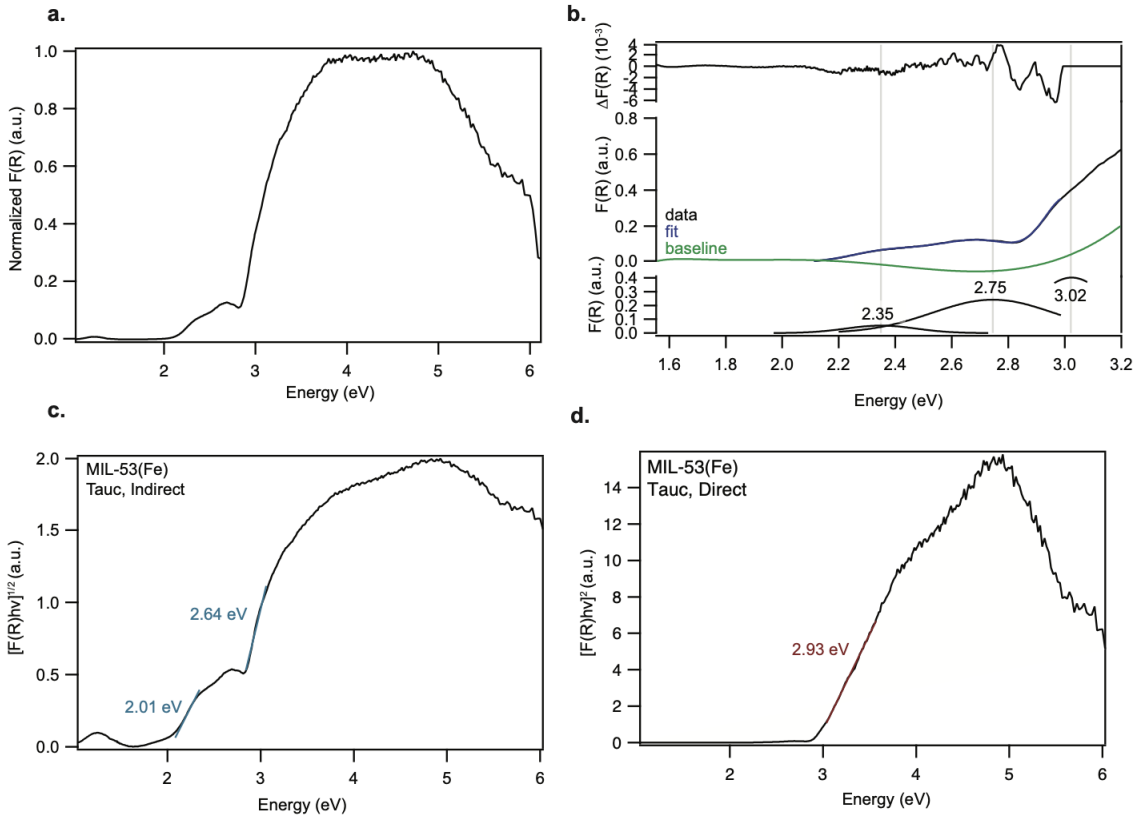

Figure B.21. Diffuse reflectance UV-vis data for MIL-53(Fe) **a)** Normalized data in Kubelka-Munk units. **b)** Gaussian fitting of normalized DRUV-vis data **c)** Tauc transformation and estimated band gap energy for an indirect assumption. **d)** Tauc transformation and estimated band gap for a direct assumption.

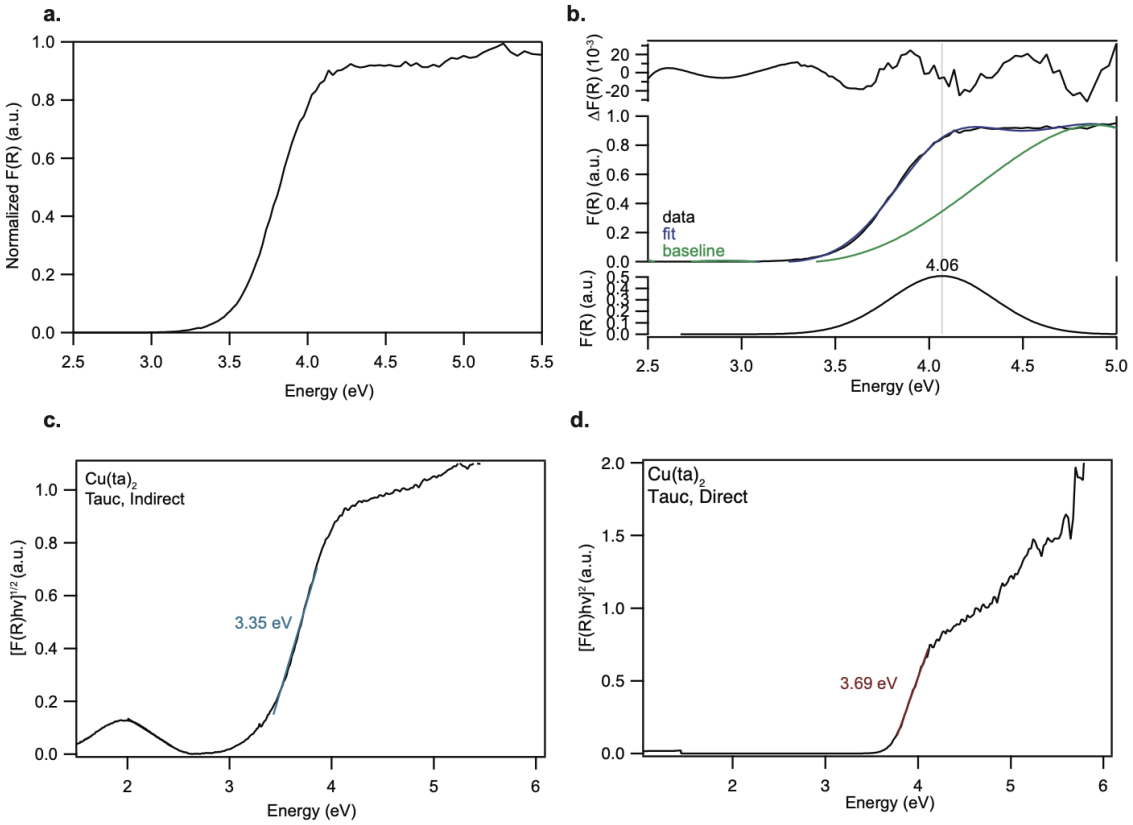

Figure B.22. Diffuse reflectance UV-vis data for Cu(triazolate)$_2$ **a)** Normalized data in Kubelka-Munk units. **b)** Gaussian fitting of normalized DRUV-vis data **c)** Tauc transformation and estimated band gap energy for an indirect assumption. **d)** Tauc transformation and estimated band gap for a direct assumption.

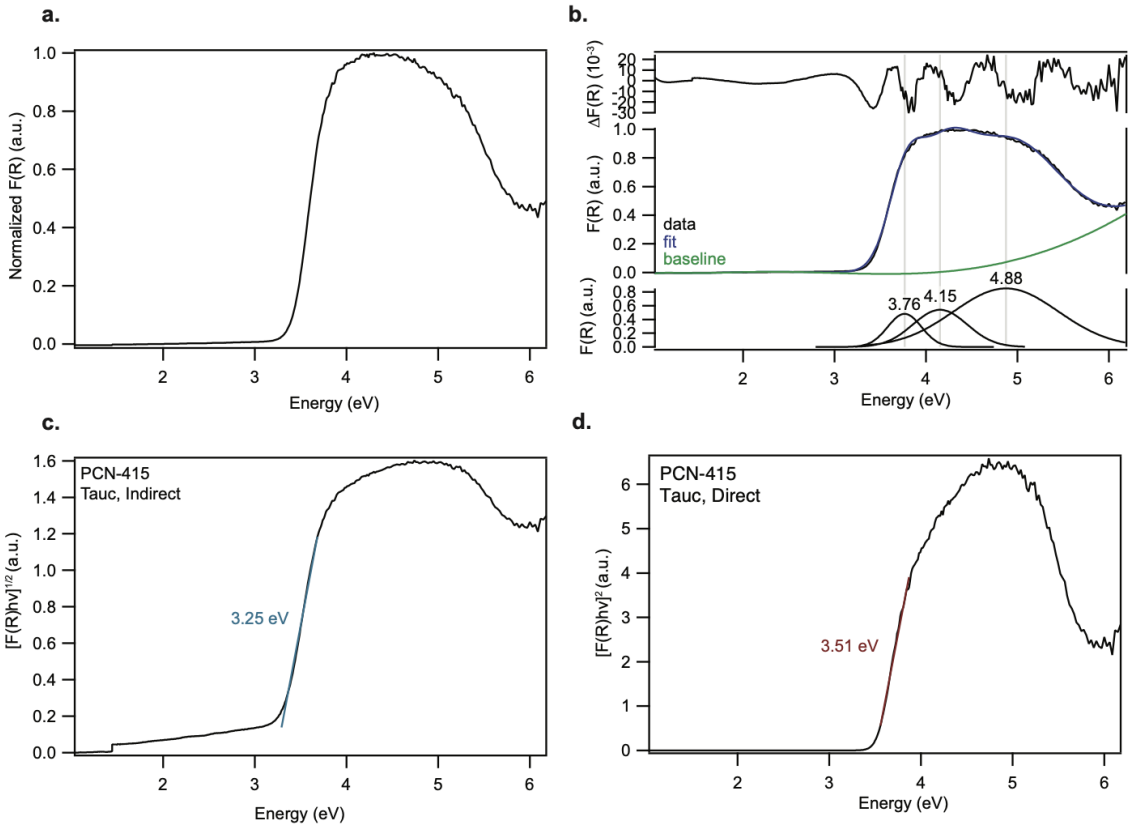

Figure B.23. Diffuse reflectance UV-vis data for PCN-415 **a)** Normalized data in Kubelka-Munk units. **b)** Gaussian fitting of normalized DRUV-vis data **c)** Tauc transformation and estimated band gap energy for an indirect assumption. **d)** Tauc transformation and estimated band gap for a direct assumption.

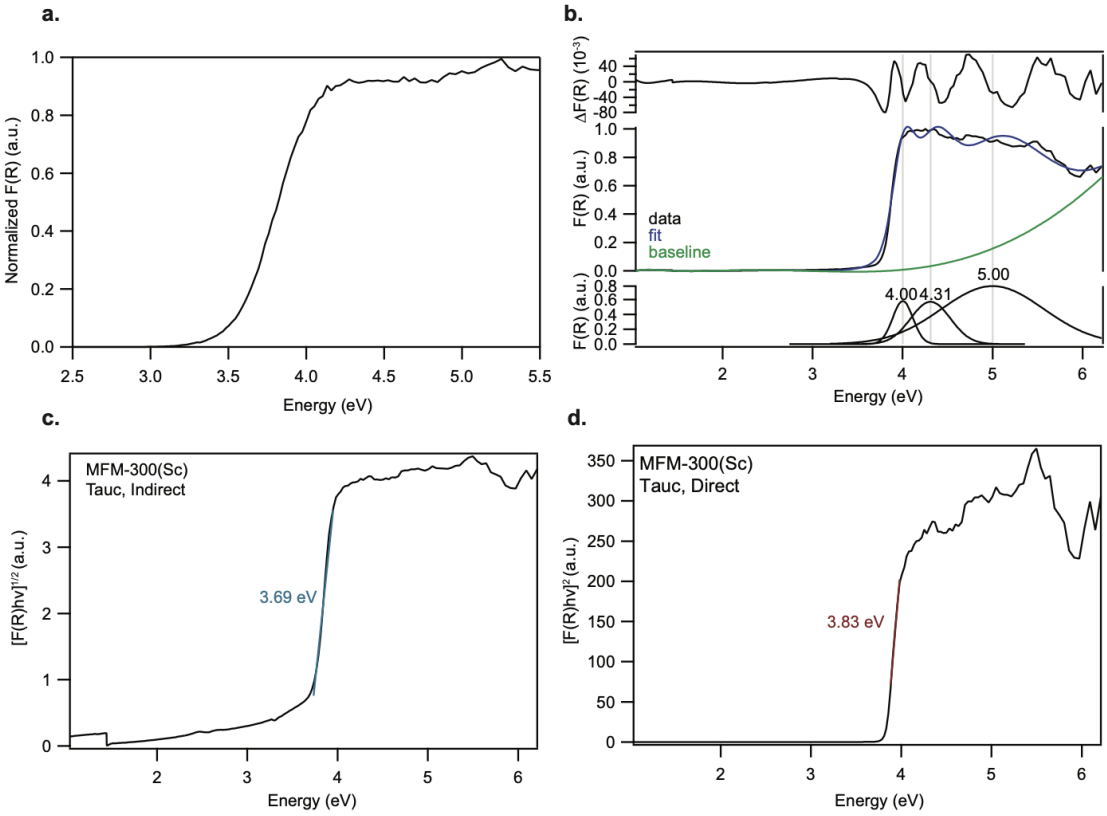

Figure B.24. Diffuse reflectance UV-vis data for MFM-300(Sc) **a)** Normalized data in Kubelka-Munk units. **b)** Gaussian fitting of normalized DRUV-vis data **c)** Tauc transformation and estimated band gap energy for an indirect assumption. **d)** Tauc transformation and estimated band gap for a direct assumption.

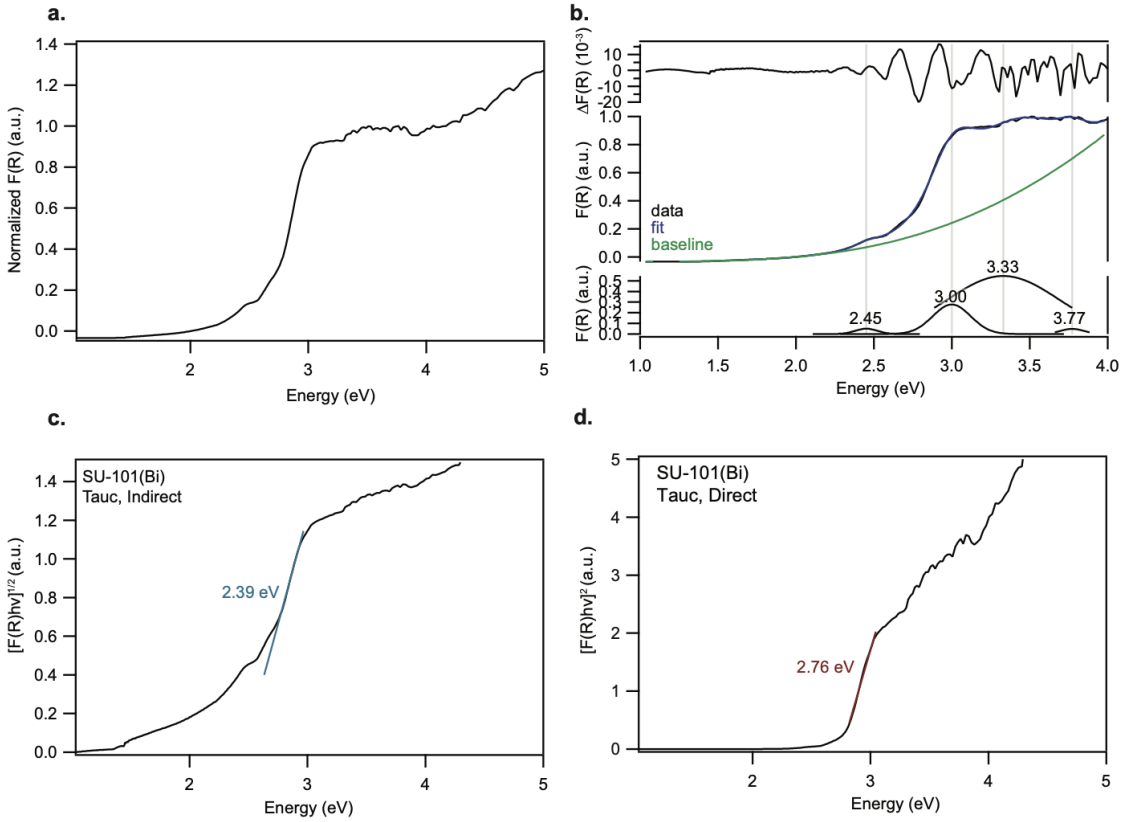

Figure B.25. Diffuse reflectance UV-vis data for SU-101(Bi). **a)** Normalized data in Kubelka-Munk units. **b)** Gaussian fitting of normalized DRUV-vis data **c)** Tauc transformation and estimated band gap energy for an indirect assumption. **d)** Tauc transformation and estimated band gap for a direct assumption.

Literature Gaussian Fits of MOF-5 and MIL-125

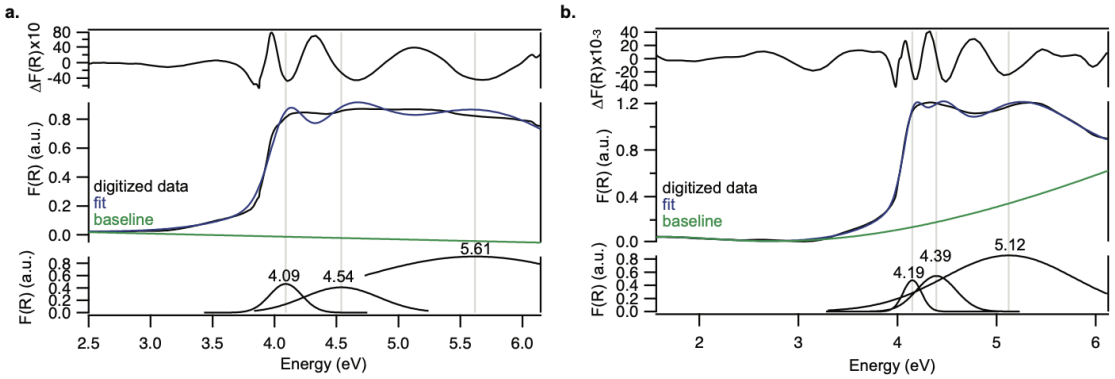

Figure B.26. Diffuse reflectance data for MOF-5 digitized and fitted to Gaussian peaks. **a)** Data originally reported by Chen et al.,[233] Tauc analysis yielded an E_{opt} of 2.92 eV. **b)** Data originally reported by Hang et al.,[232] Tauc analysis yielded an E_{opt} of 3.86 eV.

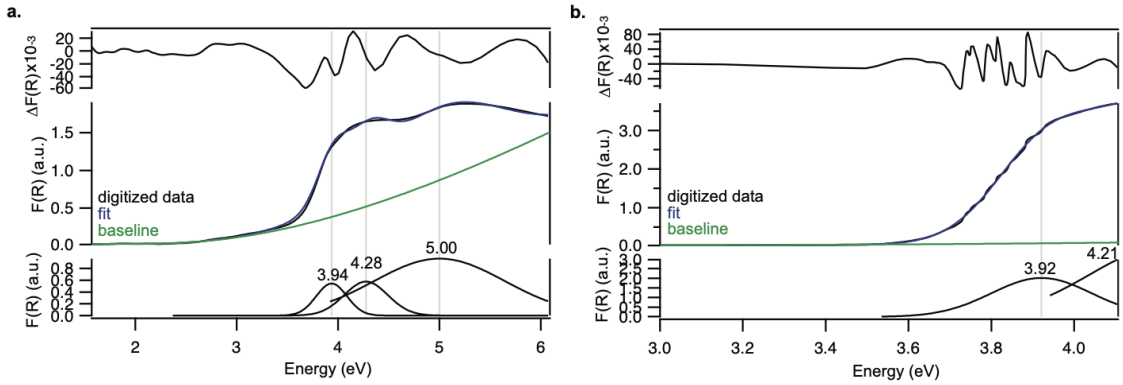

Figure B.27. Diffuse reflectance data for MIL-125 digitized and fitted to Gaussian peaks. **a)** Data originally reported by Hendon et al.,[41] Tauc analysis yielded an E_{opt} of 3.68 eV. **b)** Data originally reported by Wang et al.,[231] Tauc analysis yielded an E_{opt} of 3.8 eV.

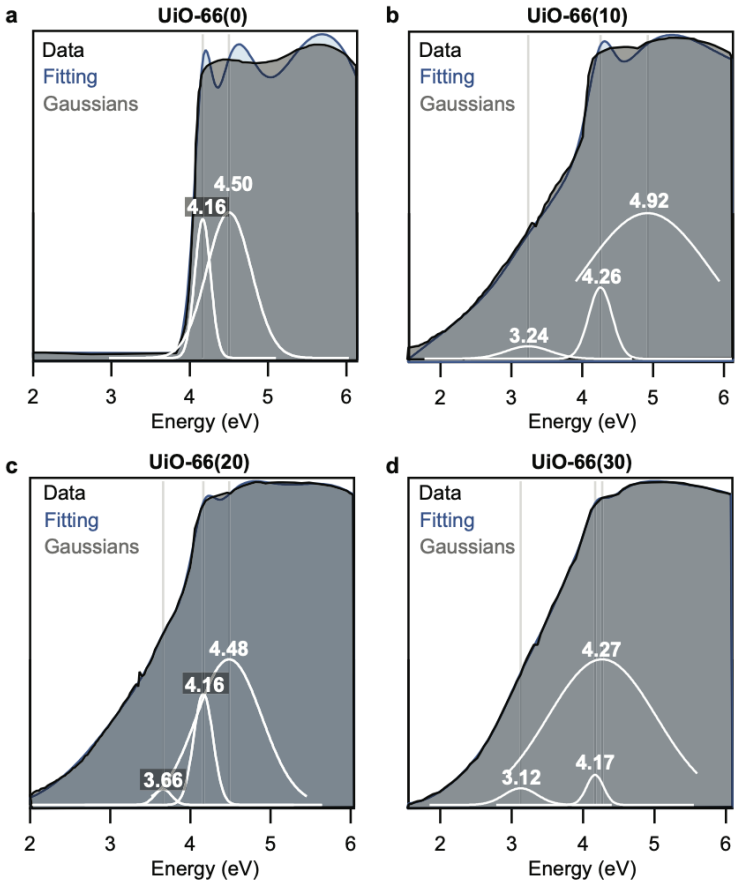

Figure B.28. Diffuse reflectance data for pristine and defective UiO-66 from Xiang et al.,[374] digitized and fitted to Gaussian peaks. **a)** UiO-66 with 0 min exposure to argon plasma, Tauc yielded an E_{opt} of 4.03 eV. **b)** UiO-66 with 10 min exposure to argon plasma, Tauc yielded an E_{opt} of 3.89 eV. **c)** UiO-66 with 20 min exposure to argon plasma, Tauc yielded an E_{opt} of 3.79 eV. **d)** UiO-66 with 30 min exposure to argon plasma, Tauc yielded an E_{opt} of 3.66 eV.

Computational Methods

Crystal structures of all MOFs were acquired and structural relaxation calculations were performed to obtain the lowest energy geometry with density functional theory (DFT) as implemented in the Vienna *ab initio* Simulation Package (VASP, version 5.4.4).[369] The geometric optimizations were performed using the GGA-PBEsol exchange correlation functional[368] with the appropriate k-point mesh corresponding to the dimensions of each crystal structure. The plane-

wave cutoff was set at 500 eV, with SCF convergence criterion of 1x10^{-6} eV and ionic convergence criterion of -0.005 eV per atom. Spin-polarized calculations were performed for all structures (unrestricted) except for HKUST-1 and Cu(TA)$_2$, where ferro-(FM) and antiferromagnetic (AFM) ordering were enforced.

The electronic band structure for each optimized structure was obtained with k-point mesh that sampled the special points within the Brillouin zone using the GGA-PBEsol exchange correlation functional. These band structures were used to elucidate if the band gap was direct or indirect. Hybrid functional-based electronic band structures were used for systems containing spin-polarized metals, where exchange may influence the frontier band ordering. To determine the band gap energy, a HSEsol06 hybrid exchange-correlation functional with 25% Hartree-Fock exchange was implemented.18 We note that the PBEsol geometry used for the single point HSEsol06 is technically no longer in equilibrium per Ref.[375]. A summary of functional dependence on geometry is presented in Ref.[219]. For MOFs with a direct band gap at the Γ point, the density-of-states along with valence band maxima (VBM) and conduction band minima (CBM) were calculated at the Brillouin zone-center (Γ point). For MOFs with indirect band gap or direct band gap at a different k-point, the appropriate k-point mesh was used to determine the most accurate band gap for such structures. Similar convergence criteria were set for these calculations.

Partial Density-of-States

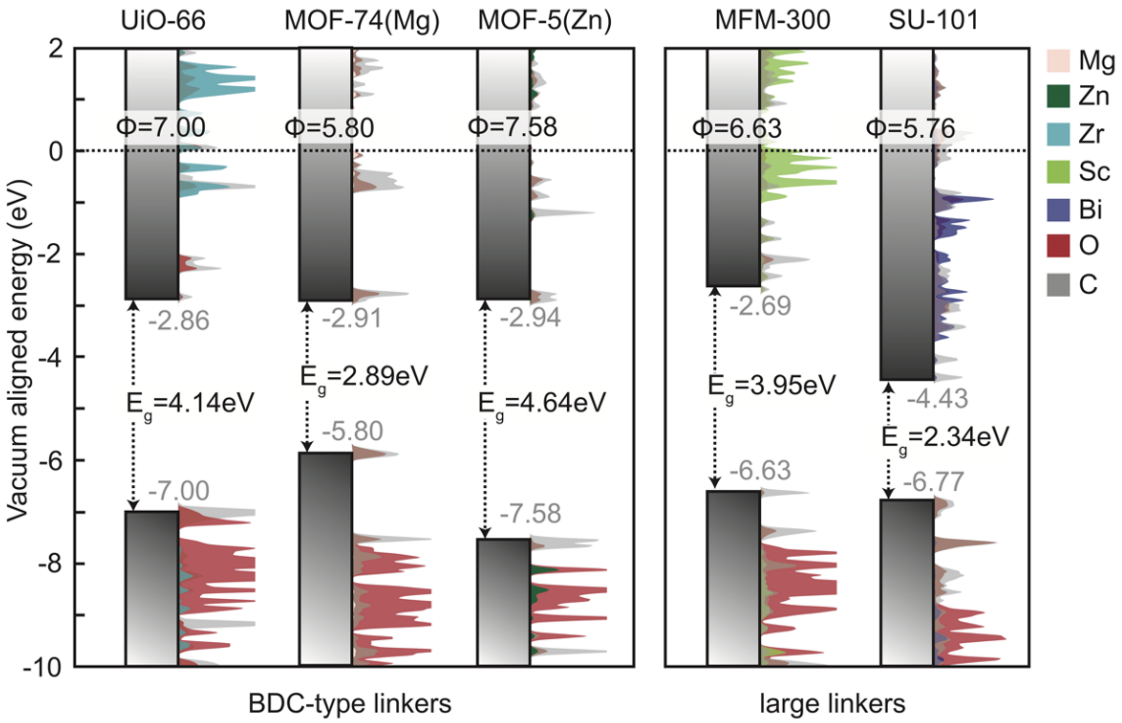

Figure B.29. Density-of-state and band gap aligned to vacuum level obtained from hybrid functionals for common MOFs with carboxylate acid linkers.

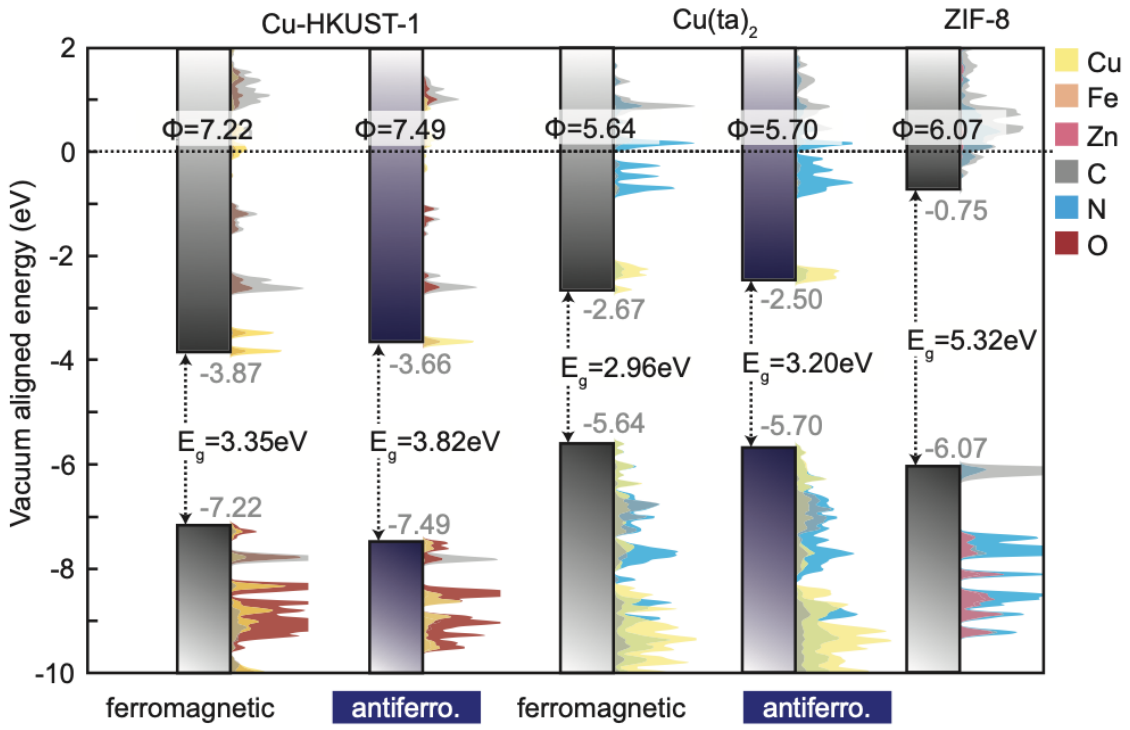

Figure B.30. Density-of-state and band gap aligned to vacuum level obtained from hybrid functionals for N-donor linker-based MOFs and for HKUST-1.

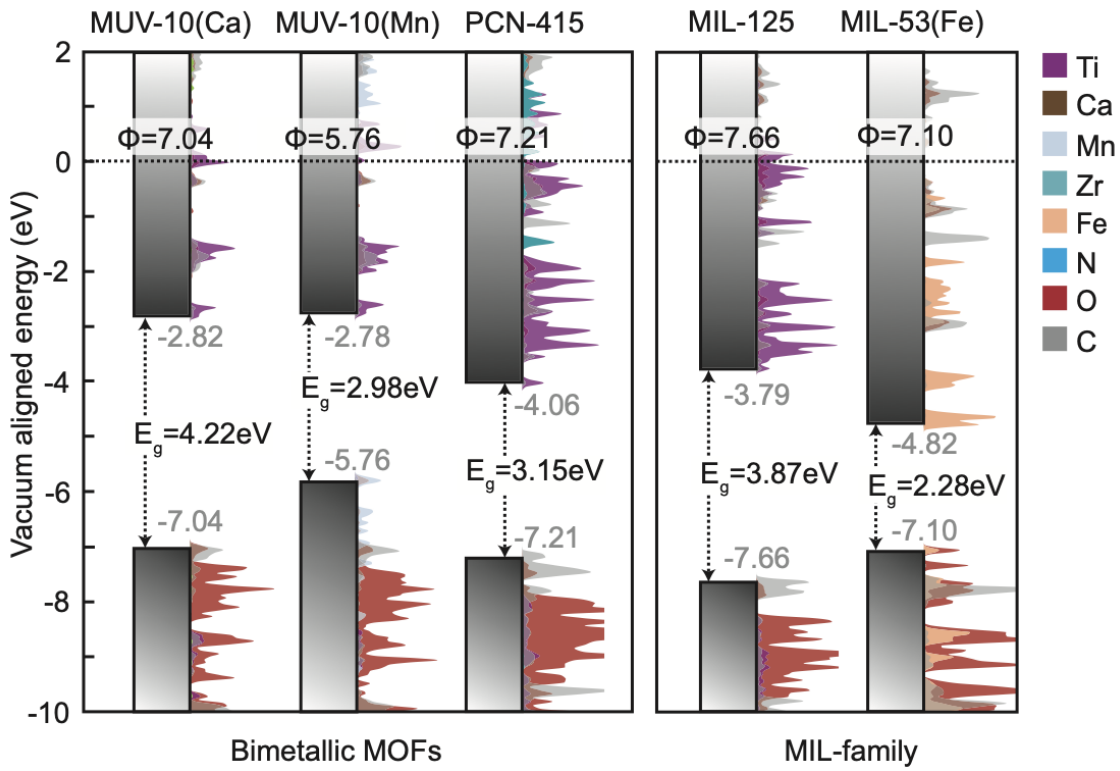

Figure B.31.]
Density-of-state and band gap aligned to vacuum level obtained from hybrid functionals for titanium-based MOFs and MIL-MOFs.

H^* pairs / cell	ΔE from empty (eV)	ΔE from empty per pair (eV)	ΔE to release single H_2 (eV)
2	-0.67	-0.67	0.67
4 – same node	-1.38	-0.69	0.72
6	-1.76	-0.59	0.38
8 – same node	-0.41	-0.10	-1.34
4 – 2 per node	-1.40	-0.70	
8 – 4 per node	-2.16	-0.54	
16 – 8 per node	-3.12	-0.39	

Table C.1. Compilation of total energy changes in two node unit cell with increasing numbers of hydrogen atoms (i.e PCET events) paired at bridging oxo pairs between titanium atoms in a computational unit cell containing two inorganic nodes, computed on a PBEsol optimized structure at the HSEsol06 level.

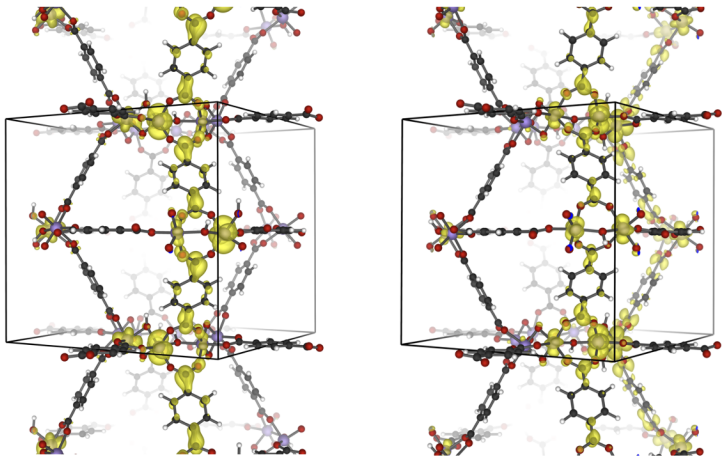

Figure C.1. The spin density associated with the radical after two PCET events occur at separate μ^2-oxo pairs in separate nodes (left), compared with the localization of spin-density on a single node with paired transfers (right) within the node.

The coupling of unpaired H^*-donated radicals through BDC antibonds is made more apparent at higher loadings. If four PCET events occur at the same node (Figure C.4, equivalent to 2 e^-1/node throughout the material) each titanium is partially reduced and the conduction band states are nearly entirely localized within the node; in contrast, isolating the PCET events between different titanium

pairs forces spin density through the linker antibonds onto the metals of adjacent nodes, FigureC.3.

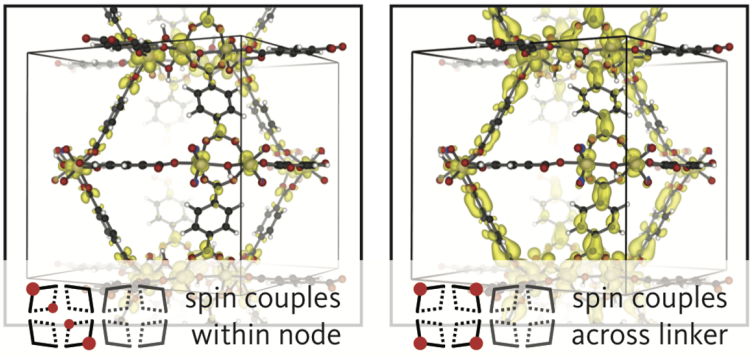

Figure C.2. The spin density for all four conduction band electrons when four PCET events occur on a single node **a)** localizes within the node when matched between disparate sets of titanium pairs, but **b)** fill organic antibonding orbitals when the individual PCET are spread across each 2-oxo pair within the node.

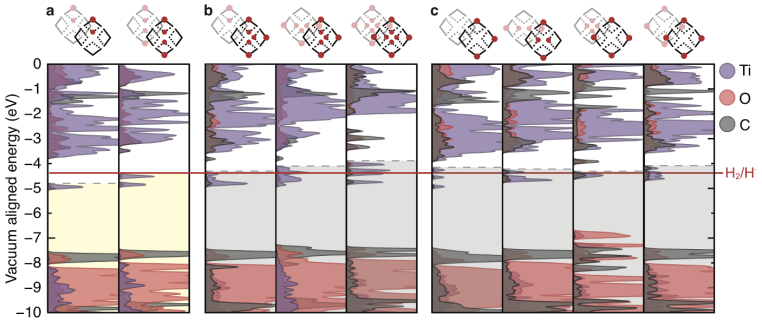

Figure C.3. Atom-projected density of states for a range of configurations and dopant concentrations sampled for this study that were otherwise not discussed in the body of the article—the most favorable conformations occur when bridging oxo pairs are both protonated during subsequent/concurrent PCET events as is apparent in the purple and red sections depicting a range of two and four PCET event possibilities.

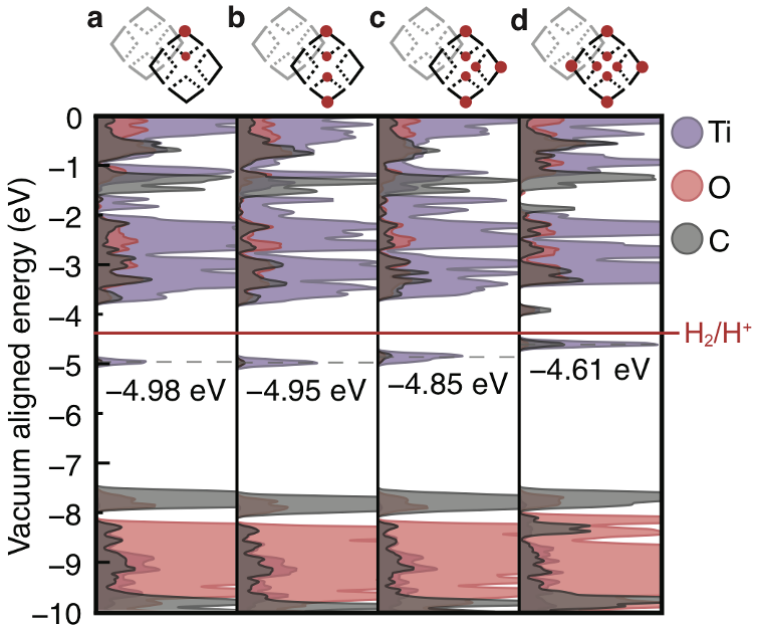

Figure C.4. Atom-projected density of states for MIL-125 with **(a)** two, **(b)** four, **(c)** six, and **(d)** eight pairs of PCET events adding to the same bridging oxo pairs of the same node showing the reaction is net-favorable up to full saturation of the node – however this too can be forced by application of a chemical reductant and coordinating Na^+ counterions.[142]

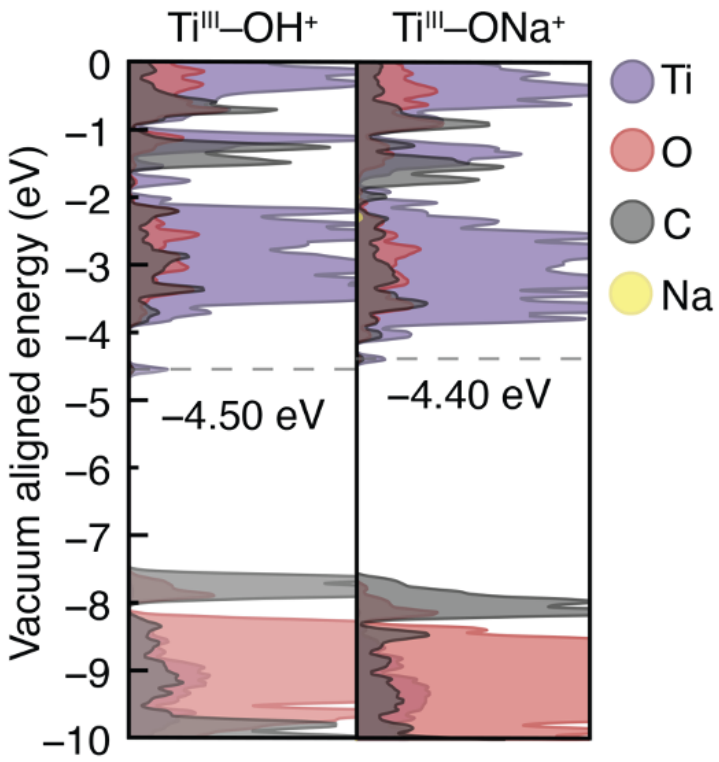

Figure C.5. A comparison of proton-coupled and sodium coupled reduction of MIL-125.

Vacuum alignment procedure

All VASP-recovered energy values were referenced to the vacuum potential by subtracting the background potential applied to the unit cell as located within the center of the largest pore. This value was obtained using the open-source code MacroDensity[217] by sampling the potential at the origin of unit cell – a plateaued potential was identified at this location by performing a scan of the potential change across the diagonal of the unit cell.

Experimental Methods

Materials and Characterization. All commercial chemicals were used as received unless stated otherwise. Titanium (IV) ethoxide (99.99%-Ti, Strem Chemicals), terephthalic acid (98% Sigma Aldrich), N,N-dimethylformamide (DMF,

ACS grade, Fisher Scientific), methanol (HPLC grade, Fisher Scientific), 1,3,5-trimethoxybenzene (99.0%, Sigma Aldrich), benzyl alcohol (BnOH, 100%, Alfa Aesar), and dimethyl sulfoxide-d6 (DMSO-d6, Cambridge Isotope). Solvothermal syntheses were conducted in 100-mL Duran Schott bottles unless otherwise stated. Sample purity was verified by powder X-Ray diffraction (PXRD) with a Bruker D2 Phaser benchtop diffractometer. Photoirradiations were carried out using a mercury arc lamp. H NMR spectra were recorded at 600 MHz, $d_1 = 30$ s, on a Bruker Advance-III-HD NMR spectrometer.

MIL-125 Synthesis. Following a procedure adapted from Dan-Hardi et. al,3 terephthalic acid (0.748 g, 4.50 mmol), N,N-dimethylformamide (DMF, 9 mL) and methanol (1 mL) were added to a Pyrex jar and sonicated for ca. 5 min to ensure complete dissolution. Under an N_2 environment, titanium (IV) ethoxide (0.684 g, 3 mmol) was added to the mixture. The reaction mixture was sealed under N_2 and heated at 150 ^{o}C for 18 hr. The contents were isolated by sequential centrifugation and decanting the mother liquor. To clean the product, the material was soaked in fresh DMF (10 mL 3×), methanol (10 mL 3×), and acetone (10 mL 3×). The product was dried using Schlenk line technique under dynamic vacuum at 180 ^{o}C and transferred into a N_2 glovebox for analysis.

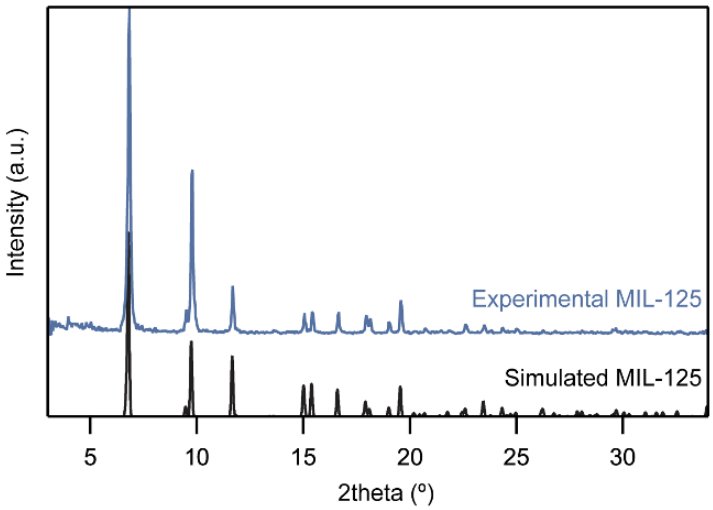

Figure C.6. Experimentally determined powder X-ray diffraction pattern versus the simulated pattern for MIL-125.

q-^{1}H NMR Photodoping. In an N_2 glove box, MIL-125 (10 mg) was placed in an air-free quartz cuvette with a small stir bar, DMSO-d_6, and an amount of BnOH (added either neat, or dilute in DMSO-d_6). The cuvette was sealed and irradiated with a mercury arc lamp while stirring. The solution was then centrifuged after irradiation, the liquid is decanted, and the standard (1,3,5-trimethoxybenzene, 10 mg) was added for quantitative analysis. After dissolution, an aliquot was taken for ^{1}H NMR and mixed with additional deuterated solvent.

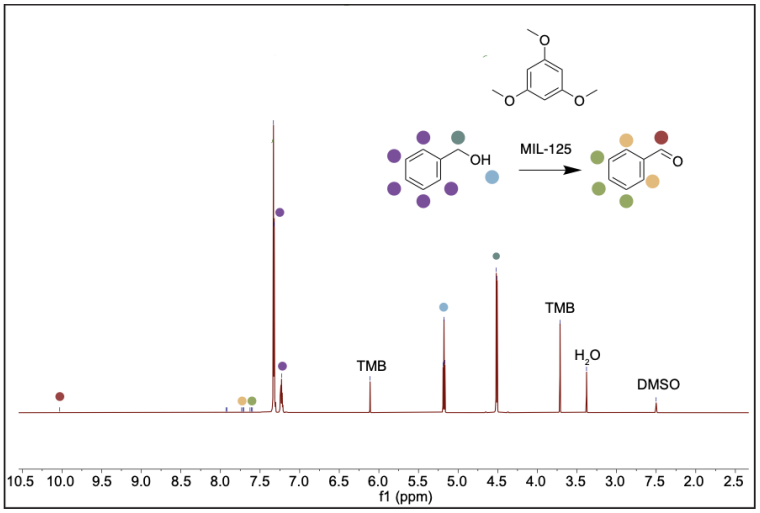

Figure C.7. ^{1}H NMR spectra for an excess amount of BnOH. A large amount of BnOH is still present in solution, marked by difference in relative peak integrations, with the small emergence of expected shifts corresponding to benzaldehyde around 10 ppm.

Preparation and Reduction of $[FeCp^*_2][BF_4]$. In an N_2 glovebox, $FeCp^*_2$ was weighed into a Schlenk flask and dissolved in ca 5 mL hexanes. In air, benzoquinone was dissolved in ca 5 mL of ethyl ether, and HBF_4 was added. The $FeCp^*_2$ and benzoquinone solutions were combined by cannula transfer, creating a cloudy dark-green mixture. This solution was left to stir for one hour, and let stand for 30 minutes, yielding a green precipitate. The flask was transferred to a benchtop N_2 glovebox, where it was vacuum filtered and washed with dry hexanes (∼40 mL). Once transferred into an N_2 glovebox, the powder was dissolved in dry MeCN. The concentration of the solution was tested via UV vis by way of a dilution of 100 µL in 3 mL MeCN in an air-free quartz cuvette with pathlength 1 cm, and the concentration was determined to be 25.09 mM by the 30 min irr. abs value at 778 nm for an absorptivity coefficient of 488 $L \cdot mol^{-1}cm^{-1}$. 1 mg of MIL-125 was added to a mixture of 250 L of stock $[FeCp^*_2]^+$, 200 L dry ethanol (excess), and 3 mL dry MeCN for a total ratio of 1Ti:1.25 $FeCp^{*+}_2$. The cuvette

was irradiated with a mercury arc lamp, and the UV-vis spectra were recorded after allowing the powder to settle. After 23 hr of irradiation with a mercury arc photolysis lamp, the vibrant green solution had reached a steady yellow color, indicative of $FeCp^*_2$ formation. Using the initial absorbance values at t=0 hr and 23 hr, a relative concentration of $FeCp^{*+}_2$ to $FeCp^*_2$ can be calculated, and thus, a solution state Fermi level can be calculated using the Nernst equation displayed in Figure C.5.

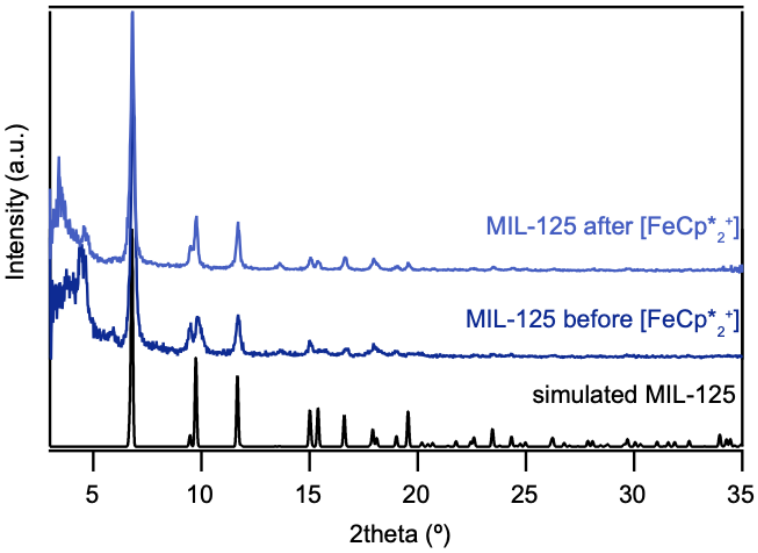

Figure C.8. PXRD of MIL-125 before and after treatment with $FeCp^{*+}_2$, displaying a full retention of its crystalline lattice and Bragg reflections.

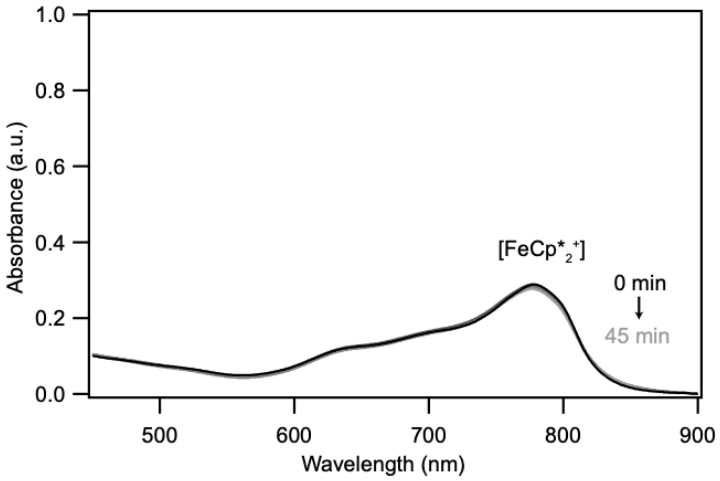

Figure C.9. Solution state UV-vis of a mixture of neat $FeCp_2^{*+}$ and ethanol, showing no reduction in absorbance after 45 min irradiation.

APPENDIX D: SUPPLEMENTARY INFORMATION FOR CHAPTER 3

Experimental Methods

Materials. All commercial chemicals were used as received unless stated otherwise. Titanium(IV) methoxide (95%, Sigma-Aldrich), titanium(IV) ethoxide (Strem Chemicals), titanium(IV) butoxide (TCI Chemicals), titanium(IV) isopropoxide (97%, Sigma-Aldrich), titanocene dichloride (TCI Chemicals), 1,4-benzenedicarboxylic acid (terephthalic acid, Sigma-Aldrich), 2-amino-1,4-benzenedicarboxylic acid (2-aminoterephthalic acid, Sigma-Aldrich), methanol (ACS grade, Fisher Scientific), N,N-dimethylformamide (DMF, ACS grade, Fisher Scientific), benzoic acid (JT Baker), p-toluic acid (MCB), 4-fluorobenzoic acid (Sigma-Aldrich), glacial acetic acid (ACS grade, Fisher Scientific), and tetrabutylammonium hexafluorophosphate (98%, Sigma-Aldrich, recrystallized 3× from ethanol).

Characterization. Sample purity was verified by powder X-Ray diffraction (PXRD) with a Bruker D2 Phaser benchtop diffractometer and infrared spectroscopy (IR) using a Bruker Alpha II compact IR with an ATR attachment in a N_2 glovebox. UV-vis-NIR spectra were collected on an Agilent Cary 5000 UV-Vis-NIR spectrophotometer in the range of 190-2200 nm or a Shimadzu Biospec-1601 and all samples were collected with a baseline solvent mixture matching the sample medium. Photoluminescence data was collected on a Horiba Jobin Yvon Fluoromax-4 Fluorimeter with an excitation wavelength of 280 nm. No fluorescence was observed in pure solvent. Gaussian fittings were performed in Igor Pro Version 6.37 using the Multipeak Fitting 2 package. For N_2 sorption experiments, samples were washed twice with DMF, MeOH, acetone, and hexanes as recommended from

Howarth *et al.*19. Samples were suspended in analysis tubes before being dried on a Schlenk at ambient temperature. Then, samples were degassed under high vacuum at 140 ^{o}C on a Micromeritics ASAP 2020, and degassing was considered complete when the outgas rate fell below 2.5 μtorr/min. All solution-state electrochemical data was collected using a Biologic SP200 in a N_2-filled glovebox. For acid digestion ^{1}H-NMR, samples were washed with methanol (3×, 10 mL) before being dried under vacuum and digested in a 20% DCl/D_2O in DMSO-d_6 mixture in air. Undissolved solids were separated by centrifugation, and the supernatant was analyzed using a Bruker Advance III-HD 600 NMR spectrometer. Scanning electron microscopy (SEM) was performed using a FEI Helios 600i instrument with 5.0 kV energy and 0.69 nA current. SEM samples were prepared by drop-casting MIL-125 suspensions onto clean silicon substrates and drying under N_2 flow. Particle sizing was performed in ImageJ using the line tool to determine crystal diameter, and histograms created in Igor Pro 6.37. The polydispersity index (PDI) was calculated by dividing the standard deviation of the Gaussian fit by the mean particle size.

Modulated Synthesis of MIL-125 NPs. A two-neck round-bottom flask fitted with a reflux condenser was charged with H_2BDC (0.352 g, 2.12 mmol) and dry DMF (5 mL). The reaction was then allowed to stir at 110 ^{o}C for 30 min. After complete dissolution of the linker, methanol (1.5 mL) and modulator were added, and the solution continued to stir under reflux for an additional 30 min. Next, the Ti^{4+} source (1.23 mmol) was added by syringe and the reaction was vigorously stirred at 110 ^{o}C under reflux. Once a precipitate was observed, aliquots ($<$ 500 μL) were taken from the reaction mixture and centrifuged at 13200 rpm for 3 min, then washed sequentially with 3 mL of cold DMF and MeOH before

crystallinity was confirmed by PXRD. Once the reaction was deemed complete by PXRD, an excess (∼20 mL) of cold DMF was added to the reaction mixture to halt the reaction. The final nanoparticles were collected by centrifugation and subsequently washed with 15 mL of cold DMF twice and then MeOH twice, and finally suspended and sonicated in fresh MeOH. For the scaled reaction, all reactants are simply increased by 3- or 10-fold.

Controlled Addition of Water to MIL-125 NP Syntheses. All manipulations were performed under an N_2-atmosphere with Schlenk techniques. Otherwise, the procedure was analogous to the modulated synthesis of MIL-125 NPs described above. All glassware was heated and dried at 120 ^{o}C and cycled 3× between vacuum and N_2 before use. MilliQ H_2O was added to DMF before modulator addition in concentrations 0.1, 0.25, 0.50, 1.0, or 2.0% v/v to DMF.

Synthesis of 38 nm NH_2-MIL-125 NPs. In a manner analogous to the synthesis of MIL-125 NPs, dry DMF (5 mL) was combined in a small glass vial with H_2O (5 µL). H_2BDC-NH_2 (0.364 g, 2.12 mmol) along with the dry, de-aerated DMF was added into a multi-neck round-bottom flask fitted with a reflux condenser. The reaction stirred at 110 ^{o}C in an oil bath under N_2 for 30 minutes, until the linker dissolved. Next, benzoic acid (1.18 g, 9.7 mmol) was added to the flask followed by methanol (1.5 mL) and stirred for 30 minutes. The Ti^{4+} source (1.23 mmol) was added, and the reaction was left to stir. Aliquots (500 µL) were taken periodically and centrifuged at 13200 rpm for 3 minutes. After, they were washed with DMF and MeOH and PXRD was taken to confirm crystallinity. Once crystallinity was confirmed, the rest of the reaction mixture was collected, and the same washing procedure was performed before drying the particles on a Schlenk line under vacuum and storing them in a scintillation vial until use.

Synthesis of 105 nm NH_2-MIL-125 NPs. In a modified procedure from Romero-Angel *et al.*,[280] a multi-neck RBF was fitted with a condenser and heated to 110 °C with an oil bath under N_2. The flask was charged with H_2BDC-NH_2 (0.3802 g, 2.12 mmol) and DMF (5 mL) and left to stir for 30 minutes. Dodecanoic acid (2.12g, 10.6 mmol) was then added followed by methanol (1.5 mL) and left to stir for 30 minutes. The Ti^{4+} source (1.23 mmol) was then added with a syringe through a septum while stirring. Aliquots (500 µL) were taken periodically to check for crystallinity by PXRD. Aliquots were centrifuged for 3 minutes at 13200 rpm and washed with DMF and MeOH. After the product was confirmed to be crystalline by PXRD, the reaction mixture was collected and washed by the same procedure used for the aliquots. The particles were then dried on a Schlenk line under vacuum and stored in a scintillation vial until use.

UV-Vis-NIR Photodoping of MIL-125 NPs. Concentrations of MIL-125 nanoparticle dispersions in methanol were determined by sonicating a "stock" solution and drying a 1 mL aliquot to determine the mass of an ensemble of activated nanoparticles. The concentrations of the "stock" solutions were thereby determined to be ∼20-30 mg/mL. A concentration of 0.025 mg/mL was deemed sufficient for achieving optical densities below 1.0 by UV-vis spectroscopy. Correspondingly, an amount of "stock" MIL-125 solution was washed with methanol (6×, 10 mL) and dried under vacuum at 110 ^{o}C to reach the final concentration of 0.025 mg/mL. The activated nanoparticles were redispersed in dry MeOH (10 mL) in an N_2 glovebox and sonicated for 30 min. to avoid particle aggregation. To a clean custom-made air-free quartz cuvette, 3.0 mL of the MIL-125 dispersion was transferred. Finally, the cuvette was irradiated for intermittent time intervals to record optical absorption spectra until no further changes are

noted in the UV-vis traces. For observation of Ti(III) d-d transitions, the procedure was identical, except that the concentration of MIL-125 NPs was increased to 0.10 mg/mL.

Cyclic Voltammetry and Open Circuit Voltage Measurements. Prior to electrochemical experiments, DMF was freeze-pump-thawed 6× and brought into an N_2 glovebox. The MIL-125 NPs were suspended in a 0.1-M $TBAPF_6$/DMF solution and transferred to a quartz cuvette fitted with a standard three-electrode cell with a platinum working electrode, a silver wire pseudo-reference electrode, and a platinum wire counter electrode. All electrodes were cleaned with dilute HNO3 before use. Data was collected in the range of -1.50 V to +1.50 V, and no Faradaic features were observed in background scans. At the end of all electrochemistry experiments, 10 mg of ferrocene was added to the solution to provide a quantitative measurement of $E_{1/2}$ versus Ag. For in situ photodoping while measuring OCV, the silver wire was shielded from the 308 nm LED to avoid photochemical degradation.

Computational Methods. A MIL-125 crystal structure was acquired from Walsh21 and truncated according to the "full linker sterics/electronics" procedure outlined by Mancuso *et al.* using Avogadro 1.2.0.22,23 Structural relaxation calculations were performed to obtain the lowest energy geometry with density functional theory (DFT) as implemented in the ORCA program system v5.0.3.24 The unconstrained geometry optimizations and orbital density calculations were performed using the RIJCOSX integral and B3LYP hybrid functional for an accurate depiction of Hartree-Fock exchange, with def2-SVP basis sets for organics (C, H, O) and def2-TZVP for titanium.

Summary of Particle Sizes and Sizing Methods

Mod:BDC	Scherrer Size (nm)	SEM Size (nm)
0	91.06	424
2.5	55.05	217
3	50.38	92.7
5	41.30	78.9
7	84.55	289
10	92.81	383

Table D.1. Comparison of crystal sizes by varying benzoic acid modulator equivalents (Mod:BDC) from PXRD and SEM.

Ti^{4+} source	Anion pKa	Scherrer Size (nm)	SEM Size (nm)
$Ti(OMe)_4$	15.50	43.49	42.7
$Ti(OEt)_4$	16.0	34.51	54.9
$Ti(OBu)_4$	16.95	41.30	78.9
$Ti(O^iPr)_4$	17.1	47.24	80.4
$TiCp_2Cl_2$	-	42.96	59.5

Table D.2. Comparison of crystal sizes by varying Ti^{4+} source anion identity from PXRD and SEM.

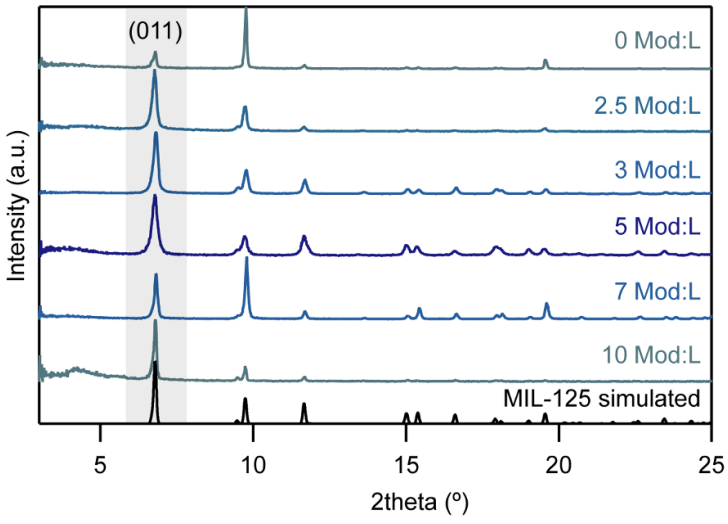

Figure D.1. PXRD pattern for all MIL-125 NCs synthesized with benzoic acid equivalents. The first reflection (011) is highlighted to emphasize peak broadening.

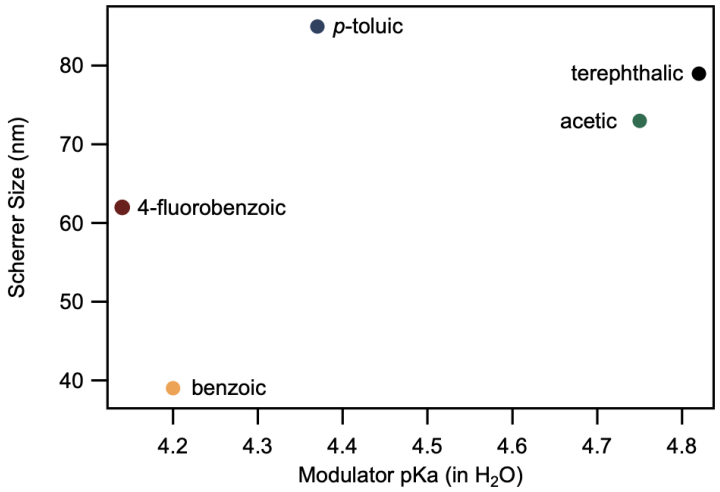

Figure D.2. Nanocrystal sizes of MIL-125 versus modulator pKa using 5 equivalents of modulator.

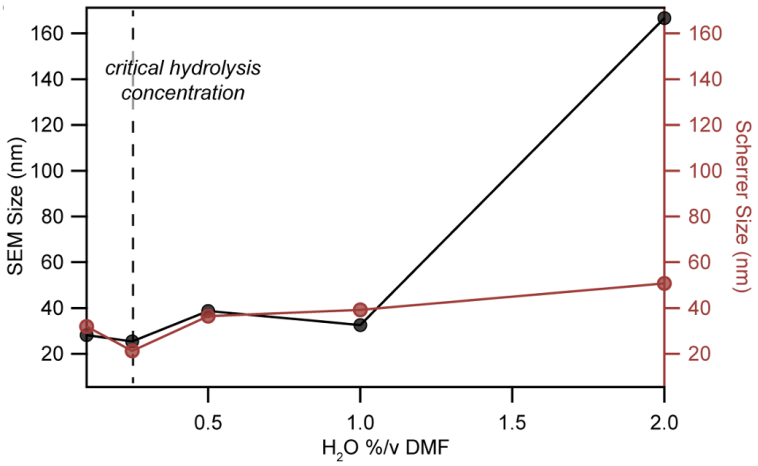

Figure D.3. Nanocrystal sizes of MIL-125 versus water content relative to DMF volume in the reaction solution.

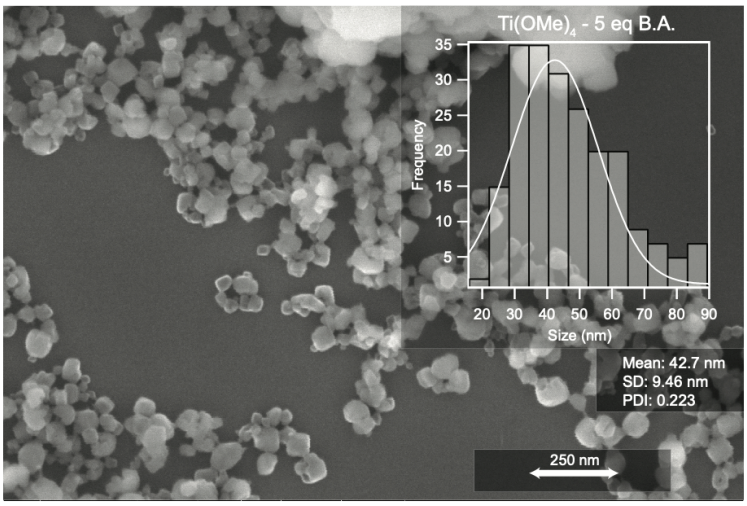

Figure D.4. SEM image and sizing histogram for MIL-125 NCs synthesized with 5 eq of benzoic acid to linker and using $Ti(OMe)_4$ as a Ti^{4+} source.

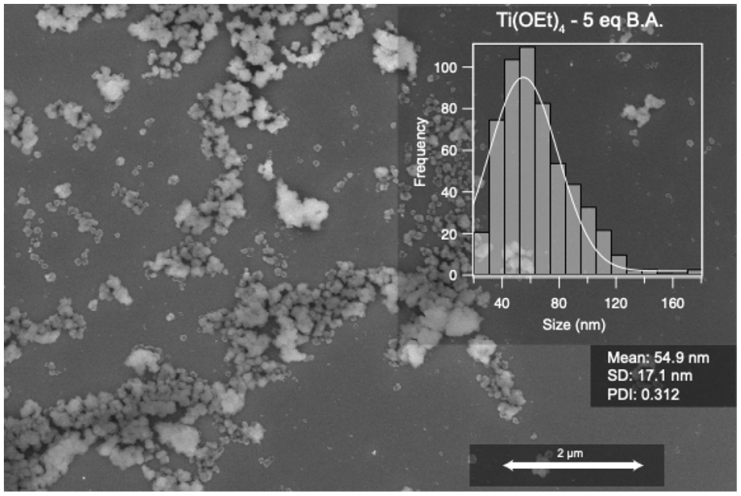

Figure D.5. SEM image and sizing histogram of MIL-125 NCs synthesized with 5 eq of benzoic acid equivalents for each linker and using $Ti(OEt)_4$ as a Ti^{4+} source.

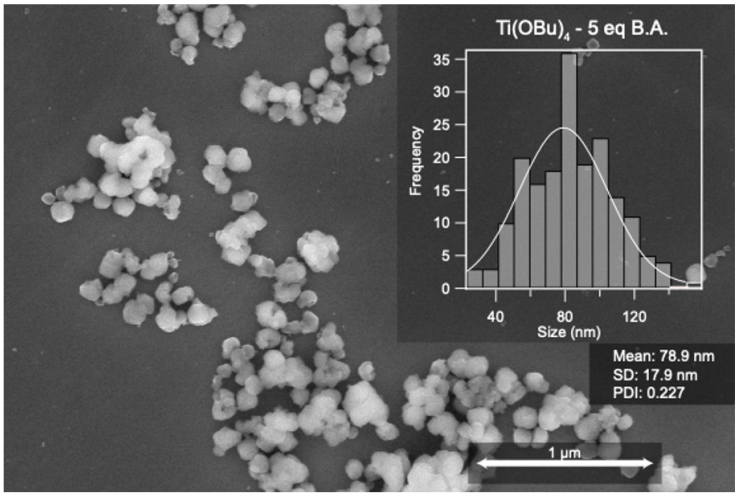

Figure D.6. SEM image and sizing histogram for MIL-125 NCs synthesized with 5 eq of benzoic acid equivalents for each linker and using $Ti(OBu)_4$ as a Ti^{4+} source.

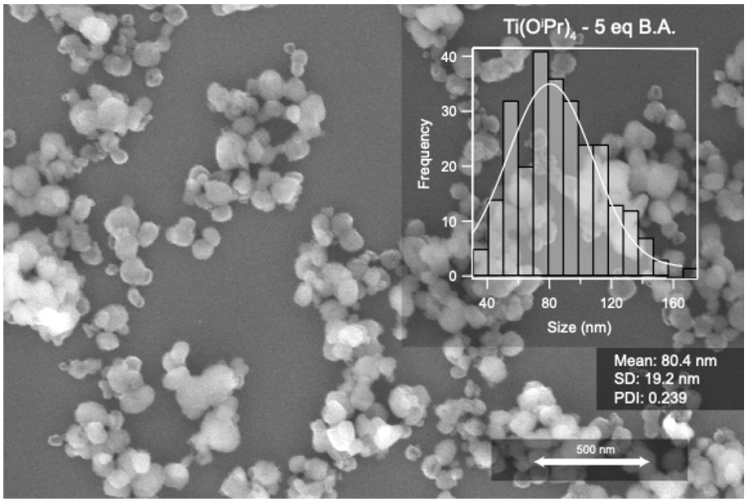

Figure D.7. SEM image and sizing histogram for MIL-125 NCs synthesized with 5 eq of benzoic acid equivalents for each linker and using $Ti(O^iPr)_4$ as a Ti^{4+} source.

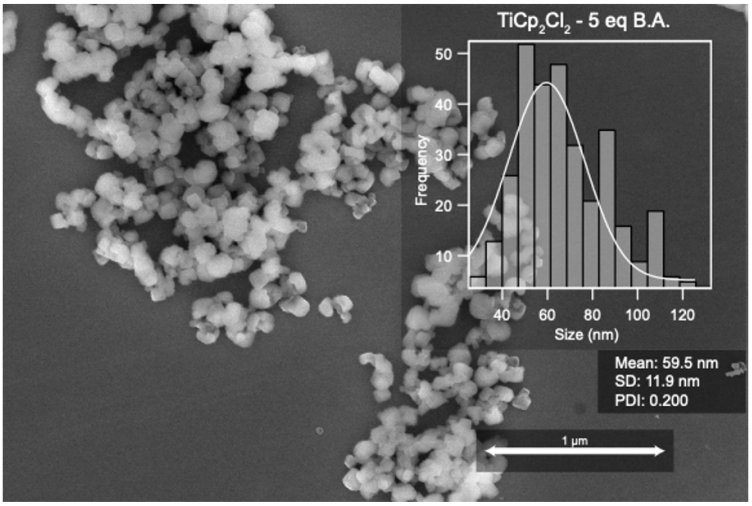

Figure D.8. SEM image and sizing histogram for MIL-125 NCs synthesized with 5 eq of benzoic acid equivalents for each linker and using $TiCp_2Cl_2$ as a Ti^{4+} source.

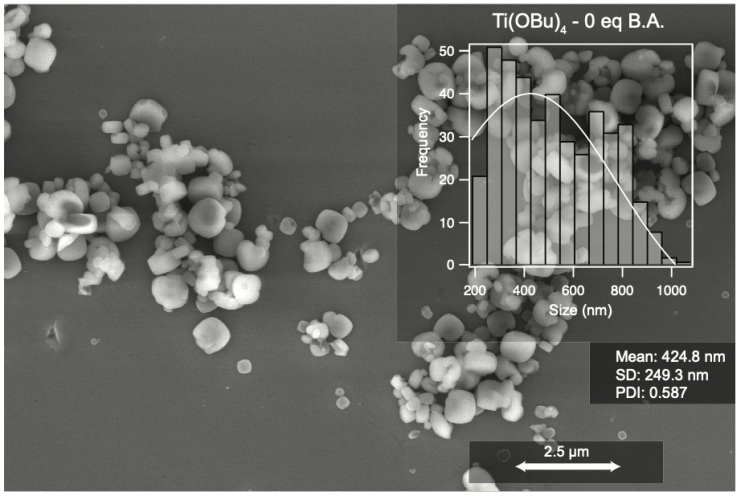

Figure D.9. SEM image and sizing histogram for MIL-125 NCs synthesized with 0 eq of benzoic acid for each linker and using $Ti(OBu)_4$ a Ti^{4+} source.

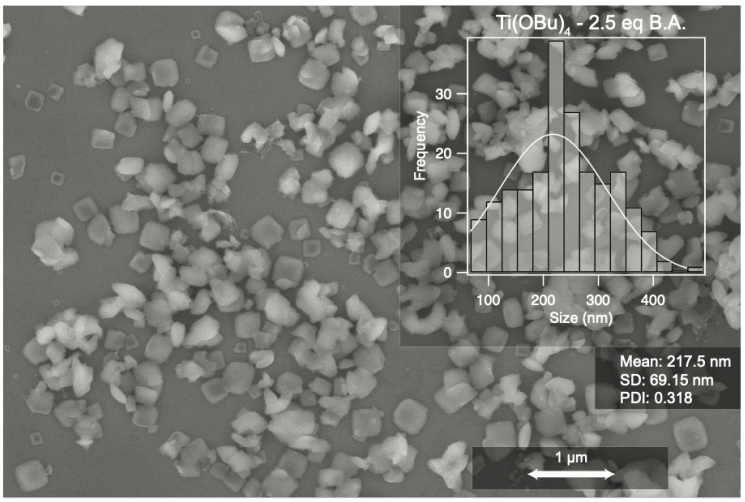

Figure D.10. SEM image and sizing histogram for MIL-125 NCs synthesized with 2.5 eq of benzoic acid for each linker and using $Ti(OBu)_4$ a Ti^{4+} source.

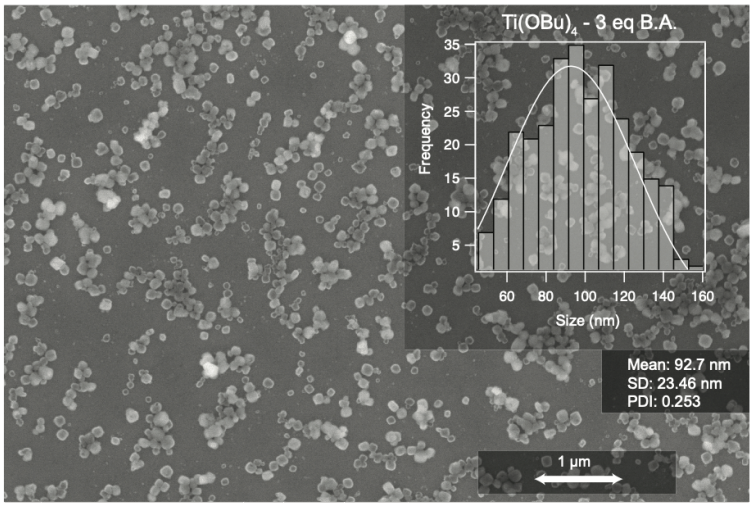

Figure D.11. SEM image and sizing histogram for MIL-125 NCs synthesized with 3 eq of benzoic acid for each linker and using $Ti(OBu)_4$ a Ti^{4+} source.

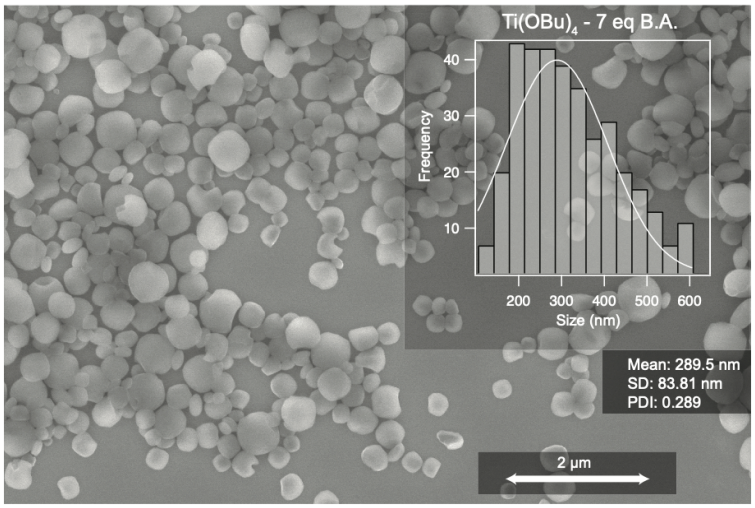

Figure D.12. SEM image and sizing histogram for MIL-125 NCs synthesized with 7 eq of benzoic acid for each linker and using $Ti(OBu)_4$ a Ti^{4+} source.

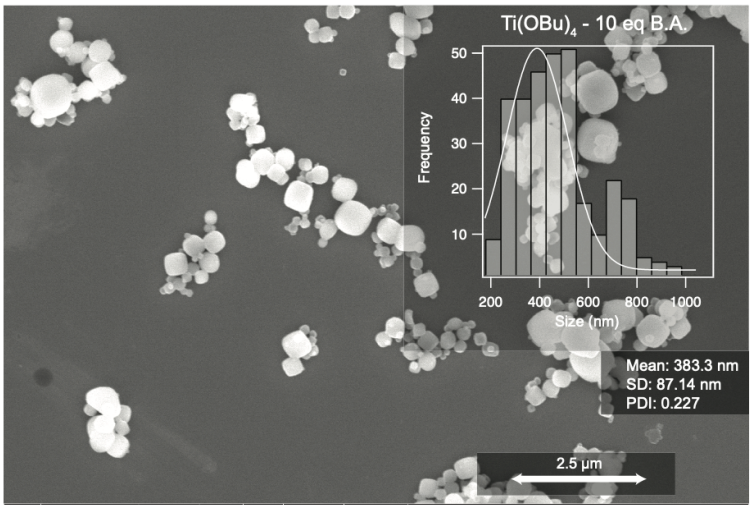

Figure D.13. SEM image and sizing histogram for MIL-125 NCs synthesized with 10 eq of benzoic acid for each linker and using $Ti(OBu)_4$ a Ti^{4+} source.

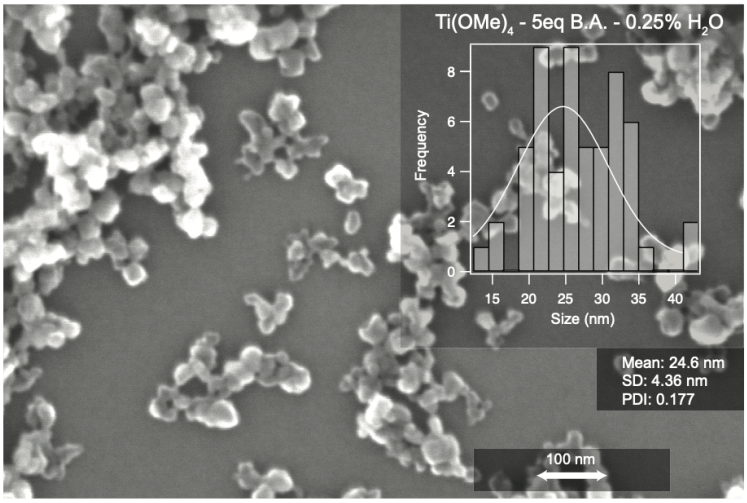

Figure D.14. SEM image and sizing histogram for MIL-125 NCs synthesized with 5 eq of benzoic acid for each linker, using $Ti(OBu)_4$ a Ti^{4+} source, and 0.25% H_2O relative to DMF in the reaction.

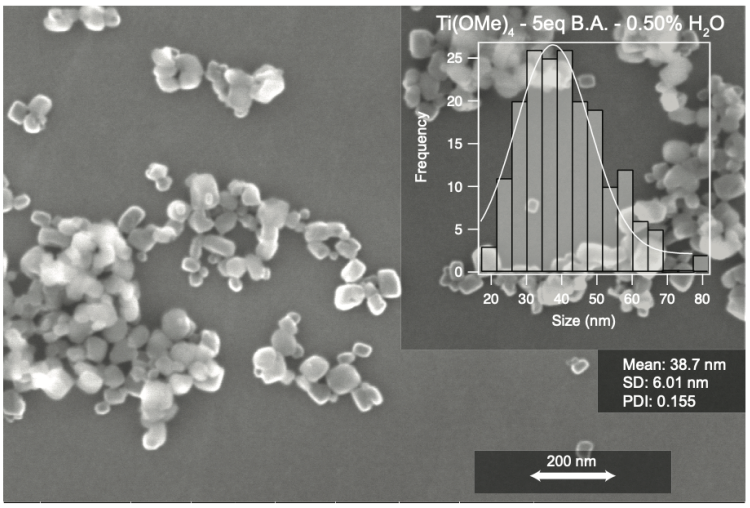

Figure D.15. SEM image and sizing histogram for MIL-125 NCs synthesized with 5 eq of benzoic acid for each linker, using $Ti(OBu)_4$ a Ti^{4+} source, and 0.50% H_2O relative to DMF in the reaction

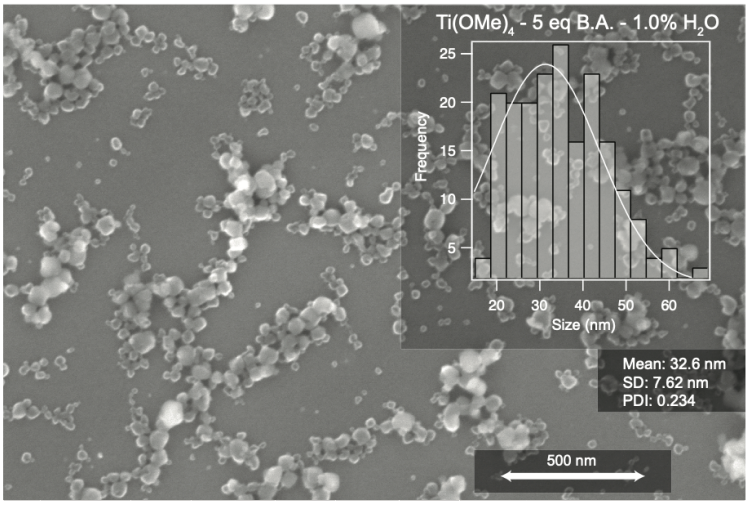

Figure D.16. SEM image and sizing histogram for MIL-125 NCs synthesized with 5 eq of benzoic acid for each linker, using $Ti(OBu)_4$ a Ti^{4+} source, and 1.0% H_2O relative to DMF in the reaction.

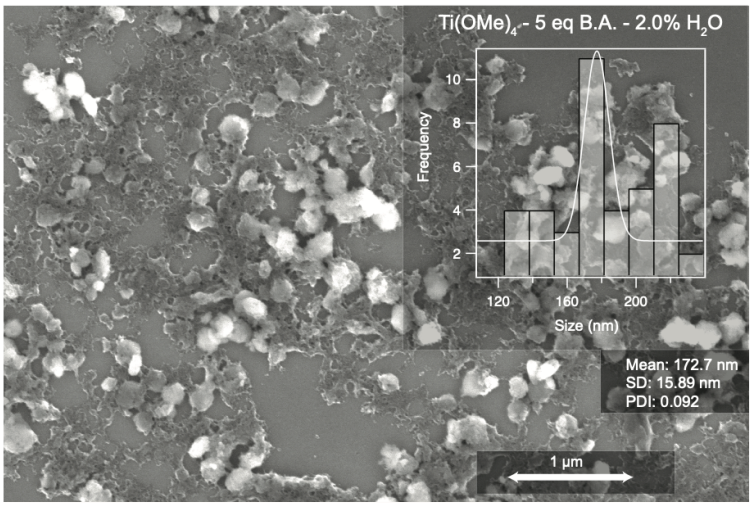

Figure D.17. SEM image and sizing histogram for MIL-125 NCs synthesized with 5 eq of benzoic acid for each linker, using $Ti(OBu)_4$ a Ti^{4+} source, and 2.0% H_2O relative to DMF in the reaction.

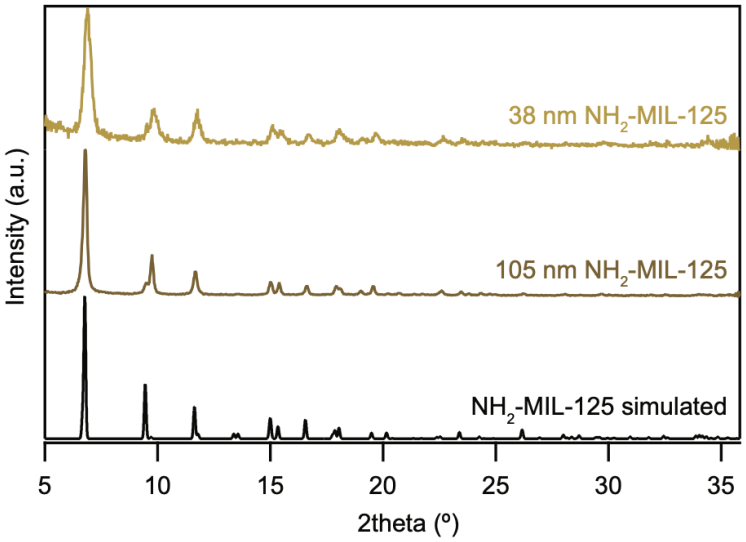

Figure D.18. PXRD patterns for all modulated NH_2-MIL-125 NCs synthesized using the reflux method with benzoic acid (38 nm) and dodecanoic acid (105 nm).

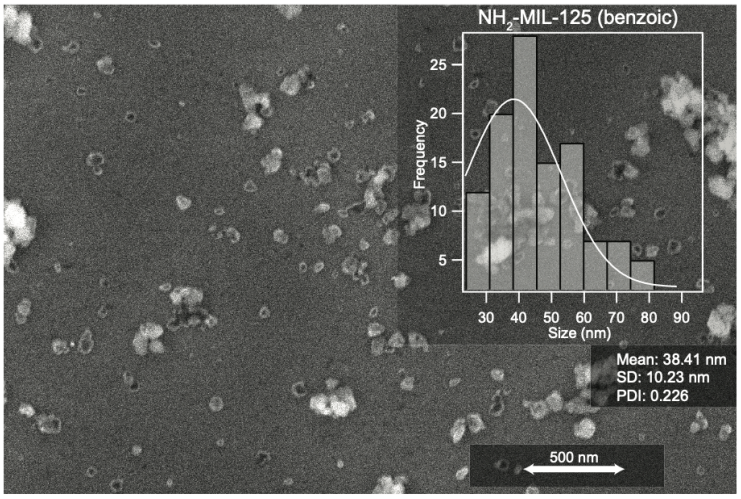

Figure D.19. SEM image and sizing histogram for NH_2-MIL-125 NCs synthesized with benzoic acid.

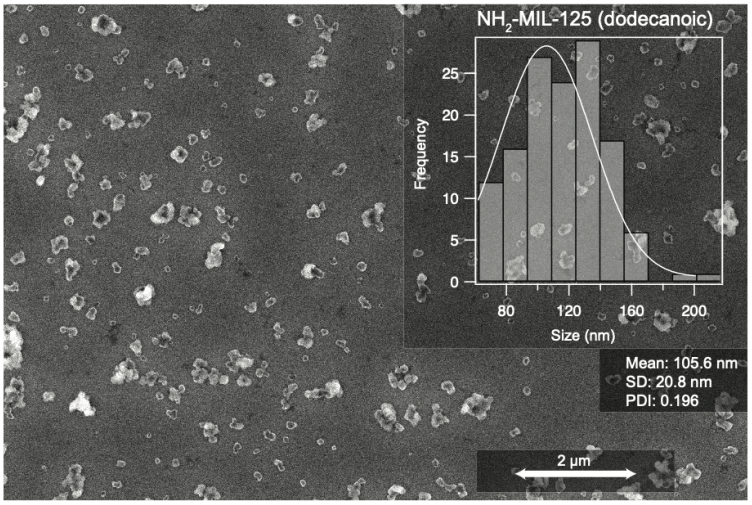

Figure D.20. SEM image and sizing histogram for NH_2-MIL-125 NCs synthesized with dodecanoic acid.

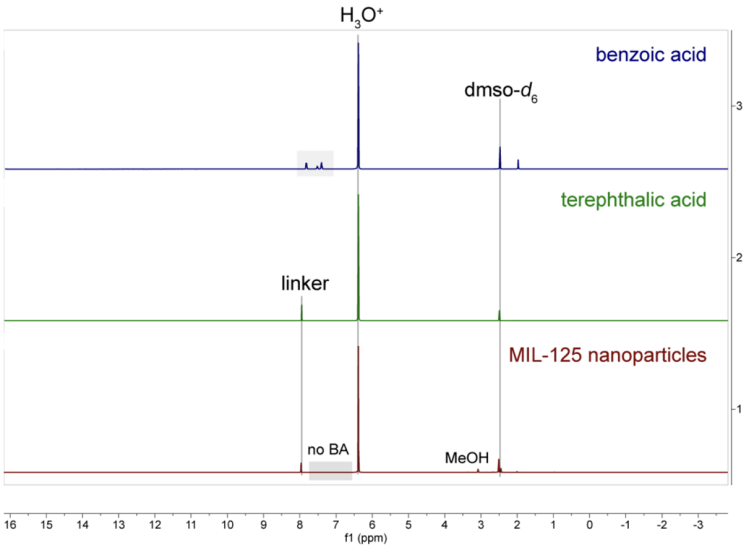

Figure D.21. Acid digestion ^{1}H-NMR of MIL-125 nanocrystals, linker, and modulator. No benzoic acid shifts were detected in the digested nanocrystals.

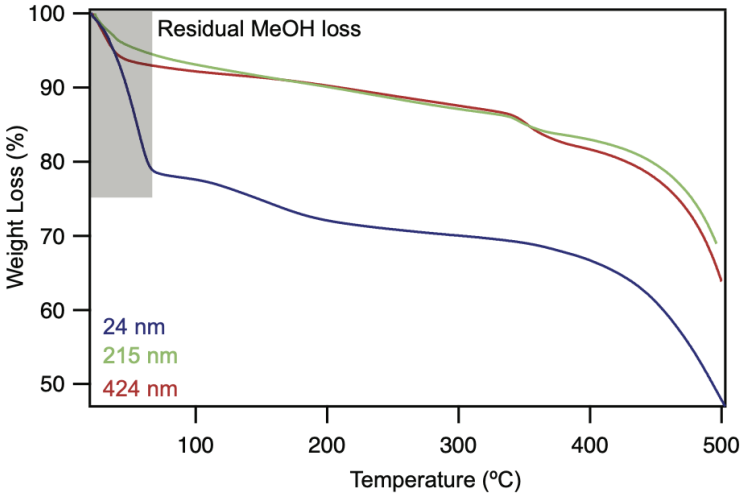

Figure D.22. Thermogravimetric analysis for three sizes of MIL-125 NCs. Residual MeOH is highlighted in the first weight loss below 100 ºC.

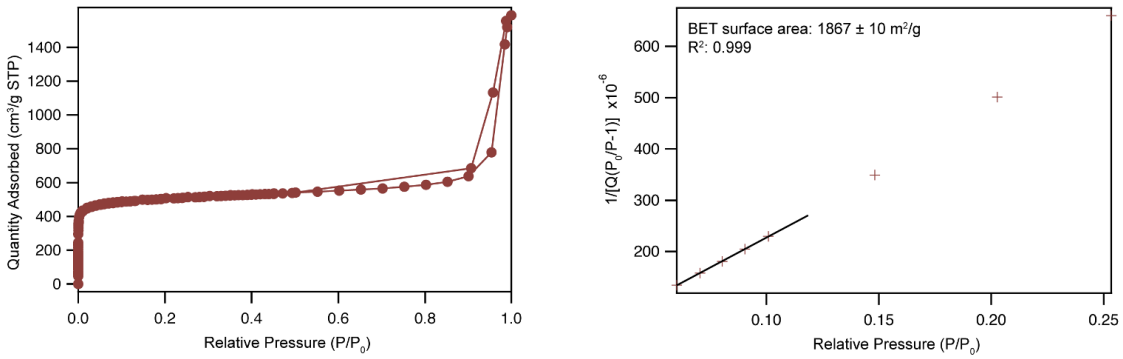

Figure D.23. Gas adsorption/desorption isotherms and BET analysis for 34-nm MIL-125 NCs.

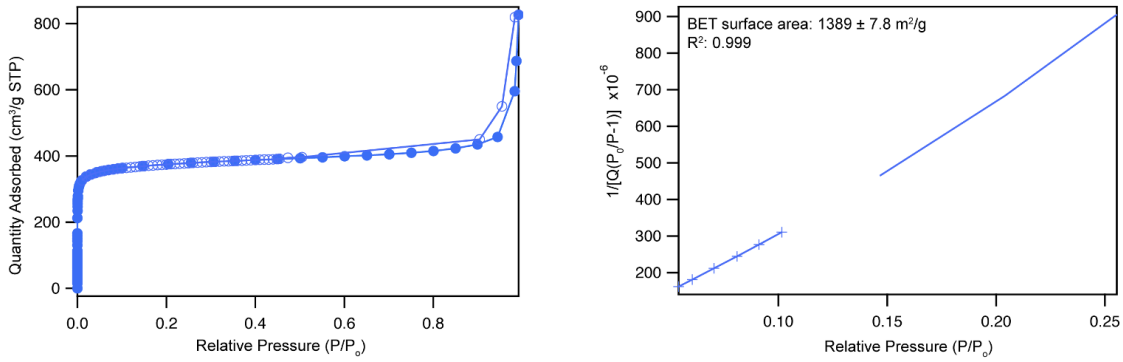

Figure D.24. Gas adsorption/desorption isotherms and BET analysis for 80-nm MIL-125 NCs.

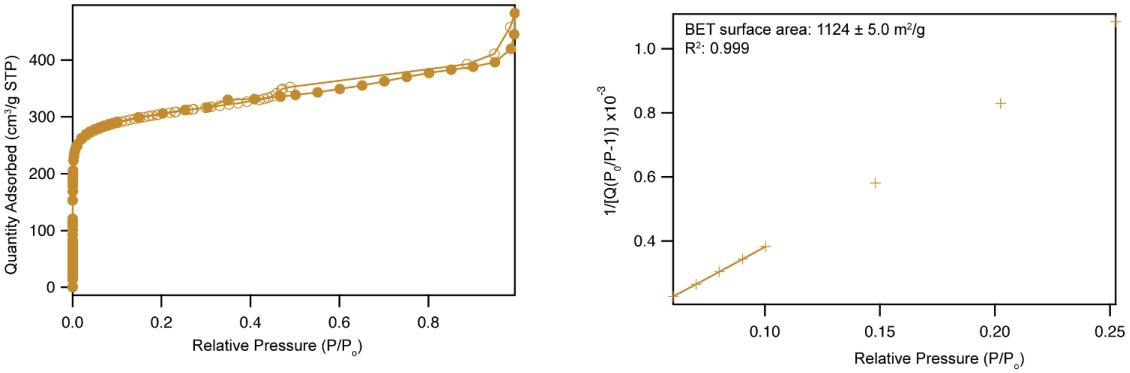

Figure D.25. Gas adsorption/desorption isotherms and BET analysis for 217-nm MIL-125 NCs.

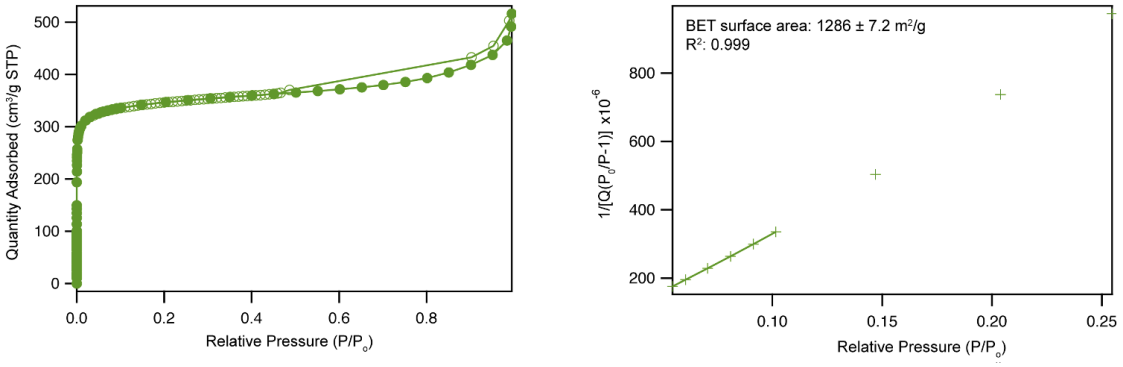

Figure D.26. Gas adsorption/desorption isotherms and BET analysis for 424-nm MIL-125 NCs.

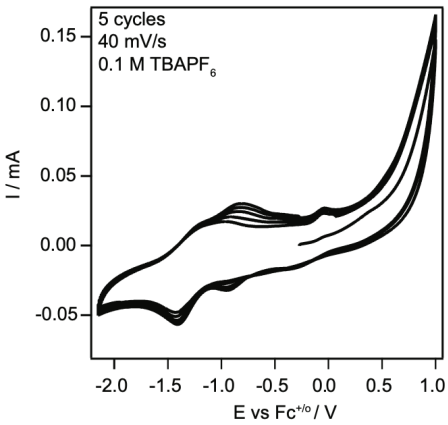

Figure D.27. Cyclability of CV traces after holding -1.75 V vs $Fc^{+/0}$ on MIL-125 colloid in DMF.

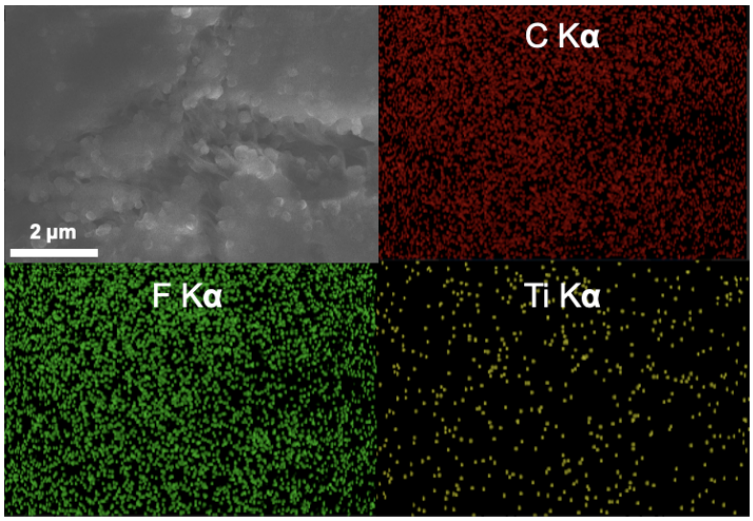

Figure D.28. SEM-EDX imaging of carbon, fluorine, and titanium in a 25 wt% MIL-125 MMM.

Element	**Apparent Concentration**	**wt %**
C	1.51	56.58
F	3.29	34.50
Ti	0.26	8.92
Total		100.0

Table D.3. SEM-EDX data results from measuring carbon, fluorine, and titanium in a 25 wt% MIL-125 MMM. (8.92(Ti) / 3.450 (F) = 25.85 wt% MIL-125 in PVDF MMM)

SEM Size (nm)	Hydrodynamic Diameter (nm)	Std. Dev.	PDI	Std. Dev	Zeta Potential (mv)	Std. Dev.
25	84.64	0.5919	0.119	0.003	-25.6	0.597
75	150.9	0.5132	0.087	0.006	-31.6	1.36
424	515.5	2.281	0.135	0.005	-34.0	0.78

Table D.4. Dynamic light scattering (DLS) results of 25, 75, and 424 nm MIL-125 methanolic colloids.

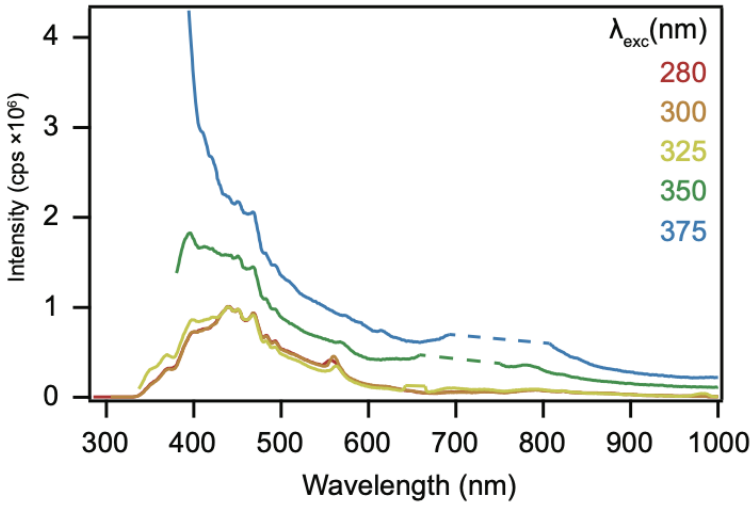

Figure D.29. Solution fluorescence spectroscopy of a 0.025 mg/mL methanolic colloid of MIL-125 excited at varying wavelengths.

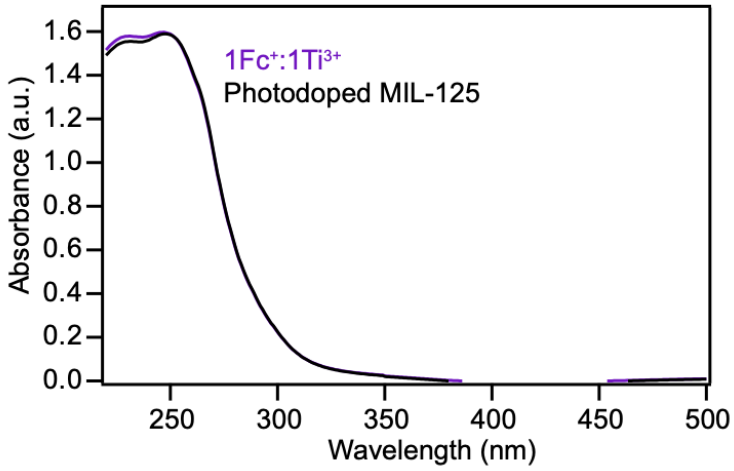

Figure D.30. Stoichiometric titration of $FcBF_4$ ($1Fc^{+}$:$1Ti^{3+}$) in a photodoped MIL-125 colloid.

APPENDIX E: SUPPLEMENTARY INFORMATION FOR CHAPTER 4.1

Experimental Methods

Materials. All commercial chemicals were used as received unless stated otherwise. Titanium(IV) butoxide (TCI Chemicals), 1,4-benzenedicarboxylic acid (terephthalic acid), methanol (ACS grade, Fisher Scientific), N,N-dimethylformamide (DMF, ACS grade, Fisher Scientific), benzoic acid (JT Baker), glacial acetic acid (ACS grade, Fisher Scientific), zinc(II) nitrate hexahydrate (Sigma-Aldrich) zirconium (IV) chloride (99.5% trace metals basis, Beantown Chemical), 2-methylimidazole (Acros 99%, Fisher Scientific), hydrochloric acid(Fisher Chemical, ACS Plus, 36.5-38%), zinc acetylacetonate hydrate(Aldrich Chem. Co.), zinc acetate dihydrate(JT Baker), sodium formate(Alfa Aesar, 98%), titanium(IV) oxide, anatase(nanopowder. <25 nm particle size, 99.7% trace metals basis, Sigma-Aldrich).

Characterization. Sample purity was verified by powder X-Ray diffraction (PXRD) with a Bruker D2 Phaser benchtop diffractometer and scanning electron microscopy (SEM) using a FEI Helios 600i instrument with 5.0 kV energy and 0.69 nA current. SEM samples were prepared by drop-casting MIL-125 suspensions onto clean silicon substrates and drying under N_2 flow. Particle sizing was performed in ImageJ using the line tool to determine crystal diameter, and histograms created in Igor Pro 6.37. The polydispersity index (PDI) was calculated by dividing the standard deviation of the Gaussian fit by the mean particle size. Variable-temperature diffuse reflectance UV-vis spectroscopy (VT-DRUV-vis) was performed on a Perkin Elmer Lambda 1050 UV/Vis/NIR spectrometer and an Agilent Cary 5000 paired with a Harrick Scientific Praying Mantis Diffuse

Reflection (DRP) accessory. A Harrick Scientific Low Temperature Reaction Chamber (CHC) that enabled introducing vacuum and heat to the sample was equipped with UV quartz. To ensure adequate reflectance, all samples were diluted with ground BaSO4. Optical gaps were extracted from VT-DRUV-vis data using Tauc analysis as described in Fabrizio *et al.*[330] To ensure thermal equilibrium, all samples' temperatures were monitored using dual thermocouples , held at the desired temperature for at least 15 minutes before measurement, and heated at a constant rate of 2 ^{o}C/min.

Synthesis of 80 nm MIL-125 NPs. A two-neck round-bottom flask fitted with a reflux condenser was charged with terephthalic acid (0.352 g, 2.12 mmol) and dry DMF (5 mL). The reaction was then allowed to stir at 110 ^{o}C for 30 min. After complete dissolution of the linker, methanol (1.5 mL) and benzoic acid (1.18 g, 10.6 mmol) were added, and the solution continued to stir under reflux for an additional 30 min. Next, the $Ti(OBu)_4$ (0.42 mL, 1.23 mmol) was added and the reaction was vigorously stirred at 110 ^{o}C under reflux. Once a precipitate was observed, aliquots ($<$ 500 µL) were taken from the reaction mixture and centrifuged at 13200 for 3 min, then washed sequentially with 3 mL of cold DMF and MeOH before crystallinity was confirmed by PXRD. One the reaction was confirmed complete by PXRD, an excess ($\sim$20 mL) of cold DMF was added to the reaction mixture to halt the reaction. The final nanoparticles were collected by centrifugation and subsequent washing with 15 mL of cold DMF and MeOH twice, then suspended and sonicated in fresh MeOH.

Synthesis of 215 nm MIL-125 NCs. The synthesis of 215 nm MIL-125 NPs is identical to the procedure above, except the mass of benzoic acid is changed to 0.713 g (6.36 mmol).

Synthesis of 424 nm MIL-125 NCs. The synthesis of 424 nm MIL-125 NPs is identical to the procedure above, except the addition of benzoic acid is excluded.

Synthesis of 25 nm UiO-66 NCs. Following a slightly modified literature procedure,[334] using Schlenk technique and under a nitrogen atmosphere, a solution of $ZrCl_4$ (0.063 g, 0.27 mmol in 5 mL of DMF) was added to a solution of terephthalic acid (0.063 g, 0.38 mmol in 5 mL of DMF) via cannula transfer. Thereafter, 330 μL of DI water was added at once. The mixture was heated at 100 ºC to reflux for 2 h under constant stirring and nitrogen atmosphere to yield a white dispersion of UiO-66 nanoparticles. After 2 h, an excess of cold DMF was added to the reaction mixture to halt the reaction and transferred to two centrifuge tubes that were placed on ice. Shortly after, the nanoparticles were collected by centrifugation and repetitively washed with 10 mL of DMF three times, then 10 mL of MeOH three times before being stored in fresh MeOH.

Synthesis of 105 nm UiO-66 NCs. Following a modified literature procedure,[335] $ZrCl_4$ (0.126 g, 0.541 mmol) was dissolved in anhydrous DMF in a 100 mL Pyrex Schott bottle under inert atmosphere. In air, hydrochloric acid (1 mL, 37%) was added to the bottle and sonicated for 20 minutes. This was followed by addition of terephthalic acid (0.123 g, 0.740 mmol) and an additional 10 mL anhydrous DMF. The bottle was sealed and placed into a fixed-temperature oven at 80 ºC for 16 h. The white product was isolated by centrifugation, and sequential washing with DMF (3×, 20 mL) and MeOH (3×, 20 mL) before being stored in fresh MeOH.

Synthesis of 4050 nm UiO-66 NCs. In a 500 mL round-bottom flask, terephthalic acid (0.099 g, 0.6 mmol) and DMF (140 mL) were magnetically

stirred for 10 mins at room temperature. Then, glacial acetic acid (20.6 mL, 0.36 mmol) was added and the temperature was increased to 120 ºC before adding a solution of $ZrCl_4$ (0.139 g, 0.6 mmol in 10 mL DMF) dropwise while stirring. Following complete addition of this solution, the stirring was halted and allowed to stand unperturbed at 120 ºC for 14 h. The resulting precipitate was centrifuged, washed twice with DMF (30 mL), and allowed to sit in MeOH for 2 h before washing twice with fresh MeOH (30 mL) and storing in new MeOH.

Synthesis of 50 nm ZIF-8 NCs. Following a modified literature procedure,[336] a solution of zinc acetylacetonate (0.175 g, 0.667 mmol) was created with 7.5 mL of MeOH in a scintillation vial. In a separate vial, a solution of 2-methyl imidazole (1.314 g, 16.0 mmol) was created by adding 22.6 mL of MeOH. At room temperature while stirring, 7.5 mL of the 2-methyl imidazole solution was added dropwise to the zinc acetylacetonate solution, and allowed to stir for 1 hour. The precipitate was isolated by centrifugation, and sequential washing with MeOH (3×, 15 mL) before being stored in fresh MeOH.

Synthesis of 205 nm ZIF-8 NCs. The synthesis of 200 nm ZIF-8 NCs is identical to the procedure above, except for the replacement of the Zn^{2+} source with zinc acetate (0.146 g, 0.667 mmol).

Synthesis of 2345 nm ZIF-8 NCs. Following a modified literature procedure,[337] zinc nitrate hexahydrate (0.588 g, 3.11 mmol) was added to MeOH (5 mL) and sonicated to combine. Separately, a solution of 2-methyl imidazole (0.325 g, 3.96 mmol) and sodium formate (0.135 g, 1.98 mmol) was created in 8 mL of MeOH. The solutions were combined and split into three 4 mL scintillation vials. The vials were heated for 16 h at 80 ºC and allowed to cool to room temperature

before handling. The precipitates were isolated by centrifugation, and sequential washing with MeOH (3×, 20 mL) before being stored in fresh MeOH.

Powder X-Ray Diffraction Data

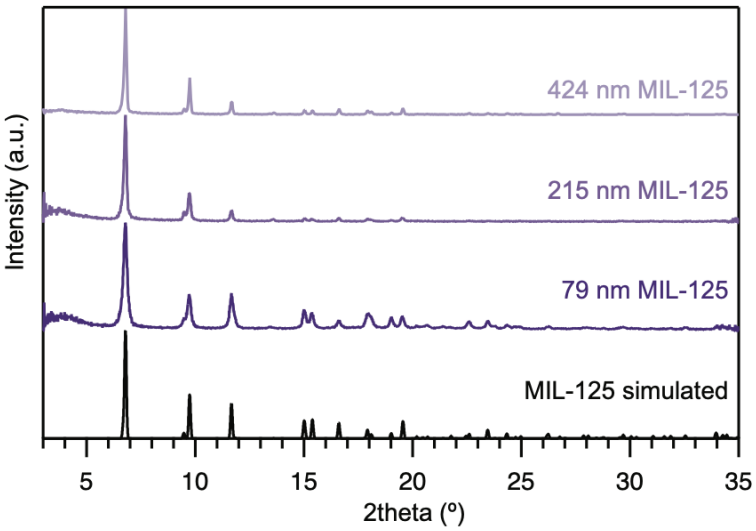

Figure E.1. PXRD patterns for three sizes of MIL-125 crystals. Scherrer sizes (from top to bottom): 73.3±17.0 nm, 54.9±10.2 nm, 38.6±2.02 nm.

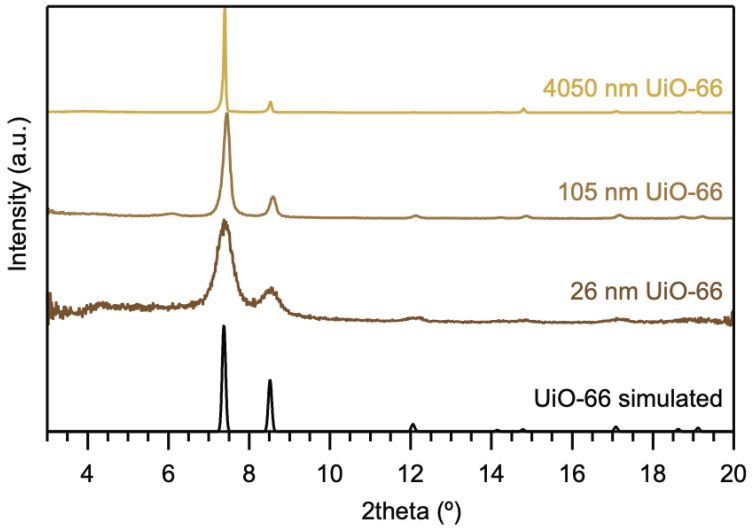

Figure E.2. PXRD patterns for three sizes of UiO-66 crystals. Scherrer sizes (from top to bottom): 110.0±21.0 nm, 47.1±7.65 nm, 15.2±0.44 nm.

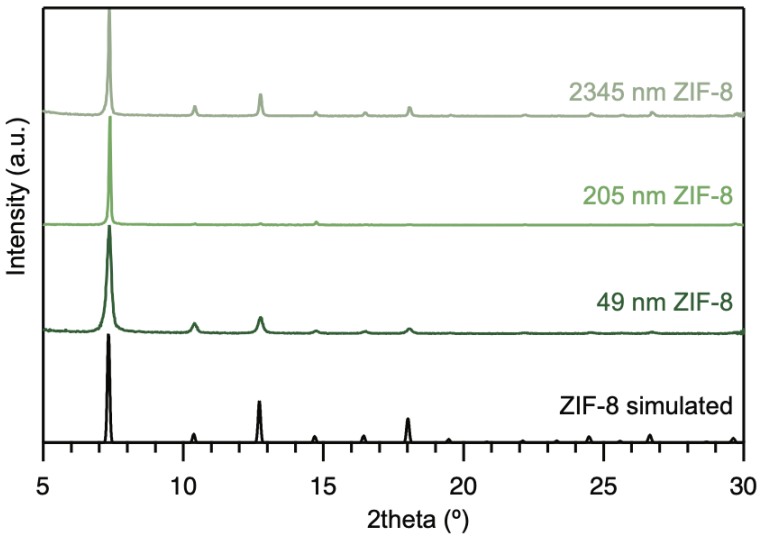

Figure E.3. PXRD patterns for three sizes of ZIF-8 crystals. Scherrer sizes (from top to bottom): 88.0±1.21 nm, 105.6±3.61 nm, 40.7±2.78 nm.

SEM Imaging and Size Distributions

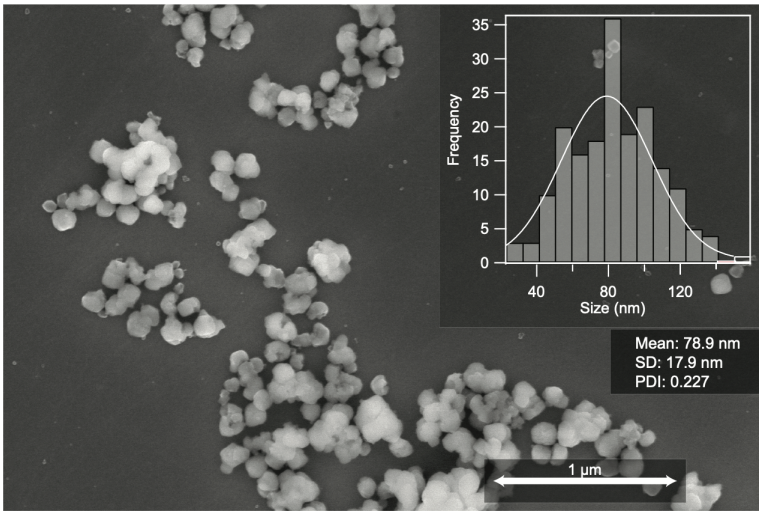

Figure E.4. Scanning electron microscopy (SEM) imaging and sizing histogram of 78.9 nm MIL-125 crystals.

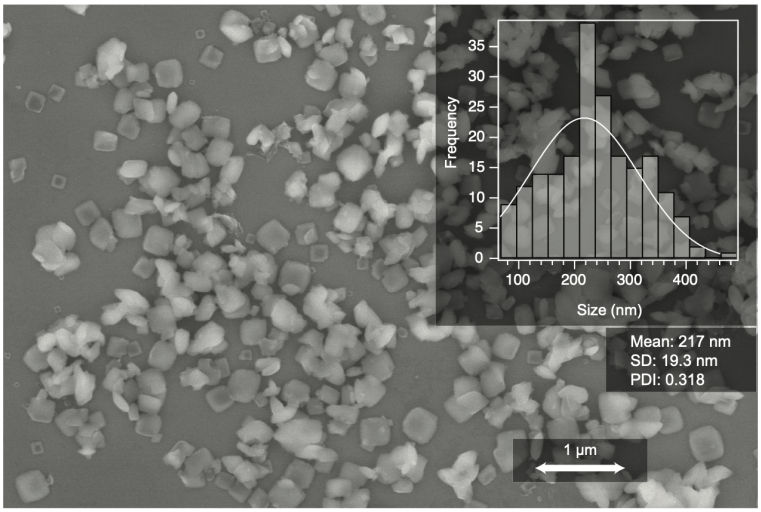

Figure E.5. Scanning electron microscopy (SEM) imaging and sizing histogram of 217 nm MIL-125 crystals.

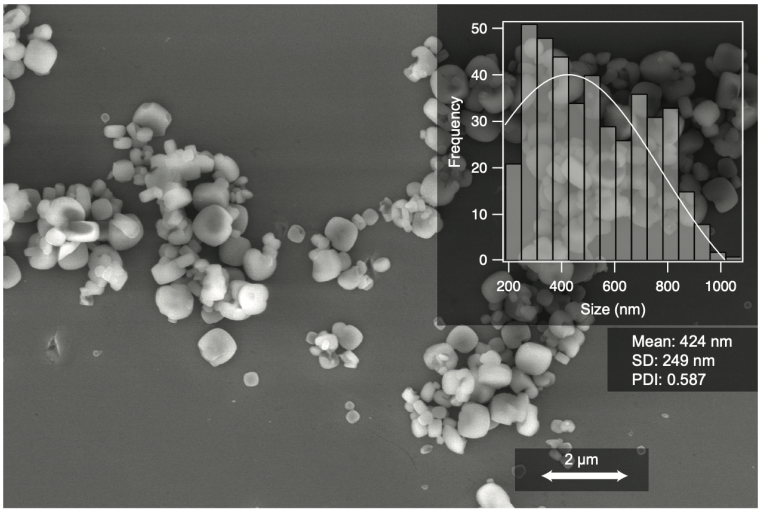

Figure E.6. Scanning electron microscopy (SEM) imaging and sizing histogram of 424 nm MIL-125 crystals.

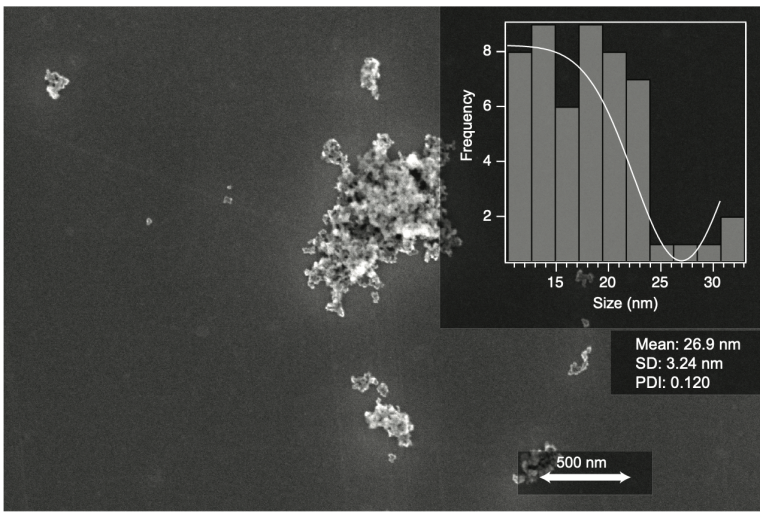

Figure E.7. Scanning electron microscopy (SEM) imaging and sizing histogram of 26.9 nm UiO-66 crystals.

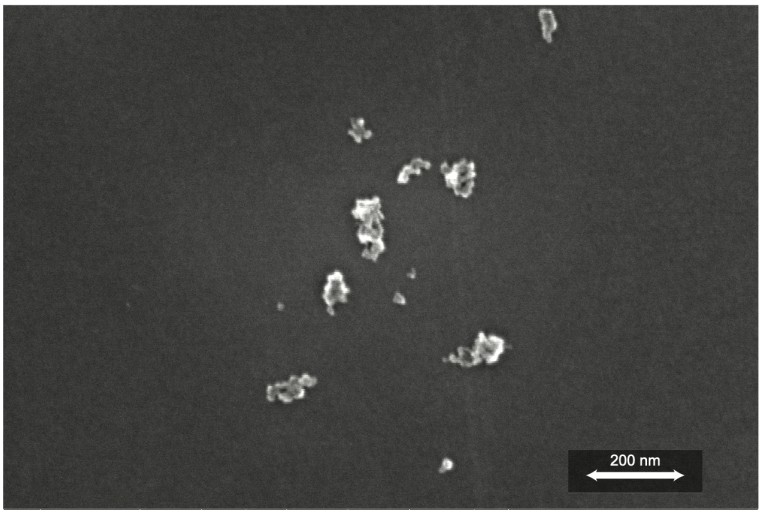

Figure E.8. Additional scanning electron microscopy (SEM) imaging and sizing histogram of 26.9 nm UiO-66 crystals.

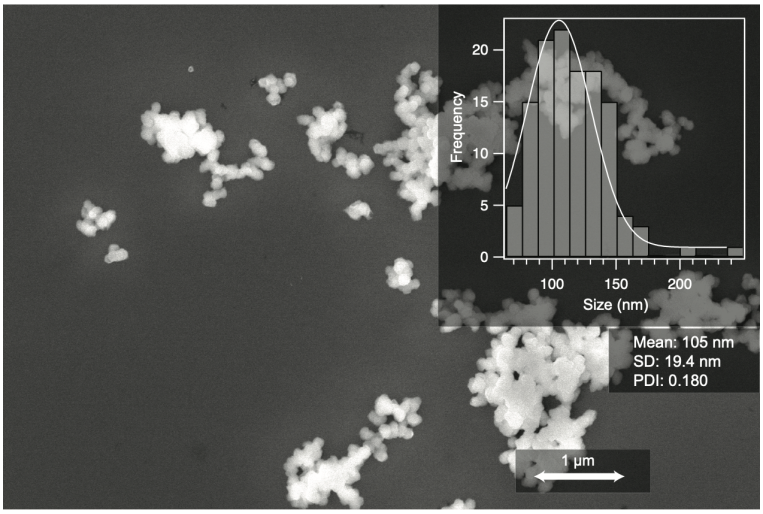

Figure E.9. Scanning electron microscopy (SEM) imaging and sizing histogram of 105 nm UiO-66 crystals.

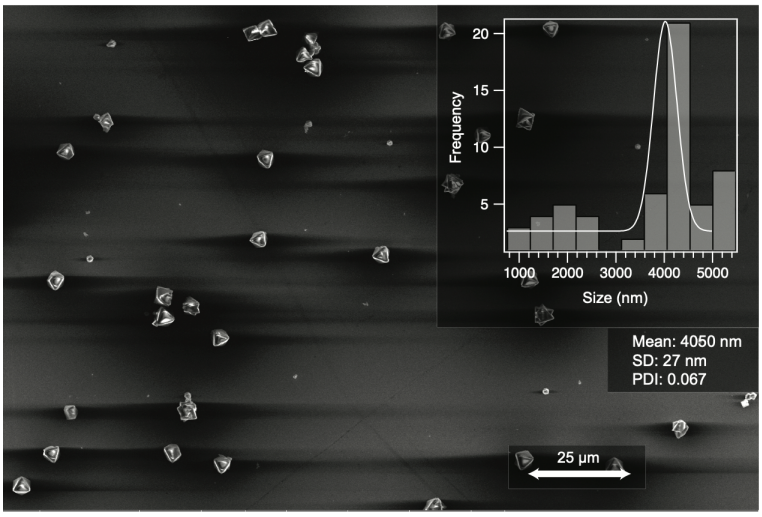

Figure E.10. Scanning electron microscopy (SEM) imaging and sizing histogram of 4050 nm UiO-66 crystals.

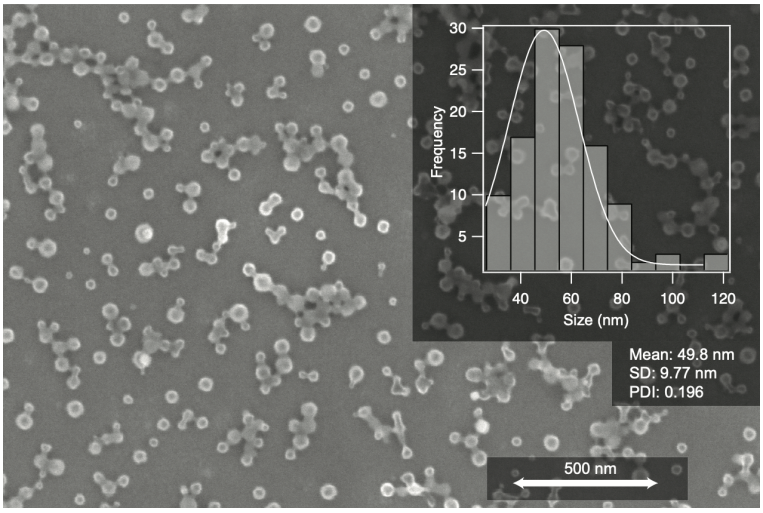

Figure E.11. Scanning electron microscopy (SEM) imaging and sizing histogram of 49.8 nm ZIF-8 crystals.

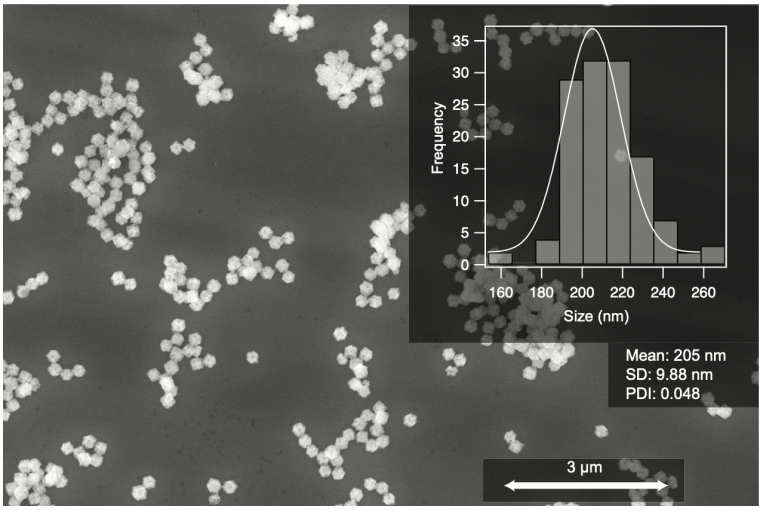

Figure E.12. Scanning electron microscopy (SEM) imaging and sizing histogram of 205 nm ZIF-8 crystals.

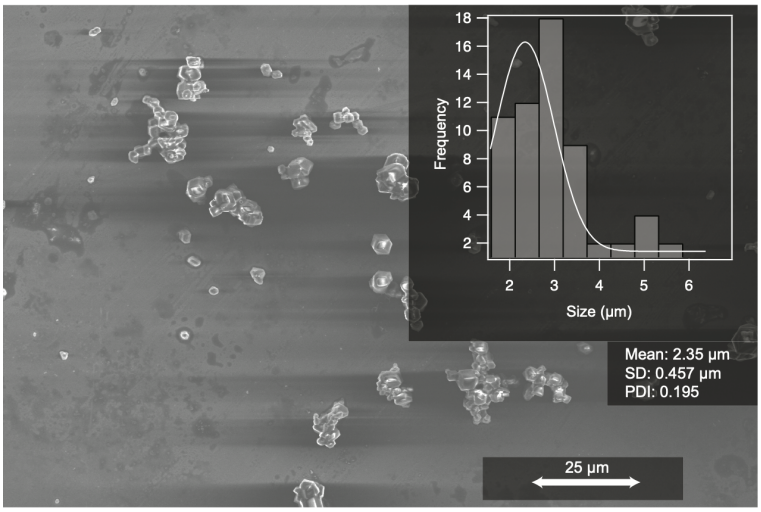

Figure E.13. Scanning electron microscopy (SEM) imaging and sizing histogram of 2345 nm ZIF-8 crystals.

Thermogravimetric Analysis

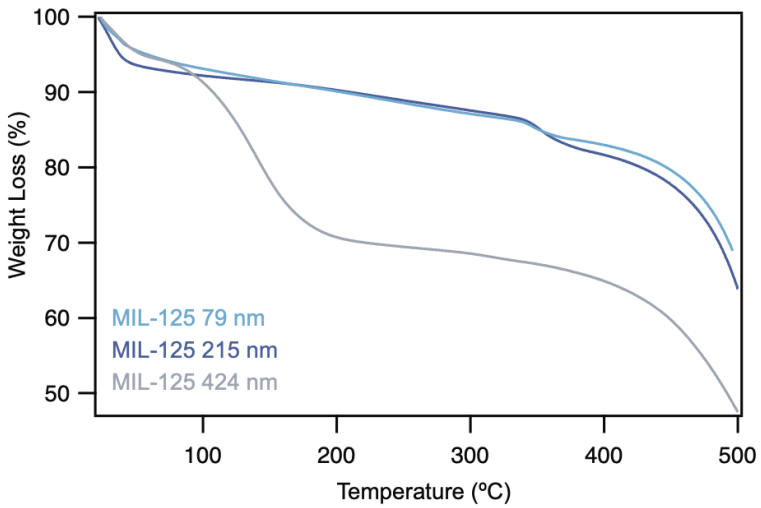

Figure E.14. TGA weight loss curves for three sizes of MIL-125 crystals.

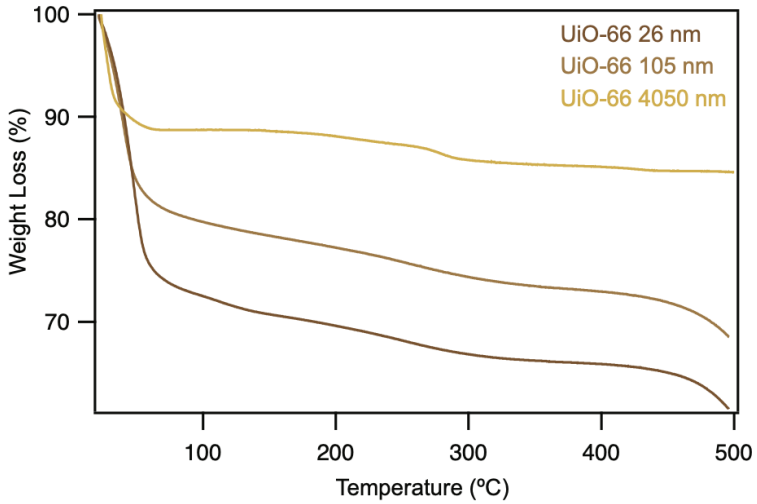

Figure E.15. TGA weight loss curves for three sizes of UiO-66 crystals.

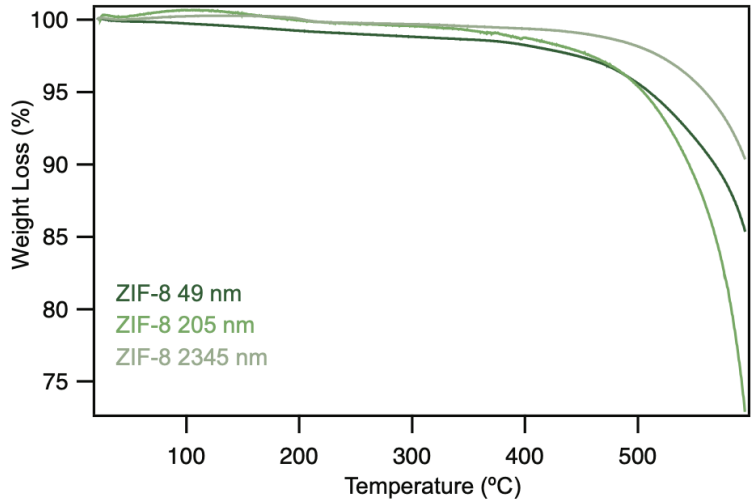

Figure E.16. TGA weight loss curves for three sizes of ZIF-8 crystals.

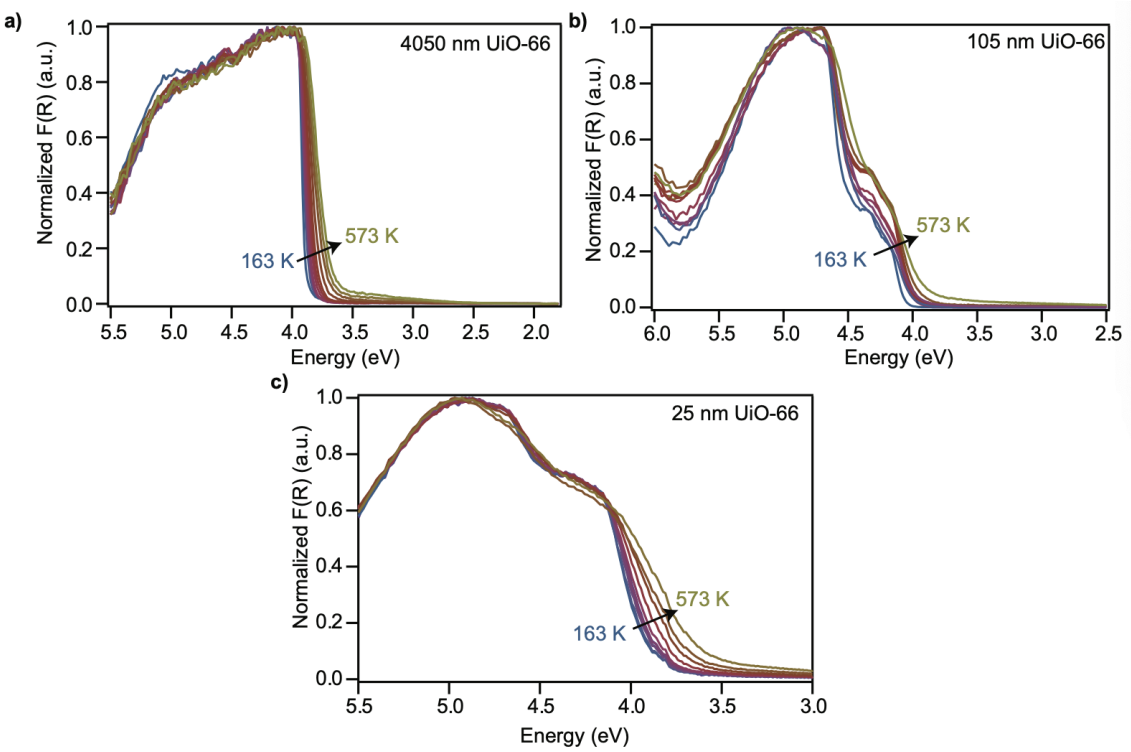

Figure E.17. VT-DRUV-vis spectra for three examined sizes of UiO-66: **a)** 4050 nm, **b)** 105 nm, **c)** 25 nm.

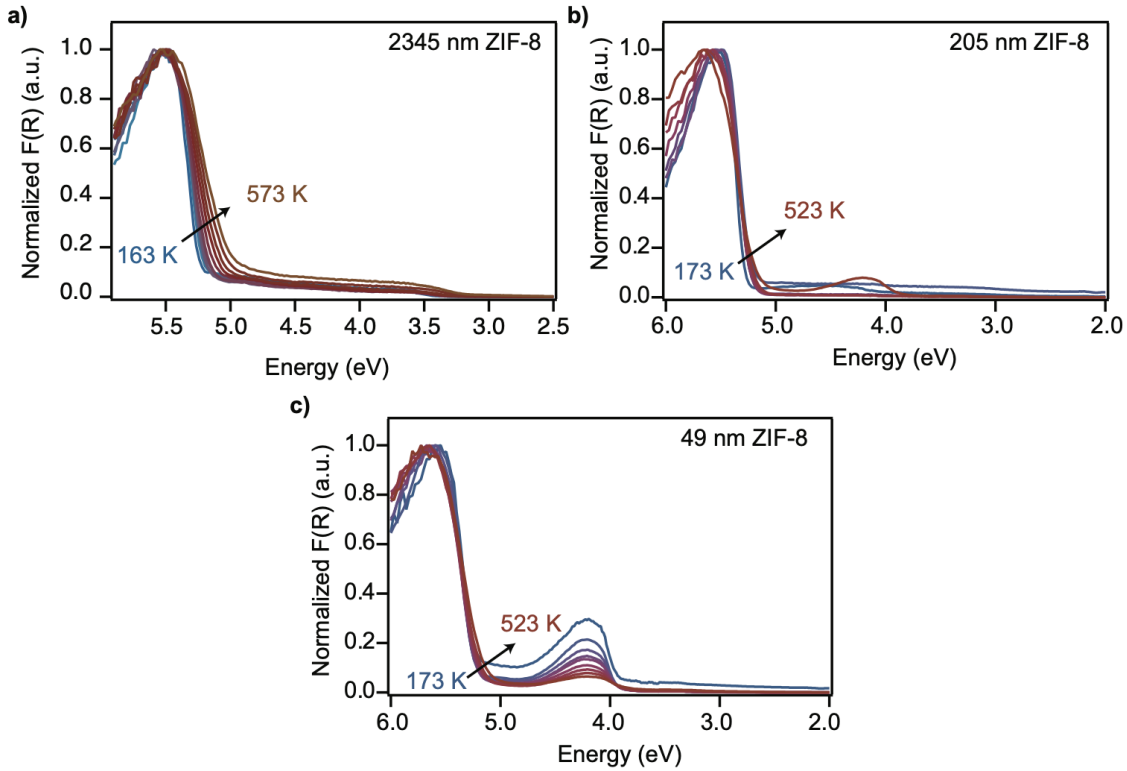

Figure E.18. VT-DRUV-vis spectra for three examined sizes of ZIF-8: **a)** 2345 nm, **b)** 205 nm, **c)** 49 nm.

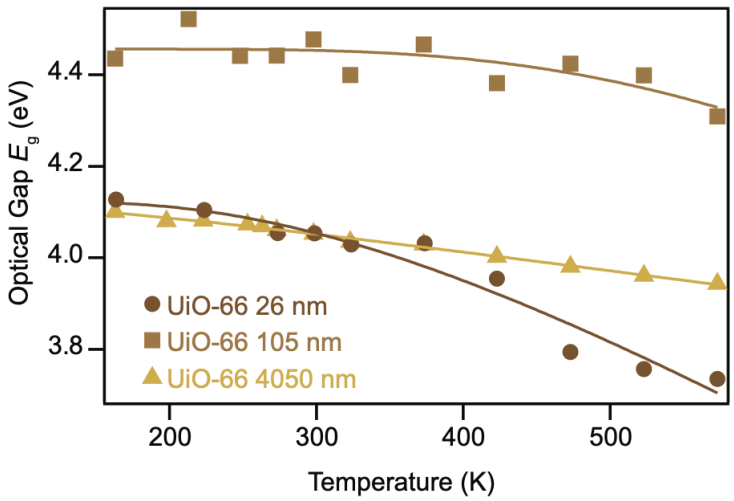

Figure E.19. O'Donnell and Chen fits for three examined sizes of UiO-66.

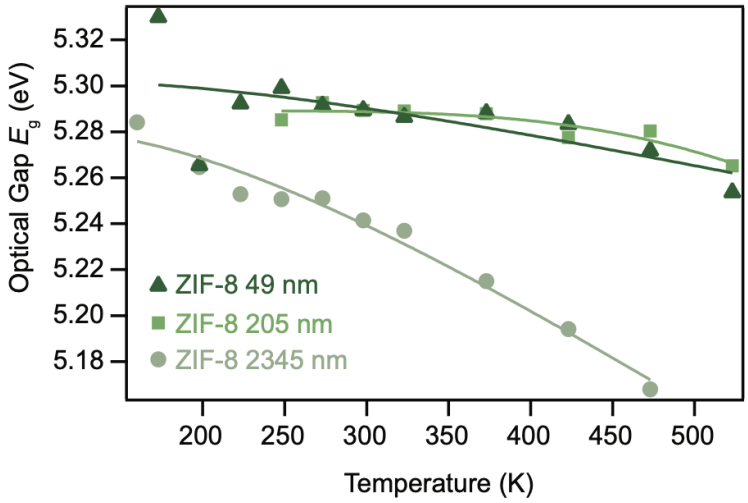

Figure E.20. O'Donnell and Chen fits for three examined sizes of ZIF-8.

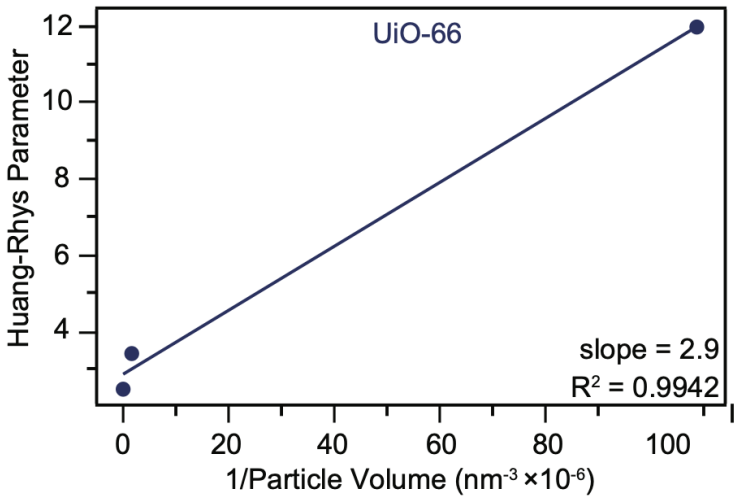

Figure E.21. Huang-Rhys parameter versus inverse particle volume for three sizes of UiO-66.

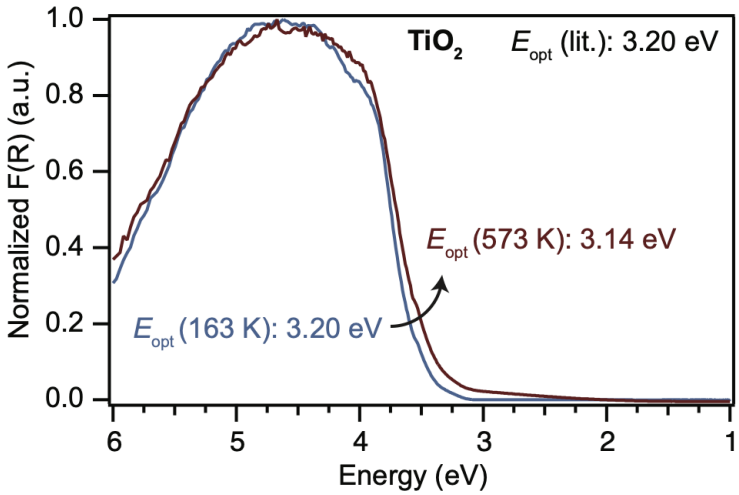

Figure E.22. VT-DRUV-vis spectra for anatase TiO_2 compared to literature values from Ref.[376]

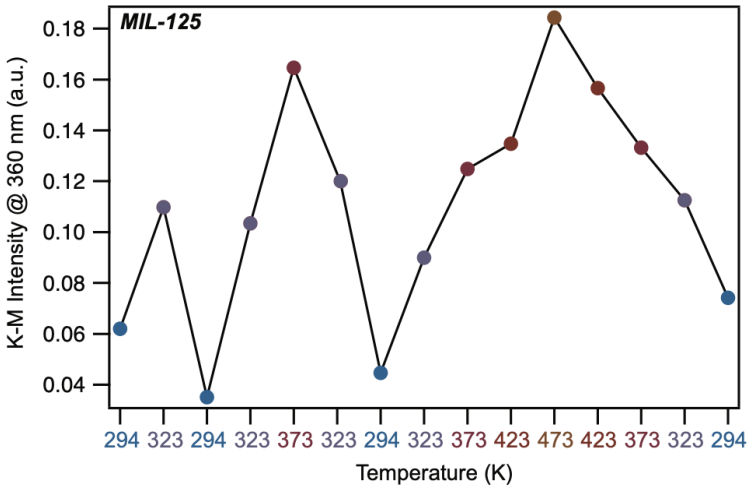

Figure E.23. Kubelka-Munk intensity at 360 nm of 79-nm MIL-125 particles recorded from VT-DRUV-vis spectra cycled over a temperature range.

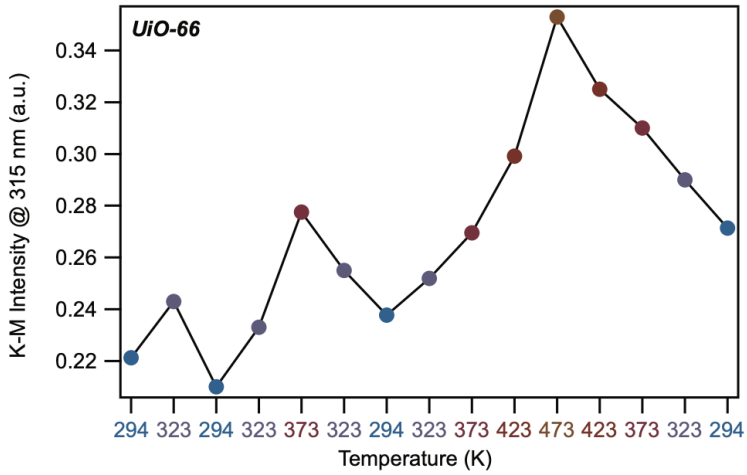

Figure E.24. Kubelka-Munk intensity at 315 nm of 26-nm UiO-66 particles recorded from VT-DRUV-vis spectra cycled over a temperature range.

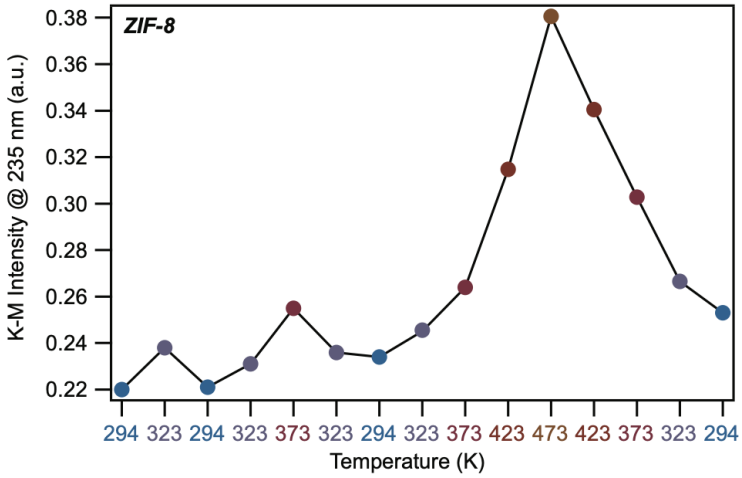

Figure E.25. Kubelka-Munk intensity at 235 nm for 49-nm ZIF-8 particles recorded from VT-DRUV-vis spectra cycled over a temperature range.

APPENDIX F: SUPPLEMENTARY INFORMATION FOR CHAPTER 4.2

Experimental Methods

Materials. All commercial chemicals were used as received unless stated otherwise: terephthalic acid (98%, Sigma Aldrich), zirconium(IV) chloride (99.5% trace metals basis, Beantown Chemical), concentrated hydrochloric acid (37%, ACS grade, Sigma Aldrich. The solvents used in all manipulations were rigorously dried using Schlenk technique and stored over molecular sieves in a nitrogen glovebox. N,N-dimethylformamide (DMF, ACS grade, Fisher Scientific) was collected from an SP-1 solvent purification system purchased from LC Technology Solutions Inc., and stored under a nitrogen atmosphere. The solvothermal synthesis of UiO-66 was either conducted in a 100-mL Duran Schott bottle, or an autoclave Parr bomb in a Yamato Convection Oven.

Characterization. Sample purity was verified by powder X-Ray diffraction (PXRD) with a Bruker D2 Phaser benchtop diffractometer. Variable-temperature diffuse reflectance infrared Fourier transform spectroscopy (DRIFTS) was performed on a Nicolet 6700 FT-IR spectrometer using a Transmission E.S.P. attachment paired with Harrick Scientific Praying Mantis Diffuse Reflection (DRP) accessory and MCT detector. A Harrick Scientific Low Temperature Reaction Chamber (CHC) that enabled introducing vacuum to the sample was equipped with UV quartz and 2 Harrick 15 $\times$ 2 mm potassium bromide windows. To maximize intensity, all samples were diluted with ground KBr. Reflectance FTIR spectra were collected in the range of 4000 – 650 cm^{-1} with 2 cm^{-1} resolution and 32 scans unless stated otherwise.

UiO-66 synthesis

Adapted from Katz *et al.*,[335] zirconium(IV) chloride (0.126 g, 0.54 mmol) was dissolved in DMF (5 mL) in a 20-mL scintillation vial under inert atmosphere. Upon exposing the vial to atmospheric conditions, concentrated hydrochloric acid (1 mL) was added, and the mixture was sonicated for 20 minutes and transferred to 100-mL Schott jar with a Teflon ring. Terephthalic acid (0.1232 g, 0.74 mmol) and DMF (10 mL) were added to the same jar and sonicated for additional 20 minutes. After contents were fully dissolved, the jar was placed in a convection oven at 80 °C overnight (12 hours). The resulting white powder was washed with DMF (2 × 30 mL) and ethanol (2 × 30 mL) over the course of 2 days and dried at room temperature.

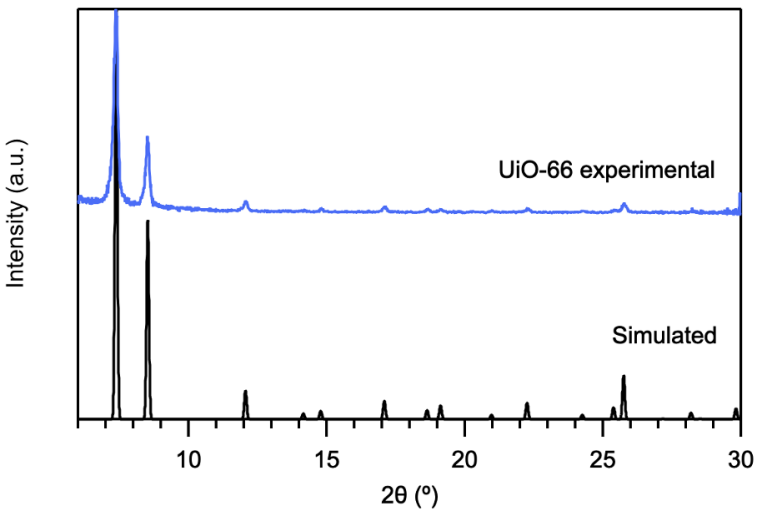

Figure F.1. Experimental and simulated X-ray diffraction patterns of UiO-66.

Global Fitting Procedure

As described in Ref.[94] and Ref.[324], the equilibrium model relies on a two Gaussian fitting in which peak position is held constant across a range of environmental conditions, and the peak width and area are allowed to shift. All

global fittings were performed in Origin Pro 2023 (10.0) Build No 10.00154 on baseline-subtracted IR stretches using a custom two Gaussian function procedure:

$$\mathrm{GFP} = \mathrm{y_o} + \frac{\mathrm{A_1}}{\mathrm{w_1} * \sqrt{\pi/2}} * \mathrm{e}^{\frac{(-2*\mathrm{x}-\mathrm{xc_1})^2}{\mathrm{w_1^2}}} + \frac{\mathrm{A_2}}{\mathrm{w_2} * \sqrt{\pi/2}} * \mathrm{e}^{\frac{(-2*\mathrm{x}-\mathrm{xc_2})^2}{\mathrm{w_2^2}}} \quad (1)$$

Where y_0 indicates offset from baseline, A_x is peak area, w_x is peak width, and xc_x is peak center. In fitting, y_0 and xc_x are shared from temperature to temperature, whereas A_x and w_x are allowed to relax to best fit the carboxylate stretch.

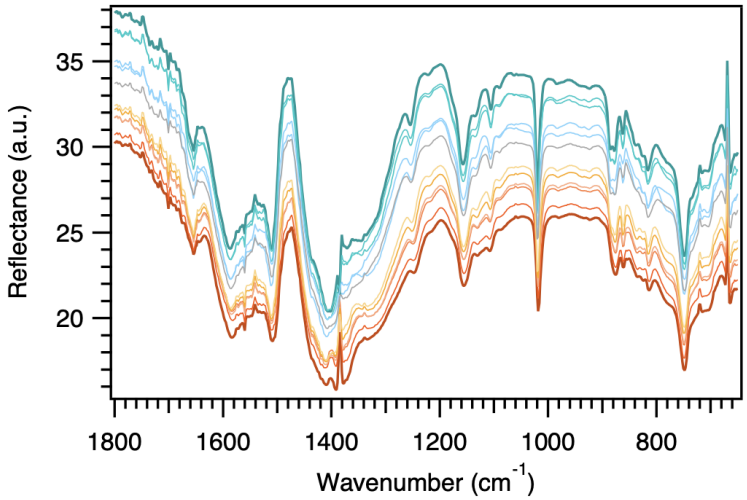

Figure F.2. Variable-temperature diffuse reflectance infrared Fourier transform spectra (VT-DRIFTS) of UiO-66 under vacuum between 300 ºC (red) and -100 ºC (turquoise).

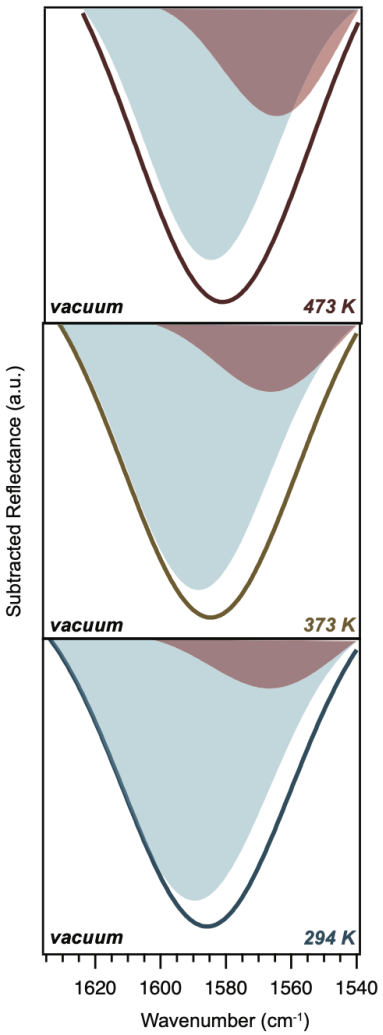

Figure F.3. Global fitting analysis of the asymmetric stretch of UiO-66 under vacuum at three temperatures.

Plot	**294 K**	**373 K**	**473 K**
$\mathbf{y}_0$	0.86 ± 0.005	0.86 ± 0.005	0.86 ± 0.005
$\mathbf{xc}_1$	1590.57 ± 5.21	1590.57 ± 5.21	1590.57 ± 5.21
$\mathbf{w}_1$	46.99 ± 0.052	45.88 ± 0.056	45.13 ± 0.078
$\mathbf{A}_1$	-292.80 ± 0.51	-256.18 ± 0.49	-160.15 ± 0.43
$\mathbf{xc}_2$	1565.83 ± 5.84	1565.83 ± 5.84	1565.83 ± 5.84
$\mathbf{w}_2$	39.52 ± 0.12	38.66 ± 0.10	41.50 ± 0.11
$\mathbf{A}_2$	-46.51 ± 0.21	-67.44 ± 0.21	-81.46 ± 0.27
$\mathbf{R}^2$	0.99990	0.99996	0.99999

Table F.1. Global fitting results for UiO-66 VT-DRIFTS under vacuum at three temperatures.

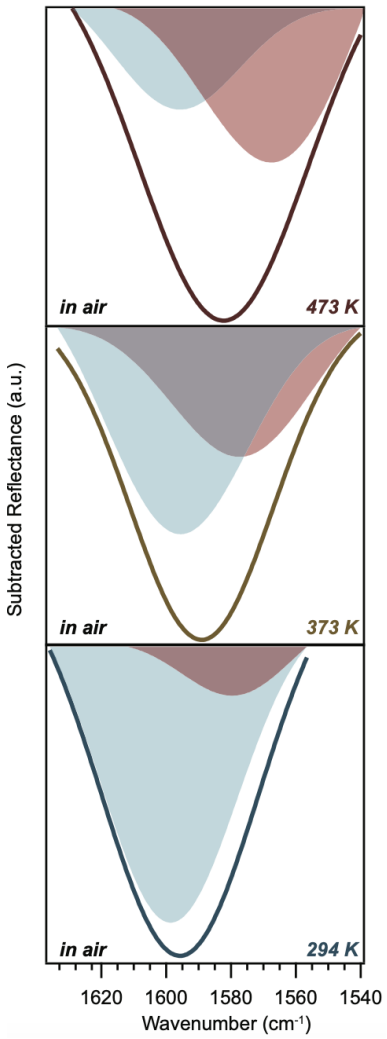

Figure F.4. Global fitting analysis of the asymmetric stretch of UiO-66 in air at three temperatures.

Plot	294 K	373 K	473 K
y_0	2.12 ± 0.18	2.12 ± 0.18	2.12 ± 0.18
xc_1	1599.11 ± 6.76	1599.11 ± 6.76	1599.11 ± 6.76
w_1	42.20 ± 7.35	45.31 ± 6.46	40.65 ± 7.36
A_1	-589.11 ± 233.03	-534.17 ± 287.59	-298.64 ± 357.14
xc_2	1578.33 ± 6.84	1578.33 ± 6.84	1578.33 ± 6.84
w_2	34.30 ± 4.11	45.78 ± 2.49	45.69 ± 1.11
A_2	-104.33 ± 218.74	-343.76 ± 272.02	-799.72 ± 345.19
R^2	0.9997	0.9977	0.9990

Table F.2. Global fitting results for UiO-66 VT-DRIFTS in air at three temperatures.

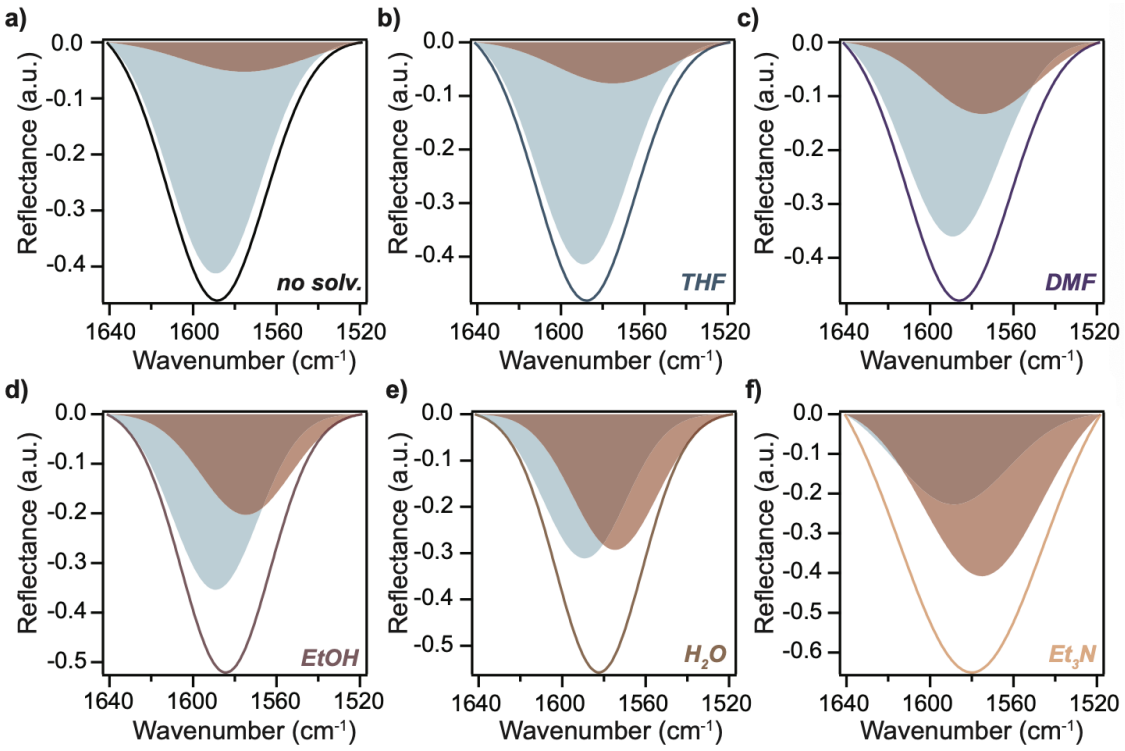

Figure F.5. Asymmetric stretch of UiO-66 globally fit to "tight" (blue) and "loose" (red) states under exposure to various solvents.

Plot	no solv.	THF	DMF	EtOH	H2O	Et3N
y_0	0.021 ± 1.59e-3	0.021 ± 1.59e-3	0.021 ± 1.59e-3	0.021 ± 1.59e-3	0.021 ± 1.59e-3	0.021 ± 1.59e-3
xc_1	1589.33 ± 0.48	1589.33 ± 0.48	1589.33 ± 0.48	1589.33 ± 0.48	1589.33 ± 0.48	1589.33 ± 0.48
w_1	44.11 ± 0.95	43.94 ± 0.94	45.60 ± 0.84	40.69 ± 0.56	39.58 ± 1.10	54.00 ± 0.71
A_1	-23.71 ± 2.29	-23.69 ± 2.98	-21.55 ± 4.69	-18.47 ± 5.70	-15.72 ± 7.65	-17.23 ± 16.15
xc_2	1574.63 ± 7.41	1574.63 ± 7.41	1574.63 ± 7.41	1574.63 ± 7.41	1574.63 ± 7.41	1574.63 ± 7.41
w_2	60.87 ± 5.78	55.08 ± 3.21	51.30 ± 1.76	42.86 ± 1.67	40.57 ± 1.63	56.20 ± 1.14
A_2	-4.67 ± 2.43	-5.85 ± 3.13	-9.14 ± 4.84	-11.15 ± 5.84	-15.10 ± 7.81	-31.95 ± 16.33
R^2	0.9996	0.9997	0.9997	0.9994	0.9992	0.9937

Table F.3. Global fitting results for UiO-66 VT-DRIFTS under exposure to vacuum, THF, DMF, EtOH, H2O, and Et3N.

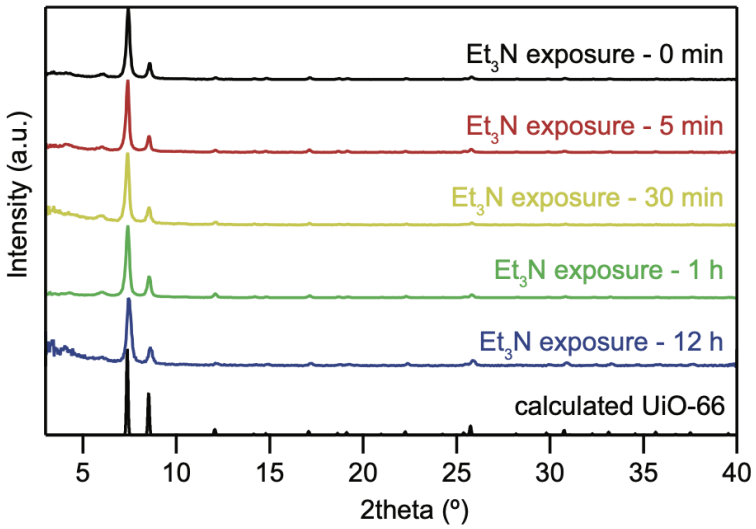

Figure F.6. Experimental and simulated powder X-ray diffraction patterns for UiO-66 after being soaked in neat Et3N for periods of time.

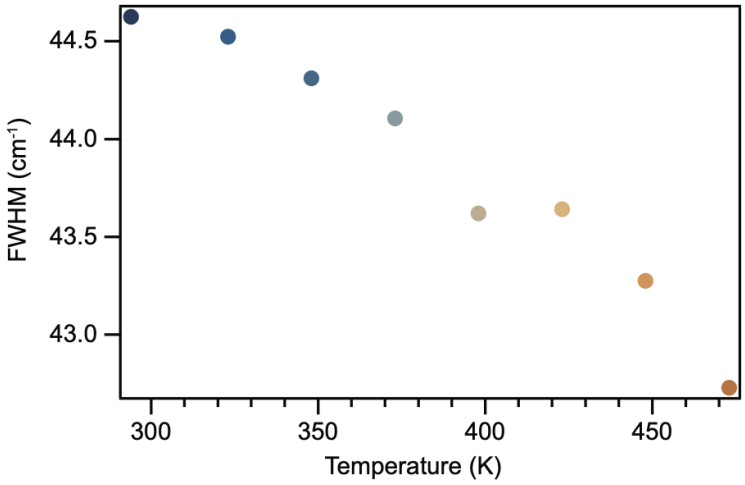

Figure F.7. Comparison of FWHM values of baseline-subtracted DRIFTS data across examined temperature range and under vacuum.

Material	**lnK**
Pyridine/ZnTPP1(5,10,15,20-tetraphenylporphyrin)	9.9-8.1
bpy/Zn^{2+}	12.4-12.2
phen/Zn^{2+}	15.1-14.8
tpy/Zn^{2+}	19.3-11.5
tpy/Fe^{2+}	16.4
tpy/Co^{2+}	19.3
tpy/Ni^{2+}	24.6

Table F.4. Stability constants for some metal-carbene and metal-pyridyl complexes, adapted from Ref.[359].

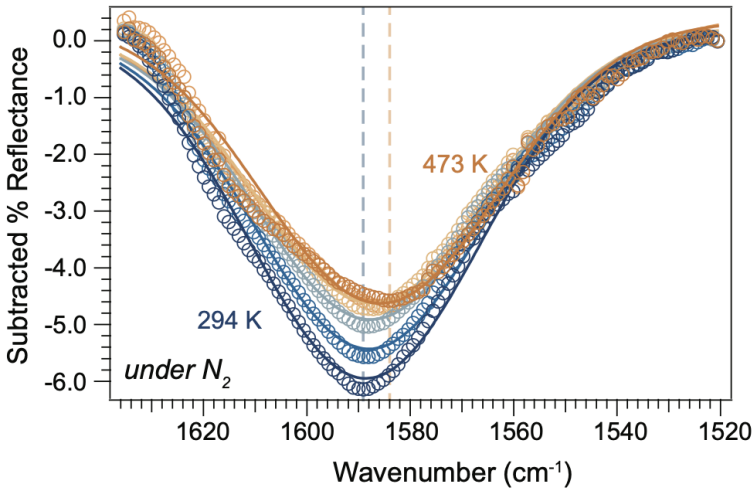

Figure F.8. VT-DRIFTS data of UiO-66 under exposure to nitrogen. Dashed lines indicate peak minima at low and high temperatures.

Plot	**294 K**	**323 K**	**373 K**	**423 K**	**473 K**
y_0	6.17E-3 ± 3.36E-6	6.17E-3 ± 3.36E-6	6.17E-3 ± 3.36E-6	6.17E-3 ± 3.36E-6	6.17E-3 ± 3.36E-6
xc_1	1591.78 ± 7.76E-3	1591.78 ± 7.76E-3	1591.78 ± 7.76E-3	1591.78 ± 7.76E-3	1591.78 ± 7.76E-3
w_1	42.85792 ± 7.58E-3	42.77811 ± 1.02E-2	42.21008 ± 1.54E-2	41.69048 ± 0.119	44.42576 ± 3.56E-2
A_1	-162.81 ± 1.35	-117.19 ± 1.43	-73.98 ± 1.38	-13.82 ± 1.76	-39.00 ± 1.70
xc_2	1585.61 ± 4.62E-2	1585.61 ± 4.62E-2	1585.61 ± 4.62E-2	1585.61 ± 4.62E-2	1585.61 ± 4.62E-2
w_2	42.86 ± 7.29E-4	42.90 ± 8.23E-4	42.46 ± 9.16E-4	42.23 ± 1.02E-3	44.83 ± 9.31E-4
A_2	-162.25 ± 1.35	-179.34 ± 1.43	-176.72 ± 1.38	-235.33 ± 1.76	-223.34 ± 1.69
R^2	1.0000	1.0000	1.0000	1.0000	1.0000

Table F.5. Global fitting results for UiO-66 VT-DRIFTS under exposure to dinitrogen.

REFERENCES

1. 2021 Tied for 6th Warmest Year in Continued Trend, NASA Analysis Shows. *Climate Change: Vital Signs of the Planet*

2. Parmesan, C.; Yohe, G. A globally coherent fingerprint of climate change impacts across natural systems. *Nature* **2003**, *421*, 37–42.

3. Armstrong McKay, D. I.; Staal, A.; Abrams, J. F.; Winkelmann, R.; Sakschewski, B.; Loriani, S.; Fetzer, I.; Cornell, S. E.; Rockström, J.; Lenton, T. M. Exceeding 1.5°C global warming could trigger multiple climate tipping points. *Science* **2022**, *377*, eabn7950.

4. Zhang, Y.; Wang, K. Global precipitation system scale increased from 2001 to 2020. *Journal of Hydrology* **2023**, *616*, 128768.

5. Steffen, W. et al. Planetary boundaries: Guiding human development on a changing planet. *Science* **2015**, *347*, 1259855.

6. Godfray, H. C. J.; Beddington, J. R.; Crute, I. R.; Haddad, L.; Lawrence, D.; Muir, J. F.; Pretty, J.; Robinson, S.; Thomas, S. M.; Toulmin, C. Food Security: The Challenge of Feeding 9 Billion People. *Science* **2010**, *327*, 812–818.

7. Chandler, D. Shining brightly. *MIT News — Massachusetts Institute of Technology* **2011**,

8. Yu, J.; Low, J.; Xiao, W.; Zhou, P.; Jaroniec, M. Enhanced Photocatalytic CO_2-Reduction Activity of Anatase TiO_2 by Coexposed 001 and 101 Facets. *Journal of the American Chemical Society* **2014**, *136*, 8839–8842.

9. Fujishima, A.; Honda, K. Electrochemical Photolysis of Water at a Semiconductor Electrode. *Nature* **1972**, *238*, 37–38.

10. Yang, F.; Liu, C.; Gao, F.; Su, M.; Wu, X.; Zheng, L.; Hong, F.; Yang, P. The improvement of spinach growth by nano-anatase TiO_2 treatment is related to nitrogen photoreduction. *Biological Trace Element Research* **2007**, *119*, 77–88.

11. Chang, W.; Sun, C.; Pang, X.; Sheng, H.; Li, Y.; Ji, H.; Song, W.; Chen, C.; Ma, W.; Zhao, J. Inverse Kinetic Solvent Isotope Effect in TiO_2 Photocatalytic Dehalogenation of Non-adsorbable Aromatic Halides: A Proton-Induced Pathway. *Angewandte Chemie* **2015**, *127*, 2080–2084.

12. Martha, S.; Sahoo, P. C.; Parida, K. M. An overview on visible light responsive metal oxide based photocatalysts for hydrogen energy production. *RSC Advances* **2015**, *5*, 61535–61553.

13. Riente, P.; Noël, T. Application of metal oxide semiconductors in light-driven organic transformations. *Catalysis Science Technology* **2019**, *9*, 5186–5232.

14. Nakata, K.; Fujishima, A. TiO_2 photocatalysis: Design and applications. *Journal of Photochemistry and Photobiology C: Photochemistry Reviews* **2012**, *13*, 169–189.

15. Schneider, J.; Matsuoka, M.; Takeuchi, M.; Zhang, J.; Horiuchi, Y.; Anpo, M.; Bahnemann, D. W. Understanding TiO_2 photocatalysis: Mechanisms and materials. *Chemical Reviews* **2014**, *114*, 9919–9986.

16. Wibowo, A.; Marsudi, M. A.; Amal, M. I.; Ananda, M. B.; Stephanie, R.; Ardy, H.; Diguna, L. J. ZnO nanostructured materials for emerging solar cell applications. *RSC Advances* **2020**, *10*, 42838–42859.

17. Zhang, Q.; Dandeneau, C. S.; Zhou, X.; Cao, G. ZnO Nanostructures for Dye-Sensitized Solar Cells. *Advanced Materials* **2009**, *21*, 4087–4108.

18. Li, L.; Wang, X.; Liu, T.; Ye, J. Titanium-Based MOF Materials: From Crystal Engineering to Photocatalysis. *Small Methods* **2020**, *4*, 2000486.

19. Dolgopolova, E. A.; Shustova, N. B. Metal–organic framework photophysics: Optoelectronic devices, photoswitches, sensors, and photocatalysts. *MRS Bulletin* **2016**, *41*, 890–896.

20. Wang, Q.; Gao, Q.; Al-Enizi, A. M.; Nafady, A.; Ma, S. Recent advances in MOF-based photocatalysis: environmental remediation under visible light. *Inorganic Chemistry Frontiers* **2020**, *7*, 300–339.

21. Yaghi, O. M.; Li, G.; Li, H. Selective binding and removal of guests in a microporous metal–organic framework. *Nature* **1995**, *378*, 703–706.

22. Moosavi, S. M.; Nandy, A.; Jablonka, K. M.; Ongari, D.; Janet, J. P.; Boyd, P. G.; Lee, Y.; Smit, B.; Kulik, H. J. Understanding the diversity of the metal-organic framework ecosystem. *Nature Communications* **2020**, *11*, 4068.

23. Li, R.; Zhang, W.; Zhou, K. Metal-Organic-Framework-Based Catalysts for Photoreduction of CO_2. *Advanced Materials* **2018**, *30*, 1705512.

24. Li, S.-L.; Xu, Q. Metal-organic frameworks as platforms for clean energy. *Energy Environmental Science* **2013**, *6*, 1656–1683.

25. Sheberla, D.; Bachman, J. C.; Elias, J. S.; Sun, C.-J.; Shao-Horn, Y.; Dinca, M. Conductive MOF electrodes for stable supercapacitors with high areal capacitance. *Nature Materials* **2017**, *16*, 220–224.

26. Wang, W.; Xu, X.; Zhou, W.; Shao, Z. Recent Progress in Metal-Organic Frameworks for Applications in Electrocatalytic and Photocatalytic Water Splitting. *Advanced Science* **2017**, *4*, 1600371.

27. Zhang, H.; Nai, J.; Yu, L.; Lou, X. W. Metal-Organic-Framework-Based Materials as Platforms for Renewable Energy and Environmental Applications. *Joule* **2017**, *1*, 77–107.

28. Fu, Y.; Sun, D.; Chen, Y.; Huang, R.; Ding, Z.; Fu, X.; Li, Z. An Amine-Functionalized Titanium Metal-Organic Framework Photocatalyst with Visible-Light-Induced Activity for CO2 Reduction. *Angewandte Chemie-International Edition* **2012**, *51*, 3364–3367.

29. Han, B.; Ou, X.; Deng, Z.; Song, Y.; Tian, C.; Deng, H.; Xu, Y.-J.; Lin, Z. Nickel Metal-Organic Framework Monolayers for Photoreduction of Diluted CO_2: Metal-Node-Dependent Activity and Selectivity. *Angewandte Chemie-International Edition* **2018**, *57*, 16811–16815.

30. Liang, R.; Jing, F.; Shen, L.; Qin, N.; Wu, L. MIL-53(Fe) as a highly efficient bifunctional photocatalyst for the simultaneous reduction of Cr(VI) and oxidation of dyes. *Journal of Hazardous Materials* **2015**, *287*, 364–372.

31. Qin, J.; Wang, S.; Wang, X. Visible-light reduction CO_2 with dodecahedral zeolitic imidazolate framework ZIF-67 as an efficient co-catalyst. *Applied Catalysis B-Environmental* **2017**, *209*, 476–482.

32. Sun, D.; Fu, Y.; Liu, W.; Ye, L.; Wang, D.; Yang, L.; Fu, X.; Li, Z. Studies on Photocatalytic CO_2 Reduction over NH_2-UiO-66(Zr) and Its Derivatives: Towards a Better Understanding of Photocatalysis on Metal-Organic Frameworks. *Chemistry-a European Journal* **2013**, *19*, 14279–14285.

33. Mancuso, J. L.; Hendon, C. H. Titanium(IV) Inclusion as a Versatile Route to Photoactivity in Metal–Organic Frameworks. *Advanced Theory and Simulations* **2019**, *2*, 1900126.

34. Nguyen, H. L. The chemistry of titanium-based metal–organic frameworks. *New Journal of Chemistry* **2017**, *41*, 14030–14043.

35. Zhu, J.; Li, P.-Z.; Guo, W.; Zhao, Y.; Zou, R. Titanium-based metal–organic frameworks for photocatalytic applications. *Coordination Chemistry Reviews* **2018**, *359*, 80–101.

36. Dhakshinamoorthy, A.; Asiri, A. M.; García, H. Metal-Organic Framework (MOF) Compounds: Photocatalysts for Redox Reactions and Solar Fuel Production. *Angewandte Chemie International Edition* **2016**, *55*, 5414–5445.

37. Li, H.; Eddaoudi, M.; O'Keeffe, M.; Yaghi, O. M. Design and synthesis of an exceptionally stable and highly porous metal-organic framework. *Nature* **1999**, *402*, 276–279.

38. Bordiga, S.; Lamberti, C.; Ricchiardi, G.; Regli, L.; Bonino, F.; Damin, A.; Lillerud, K.-P.; Bjorgen, M.; Zecchina, A. Electronic and vibrational properties of a MOF-5 metal–organic framework: ZnO quantum dot behaviour. *Chem. Commun.* **2004**, 2300–2301.

39. Alvaro, M.; Carbonell, E.; Ferrer, B.; Llabrés i Xamena, F. X.; Garcia, H. Semiconductor Behavior of a Metal-Organic Framework (MOF). *Chemistry – A European Journal* **2007**, *13*, 5106–5112.

40. Zlotea, C.; Phanon, D.; Mazaj, M.; Heurtaux, D.; Guillerm, V.; Serre, C.; Horcajada, P.; Devic, T.; Magnier, E.; Cuevas, F.; Férey, G.; Llewellyn, P. L.; Latroche, M. Effect of NH2 and CF3 functionalization on the hydrogen sorption properties of MOFs. *Dalton Transactions* **2011**, *40*, 4879.

41. Hendon, C. H.; Tiana, D.; Fontecave, M.; Sanchez, C.; D'arras, L.; Sassoye, C.; Rozes, L.; Mellot-Draznieks, C.; Walsh, A. Engineering the Optical Response of the Titanium-MIL-125 Metal–Organic Framework through Ligand Functionalization. *Journal of the American Chemical Society* **2013**, *135*, 10942–10945.

42. Horiuchi, Y.; Toyao, T.; Saito, M.; Mochizuki, K.; Iwata, M.; Higashimura, H.; Anpo, M.; Matsuoka, M. Visible-Light-Promoted Photocatalytic Hydrogen Production by Using an Amino-Functionalized Ti(IV) Metal–Organic Framework. *The Journal of Physical Chemistry C* **2012**, *116*, 20848–20853.

43. Guo, F.; Yang, M.; Li, R.-X.; He, Z.-Z.; Wang, Y.; Sun, W.-Y. Nanosheet-Engineered NH2-MIL-125 with Highly Active Facets for Enhanced Solar CO2 Reduction. *ACS Catalysis* **2022**, *12*, 9486–9493.

44. Cohen, S. M. The Postsynthetic Renaissance in Porous Solids. *Journal of the American Chemical Society* **2017**, *139*, 2855–2863.

45. Kim, M.; Cahill, J. F.; Fei, H.; Prather, K. A.; Cohen, S. M. Postsynthetic Ligand and Cation Exchange in Robust Metal–Organic Frameworks. *Journal of the American Chemical Society* **2012**, *134*, 18082–18088.

46. Kalaj, M.; Cohen, S. M. Postsynthetic Modification: An Enabling Technology for the Advancement of Metal–Organic Frameworks. *ACS Central Science* **2020**, *6*, 1046–1057.

47. Lee, Y.; Kim, S.; Kang, J. K.; Cohen, S. M. Photocatalytic CO_2 reduction by a mixed metal (Zr/Ti), mixed ligand metal–organic framework under visible light irradiation. *Chemical Communications* **2015**, *51*, 5735–5738.

48. Salcedo-Abraira, P.; Babaryk, A. A.; Montero-Lanzuela, E.; Contreras-Almengor, O. R.; Cabrero-Antonino, M.; Grape, E. S.; Willhammar, T.; Navalón, S.; Elkäim, E.; García, H.; Horcajada, P. A Novel Porous Ti-Squarate as Efficient Photocatalyst in the Overall Water Splitting Reaction under Simulated Sunlight Irradiation. *Advanced Materials* **2021**, *33*, 2106627.

49. Shen, L.; Liang, S.; Wu, W.; Liang, R.; Wu, L. Multifunctional NH_2-mediated zirconium metal–organic framework as an efficient visible-light-driven photocatalyst for selective oxidation of alcohols and reduction of aqueous Cr(VI). *Dalton Transactions* **2013**, *42*, 13649–13657.

50. Kolobov, N.; Goesten, M. G.; Gascon, J. Metal–Organic Frameworks: Molecules or Semiconductors in Photocatalysis? *Angewandte Chemie International Edition* **2021**, *60*, 26038–26052.

51. Li, C.; Xu, H.; Gao, J.; Du, W.; Shangguan, L.; Zhang, X.; Lin, R.-B.; Wu, H.; Zhou, W.; Liu, X.; Yao, J.; Chen, B. Tunable titanium metal–organic frameworks with infinite 1D Ti–O rods for efficient visible-light-driven photocatalytic H_2 evolution. *Journal of Materials Chemistry A* **2019**, *7*, 11928–11933.

52. Mohammadnezhad, F.; Kampouri, S.; Wolff, S. K.; Xu, Y.; Feyzi, M.; Lee, J.-H.; Ji, X.; Stylianou, C. Tuning the Optoelectronic Properties of Hybrid Functionalized MIL-125-NH_2 for Photocatalytic Hydrogen Evolution. 18.

53. Padial, N. M.; Castells-Gil, J.; Almora-Barrios, N.; Romero-Angel, M.; da Silva, I.; Barawi, M.; García-Sánchez, A.; de la Peña O'Shea, V. A.; Martí-Gastaldo, C. Hydroxamate Titanium–Organic Frameworks and the Effect of Siderophore-Type Linkers over Their Photocatalytic Activity. *Journal of the American Chemical Society* **2019**, *141*, 13124–13133.

54. Nguyen, H. L.; Vu, T. T.; Le, D.; Doan, T. L. H.; Nguyen, V. Q.; Phan, N. T. S. A Titanium–Organic Framework: Engineering of the Band-Gap Energy for Photocatalytic Property Enhancement. *ACS Catalysis* **2017**, *7*, 338–342.

55. Mauro, M. Dynamic Metal–Ligand Bonds as Scaffolds for Autonomously Healing Multi-Responsive Materials. *European Journal of Inorganic Chemistry* **2018**, *2018*, 2090–2100.

56. Lai, J.-C.; Jia, X.-Y.; Wang, D.-P.; Deng, Y.-B.; Zheng, P.; Li, C.-H.; Zuo, J.-L.; Bao, Z. Thermodynamically stable whilst kinetically labile coordination bonds lead to strong and tough self-healing polymers. *Nature Communications* **2019**, *10*, 1164.

57. Cruz-Cabeza, A. J.; Reutzel-Edens, S. M.; Bernstein, J. Facts and fictions about polymorphism. *Chemical Society Reviews* **2015**, *44*, 8619–8635.

58. Yang, Y.; Urban, M. W. Self-healing polymeric materials. *Chemical Society Reviews* **2013**, *42*, 7446–7467.

59. Bersuker, I. B.; Polinger, V. Z. *Vibronic Interactions in Molecules and Crystals*, softcover reprint of the original 1st ed. 1989 edition ed.; Springer: Berlin Heidelberg, 2011.

60. Thouin, F.; Valverde-Chávez, D. A.; Quarti, C.; Cortecchia, D.; Bargigia, I.; Beljonne, D.; Petrozza, A.; Silva, C.; Srimath Kandada, A. R. Phonon coherences reveal the polaronic character of excitons in two-dimensional lead halide perovskites. *Nature Materials* **2019**, *18*, 349–356.

61. Shaw, B. K. et al. Melting of hybrid organic–inorganic perovskites. *Nature Chemistry* **2021**, 1–8.

62. Barthelet, K.; Marrot, J.; Riou, D.; Férey, G. A Breathing Hybrid Organic–Inorganic Solid with Very Large Pores and High Magnetic Characteristics. *Angewandte Chemie International Edition* **2002**, *41*, 281–284.

63. Saran, R.; Heuer-Jungemann, A.; Kanaras, A. G.; Curry, R. J. Giant Bandgap Renormalization and Exciton-Phonon Scattering in Perovskite Nanocrystals. *Advanced Optical Materials* **2017**, *5*, 1700231.

64. Giustino, F. Electron-phonon interactions from first principles. *Rev. Mod. Phys.* **2017**, *89*, 63.

65. Manna, D.; Kangsabanik, J.; Das, T. K.; Das, D.; Alam, A.; Yella, A. Lattice Dynamics and Electron–Phonon Coupling in Lead-Free $Cs_2AgIn_{(1-x)}Bi_xCl_6$ Double Perovskite Nanocrystals. *The Journal of Physical Chemistry Letters* **2020**, *11*, 2113–2120.

66. Muckel, F.; Lorenz, S.; Yang, J.; Nugraha, T. A.; Scalise, E.; Hyeon, T.; Wippermann, S.; Bacher, G. Exciton-driven change of phonon modes causes strong temperature dependent bandgap shift in nanoclusters. *Nature Communications* **2020**, *11*, 4127.

67. Shaffer, D. W.; Xie, Y.; Szalda, D. J.; Concepcion, J. J. Lability and Basicity of Bipyridine-Carboxylate-Phosphonate Ligand Accelerate Single-Site Water Oxidation by Ruthenium-Based Molecular Catalysts. *Journal of the American Chemical Society* **2017**, *139*, 15347–15355.

68. *Vibronic Interactions: Jahn-Teller Effect in Crystals and Molecules*, softcover reprint of the original 1st ed. 2001 edition ed.; Springer: Dordrecht, 2001.

69. West, A. R. *Solid State Chemistry and its Applications*, 2nd ed.; Wiley: Chichester, West Sussex, UK, 2014.

70. Pajot, B. *Optical Absorption of Impurities and Defects in Semiconducting Crystals: Hydrogen-like Centres*, 2010th ed.; Springer: Heidelberg; New York, 2010.

71. Cheetham, A. K.; Bennett, T. D.; Coudert, F.-X.; Goodwin, A. L. Defects and disorder in metal organic frameworks. *Dalton Transactions* **2016**, *45*, 4113–4126.

72. Butova, V. V.; Burachevskaya, O. A.; Ozhogin, I. V.; Borodkin, G. S.; Starikov, A. G.; Bordiga, S.; Damin, A.; Lillerud, K. P.; Soldatov, A. V. UiO-66 type MOFs with mixed-linkers-1,4-Benzenedicarboxylate and 1,4-naphthalenedicarboxylate: Effect of the modulator and post-synthetic exchange. *Microporous and Mesoporous Materials* **2020**, *305*, 110324.

73. Robertson, J. Diamond-like amorphous carbon. *Materials Science Engineering R-Reports* **2002**, *37*, 129–281.

74. Wu, H.; Chua, Y. S.; Krungleviciute, V.; Tyagi, M.; Chen, P.; Yildirim, T.; Zhou, W. Unusual and Highly Tunable Missing-Linker Defects in Zirconium Metal-Organic Framework UiO-66 and Their Important Effects on Gas Adsorption. *Journal of the American Chemical Society* **2013**, *135*, 10525–10532.

75. Xu, L.; Jiang, Q.; Xiao, Z.; Li, X.; Huo, J.; Wang, S.; Dai, L. Plasma-Engraved Co3O4 Nanosheets with Oxygen Vacancies and High Surface Area for the Oxygen Evolution Reaction. *Angewandte Chemie-International Edition* **2016**, *55*, 5277–5281.

76. Xue, Z.; Liu, K.; Liu, Q.; Li, Y.; Li, M.; Su, C.-Y.; Ogiwara, N.; Kobayashi, H.; Kitagawa, H.; Liu, M.; Li, G. Missing-linker metal-organic frameworks for oxygen evolution reaction. *Nature Communications* **2019**, *10*, 5048.

77. Paskiewicz, D. M.; Tanto, B.; Savage, D. E.; Lagally, M. G. Defect-Free Single-Crystal SiGe: A New Material from Nanomembrane Strain Engineering. *ACS Nano* **2011**, *5*, 5814–5822.

78. Newman, R. C. Defects in silicon. *Reports on Progress in Physics* **1982**, *45*, 1163–1210.

79. Bumstead, A. M.; Ríos Gómez, M. L.; Thorne, M. F.; Sapnik, A. F.; Longley, L.; Tuffnell, J. M.; Keeble, D. S.; Keen, D. A.; Bennett, T. D. Investigating the melting behaviour of polymorphic zeolitic imidazolate frameworks. *CrystEngComm* **2020**, *22*, 3627–3637.

80. Bennett, T. D.; Tan, J.-C.; Yue, Y.; Baxter, E.; Ducati, C.; Terrill, N. J.; Yeung, H. H. M.; Zhou, Z.; Chen, W.; Henke, S.; Cheetham, A. K.; Greaves, G. N. Hybrid glasses from strong and fragile metal-organic framework liquids. *Nature Communications* **2015**, *6*, 8079.

81. Fonseca, J.; Gong, T.; Jiao, L.; Jiang, H.-L. Metal–organic frameworks (MOFs) beyond crystallinity: amorphous MOFs, MOF liquids and MOF glasses. *Journal of Materials Chemistry A* **2021**, *9*, 10562–10611.

82. Gaillac, R.; Pullumbi, P.; Bennett, T. D.; Coudert, F.-X. Structure of Metal–Organic Framework Glasses by Ab Initio Molecular Dynamics. *Chemistry of Materials* **2020**, acs.chemmater.0c02950.

83. Horike, S.; Nagarkar, S. S.; Ogawa, T.; Kitagawa, S. A New Dimension for Coordination Polymers and Metal–Organic Frameworks: Towards Functional Glasses and Liquids. *Angewandte Chemie International Edition* **2020**, *59*, 6652–6664.

84. Costa Gomes, M.; Pison, L.; Červinka, C.; Padua, A. Porous Ionic Liquids or Liquid Metal–Organic Frameworks? *Angewandte Chemie International Edition* **2018**, *57*, 11909–11912.

85. Gaillac, R.; Pullumbi, P.; Beyer, K. A.; Chapman, K. W.; Keen, D. A.; Bennett, T. D.; Coudert, F.-X. Liquid metal–organic frameworks. *Nature Materials* **2017**, *16*, 1149–1154.

86. Brozek, C. K.; Dincă, M. Ti^{3+}-, $V^{2+/3+}$-, $Cr^{2+/3+}$-, Mn^{2+}-, and Fe^{2+}-Substituted MOF-5 and Redox Reactivity in Cr- and Fe-MOF-5. *Journal of the American Chemical Society* **2013**, *135*, 12886–12891.

87. Brozek, C. K.; Dincă, M. Cation exchange at the secondary building units of metal–organic frameworks. *Chem. Soc. Rev.* **2014**, *43*, 5456–5467.

88. Lock, N.; Wu, Y.; Christensen, M.; Cameron, L. J.; Peterson, V. K.; Bridgeman, A. J.; Kepert, C. J.; Iversen, B. B. Elucidating Negative Thermal Expansion in MOF-5. *The Journal of Physical Chemistry C* **2010**, *114*, 16181–16186.

89. Lock, N.; Christensen, M.; Wu, Y.; Peterson, V. K.; Thomsen, M. K.; Piltz, R. O.; Ramirez-Cuesta, A. J.; McIntyre, G. J.; Norén, K.; Kutteh, R.; Kepert, C. J.; Kearley, G. J.; Iversen, B. B. Scrutinizing negative thermal expansion in MOF-5 by scattering techniques and ab initio calculations. *Dalton Transactions* **2013**, *42*, 1996–2007.

90. Schneider, C.; Bodesheim, D.; Ehrenreich, M. G.; Crocellà, V.; Mink, J.; Fischer, R. A.; Butler, K. T.; Kieslich, G. Tuning the Negative Thermal Expansion Behavior of the Metal–Organic Framework Cu_3BTC_2 by Retrofitting. *Journal of the American Chemical Society* **2019**, *141*, 10504–10509.

91. Ling, S.; Slater, B. Unusually Large Band Gap Changes in Breathing Metal–Organic Framework Materials. *The Journal of Physical Chemistry C* **2015**, *119*, 16667–16677.

92. Bueken, B.; Vermoortele, F.; Vanpoucke, D. E. P.; Reinsch, H.; Tsou, C.-C.; Valvekens, P.; De Baerdemaeker, T.; Ameloot, R.; Kirschhock, C. E. A.; Van Speybroeck, V.; Mayer, J. M.; De Vos, D. A Flexible Photoactive Titanium Metal–Organic Framework Based on a $[Ti^{IV}_3(\mu_3\text{-}O)(O)_2(COO)_6]$ Cluster. *Angewandte Chemie International Edition* **2015**, *54*, 13912–13917.

93. Ha, H.; Hahm, H.; Jwa, D. G.; Yoo, K.; Park, M. H.; Yoon, M.; Kim, Y.; Kim, M. Flexibility in metal–organic frameworks derived from positional and electronic effects of functional groups. *CrystEngComm* **2017**, *19*, 5361–5368.

94. Andreeva, A. B.; Le, K. N.; Chen, L.; Kellman, M. E.; Hendon, C. H.; Brozek, C. K. Soft Mode Metal-Linker Dynamics in Carboxylate MOFs Evidenced by Variable-Temperature Infrared Spectroscopy. *Journal of the American Chemical Society* **2020**, *142*, 19291–19299.

95. Hou, J. et al. Halogenated Metal–Organic Framework Glasses and Liquids. *Journal of the American Chemical Society* **2020**, *142*, 3880–3890.

96. Bennett, T. D.; Yue, Y.; Li, P.; Qiao, A.; Tao, H.; Greaves, N. G.; Richards, T.; Lampronti, G. I.; Redfern, S. A. T.; Blanc, F.; Farha, O. K.; Hupp, J. T.; Cheetham, A. K.; Keen, D. A. Melt-Quenched Glasses of Metal–Organic Frameworks. *Journal of the American Chemical Society* **2016**, *138*, 3484–3492.

97. Zhou, C. et al. Metal-organic framework glasses with permanent accessible porosity. *Nature Communications* **2018**, *9*, 5042.

98. Brozek, C. K.; Michaelis, V. K.; Ong, T.-C.; Bellarosa, L.; López, N.; Griffin, R. G.; Dincă, M. Dynamic DMF Binding in MOF-5 Enables the Formation of Metastable Cobalt-Substituted MOF-5 Analogues. *ACS Central Science* **2015**, *1*, 252–260.

99. Sun, C.; Skorupskii, G.; Dou, J.-H.; Wright, A. M.; Dincă, M. Reversible Metalation and Catalysis with a Scorpionate-like Metallo-ligand in a Metal–Organic Framework. *Journal of the American Chemical Society* **2018**, *140*, 17394–17398.

100. Huang, C.; Li, G.; Zhang, L.; Zhang, Y.; Mi, L.; Hou, H. Reversible Structural Transformations of Metal–Organic Frameworks as Artificial Switchable Catalysts for Dynamic Control of Selectively Cyanation Reaction. *Chemistry – A European Journal* **2019**, *25*, 10366–10374.

101. Liu, J.; Goetjen, T. A.; Wang, Q.; Knapp, J. G.; Wasson, M. C.; Yang, Y.; Syed, Z. H.; Delferro, M.; Notestein, J. M.; Farha, O. K.; Hupp, J. T. MOF-enabled confinement and related effects for chemical catalyst presentation and utilization. *Chemical Society Reviews* **2022**, *51*, 1045–1097.

102. Peralta, R. A.; Huxley, M. T.; Albalad, J.; Sumby, C. J.; Doonan, C. J. Single-Crystal-to-Single-Crystal Transformations of Metal–Organic-Framework-Supported, Site-Isolated Trigonal-Planar Cu(I) Complexes with Labile Ligands. *Inorganic Chemistry* **2021**, *60*, 11775–11783.

103. Liang, Y.; Zhang, X.; MacMillan, D. W. Decarboxylative sp^3 C-N coupling via dual copper and photoredox catalysis. *Nature* **2018**, *559*, 83–88.

104. Perry, I. B.; Brewer, T. F.; Sarver, P. J.; Schultz, D. M.; DiRocco, D. A.; MacMillan, D. W. Direct arylation of strong aliphatic C–H bonds. *Nature* **2018**, *560*, 70–75.

105. Le, C.; Chen, T. Q.; Liang, T.; Zhang, P.; MacMillan, D. W. A radical approach to the copper oxidative addition problem: Trifluoromethylation of bromoarenes. *Science* **2018**, *360*, 1010–1014.

106. Nicewicz, D. A.; MacMillan, D. W. C. Merging Photoredox Catalysis with Organocatalysis: The Direct Asymmetric Alkylation of Aldehydes. *Science* **2008**, *322*, 77–80.

107. Linsebigler, A. L.; Lu, G.; Yates, J. T. Photocatalysis on TiO_2 Surfaces: Principles, Mechanisms, and Selected Results. *Chemical Reviews* **1995**, *95*, 735–758.

108. Fei, H.; Cohen, S. M. A robust, catalytic metal-organic framework with open 2,2-bipyridine sites. *Chemical Communications* **2014**, *50*, 4810–4812.

109. Burgess, S. A.; Kassie, A.; Baranowski, S. A.; Fritzsching, K. J.; Schmidt-Rohr, K.; Brown, C. M.; Wade, C. R. Improved Catalytic Activity and Stability of a Palladium Pincer Complex by Incorporation into a Metal–Organic Framework. *Journal of the American Chemical Society* **2016**, *138*, 1780–1783.

110. Fei, H.; Cohen, S. M. Metalation of a Thiocatechol-Functionalized Zr(IV)-Based Metal–Organic Framework for Selective C–H Functionalization. *Journal of the American Chemical Society* **2015**, *137*, 2191–2194.

111. Dinča, M.; Dailly, A.; Liu, Y.; Brown, C. M.; Neumann, D. A.; Long, J. R. Hydrogen storage in a microporous metal-organic framework with exposed Mn2+coordination sites. *Journal of the American Chemical Society* **2006**, *128*, 16876–16883.

112. Feng, X.; Song, Y.; Li, Z.; Kaufmann, M.; Pi, Y.; Chen, J. S.; Xu, Z.; Li, Z.; Wang, C.; Lin, W. Metal–Organic Framework Stabilizes a Low-Coordinate Iridium Complex for Catalytic Methane Borylation. *Journal of the American Chemical Society* **2019**, *141*, 11196–11203.

113. Brozek, C. K.; Miller, J. T.; Stoian, S. A.; Dinca, M. NO Disproportionation at a Mononuclear Site-Isolated Fe^{2+} Center in Fe^{2+}-MOF-5. *Journal of the American Chemical Society* **2015**, *137*, 7495–7501.

114. Metzger, E. D.; Brozek, C. K.; Comito, R. J.; Dincă, M. Selective Dimerization of Ethylene to 1-Butene with a Porous Catalyst. *ACS Central Science* **2016**, *2*, 148–153.

115. Xiao, D. J. et al. Oxidation of ethane to ethanol by N 2 O in a metal-organic framework with coordinatively unsaturated iron(II) sites. *Nature Chemistry* **2014**, *6*, 590–595.

116. Comito, R. J.; Wu, Z.; Zhang, G.; Lawrence, J. A.; Korzyński, M. D.; Kehl, J. A.; Miller, J. T.; Dincă, M. Stabilized Vanadium Catalyst for Olefin Polymerization by Site Isolation in a Metal–Organic Framework. *Angewandte Chemie - International Edition* **2018**, *57*, 8135–8139.

117. Comito, R. J.; Metzger, E. D.; Wu, Z.; Zhang, G.; Hendon, C. H.; Miller, J. T.; Dincă, M. Selective Dimerization of Propylene with Ni-MFU-4l. *Organometallics* **2017**, *36*, 1681–1683.

118. Dubey, R. J.; Comito, R. J.; Wu, Z.; Zhang, G.; Rieth, A. J.; Hendon, C. H.; Miller, J. T.; Dincă, M. Highly Stereoselective Heterogeneous Diene Polymerization by Co-MFU-4l: A Single-Site Catalyst Prepared by Cation Exchange. *Journal of the American Chemical Society* **2017**, *139*, 12664–12669.

119. Metzger, E. D.; Comito, R. J.; Hendon, C. H.; Dincă, M. Mechanism of single-site molecule-like catalytic ethylene dimerization in Ni-MFU-4l. *Journal of the American Chemical Society* **2017**, *139*, 757–762.

120. Miner, E. M.; Gul, S.; Ricke, N. D.; Pastor, E.; Yano, J.; Yachandra, V. K.; Van Voorhis, T.; Dincă, M. Mechanistic Evidence for Ligand-Centered Electrocatalytic Oxygen Reduction with the Conductive MOF Ni_3(hexaiminotriphenylene)$_2$. *ACS Catalysis* **2017**, *7*, 7726–7731.

121. Johnson, B. A.; Bhunia, A.; Ott, S. Electrocatalytic water oxidation by a molecular catalyst incorporated into a metal-organic framework thin film. *Dalton Transactions* **2017**, *46*, 1382–1388.

122. Miner, E. M.; Wang, L.; Dincă, M. Modular O_2 electroreduction activity in triphenylene-based metal–organic frameworks. *Chemical Science* **2018**, *9*, 6286–6291.

123. Ding, Q.; Pan, Y.; Luo, Y.; Zhou, M.; Guan, Y.; Li, B.; Trivedi, M.; Kumar, A.; Liu, J. Photocatalytic and Ferric Ion Sensing Properties of a New Three-Dimensional Metal-Organic Framework Based on Cuboctahedral Secondary Building Units. *ACS Omega* **2019**, *4*, 10775–10783.

124. Pratik, S. M.; Cramer, C. J. Predicted Efficient Visible-Light Driven Water Splitting and Carbon Dioxide Reduction Using Photoredox-Active UiO-NDI Metal Organic Framework. *Journal of Physical Chemistry C* **2019**, *123*, 19778–19785.

125. Santiago-Portillo, A.; Remiro-Buenamañana, S.; Navalón, S.; García, H. Subphthalocyanine encapsulated within MIL-101(Cr)-NH_2 as a solar light photoredox catalyst for dehalogenation of -haloacetophenones. *Dalton Transactions* **2019**, *48*, 17735–17740.

126. Zhu, Y. Y.; Lan, G.; Fan, Y.; Veroneau, S. S.; Song, Y.; Micheroni, D.; Lin, W. Merging Photoredox and Organometallic Catalysts in a Metal–Organic Framework Significantly Boosts Photocatalytic Activities. *Angew. Chem. Int. Ed.* **2018**, *57*, 14090–14094.

127. Shi, D.; He, C.; Qi, B.; Chen, C.; Niu, J.; Duan, C. Merging of the photocatalysis and copper catalysis in metal-organic frameworks for oxidative C-C bond formation. *Chemical Science* **2015**, *6*, 1035–1042.

128. Guo, F.; Wei, Y. P.; Wang, S. Q.; Zhang, X. Y.; Wang, F. M.; Sun, W. Y. Pt nanoparticles embedded in flowerlike NH_2-UiO-68 for enhanced photocatalytic carbon dioxide reduction. *Journal of Materials Chemistry A* **2019**, *7*, 26490–26495.

129. Wang, C.; Xie, Z.; Dekrafft, K. E.; Lin, W. Doping metal-organic frameworks for water oxidation, carbon dioxide reduction, and organic photocatalysis. *Journal of the American Chemical Society* **2011**, *133*, 13445–13454.

130. Ji, P.; Manna, K.; Lin, Z.; Urban, A.; Greene, F. X.; Lan, G.; Lin, W. Single-Site Cobalt Catalysts at New $Zr_8(\mu_2\text{-}O)_8(\mu_2\text{-}OH)_4$ Metal-Organic Framework Nodes for Highly Active Hydrogenation of Alkenes, Imines, Carbonyls, and Heterocycles. *Journal of the American Chemical Society* **2016**, *138*, 12234–12242.

131. Ji, P.; Song, Y.; Drake, T.; Veroneau, S. S.; Lin, Z.; Pan, X.; Lin, W. Titanium(III)-Oxo Clusters in a Metal-Organic Framework Support Single-Site Co(II)-Hydride Catalysts for Arene Hydrogenation. *Journal of the American Chemical Society* **2018**, *140*, 433–440.

132. Song, Y.; Li, Z.; Zhu, Y.; Feng, X.; Chen, J. S.; Kaufmann, M.; Wang, C.; Lin, W. Titanium Hydroxide Secondary Building Units in Metal–Organic Frameworks Catalyze Hydrogen Evolution under Visible Light. *Journal of the American Chemical Society* **2019**, *141*, 12219–12223.

133. Zhang, H.; Lu, Y.; Zhang, Z. M.; Wang, E. B. A three-dimensional metal-organic framework based on hexanuclear copper units with unsaturated Cu II centers. *Inorganic Chemistry Communications* **2012**, *17*, 9–12.

134. Masoomi, M. Y.; Bagheri, M.; Morsali, A.; Junk, P. C. High photodegradation efficiency of phenol by mixed-metal-organic frameworks. *Inorganic Chemistry Frontiers* **2016**, *3*, 944–951.

135. Shen, L.; Liang, S.; Wu, W.; Liang, R.; Wu, L. Multifunctional NH_2-mediated zirconium metal-organic framework as an efficient visible-light-driven photocatalyst for selective oxidation of alcohols and reduction of aqueous Cr(vi). *Dalton Transactions* **2013**, *42*, 13649–13657.

136. Wang, D.; Huang, R.; Liu, W.; Sun, D.; Li, Z. Fe-based MOFs for photocatalytic CO_2 reduction: Role of coordination unsaturated sites and dual excitation pathways. *ACS Catalysis* **2014**, *4*, 4254–4260.

137. Guesh, K.; Caiuby, C. A.; Mayoral, ; Díaz-García, M.; Díaz, I.; Sanchez-Sanchez, M. Sustainable Preparation of MIL-100(Fe) and Its Photocatalytic Behavior in the Degradation of Methyl Orange in Water. *Crystal Growth and Design* **2017**, *17*, 1806–1813.

138. Li, G.; Li, F.; Liu, J.; Fan, C. Fe-based MOFs for photocatalytic N_2 reduction: Key role of transition metal iron in nitrogen activation. *Journal of Solid State Chemistry* **2020**, *285*, 121245.

139. Mason, J. A.; Darago, L. E.; Lukens, W. W.; Long, J. R. Synthesis and O_2 Reactivity of a Titanium(III) Metal-Organic Framework. *Inorganic Chemistry* **2015**, *54*, 10096–10104.

140. Dan-Hardi, M.; Serre, C.; Frot, T.; Rozes, L.; Maurin, G.; Sanchez, C.; Férey, G. A new photoactive crystalline highly porous titanium(IV) dicarboxylate. *J. Am. Chem. Soc.* **2009**, *131*, 10857–10859.

141. Hendon, C. H.; Tiana, D.; Fontecave, M.; Sanchez, C.; D'arras, L.; Sassoye, C.; Rozes, L.; Mellot-Draznieks, C.; Walsh, A. Engineering the Optical Response of the Titanium-MIL-125 Metal–Organic Framework through Ligand Functionalization. *Journal of the American Chemical Society* **2013**, *135*, 10942–10945.

142. Saouma, C. T.; Tsou, C. C.; Richard, S.; Ameloot, R.; Vermoortele, F.; Smolders, S.; Bueken, B.; Dipasquale, A. G.; Kaminsky, W.; Valdez, C. N.; De Vos, D. E.; Mayer, J. M. Sodium-coupled electron transfer reactivity of metal-organic frameworks containing titanium clusters: The importance of cations in redox chemistry. *Chemical Science* **2019**, *10*, 1322–1331.

143. Saouma, C. T.; Richard, S.; Smolders, S.; Delley, M. F.; Ameloot, R.; Vermoortele, F.; De Vos, D. E.; Mayer, J. M. Bulk-to-Surface Proton-Coupled Electron Transfer Reactivity of the Metal–Organic Framework MIL-125. *Journal of the American Chemical Society* **2018**, *140*, 16184–16189.

144. Cox, N.; Pantazis, D. A.; Neese, F.; Lubitz, W. Biological water oxidation. *Accounts of Chemical Research* **2013**, *46*, 1588–1596.

145. Umena, Y.; Kawakami, K.; Shen, J. R.; Kamiya, N. Crystal structure of oxygen-evolving photosystem II at a resolution of 1.9Å. *Nature* **2011**, *473*, 55–60.

146. Mukhopadhyay, S.; Mandal, S. K.; Bhaduri, S.; Armstrong, W. H. Manganese clusters with relevance to photosystem II. *Chemical Reviews* **2004**, *104*, 3981–4026.

147. Schuth, N.; Zaharieva, I.; Chernev, P.; Berggren, G.; Anderlund, M.; Styring, S.; Dau, H.; Haumann, M. K X-ray Emission Spectroscopy on the Photosynthetic Oxygen-Evolving Complex Supports Manganese Oxidation and Water Binding in the S3 State. *Inorganic Chemistry* **2018**, *57*, 10424–10430.

148. Tsui, E. Y.; Tran, R.; Yano, J.; Agapie, T. Redox-inactive metals modulate the reduction potential in heterometallic manganese–oxido clusters. *Nature Chemistry* **2013**, *5*, 293–299.

149. Tsui, E. Y.; Agapie, T. Reduction potentials of heterometallic manganese-oxido cubane complexes modulated by redox-inactive metals. *Proceedings of the National Academy of Sciences* **2013**, *110*, 10084–10088.

150. Greiner, S.; Schwarz, B.; Ringenberg, M.; Dürr, M.; Ivanovic-Burmazovic, I.; Fichtner, M.; Anjass, M.; Streb, C. Redox-inactive ions control the redox-activity of molecular vanadium oxides. *Chemical Science* **2020**, *11*, 4450–4455.

151. Kanady, E. Y. T. M. W. D. T. A., Jacob S A Synthetic Model of the Mn_3Ca Subsite of the Oxygen-Evolving Complex in Photosystem II. *Science.* **2013**, *733*, 733–737.

152. Castells-Gil, J.; Padial, N. M.; Almora-Barrios, N.; Albero, J.; Ruiz-Salvador, A. R.; González-Platas, J.; García, H.; Martí-Gastaldo, C. Chemical Engineering of Photoactivity in Heterometallic Titanium–Organic Frameworks by Metal Doping. *Angewandte Chemie - International Edition* **2018**, *57*, 8453–8457.

153. Paul, A.; Borrelli, R.; Bouyanfif, H.; Gottis, S.; Sauvage, F. Tunable Redox Potential, Optical Properties, and Enhanced Stability of Modified Ferrocene-Based Complexes. *ACS Omega* **2019**, *4*, 14780–14789.

154. Meyer, T. J.; Huynh, M. H. V.; Thorp, H. H. The Possible Role of Proton-Coupled Electron Transfer (PCET) in Water Oxidation by Photosystem II. *Angewandte Chemie International Edition* **2007**, *46*, 5284–5304.

155. Gagliardi, C. J.; Westlake, B. C.; Kent, C. A.; Paul, J. J.; Papanikolas, J. M.; Meyer, T. J. Integrating proton coupled electron transfer (PCET) and excited states. *Coordination Chemistry Reviews* **2010**, *254*, 2459–2471.

156. Gentry, E. C.; Knowles, R. R. Synthetic Applications of Proton-Coupled Electron Transfer. *Accounts of Chemical Research* **2016**, *49*, 1546–1556.

157. Hoffmann, N. Proton-Coupled Electron Transfer in Photoredox Catalytic Reactions: Proton-Coupled Electron Transfer in Photoredox Catalytic Reactions. *European Journal of Organic Chemistry* **2017**, *2017*, 1982–1992.

158. Krukau, A. V.; Vydrov, O. A.; Izmaylov, A. F.; Scuseria, G. E. Influence of the exchange screening parameter on the performance of screened hybrid functionals. *The Journal of Chemical Physics* **2006**, *125*, 224106.

159. Valdez, C. N.; Schimpf, A. M.; Gamelin, D. R.; Mayer, J. M. Proton-Controlled Reduction of ZnO Nanocrystals: Effects of Molecular Reductants, Cations, and Thermodynamic Limitations. *Journal of the American Chemical Society* **2016**, *138*, 1377–1385.

160. Song, Y.; Sanyal, U.; Pangotra, D.; Holladay, J. D.; Camaioni, D. M.; Gutiérrez, O. Y.; Lercher, J. A. Hydrogenation of benzaldehyde via electrocatalysis and thermal catalysis on carbon-supported metals. *Journal of Catalysis* **2018**, *359*, 68–75.

161. Feng, J.; He, Y.; Liu, Y.; Du, Y.; Li, D. Supported catalysts based on layered double hydroxides for catalytic oxidation and hydrogenation: general functionality and promising application prospects. *Chemical Society Reviews* **2015**, *44*, 5291–5319.

162. Dubouis, N.; Grimaud, A. The hydrogen evolution reaction: from material to interfacial descriptors. *Chemical Science* **2019**, *10*, 9165–9181.

163. Huynh, M. H. V.; Meyer, T. J. Proton-Coupled Electron Transfer. *Chemical Reviews* **2007**, *107*, 5004–5064.

164. Shannon, R. D. Revised effective ionic radii and systematic studies of interatomic distances in halides and chalcogenides. *Acta Crystallographica Section A* **1976**, *32*, 751–767.

165. Choi, C.; Back, S.; Kim, N.-Y.; Lim, J.; Kim, Y.-H.; Jung, Y. Suppression of Hydrogen Evolution Reaction in Electrochemical N 2 Reduction Using Single-Atom Catalysts: A Computational Guideline. *ACS Catalysis* **2018**, *8*, 7517–7525.

166. Carroll, G. M.; Schimpf, A. M.; Tsui, E. Y.; Gamelin, D. R. Redox Potentials of Colloidal n-Type ZnO Nanocrystals: Effects of Confinement, Electron Density, and Fermi-Level Pinning by Aldehyde Hydrogenation. *Journal of the American Chemical Society* **2015**, *137*, 11163–11169.

167. Carroll, G. M.; Brozek, C. K.; Hartstein, K. H.; Tsui, E. Y.; Gamelin, D. R. Potentiometric Measurements of Semiconductor Nanocrystal Redox Potentials. *Journal of the American Chemical Society* **2016**, *138*, 4310–4313.

168. Carroll, G. M.; Tsui, E. Y.; Brozek, C. K.; Gamelin, D. R. Spectroelectrochemical Measurement of Surface Electrostatic Contributions to Colloidal CdSe Nanocrystal Redox Potentials. *Chemistry of Materials* **2016**, *28*, 7912–7918.

169. Connelly, N. G.; Geiger, W. E. Chemical Redox Agents for Organometallic Chemistry. *Chemical Reviews* **1996**, *96*, 877–910.

170. Lee, J.; Farha, O. K.; Roberts, J.; Scheidt, K. A.; Nguyen, S. T.; Hupp, J. T. Metal–organic framework materials as catalysts. *Chemical Society Reviews* **2009**, *38*, 1450.

171. Wang, Z.; Cohen, S. M. Postsynthetic Covalent Modification of a Neutral MetalOrganic Framework. *Journal of the American Chemical Society* **2007**, *129*, 12368–12369.

172. Brozek, C. K.; Hartstein, K. H.; Gamelin, D. R. Potentiometric Titrations for Measuring the Capacitance of Colloidal Photodoped ZnO Nanocrystals. *Journal of the American Chemical Society* **2016**, *138*, 10605–10610.

173. Brozek, C. K.; Zhou, D.; Liu, H.; Li, X.; Kittilstved, K. R.; Gamelin, D. R. Soluble Supercapacitors: Large and Reversible Charge Storage in Colloidal Iron-Doped ZnO Nanocrystals. *Nano Letters* **2018**, *18*, 3297–3302.

174. Schimpf, A. M.; Ochsenbein, S. T.; Buonsanti, R.; Milliron, D. J.; Gamelin, D. R. Comparison of extra electrons in colloidal n-type Al3+-doped and photochemically reduced ZnO nanocrystals. *Chemical Communications* **2012**, *48*, 9352.

175. Schimpf, A. M.; Knowles, K. E.; Carroll, G. M.; Gamelin, D. R. Electronic Doping and Redox-Potential Tuning in Colloidal Semiconductor Nanocrystals. *Accounts of Chemical Research* **2015**, *48*, 1929–1937.

176. Boettcher, S. W.; Oener, S. Z.; Lonergan, M. C.; Surendranath, Y.; Ardo, S.; Brozek, C.; Kempler, P. A. Potentially Confusing: Potentials in Electrochemistry. *ACS Energy Letters* **2021**, *6*, 261–266.

177. Liu, H.; Brozek, C. K.; Sun, S.; Lingerfelt, D. B.; Gamelin, D. R.; Li, X. A Hybrid Quantum-Classical Model of Electrostatics in Multiply Charged Quantum Dots. *The Journal of Physical Chemistry C* **2017**, *121*, 26086–26095.

178. Hartstein, K. H.; Brozek, C. K.; Hinterding, S. O. M.; Gamelin, D. R. Copper-Coupled Electron Transfer in Colloidal Plasmonic Copper-Sulfide Nanocrystals Probed by in Situ Spectroelectrochemistry. *Journal of the American Chemical Society* **2018**, *140*, 3434–3442.

179. Andreeva, A. B.; Le, K. N.; Chen, L.; Kellman, M. E.; Hendon, C. H.; Brozek, C. K. Soft Mode Metal-Linker Dynamics in Carboxylate MOFs Evidenced by Variable-Temperature Infrared Spectroscopy. *Journal of the American Chemical Society* **2020**, *142*, 19291–19299.

180. John, S.; Soukoulis, C.; Cohen, M. H.; Economou, E. N. Theory of Electron Band Tails and the Urbach Optical-Absorption Edge. *Physical Review Letters* **1986**, *57*, 1777–1780.

181. Ikhmayies, S. J.; Ahmad-Bitar, R. N. A study of the optical bandgap energy and Urbach tail of spray-deposited CdS:In thin films. *Journal of Materials Research and Technology* **2013**, *2*, 221–227.

182. Castells-Gil, J.; M. Padial, N.; Almora-Barrios, N.; Gil-San-Millán, R.; Romero-Ángel, M.; Torres, V.; da Silva, I.; Vieira, B. C.; Waerenborgh, J. C.; Jagiello, J.; Navarro, J. A.; Tatay, S.; Martí-Gastaldo, C. Heterometallic Titanium-Organic Frameworks as Dual-Metal Catalysts for Synergistic Non-buffered Hydrolysis of Nerve Agent Simulants. *Chem* **2020**, *6*, 3118–3131.

183. Abánades Lázaro, I.; Almora-Barrios, N.; Tatay, S.; Martí-Gastaldo, C. Effect of modulator connectivity in promoting defectivity in titanium-organic frameworks. *Chemical Science* **2021**, *68*, 42–61.

184. Lee, S.; Bürgi, H.-B.; Alshmimri, S. A.; Yaghi, O. M. Impact of Disordered Guest–Framework Interactions on the Crystallography of Metal–Organic Frameworks. *Journal of the American Chemical Society* **2018**, *140*, 8958–8964.

185. Zanatta, A. R. Revisiting the optical bandgap of semiconductors and the proposal of a unified methodology to its determination. *Scientific reports* **2019**, *9*, 11225.

186. Dolgonos, A.; Mason, T. O.; Poeppelmeier, K. R. Direct optical band gap measurement in polycrystalline semiconductors: A critical look at the Tauc method. *Journal of Solid State Chemistry* **2016**, *240*, 43–48.

187. Tauc, J. Optical properties and electronic structure of amorphous Ge and Si. *Materials Research Bulletin* **1968**, *3*, 37–46.

188. Lin, K.-F.; Cheng, H.-M.; Hsu, H.-C.; Lin, L.-J.; Hsieh, W.-F. Band gap variation of size-controlled ZnO quantum dots synthesized by sol–gel method. *Chemical Physics Letters* **2005**, *409*, 208–211.

189. Khatun, N.; Rini, E. G.; Shirage, P.; Rajput, P.; Jha, S. N.; Sen, S. Effect of lattice distortion on bandgap decrement due to vanadium substitution in TiO_2 nanoparticles. *Materials Science in Semiconductor Processing* **2016**, *50*, 7–13.

190. Mehta, A.; Mishra, A.; Basu, S.; Shetti, N. P.; Reddy, K. R.; Saleh, T. A.; Aminabhavi, T. M. Band gap tuning and surface modification of carbon dots for sustainable environmental remediation and photocatalytic hydrogen production – A review. *Journal of Environmental Management* **2019**, *250*, 109486.

191. Lan, Z.-A.; Fang, Y.; Zhang, Y.; Wang, X. Photocatalytic Oxygen Evolution from Functional Triazine-Based Polymers with Tunable Band Structures. *Angewandte Chemie International Edition* **2018**, *57*, 470–474.

192. Bredas, J.-L. Mind the gap! *Mater. Horiz.* **2014**, *1*, 17–19.

193. Gindele, F.; Woggon, U.; Langbein, W.; Hvam, J. M.; Leonardi, K.; Hommel, D.; Selke, H. Excitons, biexcitons, and phonons in ultrathin CdSe/ZnSe quantum structures. *Physical Review B* **1999**, *60*, 8773–8782.

194. Chia, C. H.; Yuan, C. T.; Ku, J. T.; Yang, S. L.; Chou, W. C.; Juang, J. Y.; Hsieh, S. Y.; Chiu, K. C.; Hsu, J. S.; Jeng, S. Y. Temperature dependence of excitonic emission in cubic CdSe thin film. *Journal of Luminescence* **2008**, *128*, 123–128.

195. Shan, W.; Song, J. J.; Luo, H.; Furdyna, J. K. Determination of the fundamental and split-off band gaps in zinc-blende CdSe by photomodulation spectroscopy. *Physical Review B* **1994**, *50*, 8012–8015.

196. Knupfer, M. Exciton binding energies in organic semiconductors. *Applied Physics A* **2003**, *77*, 623–626.

197. Kshirsagar, A. R.; Blase, X.; Attaccalite, C.; Poloni, R. Strongly Bound Excitons in Metal–Organic Framework MOF-5: A Many-Body Perturbation Theory Study. *The Journal of Physical Chemistry Letters* **2021**, *12*, 4045–4051.

198. Schweitzer, B.; Bassler, H. Excitons in conjugated polymers. *H. Ba* **2000**, 6.

199. Hedin, L. New Method for Calculating the One-Particle Green's Function with Application to the Electron-Gas Problem. *Physical Review* **1965**, *139*, A796–A823.

200. van Setten, M. J.; Weigend, F.; Evers, F. The GW-Method for Quantum Chemistry Applications: Theory and Implementation. *Journal of Chemical Theory and Computation* **2013**, *9*, 232–246.

201. Konstantinova, E. A.; Minnekhanov, A. A.; Kokorin, A. I.; Sviridova, T. V.; Sviridov, D. V. Determination of the Energy Levels of Paramagnetic Centers in the Band Gap of Nanostructured Oxide Semiconductors Using EPR Spectroscopy. *The Journal of Physical Chemistry C* **2018**, *122*, 10248–10254.

202. Bleuse, J.; Perret, S.; Curé, Y.; Grenet, L.; André, R.; Mariette, H. Optical determination of the band gap and band tail of epitaxial Ag 2 Zn Sn Se 4 at low temperature. *Physical Review B* **2020**, *102*, 195205.

203. Klein, P. B.; Nwagwu, U.; Edgar, J. H.; Freitas, J. A. Photoluminescence investigation of the indirect band gap and shallow impurities in icosahedral B_12As_2. *Journal of Applied Physics* **2012**, *112*, 013508.

204. Nandan, Y.; Mehata, M. S. Wavefunction Engineering of Type-I/Type-II Excitons of CdSe/CdS Core-Shell Quantum Dots. *Scientific Reports* **2019**, *9*, 2.

205. Cademartiri, L.; Montanari, E.; Calestani, G.; Migliori, A.; Guagliardi, A.; Ozin, G. A. Size-Dependent Extinction Coefficients of PbS Quantum Dots. *Journal of the American Chemical Society* **2006**, *128*, 10337–10346.

206. Protesescu, L.; Yakunin, S.; Bodnarchuk, M. I.; Krieg, F.; Caputo, R.; Hendon, C. H.; Yang, R. X.; Walsh, A.; Kovalenko, M. V. Nanocrystals of Cesium Lead Halide Perovskites ($CsPbX_3$, X = Cl, Br, and I): Novel Optoelectronic Materials Showing Bright Emission with Wide Color Gamut. *Nano Letters* **2015**, *15*, 3692–3696.

207. Tauc, J. Optical properties and electronic structure of amorphous Ge and Si. *Materials Research Bulletin* **1968**, *3*, 37–46.

208. Mok, T. M.; O'Leary, S. K. The dependence of the Tauc and Cody optical gaps associated with hydrogenated amorphous silicon on the film thickness: l Experimental limitations and the impact of curvature in the Tauc and Cody plots. *Journal of Applied Physics* **2007**, *102*, 113525.

209. Chang, A.-L.; Nguyen, V.-H.; Lin, K.-Y. A.; Hu, C. Selective synthesis of ZIFs from zinc and nickel nitrate solution for photocatalytic H_2O_2 production. *Arabian Journal of Chemistry* **2020**, *13*, 8301–8308.

210. Wang, T.; Wang, Y.; Sun, M.; Hanif, A.; Wu, H.; Gu, Q.; Ok, Y. S.; Tsang, D. C. W.; Li, J.; Yu, J.; Shang, J. Thermally treated zeolitic imidazolate framework-8 (ZIF-8) for visible light photocatalytic degradation of gaseous formaldehyde. *Chemical Science* **2020**, *11*, 6670–6681.

211. Pulumati, N. B.; Urs MB, K.; Mandal, S.; Kamble, V. B. Underpinning the conductivity mechanism in wide bandgap metal organic framework through chemical sensing. *AIP Advances* **2020**, *10*, 085105.

212. Li, J.; Musho, T.; Bright, J.; Wu, N. Functionalization of a Metal-Organic Framework Semiconductor for Tuned Band Structure and Catalytic Activity. *Journal of The Electrochemical Society* **2018**, *166*, H3029.

213. Taddei, M.; Schukraft, G. M.; Warwick, M. E. A.; Tiana, D.; McPherson, M. J.; Jones, D. R.; Petit, C. Band gap modulation in zirconium-based metal–organic frameworks by defect engineering. *Journal of Materials Chemistry A* **2019**, *7*, 23781–23786.

214. Wang, Y. L.; Zhang, S.; Zhao, Y. F.; Bedia, J.; Rodriguez, J. J.; Belver, C. UiO-66-based metal organic frameworks for the photodegradation of acetaminophen under simulated solar irradiation. *Journal of Environmental Chemical Engineering* **2021**, *9*, 106087.

215. Syzgantseva, M. A.; Stepanov, N. F.; Syzgantseva, O. A. Effect of Ligand Functionalization on the Rate of Charge Carrier Recombination in Metal–Organic Frameworks: A Case Study of MIL-125. *The Journal of Physical Chemistry Letters* **2021**, *12*, 829–834.

216. Hlophe, P. V.; Dlamini, L. N. Synthesis of a semi-conductor-like MOF with black phosphorous as a composite for visible light-driven photocatalysis. *RSC Advances* **2019**, *9*, 37321–37330.

217. Butler, K. T.; Hendon, C. H.; Walsh, A. Electronic Chemical Potentials of Porous Metal–Organic Frameworks. *Journal of the American Chemical Society* **2014**, *136*, 2703–2706.

218. Baerends, E. J.; Gritsenko, O. V.; van Meer, R. The Kohn–Sham gap, the fundamental gap and the optical gap: the physical meaning of occupied and virtual Kohn–Sham orbital energies. *Physical Chemistry Chemical Physics* **2013**, *15*, 16408.

219. Mancuso, J. L.; Mroz, A. M.; Le, K. N.; Hendon, C. H. Electronic Structure Modeling of Metal–Organic Frameworks. *Chemical Reviews* **2020**, *120*, 8641–8715.

220. Janesko, B. G.; Henderson, T. M.; Scuseria, G. E. Screened hybrid density functionals for solid-state chemistry and physics. *Phys. Chem. Chem. Phys.* **2009**, *11*, 443–454.

221. Fabrizio, K.; Lazarou, K. A.; Payne, L. I.; Twight, L. P.; Golledge, S.; Hendon, C. H.; Brozek, C. K. Tunable Band Gaps in MUV-10(M): A Family of Photoredox-Active MOFs with Earth-Abundant Open Metal Sites. *Journal of the American Chemical Society* **2021**, *143*, 12609–12621.

222. Kalmutzki, M. J.; Hanikel, N.; Yaghi, O. M. Secondary building units as the turning point in the development of the reticular chemistry of MOFs. *Science Advances 4*, eaat9180.

223. Furukawa, H.; Cordova, K. E.; O'Keeffe, M.; Yaghi, O. M. The Chemistry and Applications of Metal-Organic Frameworks. *Science* **2013**, *341*, 1230444.

224. Ding, M.; Flaig, R. W.; Jiang, H.-L.; Yaghi, O. M. Carbon capture and conversion using metal–organic frameworks and MOF-based materials. *Chemical Society Reviews* **2019**, *48*, 2783–2828.

225. Hirao, H.; Ng, W. K. H.; Moeljadi, A. M. P.; Bureekaew, S. Multiscale Model for a Metal–Organic Framework: High-Spin Rebound Mechanism in the Reaction of the Oxoiron(IV) Species of Fe-MOF-74. *ACS Catalysis* **2015**, *5*, 3287–3291.

226. Vo, T. K.; Kim, J. Facile synthesis of magnetic framework composite MgFe2O4@UiO-66(Zr) and its applications in the adsorption–photocatalytic degradation of tetracycline. *Environmental Science and Pollution Research* **2021**,

227. Ding, J.; Yang, Z.; He, C.; Tong, X.; Li, Y.; Niu, X.; Zhang, H. UiO-66(Zr) coupled with Bi_2MoO_6 as photocatalyst for visible-light promoted dye degradation. *Journal of Colloid and Interface Science* **2017**, *497*, 126–133.

228. Zhou, L.; Liu, F.; Wang, J.; Chen, R.; Chen, Y. Effects of ligand functionalization on the band gaps and luminescent properties of a Zr_{12} oxo-cluster based metal–organic framework. *CrystEngComm* **2021**, *23*, 2961–2967.

229. Mu, X.; Jiang, J.; Chao, F.; Lou, Y.; Chen, J. Ligand modification of UiO-66 with an unusual visible light photocatalytic behavior for RhB degradation. *Dalton Transactions* **2018**, *47*, 1895–1902.

230. Wang, A.; Zhou, Y.; Wang, Z.; Chen, M.; Sun, L.; Liu, X. Titanium incorporated with UiO-66(Zr)-type Metal–Organic Framework (MOF) for photocatalytic application. *RSC Advances* **2016**, *6*, 3671–3679.

231. Wang, J.; Cherevan, A. S.; Hannecart, C.; Naghdi, S.; Nandan, S. P.; Gupta, T.; Eder, D. Ti-based MOFs: New insights on the impact of ligand composition and hole scavengers on stability, charge separation and photocatalytic hydrogen evolution. *Applied Catalysis B: Environmental* **2021**, *283*, 119626.

232. Hang, Z.; Yu, H.; Luo, L.; Huai, X. Nanoporous g-C3N4/MOF: high-performance photoinitiator for UV-curable coating. *Journal of Materials Science* **2019**, *54*, 13959–13972.

233. Chen, A.; Zhang, J.; Zhou, Y.; Tang, H. Preparation of a zinc-based metal–organic framework (MOF-5)/BiOBr heterojunction for photodegradation of Rhodamine B. *Reaction Kinetics, Mechanisms and Catalysis* **2021**, *134*, 1003–1015.

234. Yadav, A.; Panda, D. K.; Zhang, S.; Zhou, W.; Saha, S. Electrically Conductive 3D Metal–Organic Framework Featuring -Acidic Hexaazatriphenylene Hexacarbonitrile Ligands with Anion Interaction and Efficient Charge-Transport Capabilities. *ACS Applied Materials Interfaces* **2020**, *12*, 40613–40619.

235. Weinberg, D. R.; Gagliardi, C. J.; Hull, J. F.; Murphy, C. F.; Kent, C. A.; Westlake, B. C.; Paul, A.; Ess, D. H.; McCafferty, D. G.; Meyer, T. J. Proton-Coupled Electron Transfer. *Chemical Reviews* **2012**, *112*, 4016–4093.

236. Siegbahn, P. E. M.; Blomberg, M. R. A. Quantum Chemical Studies of Proton-Coupled Electron Transfer in Metalloenzymes. *Chemical Reviews* **2010**, *110*, 7040–7061.

237. Warren, J. J.; Tronic, T. A.; Mayer, J. M. Thermochemistry of Proton-Coupled Electron Transfer Reagents and its Implications. *Chemical Reviews* **2010**, *110*, 6961–7001.

238. Feher, G.; Allen, J. P.; Okamura, M. Y.; Rees, D. C. Structure and function of bacterial photosynthetic reaction centres. *Nature* **1989**, *339*, 111–116.

239. Yayla, H.; Knowles, R. Proton-Coupled Electron Transfer in Organic Synthesis: Novel Homolytic Bond Activations and Catalytic Asymmetric Reactions with Free Radicals. *Synlett* **2014**, *25*, 2819–2826.

240. *IUPAC Compendium of Chemical Terminology: Gold Book*, 2nd ed.; IUPAC: Research Triagle Park, NC, 2009.

241. Batzill, M. Fundamental aspects of surface engineering of transition metal oxide photocatalysts. *Energy Environmental Science* **2011**, *4*, 3275.

242. Copéret, C.; Chabanas, M.; Petroff Saint-Arroman, R.; Basset, J.-M. Homogeneous and Heterogeneous Catalysis: Bridging the Gap through Surface Organometallic Chemistry. *Angewandte Chemie International Edition* **2003**, *42*, 156–181.

243. Cui, X.; Li, W.; Ryabchuk, P.; Junge, K.; Beller, M. Bridging homogeneous and heterogeneous catalysis by heterogeneous single-metal-site catalysts. *Nature Catalysis* **2018**, *1*, 385–397.

244. Yin, Z.; Wan, S.; Yang, J.; Kurmoo, M.; Zeng, M.-H. Recent advances in post-synthetic modification of metal–organic frameworks: New types and tandem reactions. *Coordination Chemistry Reviews* **2019**, *378*, 500–512.

245. Tanabe, K. K.; Cohen, S. M. Engineering a Metal-Organic Framework Catalyst by Using Postsynthetic Modification. *Angewandte Chemie International Edition* **2009**, *48*, 7424–7427.

246. García-García, P.; Müller, M.; Corma, A. MOF catalysis in relation to their homogeneous counterparts and conventional solid catalysts. *Chemical Science* **2014**, *5*, 2979.

247. Drake, T.; Ji, P.; Lin, W. Site Isolation in Metal–Organic Frameworks Enables Novel Transition Metal Catalysis. *Accounts of Chemical Research* **2018**,

248. Otake, K.-i.; Ye, J.; Mandal, M.; Islamoglu, T.; Buru, C. T.; Hupp, J. T.; Delferro, M.; Truhlar, D. G.; Cramer, C. J.; Farha, O. K. Enhanced Activity of Heterogeneous Pd(II) Catalysts on Acid-Functionalized Metal–Organic Frameworks. *ACS Catalysis* **2019**, *9*, 5383–5390.

249. Feng, X.; Song, Y.; Chen, J. S.; Xu, Z.; Dunn, S. J.; Lin, W. Rational Construction of an Artificial Binuclear Copper Monooxygenase in a Metal–Organic Framework. *Journal of the American Chemical Society* **2021**, *143*, 1107–1118.

250. Wang, H.; Yuan, X.; Wu, Y.; Zeng, G.; Chen, X.; Leng, L.; Wu, Z.; Jiang, L.; Li, H. Facile synthesis of amino-functionalized titanium metal-organic frameworks and their superior visible-light photocatalytic activity for Cr(VI) reduction. *Journal of Hazardous Materials* **2015**, *286*, 187–194.

251. Fang, Y.; Ma, Y.; Zheng, M.; Yang, P.; Asiri, A. M.; Wang, X. Metal–organic frameworks for solar energy conversion by photoredox catalysis. *Coordination Chemistry Reviews* **2018**, *373*, 83–115.

252. Meng, Z.; Luo, J.; Li, W.; Mirica, K. A. Hierarchical Tuning of the Performance of Electrochemical Carbon Dioxide Reduction Using Conductive Two-Dimensional Metallophthalocyanine Based Metal–Organic Frameworks. *Journal of the American Chemical Society* **2020**, *142*, 21656–21669.

253. Fan, Y.; Ren, Y.; Li, J.; Yue, C.; Jiang, H. Enhanced Activity and Enantioselectivity of Henry Reaction by the Postsynthetic Reduction Modification for a Chiral Cu(salen)-Based Metal–Organic Framework. *Inorganic Chemistry* **2018**, *57*, 11986–11994.

254. Huang, R.; Peng, Y.; Wang, C.; Shi, Z.; Lin, W. A Rhenium-Functionalized Metal-Organic Framework as a Single-Site Catalyst for Photochemical Reduction of Carbon Dioxide: A Rhenium-Functionalized Metal-Organic Framework as a Single-Site Catalyst for Photochemical Reduction of Carbon Dioxide. *European Journal of Inorganic Chemistry* **2016**, *2016*, 4358–4362.

255. Celis-Salazar, P. J.; Epley, C. C.; Ahrenholtz, S. R.; Maza, W. A.; Usov, P. M.; Morris, A. J. Proton-Coupled Electron Transport in Anthraquinone-Based Zirconium Metal–Organic Frameworks. *Inorganic Chemistry* **2017**, *56*, 13741–13747.

256. Gaggioli, C. A.; Sauer, J.; Gagliardi, L. Hydrogen Atom or Proton Coupled Electron Transfer? C–H Bond Activation by Transition-Metal Oxides. *Journal of the American Chemical Society* **2019**, *141*, 14603–14611.

257. Horiuchi, Y.; Toyao, T.; Saito, M.; Mochizuki, K.; Iwata, M.; Higashimura, H.; Anpo, M.; Matsuoka, M. Visible-light-promoted photocatalytic hydrogen production by using an amino-functionalized Ti(IV) metal-organic framework. *Journal of Physical Chemistry C* **2012**, *116*, 20848–20853.

258. Shao, Z.; Wu, Q.; Han, X.; Zhao, Y.; Xie, Q.; Wang, H.; Hou, H. Proton coupled electron transfer: novel photochromic performance in a host–guest collaborative MOF. *Chemical Communications* **2019**, *55*, 10948–10951.

259. Liang, Z.; Qu, C.; Xia, D.; Zou, R.; Xu, Q. Atomically Dispersed Metal Sites in MOF-Based Materials for Electrocatalytic and Photocatalytic Energy Conversion. *Angewandte Chemie International Edition* **2018**, *57*, 9604–9633.

260. Llabrés i Xamena, F. X.; Corma, A.; Garcia, H. Applications for MetalOrganic Frameworks (MOFs) as Quantum Dot Semiconductors. *The Journal of Physical Chemistry C* **2007**, *111*, 80–85.

261. Ding, C.-W.; Luo, W.; Zhou, J.-Y.; Ma, X.-J.; Chen, G.-H.; Zhou, X.-P.; Li, D. Hydroxo Iron(III) Sites in a Metal–Organic Framework: Proton-Coupled Electron Transfer and Catalytic Oxidation of Alcohol with Molecular Oxygen. *ACS Applied Materials Interfaces* **2019**, *11*, 45621–45628.

262. Ghosh, S.; Castillo-Lora, J.; Soudackov, A. V.; Mayer, J. M.; Hammes-Schiffer, S. Theoretical Insights into Proton-Coupled Electron Transfer from a Photoreduced ZnO Nanocrystal to an Organic Radical. *Nano Letters* **2017**, *17*, 5762–5767.

263. Zhang, Z.; Yoshikawa, H.; Awaga, K. Monitoring the Solid-State Electrochemistry of Cu(2,7-AQDC) (AQDC = Anthraquinone Dicarboxylate) in a Lithium Battery: Coexistence of Metal and Ligand Redox Activities in a Metal–Organic Framework. *Journal of the American Chemical Society* **2014**, *136*, 16112–16115.

264. Kurtz, D. M. Oxo- and hydroxo-bridged diiron complexes: a chemical perspective on a biological unit. *Chemical Reviews* **1990**, *90*, 585–606.

265. Nasalevich, M. A.; Hendon, C. H.; Santaclara, J. G.; Svane, K.; van der Linden, B.; Veber, S. L.; Fedin, M. V.; Houtepen, A. J.; van der Veen, M. A.; Kapteijn, F.; Walsh, A.; Gascon, J. Electronic origins of photocatalytic activity in d 0 metal organic frameworks. *Scientific Reports* **2016**, *6*, 23676.

266. An, Y.; Xu, B.; Liu, Y.; Wang, Z.; Wang, P.; Dai, Y.; Qin, X.; Zhang, X.; Huang, B. Photocatalytic Overall Water Splitting over MIL-125(Ti) upon CoPi and Pt Co-catalyst Deposition. *ChemistryOpen* **2017**, *6*, 701–705.

267. Shen, L.; Luo, M.; Huang, L.; Feng, P.; Wu, L. A Clean and General Strategy To Decorate a Titanium Metal–Organic Framework with Noble-Metal Nanoparticles for Versatile Photocatalytic Applications. *Inorganic Chemistry* **2015**, *54*, 1191–1193.

268. Yuan, S.; Qin, J.-S.; Xu, H.-Q.; Su, J.; Rossi, D.; Chen, Y.; Zhang, L.; Lollar, C.; Wang, Q.; Jiang, H.-L.; Son, D. H.; Xu, H.; Huang, Z.; Zou, X.; Zhou, H.-C. [$Ti_8Zr_2O_{12}(COO)_{16}$] Cluster: An Ideal Inorganic Building Unit for Photoactive Metal–Organic Frameworks. *ACS Central Science* **2018**, *4*, 105–111.

269. Koopmans, T. Über die Zuordnung von Wellenfunktionen und Eigenwerten zu den Einzelnen Elektronen Eines Atoms. *Physica* **1934**, *1*, 104–113.

270. Janak, J. F. Proof that $\delta E/\delta n_i = \varepsilon$ in density-functional theory. *Physical Review B* **1978**, *18*, 7165–7168.

271. Pavlishchuk, V. V.; Addison, A. W. Conversion constants for redox potentials measured versus different reference electrodes in acetonitrile solutions at 25°C. *Inorganica Chimica Acta* **2000**, *298*, 97–102.

272. Harmata, A. S.; Spiller, T. E.; Sowden, M. J.; Stephenson, C. R. J. Photochemical Formal (4 + 2)-Cycloaddition of Imine-Substituted Bicyclo[1.1.1]pentanes and Alkenes. *Journal of the American Chemical Society* **2021**, *143*, 21223–21228.

273. Chen, T. Q.; Pedersen, P. S.; Dow, N. W.; Fayad, R.; Hauke, C. E.; Rosko, M. C.; Danilov, E. O.; Blakemore, D. C.; Dechert-Schmitt, A.-M.; Knauber, T.; Castellano, F. N.; MacMillan, D. W. C. A Unified Approach to Decarboxylative Halogenation of (Hetero)aryl Carboxylic Acids. *Journal of the American Chemical Society* **2022**, *144*, 8296–8305.

274. Jiang, Y.; Weiss, E. A. Colloidal Quantum Dots as Photocatalysts for Triplet Excited State Reactions of Organic Molecules. *Journal of the American Chemical Society* **2020**, *142*, 15219–15229.

275. Cai, M.; Loague, Q.; Morris, A. J. Design Rules for Efficient Charge Transfer in Metal-Organic Framework Films: The Pore Size Effect. *Journal of Physical Chemistry Letters* **2020**, *11*, 702–709.

276. Castner, A. T.; Su, H.; Svensson Grape, E.; Inge, A. K.; Johnson, B. A.; Ahlquist, M. S. G.; Ott, S. Microscopic Insights into Cation-Coupled Electron Hopping Transport in a Metal–Organic Framework. *Journal of the American Chemical Society* **2022**, *144*, 5910–5920.

277. Sun, C.; Yang, L.; Ortuño, M. A.; Wright, A. M.; Chen, T.; Head, A. R.; López, N.; Dincă, M. Spectroscopic Evidence of Hyponitrite Radical Intermediate in NO Disproportionation at a MOF-Supported Mononuclear Copper Site. *Angewandte Chemie International Edition* **2021**, anie.202015359–anie.202015359.

278. Castells-Gil, J.; Padial, N. M.; Almora-Barrios, N.; Silva, I. d.; Mateo, D.; Albero, J.; García, H.; Martí-Gastaldo, C. De novo synthesis of mesoporous photoactive titanium(IV)–organic frameworks with MIL-100 topology. *Chemical Science* **2019**, *10*, 4313–4321.

279. Howarth, A. J.; Peters, A. W.; Vermeulen, N. A.; Wang, T. C.; Hupp, J. T.; Farha, O. K. Best Practices for the Synthesis, Activation, and Characterization of Metal–Organic Frameworks. *Chemistry of Materials* **2017**, *29*, 26–39.

280. Romero-Angel, M.; Castells-Gil, J.; Rubio-Giménez, V.; Ameloot, R.; Tatay, S.; Martí-Gastaldo, C. Surfactant-assisted synthesis of titanium nanoMOFs for thin film fabrication. *Chemical Communications* **2021**, *57*, 9040–9043.

281. Walsh, A. Crystal Structures. **2021**,

282. Hanwell, M. D.; Curtis, D. E.; Lonie, D. C.; Vandermeersch, T.; Zurek, E.; Hutchison, G. R. Avogadro: an advanced semantic chemical editor, visualization, and analysis platform. *Journal of Cheminformatics* **2012**, *4*, 17.

283. Neese, F. Software update: The ORCA program system—Version 5.0. *WIREs Computational Molecular Science* **2022**, *12*, e1606.

284. Hu, S.; Liu, M.; Guo, X.; Li, K.; Han, Y.; Song, C.; Zhang, G. Effects of monocarboxylic acid additives on synthesizing metal-organic framework NH_2-MIL-125 with controllable size and morphology. *Crystal Growth and Design* **2017**, *17*, 6586–6595.

285. Sohail, M.; Yun, Y.-N.; Lee, E.; Kim, S. K.; Cho, K.; Kim, J.-N.; Kim, T. W.; Moon, J.-H.; Kim, H. Synthesis of Highly Crystalline NH_2 -MIL-125 (Ti) with S-Shaped Water Isotherms for Adsorption Heat Transformation. *Crystal Growth Design* **2017**, *17*, 1208–1213.

286. Marshall, C. R.; Timmel, E. E.; Staudhammer, S. A.; Brozek, C. K. Experimental evidence for a general model of modulated MOF nanoparticle growth. *Chemical Science* **2020**, *11*, 11539–11547.

287. Marshall, C. R.; Staudhammer, S. A.; Brozek, C. K. Size control over metal–organic framework porous nanocrystals. *Chemical Science* **2019**, *10*, 9396–9408.

288. Charton, M. *Steric Effects in Drug Design*; Topics in Current Chemistry; Springer Berlin Heidelberg: Berlin, Heidelberg, 1983; Vol. 114; p 57–91.

289. Kitao, T.; Zhang, Y.; Kitagawa, S.; Wang, B.; Uemura, T. Hybridization of MOFs and polymers. *Chemical Society Reviews* **2017**, *46*, 3108–3133.

290. Liu, G.; Chernikova, V.; Liu, Y.; Zhang, K.; Belmabkhout, Y.; Shekhah, O.; Zhang, C.; Yi, S.; Eddaoudi, M.; Koros, W. J. Mixed matrix formulations with MOF molecular sieving for key energy-intensive separations. *Nature Materials* **2018**, *17*, 283–289.

291. Chi, W. S.; Sundell, B. J.; Zhang, K.; Harrigan, D. J.; Hayden, S. C.; Smith, Z. P. Mixed-Matrix Membranes Formed from Multi-Dimensional Metal–Organic Frameworks for Enhanced Gas Transport and Plasticization Resistance. *ChemSusChem* **2019**, *12*, 2355–2360.

292. Knebel, A. et al. Solution processable metal–organic frameworks for mixed matrix membranes using porous liquids. *Nature Materials* **2020**,

293. Denny, M. S.; Cohen, S. M. In Situ Modification of Metal–Organic Frameworks in Mixed-Matrix Membranes. *Angewandte Chemie International Edition* **2015**, *54*, 9029–9032.

294. Li, X.; Zhang, Y.; Xin, Q.; Ding, X.; Zhao, L.; Ye, H.; Lin, L.; Li, H.; Zhang, Y. NH_2-MIL-125 filled mixed matrix membrane contactor with SO_2 enrichment for flue gas desulphurization. *Chemical Engineering Journal* **2022**, *428*, 132595.

295. Friebe, S.; Mundstock, A.; Unruh, D.; Renz, F.; Caro, J. NH_2-MIL-125 as membrane for carbon dioxide sequestration: Thin supported MOF layers contra Mixed-Matrix-Membranes. *Journal of Membrane Science* **2016**, *516*, 185–193.

296. Waqas Anjum, M.; Bueken, B.; De Vos, D.; Vankelecom, I. F. J. MIL-125(Ti) based mixed matrix membranes for CO_2 separation from CH_4 and N_2. *Journal of Membrane Science* **2016**, *502*, 21–28.

297. Schimpf, A. M.; Gunthardt, C. E.; Rinehart, J. D.; Mayer, J. M.; Gamelin, D. R. Controlling Carrier Densities in Photochemically Reduced Colloidal ZnO Nanocrystals: Size Dependence and Role of the Hole Quencher. *Journal of the American Chemical Society* **2013**, *135*, 16569–16577.

298. Schimpf, A. M.; Lounis, S. D.; Runnerstrom, E. L.; Milliron, D. J.; Gamelin, D. R. Redox Chemistries and Plasmon Energies of Photodoped In_2O_3 and Sn-Doped In_2O_3 (ITO) Nanocrystals. *Journal of the American Chemical Society* **2015**, *137*, 518–524.

299. Araujo, J. J.; Brozek, C. K.; Kroupa, D. M.; Gamelin, D. R. Degenerately n-Doped Colloidal PbSe Quantum Dots: Band Assignments and Electrostatic Effects. *Nano Letters* **2018**, *18*, 3893–3900.

300. Araujo, J. J.; Brozek, C. K.; Liu, H.; Merkulova, A.; Li, X.; Gamelin, D. R. Tunable Band-Edge Potentials and Charge Storage in Colloidal Tin-Doped Indium Oxide (ITO) Nanocrystals. *ACS Nano* **2021**, *15*, 14116–14124.

301. Mancuso, J. L.; Fabrizio, K.; Brozek, C. K.; Hendon, C. H. On the limit of proton-coupled electronic doping in a Ti(IV)-containing MOF. *Chemical Science* **2021**, 10.1039.D1SC03019A.

302. Ameis, R.; Kremer, S.; Reinen, D. Jahn-Teller effect of Ti^{3+} in octahedral coordination: a spectroscopic study of hexachlorotitanate ($TiCl_6^{3-}$) complexes. *Inorganic Chemistry* **1985**, *24*, 2751–2754.

303. Ballhausen, C. J. *Introduction to Ligand Field Theory*; McGraw Hill Publishing Co.: New York, 1962.

304. Harris, D. C.; Bertolucci, M. D. *Symmetry and spectroscopy: an introduction to vibrational and electronic spectroscopy*; Dover Publications: New York, 1989.

305. Morozan, A.; Jaouen, F. Metal organic frameworks for electrochemical applications. *Energy Environmental Science* **2012**, *5*, 9269.

306. Zhong, H.; Ly, K. H.; Wang, M.; Krupskaya, Y.; Han, X.; Zhang, J.; Zhang, J.; Kataev, V.; Buechner, B.; Weidinger, I. M.; Kaskel, S.; Liu, P.; Chen, M.; Dong, R.; Feng, X. A Phthalocyanine-Based Layered Two-Dimensional Conjugated Metal-Organic Framework as a Highly Efficient Electrocatalyst for the Oxygen Reduction Reaction. *Angewandte Chemie-International Edition* **2019**, *58*, 10677–10682.

307. Yang, J.; Ye, H.; Zhao, F.; Zeng, B. A Novel Cu_xO Nanoparticles@ZIF-8 Composite Derived from Core–Shell Metal–Organic Frameworks for Highly Selective Electrochemical Sensing of Hydrogen Peroxide. *ACS Applied Materials Interfaces* **2016**, *8*, 20407–20414.

308. Xia, B. Y.; Yan, Y.; Li, N.; Wu, H. B.; Lou, X. W.; Wang, X. A metal–organic framework-derived bifunctional oxygen electrocatalyst. *Nature Energy* **2016**, *1*, 15006.

309. Marshall, C. R.; Dvorak, J. P.; Twight, L. P.; Chen, L.; Kadota, K.; Andreeva, A. B.; Overland, A. E.; Ericson, T.; Cozzolino, A. F.; Brozek, C. K. Size-Dependent Properties of Solution-Processable Conductive MOF Nanocrystals. *Journal of the American Chemical Society* **2022**,

310. Rinehart, J. D.; Schimpf, A. M.; Weaver, A. L.; Cohn, A. W.; Gamelin, D. R. Photochemical Electronic Doping of Colloidal CdSe Nanocrystals. *Journal of the American Chemical Society* **2013**, *135*, 18782–18785.

311. Kamat, P. V. Manipulation of Charge Transfer Across Semiconductor Interface. A Criterion That Cannot Be Ignored in Photocatalyst Design. *The Journal of Physical Chemistry Letters* **2012**, *3*, 663–672.

312. Chen, M.; Dong, H.; Xue, M.; Yang, C.; Wang, P.; Yang, Y.; Zhu, H.; Wu, C.; Yao, Y.; Luo, W.; Zou, Z. Faradaic junction and isoenergetic charge transfer mechanism on semiconductor/semiconductor interfaces. *Nature Communications* **2021**, *12*, 6363.

313. Tvrdy, K.; Frantsuzov, P. A.; Kamat, P. V. Photoinduced electron transfer from semiconductor quantum dots to metal oxide nanoparticles. *Proceedings of the National Academy of Sciences* **2011**, *108*, 29–34.

314. Yang, K.; Yang, Z.; Zhang, C.; Gu, Y.; Wei, J.; Li, Z.; Ma, C.; Yang, X.; Song, K.; Li, Y.; Fang, Q.; Zhou, J. Recent advances in CdS-based photocatalysts for CO_2 photocatalytic conversion. *Chemical Engineering Journal* **2021**, *418*, 129344.

315. Soloviev, V. N.; Eichhöfer, A.; Fenske, D.; Banin, U. Molecular Limit of a Bulk Semiconductor: Size Dependence of the "Band Gap" in CdSe Cluster Molecules. *Journal of the American Chemical Society* **2000**, *122*, 2673–2674.

316. Harman, T. C.; Strauss, A. J. Band Structure of HgSe and HgSe–HgTe Alloys. *Journal of Applied Physics* **1961**, *32*, 2265–2270.

317. Shustova, N. B.; Cozzolino, A. F.; Reineke, S.; Baldo, M.; Dincă, M. Selective Turn-On Ammonia Sensing Enabled by High-Temperature Fluorescence in Metal–Organic Frameworks with Open Metal Sites. *Journal of the American Chemical Society* **2013**, *135*, 13326–13329.

318. Dolgopolova, E. A.; Rice, A. M.; Martin, C. R.; Shustova, N. B. Photochemistry and photophysics of MOFs: steps towards MOF-based sensing enhancements. *Chemical Society Reviews* **2018**, *47*, 4710–4728.

319. Son, H.-J.; Jin, S.; Patwardhan, S.; Wezenberg, S. J.; Jeong, N. C.; So, M.; Wilmer, C. E.; Sarjeant, A. A.; Schatz, G. C.; Snurr, R. Q.; Farha, O. K.; Wiederrecht, G. P.; Hupp, J. T. Light-Harvesting and Ultrafast Energy Migration in Porphyrin-Based Metal–Organic Frameworks. *Journal of the American Chemical Society* **2013**, *135*, 862–869.

320. Martin, C. R.; Leith, G. A.; Kittikhunnatham, P.; Park, K. C.; Ejegbavwo, O. A.; Mathur, A.; Callahan, C. R.; Desmond, S. L.; Keener, M. R.; Ahmed, F.; Pandey, S.; Smith, M. D.; Phillpot, S. R.; Greytak, A. B.; Shustova, N. B. Heterometallic Actinide-Containing Photoresponsive Metal-Organic Frameworks: Dynamic and Static Tuning of Electronic Properties. *Angewandte Chemie International Edition* **2021**, *60*, 8072–8080.

321. Cornell, H. D.; Zhu, Y.; Ilic, S.; Lidman, N. E.; Yang, X.; Matson, J. B.; Morris, A. J. Green-light-responsive metal–organic frameworks for colorectal cancer treatment. *Chemical Communications* **2022**, *58*, 5225–5228.

322. Nguyen, H. L.; Gándara, F.; Furukawa, H.; Doan, T. L. H.; Cordova, K. E.; Yaghi, O. M. A Titanium–Organic Framework as an Exemplar of Combining the Chemistry of Metal– and Covalent–Organic Frameworks. *Journal of the American Chemical Society* **2016**, *138*, 4330–4333.

323. Maza, W. A.; Morris, A. J. Photophysical Characterization of a Ruthenium(II) Tris(2,2-bipyridine)-Doped Zirconium UiO-67 Metal–Organic Framework. *The Journal of Physical Chemistry C* **2014**, *118*, 8803–8817.

324. Andreeva, A. B.; Le, K. N.; Kadota, K.; Horike, S.; Hendon, C. H.; Brozek, C. K. Cooperativity and Metal–Linker Dynamics in Spin Crossover Framework Fe(1,2,3-triazolate)$_2$. *Chemistry of Materials* **2021**, *33*, 8534–8545.

325. Murray, C. B.; Norris, D. J.; Bawendi, M. G. Synthesis and characterization of nearly monodisperse CdE (E = sulfur, selenium, tellurium) semiconductor nanocrystallites. *Journal of the American Chemical Society* **1993**, *115*, 8706–8715.

326. Fabrizio, K.; Brozek, C. Photoredox-Active Colloids and Polymer Membranes of Titanium-Based MOF Nanoparticles. **2022**,

327. Varshni, Y. P. Temperature dependence of the energy gap in semiconductors. *Physica* **1967**, *34*, 149–154.

328. Zeier, W. G.; Zevalkink, A.; Gibbs, Z. M.; Hautier, G.; Kanatzidis, M. G.; Snyder, G. J. Thinking Like a Chemist: Intuition in Thermoelectric Materials. *Angewandte Chemie International Edition* **2016**, *55*, 6826–6841.

329. O'Donnell, K. P.; Chen, X. Temperature dependence of semiconductor band gaps. *Applied Physics Letters* **1991**, *58*, 2924–2926.

330. Fabrizio, K.; Le, K. N.; Andreeva, A. B.; Hendon, C. H.; Brozek, C. K. Determining Optical Band Gaps of MOFs. *ACS Materials Letters* **2022**, *4*, 457–463.

331. Jong, M. d.; Seijo, L.; Meijerink, A.; Rabouw, F. T. Resolving the ambiguity in the relation between Stokes shift and Huang–Rhys parameter. *Physical Chemistry Chemical Physics* **2015**, *17*, 16959–16969.

332. Whalley, L. D.; van Gerwen, P.; Frost, J. M.; Kim, S.; Hood, S. N.; Walsh, A. Giant Huang–Rhys Factor for Electron Capture by the Iodine Intersitial in Perovskite Solar Cells. *Journal of the American Chemical Society* **2021**, *143*, 9123–9128.

333. Huang, K.; Rhys, A.; Mott, N. F. Theory of light absorption and non-radiative transitions in F-centres. *Proceedings of the Royal Society of London. Series A. Mathematical and Physical Sciences* **1950**, *204*, 406–423.

334. Shangkum, G. Y.; Chammingkwan, P.; Trinh, D. X.; Taniike, T. Design of a Semi-Continuous Selective Layer Based on Deposition of UiO-66 Nanoparticles for Nanofiltration. *Membranes* **2018**, *8*, 129.

335. Katz, M. J.; Brown, Z. J.; Colón, Y. J.; Siu, P. W.; Scheidt, K. A.; Snurr, R. Q.; Hupp, J. T.; Farha, O. K. A facile synthesis of UiO-66, UiO-67 and their derivatives. *Chemical Communications* **2013**, *49*, 9449–9451.

336. Schejn, A.; Balan, L.; Falk, V.; Aranda, L.; Medjahdi, G.; Schneider, R. Controlling ZIF-8 nano- and microcrystal formation and reactivity through zinc salt variations. *CrystEngComm* **2014**, *16*, 4493–4500.

337. Chen, C.; Ozcan, A.; Yazaydin, A. O.; Ladewig, B. P. Gas permeation through single-crystal ZIF-8 membranes. *Journal of Membrane Science* **2019**, *575*, 209–216.

338. Liu, X.; Demir, N. K.; Wu, Z.; Li, K. Highly Water-Stable Zirconium Metal–Organic Framework UiO-66 Membranes Supported on Alumina Hollow Fibers for Desalination. *Journal of the American Chemical Society* **2015**, *137*, 6999–7002.

339. Balakrishnan, J.; L K, P.; D, S.; Jagtap, A.; Madapu, K. K.; Dhara, S.; Rao, K. S. R. K. Temperature- and size-dependent photoluminescence in colloidal CdTe and $Cd_xZn_{1-x}Te$ quantum dots. *Journal of Physics D: Applied Physics* **2021**, *54*, 145103.

340. Schmitt-Rink, S.; Miller, D. A. B.; Chemla, D. S. Theory of the linear and nonlinear optical properties of semiconductor microcrystallites. *Physical Review B* **1987**, *35*, 8113–8125.

341. Perebeinos, V.; Chan, S.-W.; Zhang, F. 'Madelung model' prediction for dependence of lattice parameter on nanocrystal size. *Solid State Communications* **2002**, *123*, 295–297.

342. Chen, B.; Penwell, D.; Benedetti, L. R.; Jeanloz, R.; Kruger, M. B. Particle-size effect on the compressibility of nanocrystalline alumina. *Physical Review B* **2002**, *66*, 144101.

343. Abdullah, B. J.; Omar, M. S.; Jiang, Q. Size dependence of the bulk modulus of Si nanocrystals. *Sādhanā* **2018**, *43*, 174.

344. Liang, L.; Ma, H.; Wei, Y. Size-Dependent Elastic Modulus and Vibration Frequency of Nanocrystals. *Journal of Nanomaterials* **2011**, *2011*, 670857.

345. Hartwig, J. *Organotransition Metal Chemistry: From Bonding to Catalysis*; 2010.

346. Bersuker, I. B. *The Jahn-Teller Effect and Vibronic Interactions in Modern Chemistry*; Modern Inorganic Chemistry; Springer US: Boston, MA, 1984.

347. Venkataraman, G. Soft modes and structural phase transitions. *Bulletin of Materials Science* **1979**, *1*, 129–170.

348. Chakravarty, C.; Debenedetti, P. G.; Stillinger, F. H. Lindemann measures for the solid-liquid phase transition. *The Journal of Chemical Physics* **2007**, *126*, 204508.

349. Leguy, A. M.; Goñi, A. R.; Frost, J. M.; Skelton, J.; Brivio, F.; Rodríguez-Martínez, X.; Weber, O. J.; Pallipurath, A.; Alonso, M. I.; Campoy-Quiles, M.; Weller, M. T.; Nelson, J.; Walsh, A.; Barnes, P. R. Dynamic disorder, phonon lifetimes, and the assignment of modes to the vibrational spectra of methylammonium lead halide perovskites. *Physical Chemistry Chemical Physics* **2016**, *18*, 27051–27066.

350. Panzer, F.; Li, C.; Meier, T.; Köhler, A.; Huettner, S. Impact of Structural Dynamics on the Optical Properties of Methylammonium Lead Iodide Perovskites. *Advanced Energy Materials* **2017**, *7*, 1–11.

351. Gould, S. L.; Tranchemontagne, D.; Yaghi, O. M.; Garcia-Garibay, M. A. Amphidynamic Character of Crystalline MOF-5: Rotational Dynamics of Terephthalate Phenylenes in a Free-Volume, Sterically Unhindered Environment. *Journal of the American Chemical Society* **2008**, *130*, 3246–3247.

352. Liu, Z.; Wang, Y.; Garcia-Garibay, M. A. Rotational Dynamics of an Amphidynamic Zirconium Metal–Organic Framework Determined by Dielectric Spectroscopy. *The Journal of Physical Chemistry Letters* **2021**, *12*, 5644–5648.

353. Brozek, C. K.; Dincă, M. Lattice-imposed geometry in metal–organic frameworks: lacunary Zn_4O clusters in MOF-5 serve as tripodal chelating ligands for Ni2+. *Chem. Sci.* **2012**, *3*, 2110–2110.

354. Leus, K.; Vandichel, M.; Liu, Y. Y.; Muylaert, I.; Musschoot, J.; Pyl, S.; Vrielinck, H.; Callens, F.; Marin, G. B.; Detavernier, C.; Wiper, P. V.; Khimyak, Y. Z.; Waroquier, M.; Van Speybroeck, V.; Van Der Voort, P. The coordinatively saturated vanadium MIL-47 as a low leaching heterogeneous catalyst in the oxidation of cyclohexene. *Journal of Catalysis* **2012**, *285*, 196–207.

355. Leus, K.; Muylaert, I.; Vandichel, M.; Marin, G. B.; Waroquier, M.; Van Speybroeck, V.; Van der Voort, P. The remarkable catalytic activity of the saturated metal organic framework V-MIL-47 in the cyclohexene oxidation. *Chemical communications (Cambridge, England)* **2010**, *46*, 5085–5087.

356. Allendorf, M. D.; Stavila, V.; Witman, M.; Brozek, C. K.; Hendon, C. H. What Lies beneath a Metal–Organic Framework Crystal Structure? New Design Principles from Unexpected Behaviors. *Journal of the American Chemical Society* **2021**, *143*, 6705–6723.

357. Bunting, J. W.; Thong, K. M. Stability constants for some 1:1 metal–carboxylate complexes. *Canadian Journal of Chemistry* **1970**, *48*, 1654–1656.

358. Huang, C. Y.; Wang, T.; Gai, F. Temperature dependence of the CN stretching vibration of a nitrile-derivatized phenylalanine in water. *Chemical Physics Letters* **2003**, *371*, 731–738.

359. Dobrawa, R.; Würthner, F. Metallosupramolecular approach toward functional coordination polymers. *Journal of Polymer Science Part A: Polymer Chemistry* **2005**, *43*, 4981–4995.

360. Lewis, A. K. d. K.; Caddick, S.; Cloke, F. G. N.; Billingham, N. C.; Hitchcock, P. B.; Leonard, J. Synthetic, Structural, and Mechanistic Studies on the Oxidative Addition of Aromatic Chlorides to a Palladium (*N*-Heterocyclic Carbene) Complex: Relevance to Catalytic Amination. *Journal of the American Chemical Society* **2003**, *125*, 10066–10073.

361. Brozek, C. K.; Ozarowski, A.; Stoian, S. A.; Dincă, M. Dynamic structural flexibility of Fe-MOF-5 evidenced by ^{57}Fe Mössbauer spectroscopy. *Inorg. Chem. Front.* **2017**, *4*, 782–788.

362. Walton, K. S.; Snurr, R. Q. Applicability of the BET method for determining surface areas of microporous metal-organic frameworks. *J. Am. Chem. Soc.* **2007**, *129*, 8552–8552.

363. Buckingham, A. D. The quadrupole moment of the carbon dioxide molecule. 15.

364. Buckingham, A. D.; Disch, R. L.; Dunmur, D. A. Quadrupole moments of some simple molecules. *Journal of the American Chemical Society* **1968**, *90*, 3104–3107.

365. Bůžek, D.; Demel, J.; Lang, K. Zirconium Metal–Organic Framework UiO-66: Stability in an Aqueous Environment and Its Relevance for Organophosphate Degradation. *Inorganic Chemistry* **2018**, *57*, 14290–14297.

366. Cox, B. G.; Garcia-Rosas, J.; Schneider, H. Solvent dependence of the stability of cryptate complexes. *Journal of the American Chemical Society* **1981**, *103*, 1384–1389.

367. Gutmann, V. Solvent effects on the reactivities of organometallic compounds. *Coordination Chemistry Reviews* **1976**, *18*, 225–255.

368. Perdew, J. P.; Burke, K.; Ernzerhof, M. Generalized Gradient Approximation Made Simple. *Physical Review Letters* **1996**, *77*, 3865–3868.

369. Kresse, G.; Furthmüller, J. Efficiency of ab-initio total energy calculations for metals and semiconductors using a plane-wave basis set. *Computational Materials Science* **1996**, *6*, 15–50.

370. Kresse, G.; Hafner, J. Ab initio molecular dynamics for liquid metals. *Physical Review B* **1993**, *47*, 558–561.

371. Kresse, G.; Furthmüller, J. Efficient iterative schemes for ab initio total-energy calculations using a plane-wave basis set. *Physical Review B* **1996**, *54*, 11169–11186.

372. Ibarra, I. A.; Yang, S.; Lin, X.; Blake, A. J.; Rizkallah, P. J.; Nowell, H.; Allan, D. R.; Champness, N. R.; Hubberstey, P.; Schröder, M. Highly porous and robust scandium-based metal–organic frameworks for hydrogen storage. *Chemical Communications* **2011**, *47*, 8304.

373. Grape, E. S.; Flores, J. G.; Hidalgo, T.; Martínez-Ahumada, E.; Gutiérrez-Alejandre, A.; Hautier, A.; Williams, D. R.; O'Keeffe, M.; Öhrström, L.; Willhammar, T.; Horcajada, P.; Ibarra, I. A.; Inge, A. K. A Robust and Biocompatible Bismuth Ellagate MOF Synthesized Under Green Ambient Conditions. *Journal of the American Chemical Society* **2020**, *142*, 16795–16804.

374. Xiang, W.; Ren, J.; Chen, S.; Shen, C.; Chen, Y.; Zhang, M.; Liu, C.-j. The metal–organic framework UiO-66 with missing-linker defects: A highly active catalyst for carbon dioxide cycloaddition. *Applied Energy* **2020**, *277*, 115560.

375. Jackson, A. J.; Skelton, J. M.; Hendon, C. H.; Butler, K. T.; Walsh, A. Crystal structure optimisation using an auxiliary equation of state. *The Journal of Chemical Physics* **2015**, *143*, 184101.

376. Dette, C.; Pérez-Osorio, M. A.; Kley, C. S.; Punke, P.; Patrick, C. E.; Jacobson, P.; Giustino, F.; Jung, S. J.; Kern, K. TiO_2 Anatase with a Bandgap in the Visible Region. *Nano Letters* **2014**, *14*, 6533–6538.